Monitoring sismique et sismoélectrique d'un milieux poreux non-consolidé

Julia Holzhauer

École doctorale des Sciences Exactes et leurs Applications (ED 211)

Université de Pau et des Pays de l'Adour

THÈSE

pour l'obtention du grade de

DOCTEUR de l'Université de Pau et des Pays de l'Adour

Spécialité: "Géophysique"

présentée et soutenue publiquement par

Julia HOLZHAUER

le 02 juillet 2015

Monitoring sismique et sismoélectrique d'un milieux poreux non-consolidé

Seismic and seismoelectric monitoring of an unconsolidated porous medium

Directeur de thèse : **M. Jean-Paul CALLOT**, Professeur, UPPA
Co-encadrant de thèse : **M. Daniel BRITO**, Maître de conférences, UPPA
Co-encadrant de thèse : **Mme Clarisse BORDES**, Maître de conférences, UPPA

Jury

Mme Laurence JOUNIAUX,	Directrice de recherche, Université de Strasbourg	Rapporteur
M. Stéphane GARAMBOIS,	Maître de conférences, ISTerre Grenoble	Rapporteur
XXX,	XXX	Examinateur
YYY,	YYY	Examinateur

UPPA
Laboratoire des Fluides Complexes et leurs Réservoirs (LFCR)
UMR CNRS 5150, BP 1155, F-64013 Pau Cedex, France

Table des matières

Abstract

Seismic propagation within porous media is usually associated with wave attenuation and dispersion phenomena related to fluid flow. Under certain circumstances, it may also be correlated to a conversion of seismic into electromagnetic energy known as "seismoelectric". The understanding of seismoelectric phenomena, combining the theory of electrokinetic to Biot's poroelasticity, relies mainly on the formulation by Pride [1994]. On basis of these "theoretical" developments, Pride and Haartsen [1996] defined a transfer function expressing the link between the coseismic seismoelectric field and the seismic acceleration at its origin. We propose a quantitative analysis of coseismic seismoelectric couplings with the purpose of validating Pride's theory and generalizing it to partially saturated media. With this aim in view we developed a laboratory experiment involving an adjustable device for electric acquisitions, conducted within the kilohertz range on unconsolidated quartz sand. Experimental data were subsequently processed in both time and frequency domains, enabling a full analysis that embraces phase velocities, attenuations and transfer functions.

The conducted experiments focused on the impact of fluid conductivity and water saturation with regard to the coseismic seismoelectric phenomenon. Time-lapse monitoring were accordingly run under varying salinity or water content. In all scenarios, the quantitative analysis of the electric-to-seismic amplitude ratio $E/\ddot{u}$ appeared in good agreement with theoretical projections. Moreover, investigations of saturation variations, ranging from the residual water saturation ($S_w = 0.3$) to full saturation, showed that: i) the behavior of attenuations and transfer functions are directly related to fluid distribution, that greatly impacts the mechanical properties of the medium ; ii) in the very peculiar case of unconsolidated media, polarity inversion of the coseismic seismoelectric field may be experienced.

KEY-WORDS: coseismic seismoelectric, poroelasticity, electrokinetic phenomena, partial saturation, experimental geophysics.

Résumé

La propagation sismique dans les milieux poreux est classiquement associée à des phénomènes de dispersion et d'atténuation des ondes sous l'effet des mouvements fluides. Dans certaines conditions, celle-ci peut également être associée à une conversion d'énergie sismique en énergie électromagnétique dite 'sismoélectrique'. La théorie des phénomènes sismoélectriques associant la théorie de l'électrocinétique à la poroélasticité de Biot, repose en grande partie sur les développements de Pride [1994]. Sur la base de ces développements théoriques, Pride and Haartsen [1996] relient le champ électrique cosismique à l'accélération sismique qui le génère par une fonction de transfert. Nous proposons une étude quantitative des couplages sismoélectriques en vue de valider la théorie de Pride et sa généralisation en milieu non saturé. Dans ce but, nous avons développé une expérience en laboratoire sur un sable de quartz, menée dans la gamme du kilohertz sur la base d'un dispositif d'acquisition électrique modulable. Deux méthodes de traitement des signaux sont proposées, l'une temporelle, l'autre spectrale, permettant d'obtenir une analyse complète des vitesses de phase, atténuations et fonctions de transfert.

Les expériences réalisées se sont focalisées sur l'étude du rôle de la conductivité du fluide et de la saturation en eau dans le phénomène sismoélectrique cosismique. Une étude time-lapse a ainsi pu être réalisée dans des situations de changements de salinité et de contenu en eau. Dans tous les contextes, l'étude quantitative des rapports d'amplitudes des champs sismoélectriques et sismiques $E/\ddot{u}$ montre une bonne corrélation avec les prédictions théoriques. Par ailleurs, l'étude des variations de saturation dans une gamme allant de la saturation résiduelle en eau ($S_w = 0.3$) à la saturation totale, montre que : i) les atténuations et fonctions de transfert ont des comportements reliés à la distribution des fluides qui influencent fortement les propriétés mécaniques du milieu ; ii) une inversion de polarité du champ sismoélectrique peut être observée dans le cas très particulier des milieux non consolidés.

MOTS-CLEFS : sismoélectrique cosismique, poroélasticité, phénomènes électro-cinétiques, saturation partielle, géophysique expérimentale.

Chapitre 1

Introduction

Sommaire

Seismoelectromagnetic effects appear when a porous medium, formed from a solid frame filled by a fluid possibly multiphase of low to moderate salinity, is excited by a seismic wave. Due to an electrokinetic coupling initiating at the grain-fluid boundary, the induced movements from the saline fluid relatively to the frame produces a charge separation giving rise to a propagating electromagnetic field said to be "coseismic" (figure 1.1). According to the nature of the original seismic excitation, the propagating coseismic field may be electric (mainly related to a compressional P-wave), or magnetic (mainly resulting from a rotational S-wave); in both cases the seismoelectromagnetic manifestations will propagate similarly to the supporting seismic wave and will be affected by the medium properties - of either hydraulic, elastic or electric nature - in its immediate vicinity.

When the incident acoustic wave meets a discontinuity affecting the pore space in any geometrical or chemical manner (should it be a change in matrix density or a brutal variation of fluid conductivity), a seismoelectromagnetic effect of a second kind might be observed. Indeed, according to Maxwell's laws of field continuity, an electromagnetic field traversing an interface can be accommodated by a combined discontinuity of the tangential component of the magnetic field and the normal component of the electric field. Hence, to accommodate the discontinuity-induced disruption of the propagating coseismic seismoelectromagnetic wave, an electromagnetic wave acting as a vertical dipole should theoretically appear at relevant interfaces. This signal, referred to as "interfacial" and propagating at light-speed, would

typically display on the seismoelectrogram as a horizontal arrival (see figure 1.2). Yet due to its dipole nature this electromagnetic signal carrying remote information fades out rapidly, so that its detection remains challenging and its relevance still restricted to particular conditions.

Interestingly, the electrokinetic coupling also works in reverse, so that the application of an electromagnetic perturbation may induce relative pore/fluid movements causing eventually the apparition of a seismic wave. This interrelated effect is known as the "electroseismic" or "electroosmosis" phenomenon. While both the coseismic and the interfacial effects are

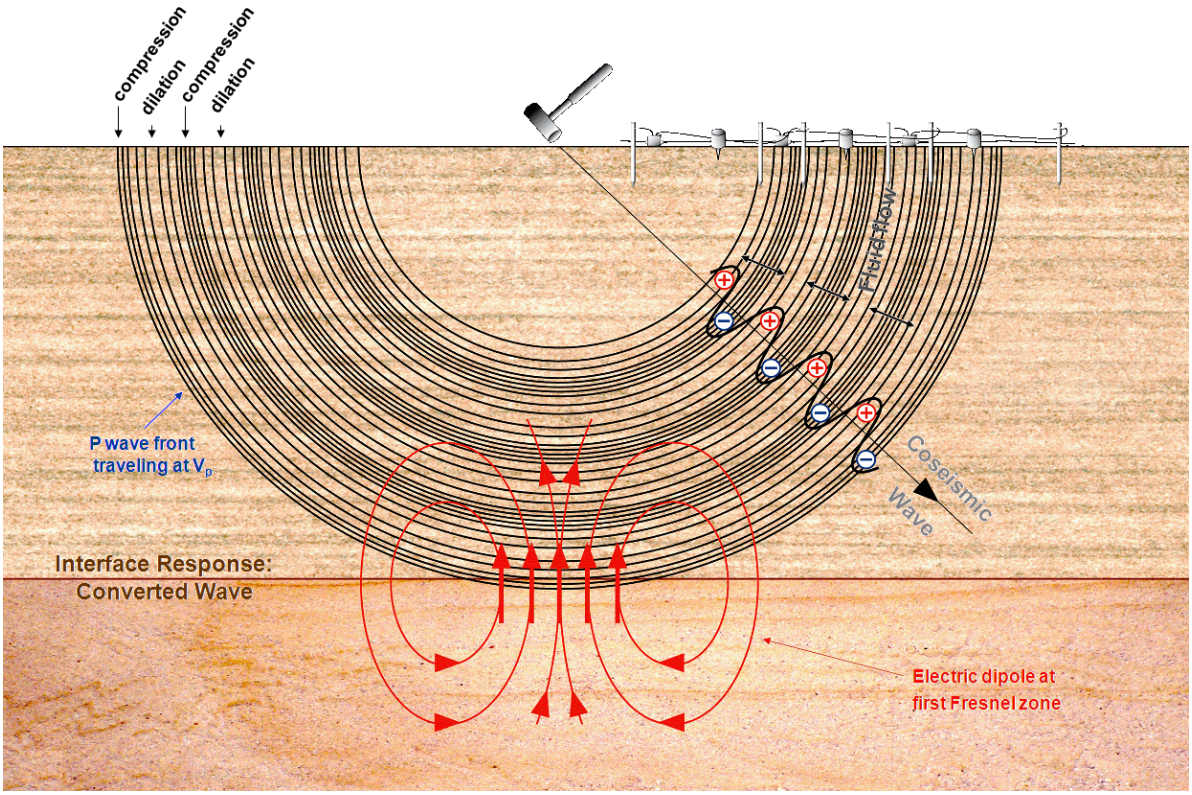

Figure 1.1: Seismoelectric effects associated with seismic propagation in a saturated porous medium : (1) Seismically induced fluid flow from compression to dilation zone creates a streaming current, the coseismic electric field, propagating together with the compression wave. (2) Heterogeneities in the coseismic field due to the incident wave front hitting an interface are adjusted by a vertical electric dipole created at the first Fresnel zone beneath the shot-point.

schematically pictured in figure 1.1 from the seismoelectric view, in our present study we will focus on the coseismic seismoelectric field in close relation to the propagating compressional P-wave. Next section proposes a global overview on the seismoelectric state of art, tackling the various aspects of theory, laboratory observations, field measurements, data processing and numerical modeling with a special eye for the coseismic seismoelectric phenomenon.

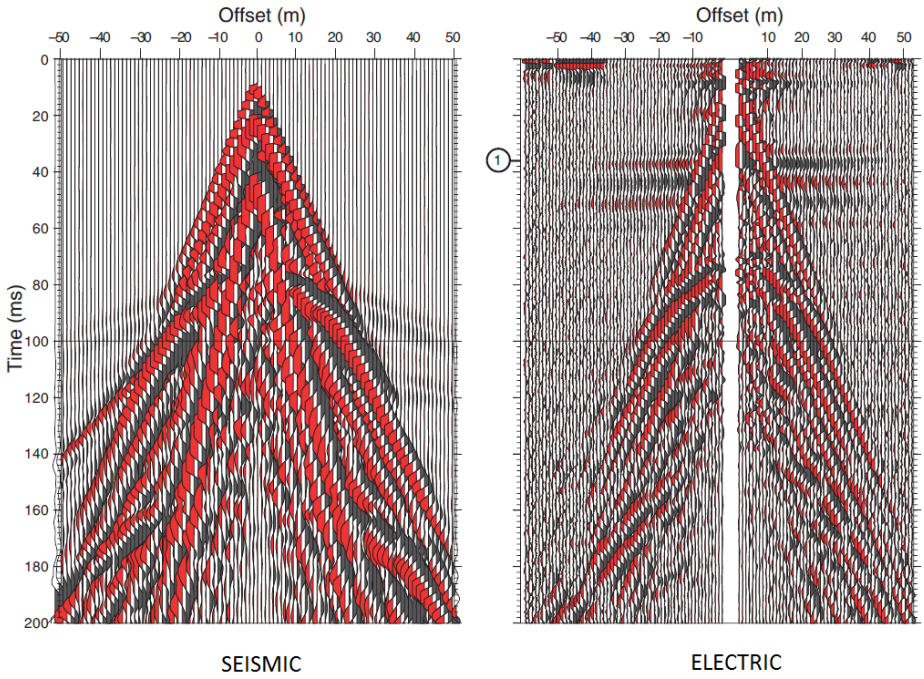

Figure 1.2: Seismic and seismoelectric supergathers revealing an electric record very similar to the seismic (coseismic part), as well as an interfacial effect displaying as a flat arrival noted (1). Trace spacing is $1m$ and the root mean-square amplitude of each trace has been normalised to be the same value (from Dupuis et al. [2007]).

1.1 State of the art regarding the coseismic seismoelectric field

1.1.1 Historical background

The first mention of the possible combined use of seismic and electric surveys (electric field monitoring during seismic excitation) are mentioned as early as the 1930s. Following observations by Blau and Statham [1936], Thompson [1936] suggested using the combination (producing what he refers to as the seismic-electric effect) as an exploration tool. At that time, however, he was merely thinking in terms of seismically induced resistivity modulation and not electrokinetic coupling. A few years later Ivanov made similar field observations and besides the hypothesis of an acoustically induced resistivity modulation he also proposed a possible electrokinetic coupling effect he called seismic-electric effect of the second kind [Ivanov, 1939] - [Ivanov, 1940].

Frenkel [1944], attempted to develop a quantitative theory to explain Ivanov's observations. He formulated the first complete set of equations governing the acoustics of isotropic porous media. But some errors and simplifications prevented him from enunciating a fully valid theory of poroelasticity [Pride and Garambois, 2005], as Biot would achieve a decade later. Nevertheless, Frenkel's analysis did already account for the coseismic component of the seismoelectric phenomena, while his interest seems to have provoked the first surge of investigation into poroelasticity. In his 1956 papers, Biot [1956a] - [Biot, 1956b] divides his consideration on the linear theory of porous media acoustics into two distinct frequency domains with regard to the validity of Poiseuille flow assumption by introducing the Biot

critical frequency. He stated the existence of one rotational (*S-type*) and two dilatational (*P-type*) waves, subsequently referred to as *P-fast* and *P-slow*, the latter highly dispersive and diffusive resembling heat conduction. In a later paper Biot [1962a] emphasizes the role this slow wave could play in electrokinetic effects, regarding the enhanced fluid velocity it induces within the pores. The next theoretical step to couple Biot's theory with electrokinetics and to account for Onsager's reciprocity was taken by Neev and Yeatts [1989]. But, in accordance with Frenkel's approach, they did not consider the full set of Maxwell's equation, leading to the ignoring of any seismomagnetic effect. The breakthrough of seismoelectromagnetics was finally enabled by Pride's formulation of the underlying theory, as described hereafter.

1.1.2 Theory

The theoretical background for seismoelectric phenomena was provided by Pride [1994] who proposed a set of equations based on Biot's theory including electrokinetic coupling and Maxwell's equations. Among other things, his theory accounts for Biot's slow wave, confirms the generation of an electric field by *P-waves* and predicts the appearance of its magnetic counterpart with traveling *S-waves*. In light of this complete theory, the first dynamic transfer functions for the coseismic seismoelectric field were proposed a few years later by Pride and Haartsen [1996] for both transverse and longitudinal waves. Using low-frequency assumptions, Garambois and Dietrich [2001] proposed a linear expression linking the coseismic electric field to the seismic acceleration, applicable to field measurements at seismic frequencies. For the coseismic magnetic field, unobserved at that point, they predicted a rough proportionality to the grain velocity. Ultimately, theoretical investigations enforced by observations confirmed the role of the Biot slow-wave in the enhancement of the seismoelectric response, proving of particular relevance in the detection of thin layers [Pride and Garambois, 2002]. Lately, seismic interferometry methods using Green functions [Wapenaar et al., 2006; Wapenaar and Fokkema, 2006; Slob and Wapenaar, 2007] have been adapted to provide impulsive seismoelectric response of the porous medium equivalent to usual transfer functions. This method was first implemented for interfacial [Wapenaar et al., 2008; De Ridder et al., 2009] and coseismic [Schoemaker et al., 2012] seismoelectric before being extended by Gao and Hu [2010] to the seismomagnetic aspects.

Pride's theory being originally formulated for a fully-saturated porous medium, one important improvement concerns its adaptation to partial saturation conditions. While Biot poroelasticity relations may be adjusted by defining effective fluid properties (Teja and Rice [1981] - Wood [1955] - Brie et al. [1995]), saturation-dependency of electrokinetics is still discussed. It has been the subject of numerous theoretical developments initially proposed for the continuous spontaneous potential, some based on volume-averaging methods [Linde et al., 2007; Revil et al., 2007] others capillary models [Jackson, 2008, 2010], the first highlighting the role of the electrolyte wettability while the other focuses on the thickness of the electrical double layer. Yet, to account for experimental observations, further empirical laws are often required [Guichet et al., 2003; Allègre et al., 2012]. Eventually, the question of partial saturation has been directly broached under a seismoelectric angle [Revil et al., 2013; Warden et al., 2013]. These saturation-dependent aspects, of particular interest in the

context of our work, will be detailed in following chapter.

The interfacial seismoelectric also resorted to theoretical development for calculation of seismic to electric energy conversion. Ray theory was indeed implemented by White [2005] for mathematical asymptotic description of interfacial electroseismic phenomena, while Schakel and Smeulders [2010] appealed to the concept of effective densities. Both approaches enabled the determination of adapted reflection and transmission coefficients at the interface.

1.1.3 Laboratory observations

The first seismoelectric lab observations were conducted as early as the 1960's in the former Soviet Union. From the start these studies dealt with the impact of fluid properties on seismoelectric observations. One group in particular, led by Parkhomenko [1971], proposed that electric amplitudes increase with water content until reaching the optimal saturation, which would correspond to the completion of the bound water content, before marking a slight decrease [Parkhomenko et al., 1964]. In a further work Parkhomenko and Gaskarov [1971] combined saturation variation to changes in the fluid conductivity and qualitatively observed the diminution of the coseismic seismoelectric response with increasing salinity. These type of seismoelectric lab experiment were eventually resumed by Ageeva et al. [1999] who introduced additional frequency variations. They observed that the ratio of the electric field to the liquid-phase pressure at various frequencies varied directly with water content and residual saturation and inversely with salinity, porosity and permeability.

About this period, a MIT group took a new approach by developing a borehole lab apparatus involving Stoneley waves (*i.e.* surface wave composed of *P*- and *SV-waves* ideally causing electric as well as magnetic coseismic effects) in which they observed coseismic and interfacial seismoelectric signals, as well as electroosmosis [Zhu et al., 1999]. They later conducted innovative crosshole measurements using two small-scale boreholes separated by a fracture with adjustable aperture that generated interfacial signals showing amplitudes depending on the fracture aperture [Zhu and Toksöz, 2003]. Further experimental measurements of seismoelectric interface response were performed by Schakel et al. [2011a] [Schakel et al. [2011c] - Schakel et al. [2011b] - Smeulders et al. [2014]] that eventually aimed at a quantitative description of the conversion phenomenon.

On their borehole laboratory model, Zhu and Toksöz [2005] finally reported the observation of seismomagnetic coseismic signals using a Hall-effect sensor (the use of such sensor ideally preventing the detection of magnetic signals induced by the transient nature of seismoelectric fields). Contemporaneously, quantitative measurements led by Bordes [2005] in an underground low-noise laboratory confirmed experimentally the existence of the coseismic seismomagnetic field and its dependency on shear-waves, as predicted by Pride's theory [Bordes et al., 2006] -[Bordes et al., 2008]. Due to its dimness, the observation of the seismomagnetic signal have only been achieved under controlled lab conditions and not yet reported in the field.

In the meantime Zhu et al. [2000] investigated experimentally the coseismic electric amplitudes dependency to fluid conductivity and concluded to its decreasing with increasing fluid conductivity. They refined that conclusion a few years later, as they worked with very

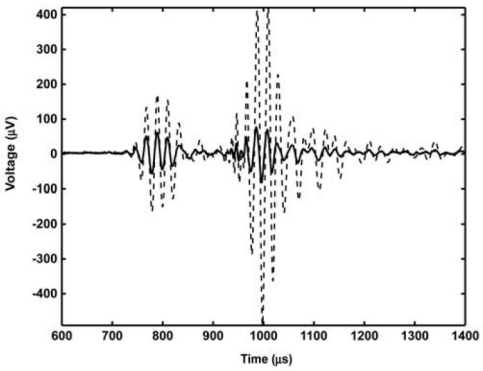

Figure 1.3: Times series of the seismoelectric signal measured at 35 cm from the source in loose glass microspheres for conductivities of 0.0052 S/m in dashed line and 0.12 s/m in plain line (from Block and Harris [2006]).

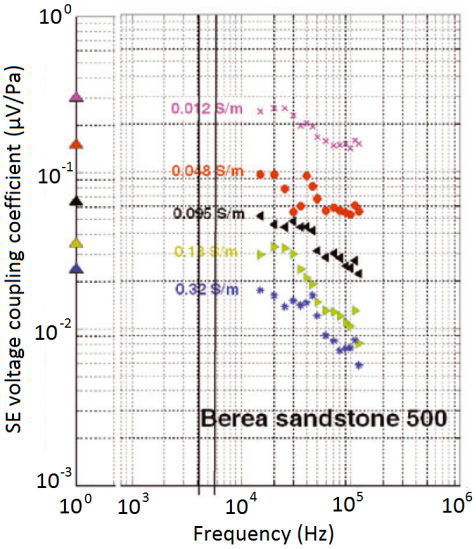

Figure 1.4: Measured DC coupling coefficients and seismoelectric voltage coupling coefficients at high frequencies ($15 - 120\ kHz$) for Berea sandstone saturated with NaCl solution of the different concentrations shown by the different colours and different values (from Zhu and Toksöz [2013]).

low salinities, by stating that this behaviour was typical for a double layer saturated by counterions, while it would be reversed as long as the electrical double layer would lack counterions [Zhu and Toksoz, 2003]. A further experiments on similar aspects, conducted by Block and Harris [2006] in a sand column, confirming the expected tendency of electric amplitudes to diminish with increasing conductivity (figure 1.3). Finally Zhu and Toksöz [2013] conducted extensive and quantitative dynamic measurements of seismoelectric coupling coefficient under varying salinity ($0.1 - 0.3\ S/m$): the seismoelectric coupling would decrease with increasing salinity and increasing frequency (figure 1.4). Results of these last two studies will be shown further in this work. Aside from conductivity, Bordes [2005] performed some laboratory observations with regard to water content and observed a local maximum in coseismic amplitudes associated to the vadose zone next to the water front in the low frequency domain. Yet, recent extensive measurements of coseismic seismoelectric signal with water saturation by Bordes et al. [2015] within the [0.3 - 0.9] range showed a seismoelectric ratio $E/\ddot{u}$ rather stable despite large saturation variations (figure 1.5).

Note that the streaming potential, more extensively investigated under varying fluid condition than seismoelectric, may also be considered as a coseismic seismoelectric signal at the zero-frequency limit. Viewed from this point, many results obtained on streaming potential laboratory studies may be relevant for seismoelectric[1]. Hence, while Ishido and Mizutani [1981] investigated the impact of many fluid parameters such as pH, temperature and salinity on the zeta potential of different rocks, Jouniaux and Pozzi [1995] studied the permeability dependency of streaming potentials to various fluid conductivities and observed an increase in permeability related to the variation of surface conductivity. Reppert et al. [2001] reported

[1]It would be relevant for static low-frequency approximation but may even be integrated to the complete dynamic seismoelectric formulation when affecting frequency-independent parameters as the electrokinetic coupling coefficent C_{EK}.

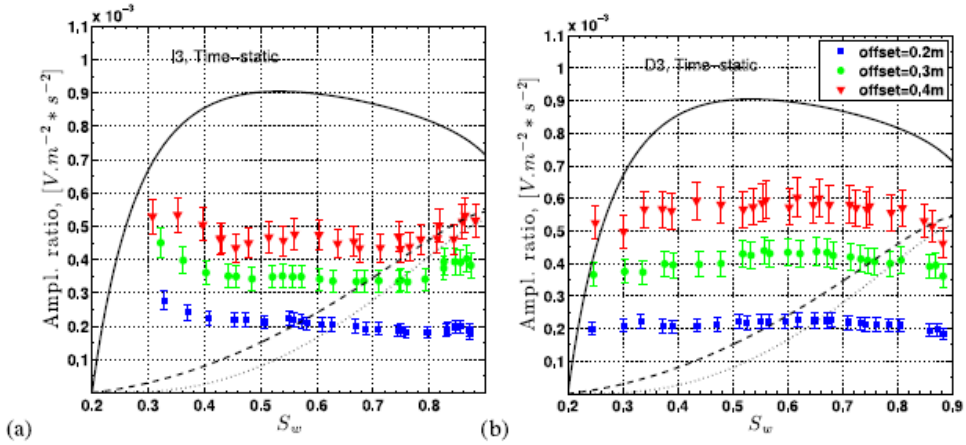

Figure 1.5: Amplitude ratio from seismoelectric to seismic field as a function of S_w measured on uncompacted Landes sand during the third cycle of imbibition (I3) and drainage (D3) at offsets = 0.2m (blue square), at offsets = 0.3m (green circle)and offset = 0.4m (red triangles). The amplitude ratios are obtained by picking the maximal amplitude in the time signal (from Bordes et al. [2015]).

on the frequency dependency of both streaming potential and electroosmosis in capillaries; in particular they demonstrated that electroosmosis coupling coefficients become frequency dependent when evolving to inertial flow , a transition which depend on capillary radius [Reppert and Morgan, 2002]. Guichet et al. [2003] conducted first electrokinetic experiments under partial saturation in a sand-column filled with Fontainebleau sand and concluded to a linear dependency of the electrokinetic coupling on saturation. The experiment has been further developed by Allègre et al. [2010] who presented a continuous monitoring with saturation of the electrokinetic coupling coefficient. Instead of linear variations, they observed a maximum value of the absolute electrokinetic coupling coefficient at an incomplete water saturation of $0.6 - 0.8$ visible in figure 1.6.

As we know, the seismoelectric method has its counterpart in the electroseismic phenomenon, where fluid motion induced through electric excitation leads to the propagation of an acoustic wave within the porous media. As already mentioned, a first qualitative experiment by Zhu et al. [1999] enabled the observation of an electrically generated Stoneley wave. A further quantitative attempt was reported by Deckman et al. [2005]: in contradiction with the prevailing theory by Pride [1994], stating that seismoelectric and electroosmosis coupling coefficients should be identical with regards to Onsager's reciprocity, their results pointed at distinct values of coupling coefficients for both regime.

1.1.4 Field measurements

Following Frenkel's and Biot's work on poroelasticity, seismoelectric field measurements have gradually been reported in the scientific literature starting from the 50's. This first surge includes Martner and Sparks [1959] who first observed interfacial seismoelectric response, whereas Broding et al. [1963] focused on the observability of coseismic seismoelectric response while Long and Rivers [1975] intended to explain seismoelectric observation as resistivity modulations. Concomitantly, many seismoelectric investigations were undertaken in the former Soviet Union as reported by Neishtadt et al. [2006].

The rebirth of seismoelectrics, after a first bloom between the late 30's and the early 70's,

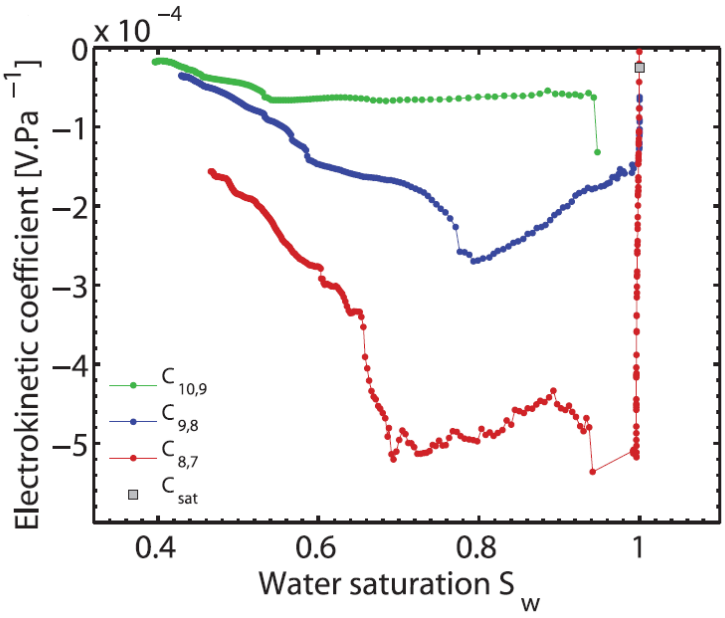

Figure 1.6: Raw (*i.e.* non-normalized) electrokinetic coefficient $C_{EK}(S_w)$ for drainage experiment on silica sand. The grey square is measured at full saturation and equals $-2.5\ \mu V.Pa^{-1}$ (from Allègre et al. [2010]).

begins with the ground-breaking work of Thompson and Gist [1993], in trying to validate the seismoelectric method as a reservoir exploration tool. As well as detecting interfacial seismoelectric signals at the record depth of 300 m, they also ran the first electroosmotic field measurements, injecting 150 A through a 300 m active dipole using 15 m^2 of buried aluminium foil. They reported a greater sensitivity of electroosmosis to low permeability rocks, the opposite of their seismoelectric result which showed larger signals from high permeability rocks. The increased efficiency of the electroseismic conversion over the seismoelectric conversion led them to concentrate their efforts in this area. This research group developed a complete electroseismic surveying system and confirmed the potential of the electroseismic method for reservoir (gas sand) characterization, with conversions recorded at depths of up to 1000 m depth; further second-order electroseismic conversions, apparently stemming from carbonate oil reservoirs at even greater depth, were detected but are not yet fully understood [Thompson et al., 2007].

Indeed with the publication of Pride [1994] theory, the understanding, recognition and optimisation of the seismoelectric measurement grow central. Hence, as Butler et al. [1996] observed nearly simultaneous arrivals at widely separated receivers they tested the electrokinetic nature of this interfacial seismoelectric signal by discriminating other possible phenomena (such as piezoelectricity or resistivity modulation to which they first also referred to as being "seismoelectric" - Russell et al. [1997]). Characteristics such as the linearity to the square root of source energy and polarity change of this electric signal regarding to the source position, supported its electrokinetic origin [Butler et al., 1999]. About the same time, Beamish [1999], who already reported on seismoelectric potentials and advances in a review paper [Beamish and Peart, 1998], conducted extensive field studies with systematic comparative data acquisition. He experimented on electrode nature (steel or lead rods and un-polarisable electrodes) and dipole length. He stated that the inner electrode controls both amplitude and character of the received electric signal. He also experimented with various

electrode layouts, exploiting phase asymmetry to improve the signal/noise separation. Original trench-experiment by Haines et al. [2007] (described further in this section) enabled to disclose the previously undocumented direct field, sort of interfacial response taking place directly beneath the hammer plate due to soil compaction, as well as to observe the Lorentz field induced by moving hammer plate within the earth's magnetic field. Finally, extensive field work were undertaken by Strahser [2006], who concentrated on optimizing seismoelectric field measurement techniques and identifying different terrains suitability to seismoelectric investigations. Along with slowness, EM-wave polarisation were brought up as possible distinctive feature [Strahser et al., 2007] for extraction of interface response. The measuring of vertical and transverse dipoles along the horizontal profile, in complement to the usual radial ones, enabled to test this polarisation assumption, which remained inconclusive. On a similar surface profile,

Yet, stimulated by Thompson and Gist [1993] results numerous seismoelectric field investigations concentrated on the interface response, being made especially appealing as instantaneous interfacial seismoelectric signals, if observable, may precede the seismic arrival, potentially enabling earthquake prediction. Hence, Garambois and Dietrich [2001], Strahser et al. [2007], Dupuis et al. [2007] and Dean and Dupuis [2011] were successively able to identify interface responses generated at the water table. On occasions, the interface response would be attributed to the vadose zone, a partially-saturated and shallow thin-layer unresolved by seismic Dupuis et al. [2007]. A further study [Kulessa et al., 2006] implemented this method for glacier exploration, eventually gaining insight into the glacier structure and its basal dynamic. In the meanwhile, in an attempt at separating the coseismic from the interface response, Haines [2004] proposed an original field layout involving horizontally stratified layers-geometries achieved by digging and filling trenches as to position the surface receptors "below" the custom-made interface. By doing so, the first arrival would consist in a unspoiled interfacial response. However the observability of the interface response remained quite deceiving: though evidence of seismic to electric conversions at the water-table were often reported the observation remained near-surface no matter the seismic energy involved[2].

In matter of coseismic seismoelectric, downhole seismoelectrics (or VSEP for Vertical SeismoElectric Profiling) has rapidly been given consideration for providing a new local logging tool. Indeed, first investigations of that kind had already been reported by Parkhomenko and Gaskarov [1971] in the early 70's. Since that early stage, VSEP has proved to be capable of detecting changes in porosity within the same clay unit after having the electric data normalised by the seismic acceleration or velocity (providing a local $E/\ddot{u}$, resp. $E/\dot{u}$, ratio) and corrected from the conductivity log [Dupuis and Butler, 2006], which appeared to be inversely correlated to the $E/\dot{u}$ ratio (see figure 1.7. Similar results were obtained by [Mikhailov et al., 2000] regarding coseismic sensitivity to porosity for a propagating Stoneley wave (generated by direct hammering of the surface casing), while permeability seemed to affect the behaviour of the seismoelectric coupling coefficient (later known as L_{EK}). Renewed borehole observations by Guan et al. [2013] confirmed the preferential impact of porosity on

[2]As in Dean and Dupuis [2011] study were a 30.000 kg vibrator source was necessary to correctly image a water-table by 15 m depth

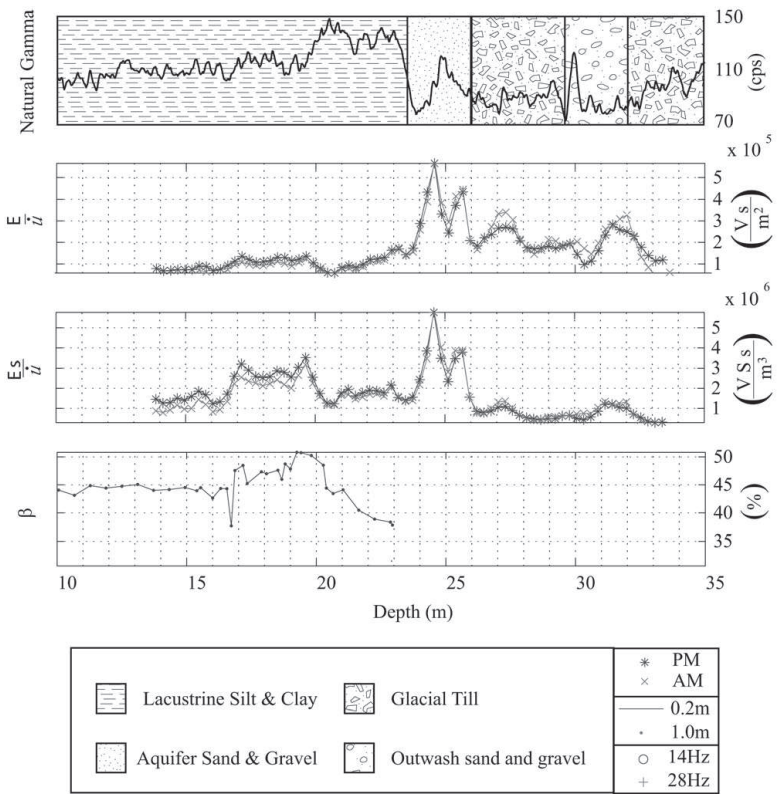

Figure 1.7: Comparison of seismoelectric log normalised by seismic velocity $E/\dot{u}$, to logs of natural gamma, porosity (notedβ) or to itself when normalised by conductivity ($E\,s/\dot{u}$).

$E/\ddot{u}$, while permeability seemed to affect the phase tangent to this ratio, picking at a distinctive frequency that decreases with increasing permeability (as does the Biot characteristic frequency). For other data sets the main dependency seemed to be on pH (directly impacting the ζ potential) followed by porosity, instead of fluid's conductivity [Strahser, 2006]. On coseismic surface profile, Strahser et al. [2011] also observed the dependency of coseismic seismoelectric to water-content in-field. Finally, diverting the borehole seismoelectric from it initial coseismic purpose, Dupuis et al. [2009] used the dense vertical sampling provided by downhole electrode array for investigating the generation of the interface response: they observed its spatial and temporal polarity reversal, while showing the polarity dependency on the growth rate of the source zone at the interface (including vertical extent).

1.1.5 Data processing

Seismoelectric data processing usually tackles two main issues : first the removal of anthropogenic noise on the electric and /or magnetic records, second the signal selection enabling the extraction of identified arrivals of interest, or in this specific case, the separation of the interface from the coseismic seismoelectric response.

Relatively to noise removal, an adaptive filtering procedure for powerline harmonics reduction has been proposed [Butler and Russell, 1993], using either a sinusoidal subtraction based on Fourier transform or an empirical block subtraction. An evolved form of the sinusoidal subtraction, referred to as "frequency revision", was lately published by the same authors [Butler and Russell, 2003]: its main advantage over the previous filter is to allow

for slight variation of the powerline fundamental frequency and to be valid for any window length. Occasionally, a remote electric reference was used to remove telluric current [Thompson and Gist, 1993] - [Mikhailov et al., 1997] - [Mikhailov et al., 2000]. Another empirical approach for coherent noise subtraction consists in using the phase asymmetry of the seismoelectric signal about the shotpoint to apply phase difference filtering [Thompson and Gist, 1993] - [Beamish, 1999]. For particularly robust man-made noise, Beamish reported the use of a delay-line filter [Beamish, 1999].

As to signal selection, we have to distinguish between the extraction of coseismic or interface seismoelectric. Concerning the extrusion of the interfacial response from seismoelectric records, most available techniques appeal to the propagation velocity contrast between pure EM and seismic waves. Those velocity filters can be implemented as frequency-wavenumber f-k filters [Strahser et al., 2007], or applied in the Radon domain filtering (filter, also referred to as τ-p) [Haines, 2004]. In both cases, simultaneous arrivals will be projected on the ordinate axis and can be selected by truncating all the arrivals with move-outs. Yet those methods conserve part of the coseismic information that has been attributed infinite apparent velocity, as is typical for signals at the summit of reflection hyperbolas. A more efficient extraction of interface response may be achieved by prediction error filter, which combines a velocity filter to assumptions on the amplitude and characteristic pattern of the (dipolar) wanted signal, hence relying on empirical parameter determination through extensive experimentation [Haines et al., 2007]. Finally the method of the continuous wavelet transform (CWT or curvelets), exposed by Warden [2012] and Warden et al. [2012], takes advantage from the likeness of the coseismic signal to actual seismic: the seismic component is used for prediction of the coseismic electric waveform enabling its complete retrieval or suppression from the electric record.

1.1.6 Numerical modelling

The first seismoelectric modeling attempt drawing upon Pride's theory was reported by his working group in the mid 90's [Haartsen, 1995] - [Haartsen and Pride, 1997]. This model numerically determined the full-waveform seismoelectric response in a stratified porous media using a global matrix method. By enabling the simultaneous solving of both the mechanical and electromagnetic problem, these first simulations report the decoupling of the seismoelectromagnetic wave into two sets of vertical ($PSVTM$) and horizontal ($SHTE$) polarisation of the wave system, giving ways to seismoelectric and seismomagnetic fields respectively. A further 1D approach by Garambois and Dietrich [2002], relying on Pride's theory, is based on the calculation of the seismic reflection and transmission coefficients at each layer boundaries. This model, also accounting for Biot slow wave enables separate representation of the coseismic and the interfacial seismoelectric signal. An important result was the identification of the interface-portion involved in the generations of seismoelectromagnetic wave conversions as being the first Fresnel zone. It has been eventually adapted to partial saturation conditions by means that are to be described in coming chapter [Warden et al. [2013] - Zyserman et al. [2015]]. Further 1D models were proposed by Grobbe and Slob [2013], who developed a code adapted to analytical simulation of seismoelectric and electroseismic based

on explicit homogeneous space solutions, and by Gao and Hu [2010] under consideration of a double couple source typical of earthquake generation.

In parallel, the first 2D approaches were launched. The first attempt came again from Pride's group [Haines and Pride, 2006]: using a finite-difference algorithm, they computed the first seismoelectric model accounting for realistic subsurface heterogeneities. Yet for simplification's sake, they had to neglect seismomagnetic phenomena and to solve the fluid/matrix displacement and the resulting electric current sequentially, disregarding Onsager's reciprocity. Simplification of the simulation by electrokinetic decoupling had already proved relevant for analytical modelling [Hu et al., 2007], in this case though neglecting the reverse coupling, model confirmed the importance of Biot slow wave for seismoelectric detection of thin layers and dike geometries. A further 2D modelling using finite difference in sequential approach have been subsequently proposed by Singarimbun et al. [2009]. In the meanwhile, the finite element method (FEM) was implemented to perform 2D simulation of full-waveform electroseismic [Zyserman et al., 2010] or seismoelectric [Revil and Jardani, 2010] predictions. Last, a 2D-model computed by using FEM multiphysics software allows for real coupled solution by taking Onsager's reciprocity into account [Kröger et al., 2014]. The impending simulations accounts for all three kinds of seismoelectric effects predicted by the theory and actually observed in-field - direct, coseismic and interface response while providing an improved understanding of the seismoelectric wave generation especially at confined units, yet it neglects the Biot slow wave.

This various simulations enabled sensitivity analysis depending on various parameter contrasts ranging from electric to mechanical properties. It could numerically be ascertained that porosity, permeability, as well as fluid's viscosity and conductivity should count among the most influential parameters in the generation of the interfacial EM signal, ahead of other parameters like densities, elastic moduli, dielectric permittivities, temperature and tortuosity [Garambois and Dietrich, 2002]. The converted EM wave should be particularly sensitive to strong porosity or fluid salinity contrast [Garambois and Dietrich, 2002] - [Kröger, 2007]. Looking specifically at boreholes, other numerical studies, focusing on Stoneley waves at kiloherz frequencies, showed an almost linear increase of acoustic to electric conversion rate $E/\ddot{u}$ with the logarithm of permeability as well as a slight increase in this same ratio for an increase in porosity [Zhu et al., 2008]. These results have to be compared to the analytical solution offered by Mikhailov [1998] for identical wave type, where $E/\ddot{u}$ was said to be highly dependent on porosity and nearly insensitive to permeability below Biot critical frequency.

As a conclusion, when it comes to the modeling of the seismoelectric effects, one is still restricted to the forward simulation. But different existing models have successfully accounted for at least both the coseismic and the converted electromagnetic field. Many of these models still have to be validated and parameterised by predicting field observation on well-known test-fields.

1.2 Aim of the thesis

From preceding literature overview, no to mention its inherent electrokinetic nature, we may understand that seismoelectric has generally been expected to show some aptitudes for hydraulic characterization of porous media. Hence, among the new developing geophysical methods, seismoelectric may eventually become a tool for reservoir characterisation combining seismic and electric imaging abilities. Yet, such perspective requires a comprehensive understanding of the underlying phenomena and their dependency to involved medium parameters, as well as the preliminary development of reliable quantitative measuring.

With this prospect, the central aim of this work was to perform quantitative measurements of the coseismic seismoelectric field for comparison to predictions by Pride [1994]. Our object of testing will be the coseismic seismoelectric transfer function identified as the $E/\ddot{u}$ ratio, as such measurements of the electric field and the seismic acceleration will demand equal precision. Finally, for the data to be properly simulated we need to characterize the medium: in this light, the controlled environment of a sandbox experiment appears best-suited.

As this laboratory investigation was developed after the respective works by Barrière et al. [2012] and Bordes et al. [2015] regarding saturation-dependent behaviour of seismic attenuation and coseismic seismoelectric field relatively to the theory of poroelasticity, our further ambition is to complete both studies. Practically, this objective demands to widen the frequency domain of investigation and extend the saturation-dependent observations to full saturation conditions. To interpret the seismic information we will resort to usual seismic attributes - as velocity dispersion, attenuation or inverse quality factor - and extend them to coseismic seismoelectric characterization.

From a material point of view, this experiment requires short wavelengths for propagation observation at sub-metric laboratory dimension. With its moderate propagation velocity and its granular matrix easily described by granular models, unconsolidated quartz sand appears particularly adapted to our purpose. Yet such dispersive media might challenge the extension of our experimental frequency-band to several kilohertz. Under such condition, frequency-band extension might be achieved by stacking signals. As a conclusion, the acoustic source should be wide-band (either by being extremely impulsive or sinusoidal), highly reproducible and necessarily low EM-noise.

Once the source-related issues solved, we will proceed to the coseismic seismoelectric measurements. First variations in the $E/\ddot{u}$ ratio will be imposed by the easily adjustable fluid conductivity, which impact on seismoelectric field has been widely documented. A conclusive comparison to Pride's model prediction would validate our experiment and authorize the monitoring under variable saturation conditions.

1.3 Thesis outlines

The present thesis work will be divided into five additional chapters. Next chapter, being Chapter 2, will begin with generalities on porous medium parameters. It will subsequently

introduces general electrokinetics concepts as well as Biot's poroelasticity and Pride's seismoelectric theory. In relation to those models, general limitations will be addressed, before developing partial saturation approaches and looking for additional sources of seismic attenuation in possible relation to grain friction. Next, we will run a sensitivity analysis on the dynamic expression by Pride [1994] of the coseismic seismoelectric relatively to hydraulic, elastic or electric parameters of the porous medium. Eventually we will investigate the origin of a possible polarity inversion of the coseismic electric field under partial saturation and prove its connection with fluid distribution.

Chapter 3 will be more technical, as it will present our experimental set-up with details on measurements protocols, source characteristics and sandbox instrumentation among others. In this section we will also define the attributes of our unconsolidated sand, partly on basis of laboratory measurements, partly on literature and granular models prediction. These parameters will lately serve in the computation of Pride prediction for comparisons to actual experimental data.

In Chapter 4, a first part presents the different methods employed for signal processing in both time and frequency domain. Following the description of first arrival selection, we will see how velocity dispersion, attenuation and inverse quality factor, all common seismic attributes, may be calculated in the spectral domain. All methods will be tested on a simple propagating synthetic. In a second part, we will appeal to real experimental data for optimisation of the coseismic seismoelectric field reconstruction from original electric potential records. By adjusting the length and the position of the electric dipole relatively to its corresponding accelerometer, we will see how similar either records can get.

In Chapter 5 the results from seismoelectric acquisitions at variable saturation will be exposed. It will begin with a classical seismic approach, addressing velocity dispersion, attenuation and inverse quality factor for both the seismic and the coseismic seismoelectric. The experimental results will be tested against asymptotic model curves combining fluid losses by macroscopic flow, typical of Biot poroelasticity, to losses by grain friction. In a last section, the data will be observed under the light of the transfer function $E/\ddot{u}$ and compared to computation after Pride's theory adapted to partial saturation. After preliminary observation of its dependency on fluid conductivity, explanation of the $E/\ddot{u}$ evolution with saturation, marking a polarity change between full and residual saturation, will conclude this work.

Chapter 6 will eventually conclude this thesis by offering a global review of the main results and some perspectives to this work.

Chapitre 2

From electrokinetics and poroelasticity to seismoelectrics

Sommaire

2.1 Definition of the petrophysical properties of the medium

Seismoelectric phenomena are the result of a double stage coupling: first a poroelastic coupling linking the displacement of a porous frame to that of its fluid filling, second an electrokinetic coupling connecting fluid movement to the generation of an electromagnetic field. As a result, they involve numerous parameters that we hereafter gather under three categories. First, we will define hydraulic properties of the matrix as porosity, tortuosity and permeability. Second, we tackle the mechanical properties of the porous medium with special attention given to Gassmann's approach. Finally we will introduce the fluid and electrical properties as conductivity, relative permeability, viscosity and fluid compressibility with a highlight on the consideration of saturation in the effective fluid model. Definition of these parameters in their low-frequency assumption as well as gross estimation of their expected values will be given; if parameters are subjected to frequency-dependency at higher frequencies, their dynamic behavior will be exposed at a further stage of this chapter.

2.1.1 Geometrical and transport properties

A porous medium may usually be seen as an assemblage of grains, unconsolidated or cemented, forming a more or less compact frame, yet leaving some voids at the contact between solid elements. When interconnected, these voids, referred to as pores, will be filled with fluids. The fluid phase may count one or more constituents that may be miscible or not. For immiscible fluids, as are air and water, the mixture may adopt different homogeneity degrees. Characteristics of a porous medium will consequently depend from the properties of the solid constituents usually given by literature, from the way solid elements are organised and from properties of the saturating fluid. We discuss here the transport properties characterising the medium and linked to the arrangement of the frame, while proposing some method to estimate characteristics of an uncompacted random granular packing.

Porosity ϕ

Porosity is a dimensionless quantity expressing the ratio of voids (or pores) relatively to a bulk volume of porous medium. Yet pores may be connected or isolated, the later case being common to igneous rocks in which gas bubbles may be trapped as the magma turns to a solid. From a storage and an hydraulic point of view, the only contributing pores will be the connected ones. Being V_v the volume of connected pores (or voids) within a cubic

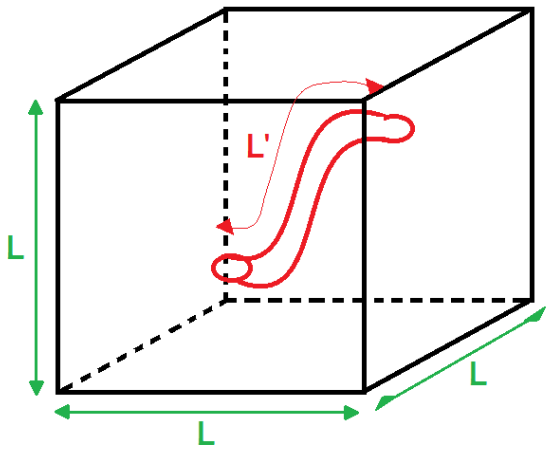

Figure 2.1: Tortuous capillary within an elementary volume designed as a cube of side-length L. Within this elementary volume, the pore volume correspond to the capillary volume, and tortuosity α_∞ equals L'/L.

sample of characteristic length L, porosity will consequently be considered to equal:

$$\phi = \frac{V_v}{L^3} \tag{2.1}$$

For unconsolidated sediments, in the absence of cement jointing the grains, porosity is essentially connected and will depend on compaction. For instance, porosity of a Fontainebleau or a Landes silica sand, both characterised by mean grain diameter of 250 μm and a monodisperse granular distribution, is known to vary between 0.34 when compacted [Maalej, 2007] up to 0.41. For marine unconsolidated sediments of unimodal granular distribution, Hamilton [1974] proposed an empirical relation, to which those silica sands would qualify, linking porosity to the mean grain diameter d_g:

$$\phi = 0.3105 - 0.0552\frac{ln(d_g^3)}{ln(2)} \tag{2.2}$$

According to this relation and given $d_g = 250.10^{-6}m$, a porosity ϕ of 42% is expected. Therefore, Hamilton's relation seems relevant for uncompacted sands characterisation.

Yet in opposition to eq. (2.2), for a packing of ideally identical spherical grains, theory concludes that porosity should not depend on grain size but on packing geometry. For organised packing, geometrical arguments predicts porosities ranging from 0.259 for the hexagonal close pack up to 0.476 for the simple cubic pack, the dense random pack being expected to adopt an intermediate porosity of 0.36 [Mavko et al., 2003].

To measure porosity one may report the mass m_{dry} of the dry solid to the volume V of the sample, and deduce V_v knowing the density of the solid phase ρ_s, so that:

$$\phi = 1 - \frac{m_{dry}}{\rho_s V} \tag{2.3}$$

An alternate way will be to perform a double weighting. In this last case, the imbibed sample of mass m_{tot} is being weighted before being put to dry in an oven. Once dried, the sample,

now of mass m_{dry}, is weighted again. Being ρ_f the density of the saturating fluid, porosity would be estimated as $\phi = (m_{tot} - m_{dry})/\rho_f$. Yet, if saturation remains incomplete as is often the case for simple imbibition [Cadoret et al., 1995], porosity may be underestimated by those methods. As a solution, the sample would have to be imbibed under depressurisation.

Tortuosity α_∞

A further dimensionless parameter of importance for hydraulic characterisation of a porous medium is tortuosity α_∞. This quantity, conformably to definitions given by Biot [1962b] or Berryman [1981], characterises the length of the actual path L' travelled by a fluid between two points, relatively to the size of the segment-line L connecting those two points (see figure 2.1). Tortuosity is hence defined as:

$$\alpha_\infty = \frac{L'}{L} \tag{2.4}$$

For a straight capillary, tortuosity will be minimal and equal unity. For granular material of unimodal distribution, Berryman [1981] proposed a theoretical formulation developed after Biot's poroelasticity relations. It relates tortuosity α_∞ to porosity ϕ with consideration of the grain geometry through a variable r that equals 0.5 for spherical grains and lies between 0 and 1 for other ellipsoidal shapes.

$$\alpha_\infty = (1 - r)\left(1 + \frac{1}{\phi}\right) \tag{2.5}$$

For a porosity of 42 $\pm$ 2% within a porous medium constituted of spherical grains, this equation predicts a tortuosity of 1.7 $\pm$ 0.05.

Formation factor F

A further way to estimate tortuosity is through measurements of the formation factor F. Formation factor F may appear as a condensed expression of the medium hydraulic properties. It has been given a number of equivalent definitions, some theoretical others more empirical.

It was first defined electrically by Archie [1942] as the ratio of the bulk electric conductivity σ_b relatively to the fluid electric conductivity σ_f:

$$F = \frac{\sigma_f}{\sigma_b} \tag{2.6}$$

Hence, by measuring the electric resistivity on a sample of known length, saturated by a fluid of known conductivity, formation factor may be accessed experimentally.

Archie rapidly reckoned that this electrically defined parameter would have connections to the hydraulic properties. On basis of resistivity logs he determined an empirical power-law linking F to porosity ϕ:

$$F = \phi^{-m} \tag{2.7}$$

where parameter m is known as the cementation exponent. For an open fracture, it would take a minimal value of 1; m would increase for increasing cementation of the medium. For most sedimentary rocks, it is expected to vary between 1.3, typical for unconsolidated spherical grains, up to 2.5, sandstones ranging by 2 [Mavko et al., 2003].

Fontainebleau or Landes sand are consequently expected to show cementation factors slightly superior to 1.3 and well below 2. Hence, when considering a porosity of 42%, formation factor should verify $3.1 \leq F < 5.7$. An hydraulic analogy to the originally electrically defined formation factor F was finally proposed on basis of a capillary model as defined by Brown [1980] and used by Pride [1994], being:

$$F = \frac{\alpha_\infty}{\phi} \tag{2.8}$$

Indeed, neglecting the surface conductivity, the resistance between two point may be seen from two points of view. First, as the resistance r_f of the water phase, second as that r_b of the bulk medium, giving within a cubic sample of characteristic length L:

$$r_f = \frac{1}{\sigma_f}\frac{L'}{\phi L^2} \tag{2.9}$$

$$r_b = \frac{1}{\sigma_b}\frac{L}{L^2} \tag{2.10}$$

so that finally, for $r_f = r_b$, we come back to:

$$\frac{\sigma_f}{\sigma_b} = \frac{L'}{\phi}\frac{1}{L} = \frac{\alpha_\infty}{\phi} \tag{2.11}$$

With respects to aforementioned bounds on formation factor F observed for a porosity of 42%, tortuosity of a Fontainebleau or Landes sand would be expected within the $[1.3 - 2.4]$ range. The estimation of 1.7 given by relation (2.5) falls within this range, being closer to the lower bound as anticipated.

Permeability k_0

Intrinsic permeability k_0, expressed as a surface, characterises the flowing facility within a porous medium. This parameter was first introduced by Darcy [1857], as he noted that in steady-state condition, under laminar flow, fluid flux q depends linearly on the gradient of the pressure drop. The linearity coefficient, also known as the hydraulic conductivity K (homogeneous to a velocity), would depend on the dynamic viscosity of the fluid η_f and on an intrinsic property of the medium: its permeability k_0. Hence for newtonian fluids (for which viscosity is independent from flow velocity), intrinsic permeability may be experimentally measured according to Darcy's phenomenological law:

$$q = \frac{Q}{S} = \frac{k_0}{\eta_f}\frac{\Delta P_f}{l} \tag{2.12}$$

where Q is the flow $[m^3.s^{-1}]$ for a cylindrical sample of length l and section S. Though this parameter has a high dynamic covering many orders of magnitude, observed permeabilities rarely trespass $10^{-9}m^2$, hence it may be expressed in darcy units such as $1D = 10^{-12}m^2$. For unconsolidated sand, permeability are usually expected to lay within the range $[1 - 100\ D]$.

Despite the apparent simplicity of Darcy's experiment, methods for in situ measurements of permeability are scarce. Consequently, a variety of models have arisen to infer permeability from more accessible parameters of the medium, as porosity ϕ or effective grain diameter $\bar{d}$. This last diameter, usually identified as diameter d_{10} so that the fraction of grains with a diameter comprised within $[0 - d_{10}]$ would represent 10% of the whole sand mass, would be inferior to mean grain diameter d_g. We will see further in this section how we estimated from d_g the $\bar{d}$ diameter required in theoretical permeability models as that from Kozeny-Carman or Glover-Walker.

Kozeny-Carman model As one of the most popular, the Kozeny-Carman model [Carman and Machefer, 1961] was developed in analogy to Poiseuille capillary flow within a tubular pipe of radius R presenting a circular cross section. In its initial form, the Kozeny-Carman relation for straight capillary gave $k = \phi R^2/8$,where permeability clearly increases with increasing pore radius. It was soon adapted to tortuous capillary as:

$$k_{kc} = \frac{\phi R^2}{8\alpha_\infty^2} \tag{2.13}$$

When not of capillary type, permeability of the connected pore space may be interpreted in terms of specific surface area S_p/V_{tot}, S_p being the cumulated pore surface. For spherical grains of unimodal distribution centered on mean grain diameter d_g, the specific surface area is easily deduced from geometrical arguments (see development in the appendices 7.3.2). It eventually enables the generalised reformulation of Kozeny-Carman permeability as:

$$k_{KC} = \frac{1}{36K_0\alpha_\infty^2}\frac{\phi^3}{(1-\phi)^2}\bar{d}^2 \tag{2.14}$$

K_0 being a form factor equalling 2 for random packing of spherical grains [Mota et al., 2001].

Glover-Walker model: As an alternate approach for intrinsic permeability determination, Glover and Walker [2009] proposed the Θ transform defined in agreement with electrokinetic properties, in an effort to connect the effective grain diameter $\bar{d}$ to the effective pore diameter d_p, as:

$$\bar{d} = \Theta d_p \tag{2.15}$$

where Θ may be expressed as a function of the cementation factor m, the packing constant a and porosity ϕ:

$$\Theta = \sqrt{\frac{am^2}{8\phi^{2m}}} = \sqrt{\frac{am^2F^2}{8}} \tag{2.16}$$

The intrinsic permeability of the porous medium may then be estimated by the Glover-Walker model using the above mentioned d_p, associated to the Archie's definition of formation factor F.

$$k_{GW} = \frac{d_p^2}{32F} = \frac{d_p^2\phi^m}{32} \tag{2.17}$$

For a random arrangement of uncompacted spherical grains would be consistent with a cementation factor $m = 1.45$, the packing constant $a = 8/3$ and a porosity of approximately 0.4.

Conclusions Having defined the models of permeability, we propose to compare them relatively to a normal Gaussian grain-size distribution, where the expected value equals the mean grain diameter d_g. The variance will be determined by analogy to a real grain distribution observed on Fontainebleau sand visible in figure 2.2, for which $\phi = 0.4$, $d_g = 208\mu m$ and $d_{10} = 144\ \mu m$ [Hama et al., 2014]. From the experimental points, marked as red asterisks, we reconstructed a smoothed cumulated weight curve in black, and adapted the variance of the modeled blue Gaussian curve $exp(-(x-d_g)^2/(2\sigma^2))/(\sigma\sqrt{2\pi})$ to optimize the fit. A reasonable agreement was obtained for the variance $\sigma^2 = d_g^2/16$.

On this basis, we calculated the effective grain size for any given mean diameter d_g, while considering a random spherical grain packing of porosity $\phi = 0.42$ and tortuosity $\alpha_\infty = 1.65$. While those pieces of information allow to calculate k_{KC}, estimation of k_{GW} required knowledge of cementation factor $m = 1.45$ and packing constant $a = 8/3$. This would cause Θ to lay by 3. Results of these computations are to be found in table 2.1.

As it appears following those calculations, permeability model based on grain size distribution and characteristics of the pore volume predict a permeability of approximately 30 D for $d_g = 250\ \mu m$. Though the Carman and Machefer [1961] and the Glover and Walker [2009] model follow two distinct approaches, predicted permeabilities happen to be quite similar, differing by approximately 10%. Indeed we show in appendices 7.3.2 that both models may be reduced to the same expression in hydraulic radius $r_h = d_p/4$ as:

$$k_0 = \frac{\phi r_h^2}{2\alpha_\infty^2} \tag{2.18}$$

Yet, these models are extremely dependent on porosity, given that a change of porosity by 2.5% will induce a permeability variation going up to 20% (see figure 2.3).

The theoretical tools developed here for permeability prediction with regard to porosity ϕ, mean pore diameter d_p or mean grain diameter $\bar{d}$ will be later recollected as a justification

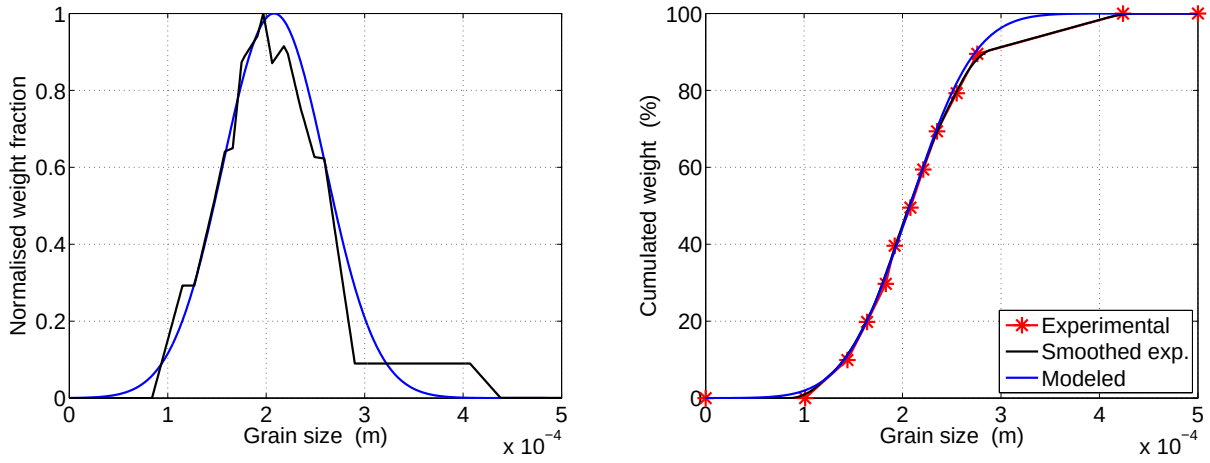

(a) (b)

Figure 2.2: (a) Granulometry distribution, as normalised volume fraction, for a Fontainebleau sand of mean grain diameter $d_g = 208\ \mu m$. (b) Cumulated weight curve given in percentage on which d_{10} may be read. Curves in black were reconstructed from real granulometry data taken from Hama et al. [2014], marked as red asterisks in (b). Blue curves were obtained from a normal Gaussian distribution centered on $\tau = d_g$ and of characteristic width $\sigma = d_g/4$ (see eq. (4.5) for a Gaussian curve).

d_g (μm)	$\bar{d}$ (μm)	d_p (μm)	k_{GW} (D)	k_{KC} (D)
100	68	23	4.7	5.4
150	102	34	10.3	11.7
200	135	45	18	20.5
208	**144**	**48**	**20.5**	**23.3**
250	170	57	28.9	32.9
300	204	68	41	46.8
400	270	90	72	81.9

Table 2.1: Examples of effective grain and pore diameter $\bar{d}$ and d_p, associated to intrinsic permeability according to the Glover-Walker (k_{GW}) and the Kozeny-Carman (k_{KC}) models. These models were calculated for normal gaussian size-distribution of spherical grains with expected value d_g and variance $d_g^2/4$. Grain packing is computed having porosity $\phi = 0.42$, cementation factor $m = 1.45$, packing constant $a = 8/3$ and tortuosity $\alpha_\infty = 1.65$, causing Θ to lay by 3. Error on k_{GW} or k_{KC} when mistaking ϕ by 2.5% will be of 5%. The line in bold characters is based on experimental values from Hama et al. [2014].

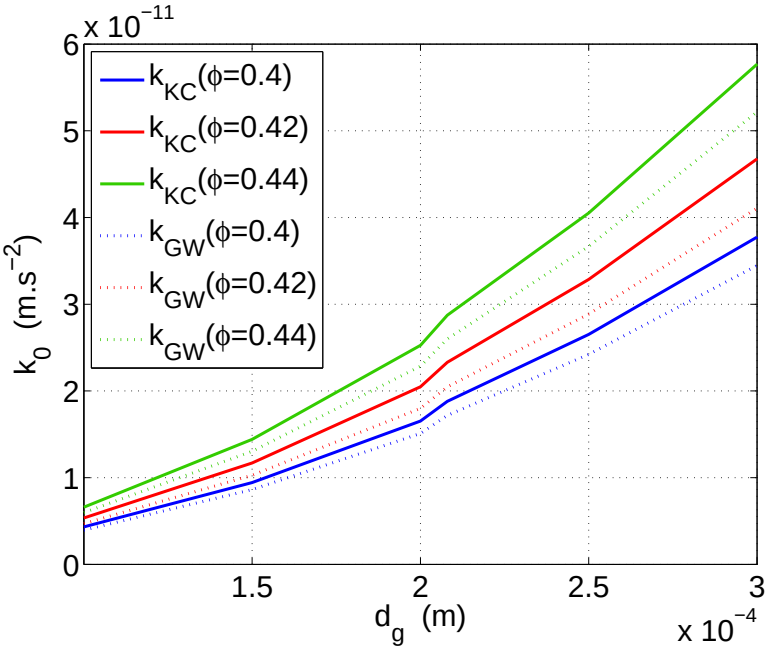

Figure 2.3: Permeability predicted by Kozeny-Carman (k_{KC}) and Glover-walker (k_{GW}) for various porosities, depending on the mean grain diameter d_g, center of a normal grain size distribution of variance $\sigma^2 = d_g^2/16$.

of our permeability estimation of the medium (see section 3.1.2).

2.1.2 Mechanical properties

Having dealt with the transport properties, we now consider the mechanical characterisation of a porous medium. The mechanical behaviour of a material is often characterised by its propagation velocities, primarily determined by bulk densities and incompressibilities of the material. Yet, as a porous medium results from a combination of a solid and a fluid phase, some notations have first to be introduced. Hence, we will note ρ_s the density of the solid phase, sometimes also called grain density, and ρ_f the density of the fluid saturating the pores. Modulus K_S will be known as the intrinsic bulk modulus of the solid and G_S as the solid intrinsic shear modulus, while modulus K_f will be reckoned as the fluid bulk modulus.

Bulk density ρ

Bulk density ρ of a biphasic medium is given by a simple arithmetic average, where each phase density is modulated by its volume fraction, so that:

$$\rho = (1 - \phi)\rho_s + \phi\rho_f \tag{2.19}$$

General introduction on different moduli

Modulus or incompressibility K characterises the ability of a material to resist deformation when being put under pressure; it's general expression will consequently be of the form $K = -\delta P/(\delta V/V_0)$.

Yet under different conditions, the response may be different. Therefore, for a porous material, one has to distinguish between a drained and a undrained case. For the drained bulk modulus K_D, fluid can freely flow out ensuring constant fluid pressure p_f while confining pressure P_c variates. In the undrained case the fluid can not escape the pores, so that being $\mathbf{w}$ the relative fluid displacement with respect to frame displacement $\mathbf{u}$, measuring conditions for K_U should verify $\nabla.\mathbf{w} = 0$. Hence under a triaxial test, values of K_D and K_U may be obtained from comparing changes in confining pressure P_c to the volume variation response of the sample:

$$K_D = -\left(\frac{\delta P_c}{\delta V/V_0}\right)_{\delta p_f=0} \tag{2.20}$$

$$K_U = -\left(\frac{\delta P_c}{\delta V/V_0}\right)_{\nabla.\mathbf{w}=0} \tag{2.21}$$

Should the measurement of K_D occur on a dry or a water saturated sample, as long as the fluid is not prevented from flowing out, measurements should be equivalent[1]. The drained bulk modulus K_D is consequently identified as the bulk modulus of the dry frame and will be noted K_{fr}. However for an unconsolidated material this is not absolutely true: the introduction of a small quantity of liquid, by moistening the grain surface, will modify the mechanical behaviour of the frame [Mavko et al., 2003]. As for K_U, we explain in next paragraph how it came to be known as the Gassmann modulus noted K_G.

In case of an undrained compression, to cope with the reduced pore volume while fluid is prevented to flow out, fluid pressure p_f will have to increase. The increase of p_f will be characterised by the dimensionless Skempton's coefficient B_S defined as:

$$B_S = \left(\frac{\delta p_f}{\delta P_c}\right)_{\nabla.\mathbf{w}=0} \tag{2.22}$$

and which can be deduced from K_S, K_f, K_{fr} and ϕ according to following relation:

$$B_S = \frac{1/K_{fr} - 1/K_S}{1/K_{fr} - 1/K_S + \phi(1/K_f - 1/K_S)} \tag{2.23}$$

Hence, K_{fr} and K_G may be determined from triaxial tests. Yet, for monodisperse granular material of spherical shape, frame modulus K_{fr} may also be theoretically approached from the hertzian contact theory (Hertz [1882],Mindlin [1949]). Based on experimental works by Murphy [1982] and further theoretical development of this theory by Walton [1987], Barrière [2011] presented a scope of expressions for determination of K_{fr} for an unconsolidated Landes sand from porosity, effective pressure, coordination number or modula K_S and G_S [Pride, 2005]. The value that is to be used in computations as our K_{fr} results from his investigations.

Moreover, in the aforementioned theory developed by Walton [1987], frame shear mod-

[1]As a matter of fact this stays true as long as the effective pressure $P_e = P_c - p_f$ remains equivalent, since a change in effective pressure would increase grain contact and play in favour of a matrix solidification and an increase of K_D [Barrière, 2011].

ulus G_{fr} was expected to be linearly dependent on K_{fr}, the linearity coefficient depending on the rugosity of the grains. While the highest coefficient, combining the values of K_S and G_S, would correspond to the highly rugous "no-slip limit", the lowest bound valued at 3/5, also called "slip-limit", would characterize ideally smooth spheres. This last estimation would typically be relevant for an unconsolidated and uncompacted granular media assembled from spherical grains of unimodal granulometry. For uncompacted Fontainebleau sand or Landes sand the frame shear modulus may hence be taken as:

$$G_{fr} = \frac{3}{5} K_{fr} \tag{2.24}$$

As fluid phase plays no role in shearing processes, there is no need to distinguish between drained and undrained shear modula, the only shear modulus of the frame being G_{fr}.

Gassmann modulus and Biot coefficients: introducing incompressibilities C, M and K_G

While standard elasticity is fully defined by the knowledge of two elastic moduli (see section 2.3.1), poroelasticity requires the definition of further poroelastic moduli coupling the fluid and the frame to characterize the medium. Yet, as direct moduli measurements requires specific devices, some models have been developed to permit their calculation on theoretical basis. Hence, while contact grain theory permitted to evaluate K_{fr} in the absence of lab measurements, a formulation by Gassmann [1951] allowed to deduce the saturated undrained bulk modulus $K_U = K_G$ from the dry frame bulk modulus K_{fr} without making any assumption on pore geometry, according to the relation:

$$\frac{K_U}{K_S - K_U} = \frac{K_{fr}}{K_S - K_{fr}} + \frac{K_f}{\phi(K_{fr} - K_f)} \tag{2.25}$$

This relation would assume the homogeneity of the solid phase and a statistical isotropy of the pore space, as well as the neglecting of the inertial and scattering effects. It consequently requires pore pressure to equilibrate at mesoscopic scale compatible with a low frequency approach. It was eventually reformulated as

$$K_G = \frac{K_{fr} + \phi K_f + (1+\phi) K_S \Delta}{1 + \Delta} \tag{2.26}$$

$$\Delta = \frac{K_f}{\phi K_s^2} \left[(1-\phi) K_S - K_{fr} \right] \tag{2.27}$$

Note that this expression of K_G meets with Biot's formulation in the low-frequency limit (see section 2.3.2).

Besides the already described drained and undrained bulk modulus, Gassmann [1951] and Biot [1962b] introduced a variety of poroelastic coefficients, homogeneous to a bulk modulus, known as the coupling coefficient C and the fluid accumulation coefficient M. In terms of partial derivative these quantities, often referred to as Biot's coefficients and

associated to variations in fluid pressure, may be defined as:

$$C = \left(\frac{\delta p_f}{\delta V/V_0}\right)_{\nabla.\mathbf{w}=0} \tag{2.28}$$

$$M = \left(\frac{\delta p_f}{\delta V/V_0}\right)_{\nabla.\mathbf{u}=0} \tag{2.29}$$

where $\mathbf{u}$ would be the frame displacement. Under a more practical form, Biot's coefficients may be developed as[2]:

$$C = \frac{K_f + K_S\Delta}{1+\Delta} \tag{2.30}$$

$$M = \frac{1}{\phi}\frac{K_f}{1+\Delta} \tag{2.31}$$

Finally, a last modulus, known as the undrained P-wave modulus H, was defined on basis of K_G and G_{fr}:

$$H = K_G + \frac{4G_{fr}}{3} \tag{2.32}$$

For an undrained saturated medium, fast P-wave velocity should verify $V_p = \sqrt{H/\rho}$.

2.1.3 Fluid and electrical properties

At this stage, we consider the fluid phase to be a monophasic water electrolyte of low salinity, obtained by dissolution of NaCl salt. These values would hence be relevant at full water saturation. Since many fluid properties are influenced by temperature and viscosity, we evaluate here the variation range of the electric fluid conductivity, fluid viscosity and relative permittivity with respect to moderate change in salinity and temperature. All hereafter presented formulations were gathered in a paper by Glover and Déry [2010]; in the followings, only original references will be cited. A definition of the zeta potential will be given in the next section.

Salinity C_f and electric conductivity σ_f

Electrical conductivity of the bulk fluid can usually be calculated from the salinity C_f and the temperature. Here is a formulation proposed by Sen and Goode [1992] to express fluid conductivity:

$$\sigma_f = \left(5.6 + 0.27T_C - 0.000151T_C^2\right)C_f - \left(\frac{2.36 + 0.099T_C}{1 + 0.214C_f}\right)C_f^{3/2} \tag{2.33}$$

As a matter of fact, when dealing with very low salinities (inferior to 8.10^{-3} mol/L corresponding to a maximum fluid conductivity of 10 mS/m) at room temperature, fluid

[2]Note that knowing Skempton's coefficient B_S, Biot's coefficients may also be written as: $C = B_S K_G$ and $M = B_S^2 K_G/(1 - K_{fr}/K_G)$, while Gassmann modulus may be expressed as $K_G = \frac{K_{fr}}{1-B_S(1-K_{fr}/K_G)}$.

conductivity can be considered proportional to salinity C_f. This is consistent with observations on figure 2.4a, where for moderate salinities of $[0 - 0.001\ mol.l^{-1}]$, fluid conductivity increases linearly from 0 to 10.3 mS/m. An additional variation of temperature by $\pm 2°C$ will induce a change of conductivity by 4.5%.

Viscosity η_f

Dynamic viscosity characterises the frictional forces acting within a fluid as it flows. The higher the viscosity, the more difficult will be the flow. When dealing with viscosity, two types of behaviour may be observed:

- first, a newtonian behaviour where viscosity does not change with flow velocity. This behaviour is a prerequisite for application of Darcy's law, Navier-Stokes equations... Low salinity electrolyte, gas vapour and liquid would display such behaviour in usual conditions.

- second, a non-newtonian behaviour as may be experienced for mud, gels, shifting sands. As they do not intervene in our study, they are not to be further discussed here.

Dynamic viscosity is expressed in Poiseuille $[Pa.s^{-1}]$ and may variate by several orders of magnitude. For any given fluid, viscosity will be impacted by temperature ; for an electrolyte increasing salinity will also increase viscosity of the liquid. Considering water-based electrolyte, Phillips et al. [1978] estimates the viscosity of the liquid to be Phillips et al. [1978]:

$$\eta_f(T_C, C_f) = e_1 + e_2 \exp(\alpha_1 T_C) + e_3 \exp(\alpha_2 C_f) + e_4 \exp(\alpha_3 T_C + \alpha_4 C_f) \tag{2.34}$$

where $e_1 = 4.95166\ 10^{-5}\ Pa.s$, $e_2 = 6.034658\ 10^{-4}\ Pa.s$, $e_3 = 9.703832\ 10^{-5}\ Pa.s$, $e_4 = 1.025107\ 10^{-3}\ Pa.s$, $\alpha_1 = -0.06653081\ °C^{-1}$, $\alpha_2 = 0.1447269\ mol.L^{-1}$, $\alpha_3 = -0.02062455\ °C^{-1}$ and $\alpha_4 = 0.1301095\ mol.L^{-1}$. The original equation reports to molality but, since our salinities are low, it is possible to use molarity C_f in place of molality.

Variations of viscosity with changes in applied temperature or salinity may be seen in figure 2.4b. We see that for low salinities C_f within $[0 - 1\ mmol.l^{-1}]$ (upper σ_f by about 10 mS/m), impact of salinity will be negligible in comparison to that of temperature T_C for which a change by $\pm 2°C$ may trigger an appreciable variation of σ_f by about 5 %. In the future we will resort to this expression when evaluating our electrolyte viscosity.

Relative permittivity κ_f

Permittivity ϵ characterises how easily an electric field might interact with a medium, the higher the permittivity of a medium, the more it will be affected by the electric field (so that $\epsilon_{air} < \epsilon_{water}$). It is obtained from the product of vacuum permittivity $\epsilon_0 = 8.8542\ 10^{-12}\ F/m$ by the relative permittivity of the medium κ, so that $\epsilon = \epsilon_0 \kappa$.

Similarly to viscosity, the relative permittivity of fluid κ_f depends on both the temperature and the salinity of the electrolyte. For a water-based electrolyte, this dependency should behave accordingly to Olhoeft's equation published in Revil et al. [1999]:

$$\kappa_f(T_K, C_f) = a_0 + a_1 T_K + a_2 T_K^2 + a_3 T_K^3 + c_1 C_f + c_2 C_f^2 + c_3 C_f^3 \tag{2.35}$$

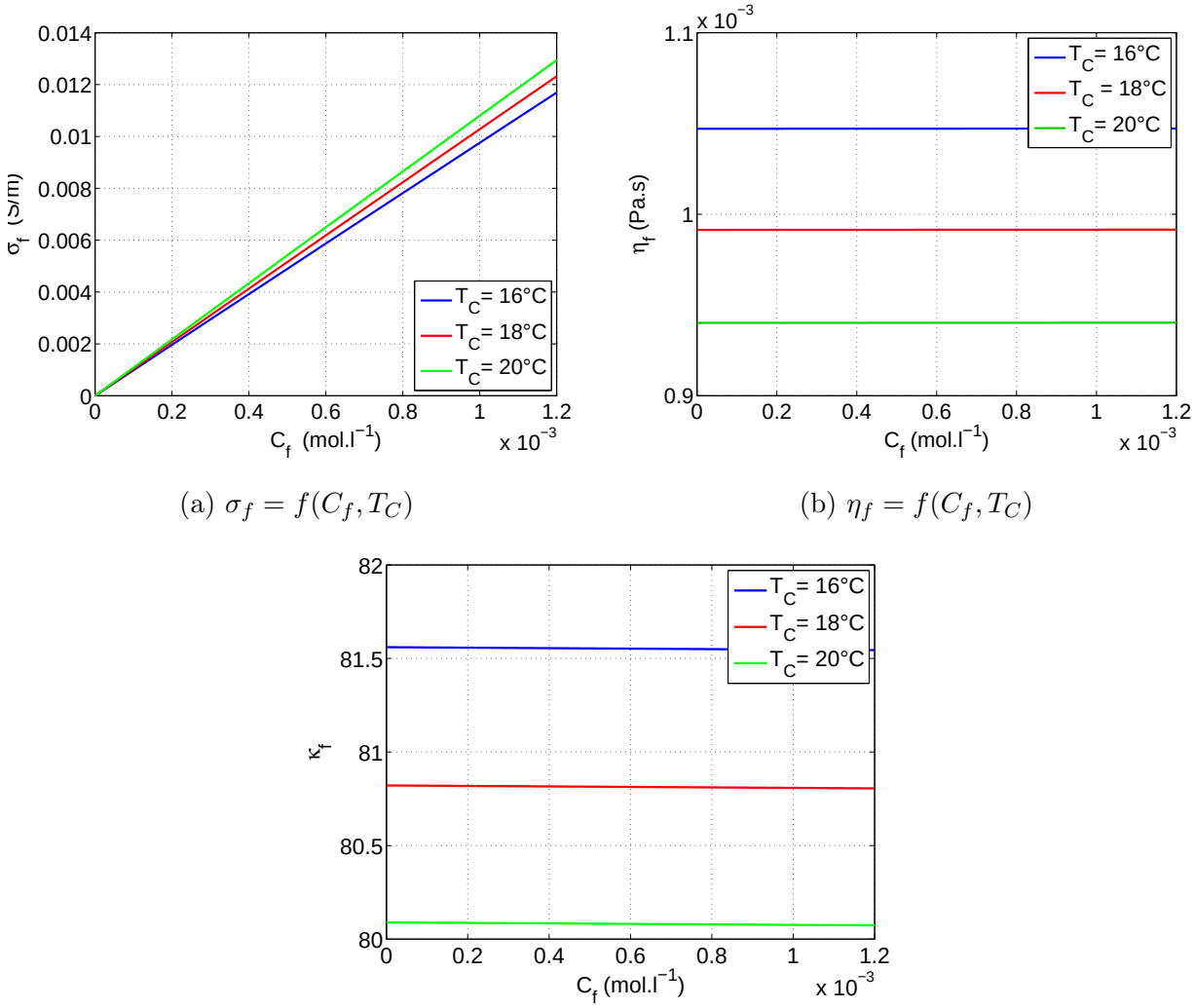

(a) $\sigma_f = f(C_f, T_C)$

(b) $\eta_f = f(C_f, T_C)$

(c) $\kappa_f = f(C_f, T_C)$

Figure 2.4: Variations of fluid parameters as (a) fluid conductivity σ_f , (b) fluid dynamic viscosity η_f and (c)fluid relative permittivity with respect to temperature and salinity changes.

where $a_0 = 295.68$, $a_1 = -1.2283\ K^{-1}$, $a_2 = 2.094\ 10^{-3}\ K^{-2}$, $a_3 = -1.41\ 10^{-6}\ K^{-3}$, $c_1 = -13\ L.mol^{-1}$, $c_2 = 1.065\ L^2.mol^{-2}$ and $c_3 = -0.03006\ L^3.mol^{-3}$.

Figure 2.4c, shows that for a maximal salinity C_f ranging by 1 $mmol.l^{-1}$ (corresponding to $\sigma_f \approx 10\ mS/m$), impact of salinity will be negligible in comparison to that of temperature T_C. In this last case, a change by $\pm 2°C$ may trigger a variation of κ_f by about 1 %. In the future we will resort to this expression when evaluating our electrolyte relative permittivity.

2.2 Principles of electrokinetic phenomena

2.2.1 The electrical double-layer

When a relative movement occurs within a porous medium between the solid and the fluid phase, one assists to the apparition of a macroscopic electric potential due to a perturbation of the charge distribution by fluid flow. This 'streaming potential' is the result of an electrokinetic coupling at the pore/fluid interface: defaults in the crystalline structure of the

solid phase causes grain surface to be charged and to adsorb counter-ions from the moving electrolyte. It eventually leads to a charge separation causing an electric streaming current to appear.

While first account of this electrokinetic phenomenon was given by Reuss [1809], the first theoretical models describing electrokinetic behaviour at pore/fluid interface have been given by Quincke [1861] and Helmholtz [1879]. We give here a rapid overview of the theoretical developments on electrokinetics, based on the works by Allègre [2010] and Warden [2012].

Helmholtz model

With analogy to an electric capacitor, the first models of electrical double layer (EDL) were thought as two successive infinitely fine layers, the first being constituted of adsorbed ions while the second would host the associated counter-ions, at some fixed distance from the grain surface. With this distributions of cations and anions as two parallel layers the electric potential would decrease linearly with increasing distance to the pore/fluid interface. Yet this model assumes stiff layer boundaries while a stiff organisation is incompatible with considerations of thermal agitation and electrostatic attraction. Hence, while those effects play an important role in the organisation of the EDL, notably for low-salinity electrolytes, the Helmholtz model does not account for them.

Gouy-Chapman-Stern model

The initial Helmholtz model is consequently modified by Gouy [1910] and Chapman [1913] to allow for a diffuse double layer. Within this diffuse layer, the charges are distributed statistically following a Boltzmann distribution: the charge density diminishes exponentially with increasing distance to the interface. Yet this model considers only punctual charges and cannot account for the actual dimensions of the ionic charge carriers.

Eventually, Stern [1924] proposed a model combining Helmhotz's stiff double layer, renamed 'inner' and 'outer Stern layer', to Gouy-Chapman's diffuse layer (see figure 2.5). Within the compact layers, ions are either adsorbed to the surface or in electrostatic equilibrium with the adsorbed charges: the electric potential decreases linearly with the distance to the grain surface, each layer having its own slope (lower part of figure 2.5). Yet, since those stiff layers do not fully compensate the surface charge, a diffuse layer forms, in which the potential takes an exponential decrease until finally reaching neutrality.

As fluid moves, part of the fluid remains locked to the frame: the surface of fluid-flow initiation, called 'shear plane', is located within the diffuse layer. The potential on that shear plane is called zeta potential ζ.

2.2.2 Introduction to the zeta potential ζ

Under the thin-double-layer assumption, the distance of the shear plane to the grain surface being immensely fine, the shear plane is identified to the outer Stern-layer (OSL). The zeta potential is identified to the potential $[V]$ at the shear plane. Hence, as the charges within the diffuse layer present a Boltzmann distribution, knowing the electric potential

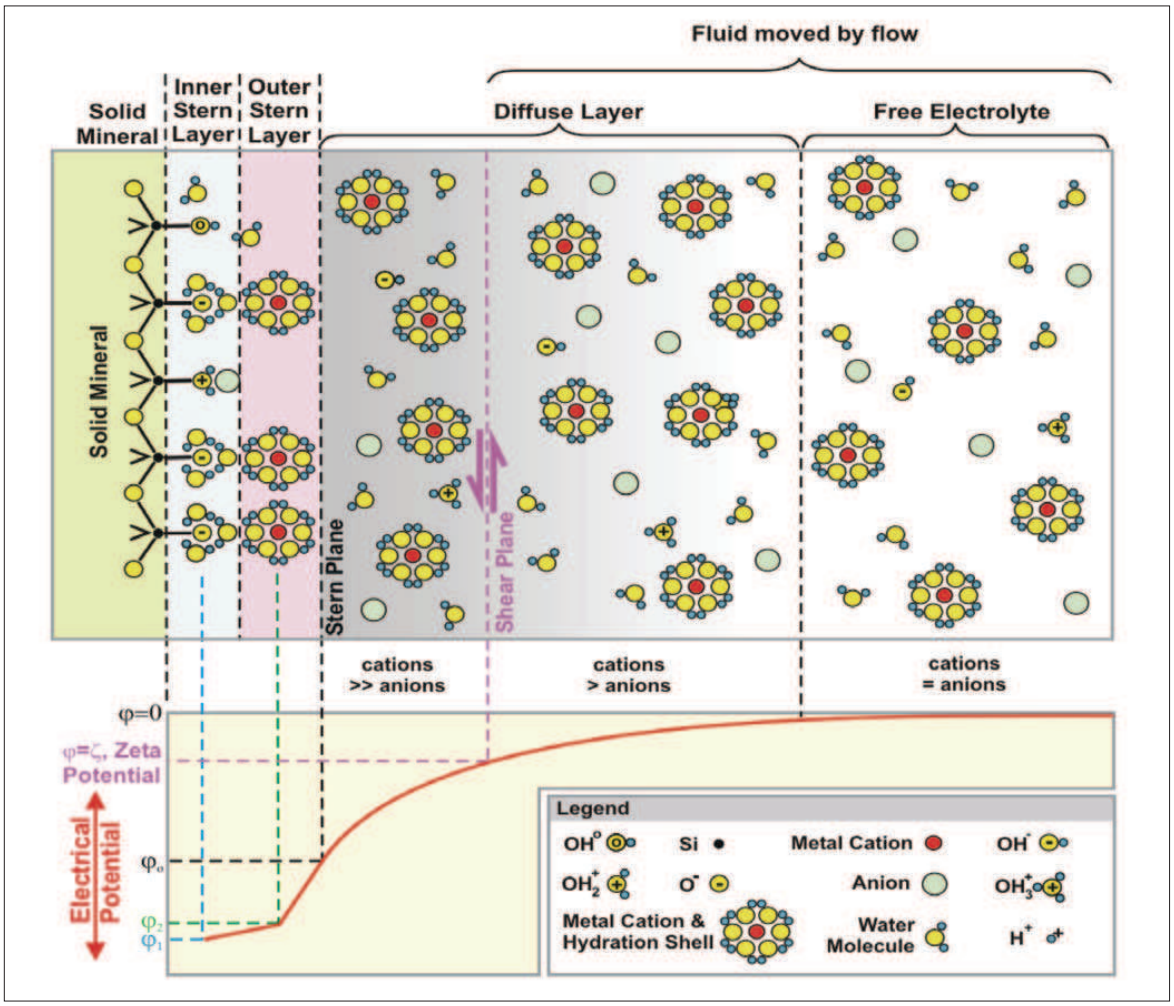

Figure 2.5: Schematic representation of the electrical double layer at the interface between a silica matrix and the pore water. The rock may form three types of surface sites: positive $SiOH_2^+$, neutral $SiOH$ and negative SiO^-. The relative concentrations of these sites depend upon the fluid pH, which tends to favour negative sites under classical reservoir fluid conditions. Hydrated positive ions are adsorbed to these sites, yet as the adsorbed positive ions cannot cancel out all of the negative surface charge, there exists a fluid diffuse layer which has an excess positive charge, which falls off exponentially until there are equal numbers of positive and negative ions. Movements of fluid through the rock moves the electrically neutral bulk fluid and that portion of the diffuse layer, further from the surface, that is beyond the electrically positive shear-plane. Thus the fluid flow separates charge which creates the streaming potential and ultimately a streaming counter-current(from Glover and Jackson [2010]).

$\psi(0) = \zeta$ allows to calculate potential $\psi(\chi)$ at any given distance χ from the OSL. This may eventually give the distance of the electroneutral plane to the OSL and provide an estimation of the EDL dimensions.

Many factors may influence the dimensions of the EDL and impact ζ. A systematic study by Ishido and Mizutani [1981] showed the particular role played by various fluid properties as pH, fluid conductivity σ_f and temperature T; their results for measurements on quartz are shown in figure 2.6. The ζ-dependency to temperature is shaped as a bell-curve possibly traducing the competition between thermal effects some helping other preventing the sustainability of the EDL (for possible questions of thermal agitation and ionic mobilities). Considering the further fluid parameters, while the dependency in pH shows a monotonic decrease of a negative ζ potential with increasing pH (ζ increases in absolute value), its evolution with fluid conductivity conducts to a sign change (meaning that the absolute value decreases before re-increasing) with apparition of a plateau after a first ramp. We present some empirical models obtained on quartz sand regarding ζ-dependency to those last two parameters.

Expressions of zeta potential ζ with pH

As pointed out by Ishido and Mizutani [1981] in figure 2.6a, the zeta potential is highly dependent on pH. In an experiment dealing with crushed Fontainebleau sandstone saturated by a NaCl electrolyte Lorne et al. [1999] determined an empirical law for pH correction within the $[5.7 - 8]$ pH range:

$$\zeta(pH_1) = \zeta(pH_0)\,[1 + (0.068 \pm 0.004) \times (pH_1 - pH_0)] \tag{2.36}$$

From figure 2.7, presenting the experimental data on which this empirical law has been based, we may also collect a ζ potential estimation of $\zeta = -25 \pm 3mV$ at $pH = 7$ and $\sigma_f = 10\,mS/m$, possibly relevant for our silica sand material characterisation.

Expressions of zeta potential ζ with salinity

Some authors have proposed an expression of the zeta potential ζ in relation to the fluid molarity C_f. Yet, as can be seen in figure 2.6b the absolute increase or decrease of the ζ value appears to depend on the salinity range. First expression proposed by Pride and Morgan [1991] for a NaCl electrolyte of low salinity predicts an increase of ζ with increasing salinity (meaning a decrease of the absolute ζ value with increasing fluid conductivity).

$$\zeta = 0.008 + 0.026\ log_{10}(C_f) \tag{2.37}$$

This relation would lead to a zeta potential ranging from $-95\ mV$ to $-69\ mV$ for salinity increasing from $10^{-4}\ mol.l^{-1}$ to $10^{-3}\ mol.l^{-1}$ (corresponding approximately to conductivities within $1\ mS/m$ to $10\ mS/m$).

For a silica sand ($SiO_2 \approx 98\%$) of mean grain diameter $300\mu m$, Guichet et al. [2003]

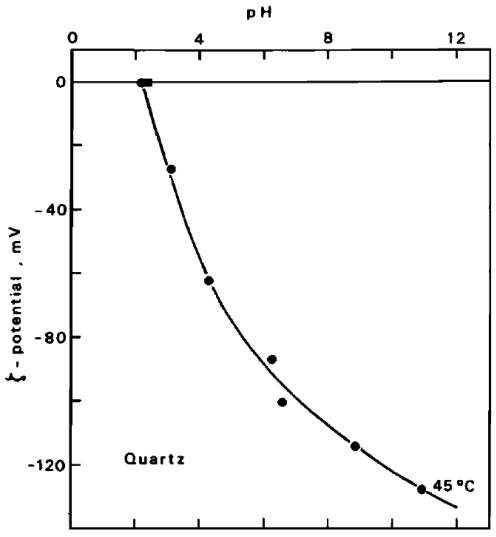

(a) $\zeta(pH)$

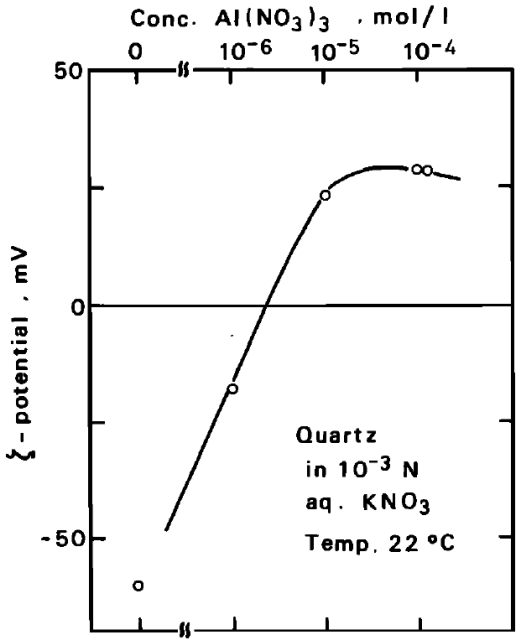

(b) $\zeta(C_f)$

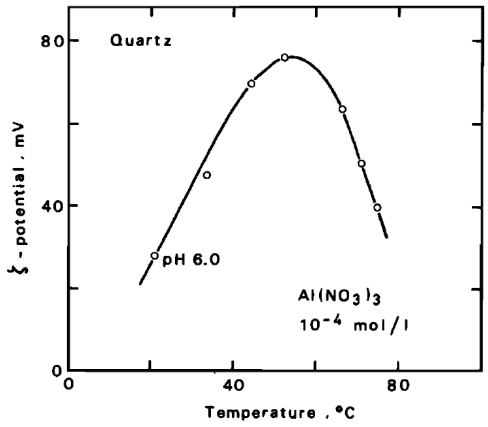

(c) $\zeta(T_C)$

Figure 2.6: Variation of the ζ potential of quartz as a function of pH (a), $Al(NO_3)_3$ concentration (b), temperature (c). The aqueous solution contains $10^{-3}N$ of KNO_3 as a supporting electrolyte (from Ishido and Mizutani [1981]).

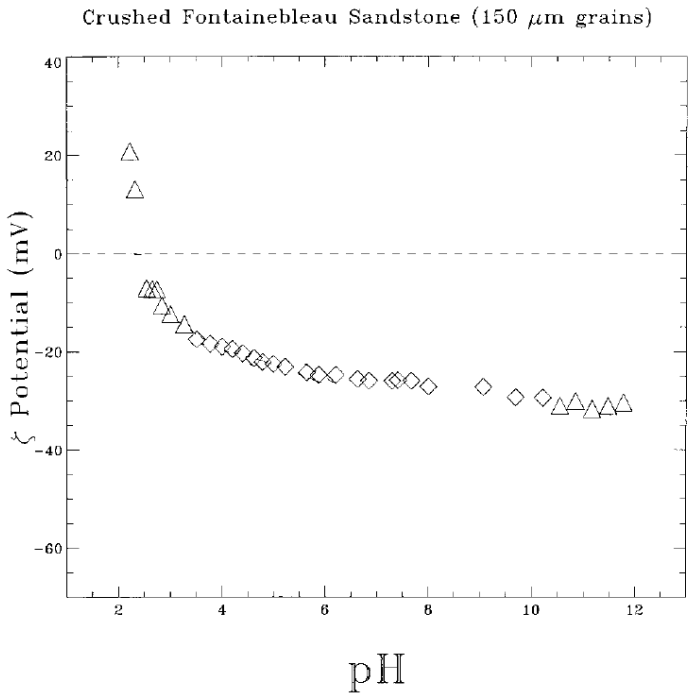

Figure 2.7: ζ potential inferred from streaming potential measurements using crushed Fontainebleau sandstone, as a function of pH for NaCl/HCl/NaOH solutions. Diamonds correspond to measurements with an electrolyte resistivity of 100 $\Omega.m$ (meaning $\sigma_f = 10mS/m$). Triangles correspond to measurements for which the resistivity is controlled by the pH and cannot be maintained at 100 $\Omega.m$. The measurement experimental errors are of the size of the symbols (from Lorne et al. [1999]).

provides an empirical dependency of ζ on conductivity σ_f within the range $[10 - 25\ mS/m]$:

$$\zeta = -0.0146 \times \ln(\sigma_f) - 0.0854 \tag{2.38}$$

Dependency was expressed in conductivity rather than salinity due to the abundance of different saline species in the saturating fluid (obtained by equilibrating the medium with distilled water). Yet the evolution of ζ with salinity is opposed to that predicted by previous model, predicting $\zeta = -19mV$ for a conductivity of 10 mS/m.

Estimations by both models of the zeta potential at a given conductivity of 10 mS/m are extremely divergent. A last alternative is to rely on the definition of the electrokinetic coupling coefficient and deduce ζ from a C_{EK} value (defined in following section 2.2.3) given for a comparable material within the literature [Bordes et al., 2015]. Following this approach, C_{EK} values from Guichet et al. [2003] on a medium-size silica-sand fully saturated by a water-electrolyte of conductivity $9.5 \pm 0.5\ mS/m$ and $pH = 8 \pm 0.5$ gave an average zeta potential of $-24 \pm 4mV$ (consistent with Lorne et al. [1999] measurements). We will come back to the question of zeta potential estimation in section .

2.2.3 Expression of the electrokinetic coupling coefficient C_{EK}

We saw that the saturation of a porous medium by an electrolyte induces the apparition of an electrical double layer. By application of a pressure gradient, the fluid will move relatively to the frame, starting from the shear plane located within the diffuse layer. The dragging of the excess charges, with the fluid located between the shear plane and the electroneutral

plane, results in the apparition of a convection current J_P related to the pressure gradient ∇P. To ensure local neutrality of the electrolyte, the apparition of a local potential difference V is counter-balanced by a re-equilibrating conduction current J_V scaling with ∇V. The associated current densities I_P and I_V may be expressed as $[A.m^{-2}]$:

$$I_P = \frac{\epsilon_0 \kappa_f}{\eta_f F} \nabla P \tag{2.39}$$

$$I_V = \frac{\sigma_f}{F} \nabla V \tag{2.40}$$

At the equilibrium the current densities verify $I_P = I_C$ allowing to deduce an estimation of the ratio $\nabla V / \nabla P = \Delta_V / \Delta_P$. This ratio in $[V.Pa^{-1}]$, known as the electrokinetic coupling coefficient C_{EK}, is formulated as:

$$C_{EK} = \frac{\epsilon_0 \kappa_f \zeta}{\eta_f \sigma_f} \tag{2.41}$$

Coupling coefficient C_{EK} decreases with increasing viscosity or conductivity of the fluid, the first resisting the fluid dragging while the other temper the loss of some ions from the bulk fluid to the adsorbed layer. Conversely, the coupling coefficient increases with increasing fluid permittivity or increasing zeta potential. Practically, this relation is the key to experimental determination of the zeta potential by electrofiltration experiments for well-known fluid parameters.

2.3 Theory of poroelasticity

In a first approximation, geomaterials submitted to seismic excitation are sometime modeled as elastic solids. Elasticity however does neither account for the amplitude attenuation observed as the seismic wave propagates, nor for waveform modification due to velocity dispersion (see figure 2.8). Poroelasticity on the contrary reflects on the porous microstructure of the material and on the conjugate effect of the filling phase.

After a short introduction on fundamental elasticity, we will discuss the development made by Biot as he proposed standard poroelasticity. We will then tackle the later generalisation of Biot's theory by Pride, as he introduced frequency-dependent elastic moduli and took coupled electrokinetic effects into account.

2.3.1 Fundamental elasticity

Elasticity implies an immediate response of the elastic medium to a stress changes, and the immediate return to the equilibrium state once the stress has been removed. In the simplest isotropic linear case, elasticity is ruled by Hooke's law:

$$\sigma_{ij} = \lambda \delta_{ij} \epsilon_{kk} + 2\mu \epsilon_{ij} \tag{2.42}$$

$$\epsilon_{ij} = \frac{1}{E} \left((1+\nu)\sigma_{kij} - \nu \delta_{ij} \sigma_{kk} \right) \tag{2.43}$$

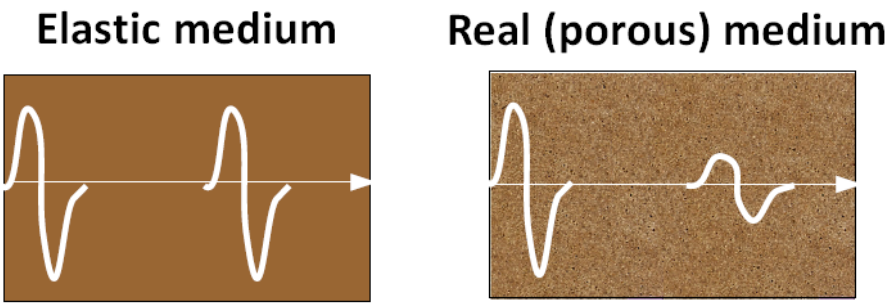

Figure 2.8: Effect of an elastic medium or a poroelastic medium on a propagating acoustic wave: in the second case the wave is attenuated and the arrival widens with velocity dispersion.

Stress and strain tensors, σ_{ij} and ϵ_{ij} are related via a set of interdependent elastic parameters, totally defined by the knowledge of two of them. Hence while first expression of Hooke's law involves Lamé's parameter λ and μ, the last also known as the shear modulus, second expression entails Poisson's ratio ν and Young's modulus E. This system of interdependent elastic parameters is completed by bulk modulus or modulus K and P-wave modulus M. Rheologic analogical to linear elasticity is a spring of rigidity modulus E.

2.3.2 Biot's theory

A poroelastic behavior can be seen as a solid/fluid coupling where on the one hand a change in applied stress, supported by the solid frame produces a change in fluid pressure or fluid mass, whereas on the other hand, a change in fluid pressure or mass induces a change in the volume of the porous material [Wang, 2000]. Under this light, porous behavior appears fully determined by four parameters,

- stress tensor σ
- volumetric strain tensor ϵ such that $\epsilon = \delta V/V_0 = \nabla \cdot \mathbf{u}$
- fluid pressure p_f that traduces a drained mode if its variation is set to zero
- increment of fluid content ξ which equals the opposite of the relative fluid displacement divergence $\nabla \cdot \mathbf{w} = \phi(u_f - u)$ [Biot, 1962b]

It appears that σ and ϵ characterize the solid phase, while ξ and p_f stand for the fluid phase. Note that standard Biot formulation postulates full saturation of the medium by a single fluid. Hence, according to Wang [2000], bases of the Biot's theory relies on the coupling of two linear constitutive equations combining this four quantities as in the model:

$$\begin{cases} S_2 = & a_{11}S_1 + a_{12}F_1 \\ F_2 = & a_{12}S_1 + a_{22}F_1 \end{cases} \tag{2.44}$$

where S_1, S_2 refers to solid phase variables while F_1, F_2 stands for fluid variables. Actual displacement $\mathbf{w}$ and $\mathbf{u}$ will result from competing viscous effects (caused by the dragging of one phase on the other) and inertial effects (for which a phase opposes motion under its own weight). These competing effects announce a dependency in frequency: indeed, as viscous effects require some time to take place (viscous delay), this effect will prevail at lower

frequencies, while inertial ones will dominate in the higher frequency-range.

Biot's mechanical equations

A system of this form is indeed to be found in Biot [1962b] actual formulation of his theory for isotropic poroelastic response, expressed by a system of five equations:

$$\begin{aligned}
\nabla \cdot \tau^D - \nabla P_c &= -\omega^2 \left(\rho \mathbf{u} + \rho_f \mathbf{w}\right) && (2.45)\\
\nabla p_f &= -\omega^2 \rho_f \mathbf{u} - i\omega \frac{\eta_f}{k(\omega)} \mathbf{w} && (2.46)\\
\tau^D &= G_{fr} \left(\nabla \mathbf{u} + \nabla \mathbf{u}^T - \frac{2}{3} \nabla \cdot \mathbf{u} I\right) && (2.47)\\
-P_c &= K_G \, \nabla \cdot \mathbf{u} + C \, \nabla \cdot \mathbf{w} && (2.48)\\
-p_f &= C \, \nabla \cdot \mathbf{u} + M \, \nabla \cdot \mathbf{w} && (2.49)
\end{aligned}$$

where τ^D is the deviatoric stress tensor, P_c is the confining pressure and the quantities K_G, G_{fr}, C and M are incompressibilities and I is the identity matrix.

First two equations present a physical coupling between the force balances and generalized Darcy's law; in a low-frequency approximation, dynamic permeability $k(\omega)$ will be identified to the intrinsic permeability of the medium k_0 to finally recover the original form of Darcy's law. This system of equations sign the frequency-dependent (or dynamic) behaviour of poroelasticity.

Mid equation gives the contribution of the average shear stress. Finally, last two equations define a physical coupling between confining pressure P_c and fluid pressure p_f by introducing Biot coefficients C and M and Gassmann modulus K_G. This last system of equations is of the form announced in expression (2.44).

Main results of Biot's theory

By reckoning that in a fully saturated porous medium, the relative fluid and frame motion was simultaneously driven by both viscous and inertial effects, Biot [1956a,b] concluded to the existence of three volume waves, where only two were classically expected. Aside to the well-known rotational S-wave (a shearing wave not propagating within fluids) Biot identified the equally familiar fast P-wave (a fast-travelling compressional wave commonly identified as the first arrival) and a less expected slow P-wave.

This last wave, also referred to as the Biot slow-wave, was named as such for sharing a purely divergent nature with the fast P-wave, while being slower by up to one order of magnitude. Its absence from previous field records may be attributed to its very high attenuation, the Biot slow-wave resulting from fluid-pressure diffusion. From a microscopic point of view, while frame and fluid compression occur in phase in the fast P-wave, they are out of phase for the Biot slow-wave. Practically, it means that in this last case a region of high fluid pressure corresponds to a frame expansion (as if fluid pressure caused it to bulge), while frame contraction is observed at low-fluid pressure [Haartsen and Pride, 1997].

Apart from accounting for three wave-modes, the poroelasticity theory as developed by Biot does also depend on frequency. We already mentioned the respective role of viscous and inertial flow. We noted that viscous effects, typically governing Poiseuille flows, would dominate in the lower frequency-range, while inertial flow would rather prevail at higher frequencies, as displacements occur so swiftly that fluid-pressure equilibration is incomplete. The characteristic frequency marking the transition from one domain to the other was identified by Biot as:

$$f_{Biot} = \frac{\phi \eta_f}{2\pi \alpha_\infty \rho_f k_0} \tag{2.50}$$

At that particular frequency, the viscous forces equal the inertial ones and energy losses are expected to be maximal. With this formulation we understand how Poiseuille flow might be maintained to higher frequencies with higher porosity ϕ or lower permeability values k_0, both factors favouring lower fluid velocity. Large fluid viscosity η_f also enforces viscous effects while increasing fluid density ρ_f precipitates the transition to inertial flow. Hence, for an unconsolidated sand of porosity $\phi = 0.42$, tortuosity $\alpha_\infty = 1.65$ and permeability $k_0 = 20\ D$, f_{Biot} would be higher in dry (air-saturated) sand than in the water-saturated equivalent: respective attenuation maxima should be located at 30.4 kHz and 2 kHz. Consequently, f_{Biot} will clearly depend upon the water content.

This frequency dependency is particularly visible in previous equation (2.46) as it is born by the factor:

$$\tilde{\rho}(\omega) = i\omega \frac{\eta_f}{k(\omega)} \tag{2.51}$$

enabling to rewrite the initial equation system formed by eq. (2.45) and (2.46) as:

$$\begin{cases} \nabla \cdot \tau^D - \nabla P_c = & -\omega^2 \left(\rho \mathbf{u} + \rho_f \mathbf{w}\right) \\ \nabla p_f = & -\omega^2 \left(\rho_f \mathbf{u} + \tilde{\rho}(\omega) \mathbf{w}\right) \end{cases} \tag{2.52}$$

Under this form we better understand the denomination of $\tilde{\rho}(\omega)$ as the effective density, characterizing the frequency-dependent fluid mobility. The definition of effective density $\tilde{\rho}(\omega)$ includes dynamic permeability $k(\omega)$ expressed as:

$$k(\omega) = k_0 \left[\sqrt{1 - i\frac{\omega}{\omega_c}\frac{4}{m}} - i\frac{\omega}{\omega_c} \right]^{-1} \tag{2.53}$$

where $\omega_c = 2\pi f_{Biot}$ is the characteristic Biot pulsation. Then by defining an auxiliary parameter γ and the global expression for P-wave slownesses after Pride [2005] as:

$$\gamma(\omega) = \frac{\rho M + \tilde{\rho}(\omega) H - 2\rho_f C}{HM - C^2} \tag{2.54}$$

$$s_{pf,ps}(\omega) = \left(\frac{1}{2}\gamma(\omega) \mp \frac{1}{2}\sqrt{\gamma(\omega)^2 - \frac{4(\tilde{\rho}(\omega)\rho - \rho_f^2)}{MH - C^2}} \right)^{1/2} \tag{2.55}$$

for fast or slow P-waves (respectively $'-'$ and $'+'$ sign, identified by the indices $_{pf}$ or $_{ps}$), we may eventually define the frequency-dependent attenuation $\alpha_{pf,ps}$, the velocity dispersion $V_{pf,ps}$ and the inverse quality factor $Q^{-1}_{pf,ps}$ associated to Biot's poroelasticity by considering real or imaginary part of the complex slowness $s_{pf,ps}$:

$$\alpha_{pf,ps}(\omega) = \omega\, Im(s_{pf,ps}(\omega)) \tag{2.56}$$

$$V_{pf,ps}(\omega) = \frac{1}{Re(s_{pf,ps}(\omega))} \tag{2.57}$$

$$Q^{-1}_{pf,ps}(\omega) = 2\,\frac{Im(s_{pf,ps}(\omega))}{Re(s_{pf,ps}(\omega))}\,\frac{2\alpha_{pf,ps}(\omega)\,V_{pf,ps}(\omega)}{\omega} \tag{2.58}$$

In our experimental measurement we will essentially focus on seismic attributes of the fast P-wave, so that beyond this point we will rename $V_{pf} = V_p$, $\alpha_{pf} = \alpha_p$ and $Q^{-1}_{pf} = Q^{-1}_p$.

Assumptions and limitations

The applicability of Biot's theory relies on five hypothesis (Biot [1956a], Pride [2005]:

- Pore size is negligible in comparison to wavelength, so that the medium might be considered as macroscopically homogeneous;

- Strains are small, in order to stay within the linear elasticity domain;

- Solid frame is considered elastic and isotropic, causing its elastic moduli to be respectively real and scalar;

- Pore volume is interconnected, continuous and fully saturated by a single fluid phase;

- Intergrain friction is negligible, so that causes for wave attenuations are limited to macroscopic fluid flow due to pressure gradients.

When considering an unconsolidated porous medium under probable partial saturation, the most limiting assumptions of the would concern the last two items. Efforts for generalisation of Biot's poroelasticity to partial saturation and for extending its consideration of energetic losses to intergrain friction will be presented in section 2.4.2 and 2.4.1 respectively.

2.3.3 Attenuation in standard Biot theory

The first theoretical keys to the understanding of fluid-induced viscous effect were given by Biot in a series of articles, thought as an extension to the work of Terzaghi [1943]. It tackled macroscopic fluid flow in fully saturated media, induced by solid frame dragging and pressure gradients between peaks and trough of the wave. This approach assumed perfect elasticity of the frame and was knowingly devoid of any solid friction concern. In Biot's approach, the quantified interaction of fluid and frame permitted to define different frequency domains with distinct viscous behavior. His frequency division recognizes three main transition frequencies (expressions can be found in table 2.2):

- the Biot frequency f_{Biot} marking the transition between viscous and inertia-driven flow as the frequency increases;

- the characteristic frequency for wavelength-scale fluid-pressure equilibration f_λ which occurs when the macroscopic fluid pressure just has time to equilibrate in a wave period

[Pride, 2005].

- the frequency f_{Poise} limiting laminar flow, for which Poiseuille conditions apply ; for our type of high-porosity granular material it may be inferior to f_{Biot} by one order of magnitude thus corresponding to seismic range.

If submitted to a frequency f inferior to both f_{Biot} and f_{Poise}, the medium would display low-frequency behavior, meaning that elastic moduli would be real frequency-independent quantities. In this case, velocity dispersion is expected to be negligible and Q^{-1} should vary as f. For much higher frequencies and consequently turbulent flow, Q^{-1} is predicted to vary as $f^{-1/2}$ [Pride, 2005]. The associated phase velocity should increase with frequency, however in the range of parameters computed by Biot [1956b] the increase was limited to 15% on a frequency range of $[0-10\ f_{Biot}]$. As a result, according to Biot theory major attenuation Q^{-1} due to fluid pressure equilibration should be observed for frequencies close to f_{Biot}. Johnson and Plona [1982] and Winkler [1985] proposed an approach of Biot's theory in terms of a viscous skin depth $\sqrt{\eta_f/(\pi\rho_f f)}$ relatively to pore size and shear stress relaxation. At low frequencies the skin depth is larger than the pore size and the fluid is locked to the frame while at high frequencies viscous effects are limited to such a small skin depth that fluid inertia prevails. They concluded that attenuation by viscous drag should only be significant at intermediate frequencies, when viscous skin depth is comparable to pore size, which coincides with f_{Poise}.

Yet, measured attenuation on porous media are essentially underestimated by the standard Biot approach. Further attenuation contributions are consequently sought in the limiting assumption to the Biot theory.

2.4 Development on Biot's theory

Two major limitations in the direct application of Biot's theory for poroelasticity to geomaterials are his assumptions concerning the perfect elasticity of the solid phase and the monophasic nature of the fluid phase. Hence, extensions of the Biot's theory were made in order

- to account for possible viscous loss not restrained to pore-fluid interaction but also extended to friction within the solid frame

- to take the role of partial saturation into consideration.

The present section deals with the effect of these new considerations on properties of the porous medium, the impacts on seismic wave attributes are to be broached in a coming chapter.

2.4.1 Adaptation to viscous behavior of granular material: toward the Biot-Stoll model

A first reason for attenuation underestimation may be the neglecting of frictional losses at grain contacts. This phenomenon should be particularly important for unconsolidated porous

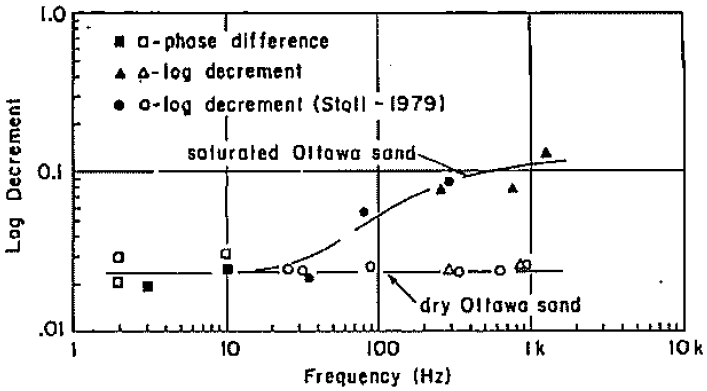

Figure 2.9: Logarithmic decrement versus frequency for water-saturated and dry Ottawa sand(from Stoll [1985]).

media as for marine sediments. After having introduced the main characteristics of viscous behaviour, we will report literature observations that participated to the acknowledgement of frictional losses contributions to attenuation. We will eventually show how specific answers may be brought by the Biot-Stoll model combining Biot theory to solid friction (Stoll [1974], Stoll [1977], Stoll [1985]).

Characteristics of viscoelastic losses

While elasticity is rheologically identified as a spring showing linear dependency of strain to stress, viscosity will be represented as a damper, traducing linearity of deformation rate relatively to the applied stress. Hence, conversely to elasticity presuming instantaneous response, viscous behaviour differs by the delay observed between stress application and the appearance of a related strain. As a result, in a viscoelastic context, elastic moduli will become complex and the phase will express the viscous delay.

Considering a complex modulus $Mo^* = Mo_r + iMo_i$, for strains restricted to small amplitudes, intrinsic damping may be estimated by various equivalent ways [Stoll, 1985]:

$$\frac{1}{Q} = \frac{\delta}{\pi} = \frac{Mo_i}{Mo_r} = tan\ \theta \tag{2.59}$$

where Q would be the quality factor and δ the logarithmic decrement of the Mo^* modulus, while θ would qualify as the phase delay between stress and strain under harmonic loading[3]. A viscoelastic modulus can subsequently be written as:

$$Mo^* = Mo_r \left(1 + i\frac{\delta}{\pi}\right) \tag{2.60}$$

With such definitions, quality factor Q is expected to have the same dependency on frequency than the logarithmic decrement δ. For instance, according to figure 2.9, for dry sand there should be no dependency of Q on frequency.

[3]Note that under sheer viscous behaviour, we would verify that $Mo^* = iMo_i$ is an imaginary number, causing quality factor Q to be zero and the energy loss to be total Barrière [2011].

Reported observations on frictional attenuation

As soon as the 1940's, Born [1941] advocates two major causes for energy dissipation by intrinsic attenuation during wave propagation. The first dissipation mechanism is assumed to be of viscous nature. Energy losses by viscous processes should be frequency-dependent, for they are proportional to particle velocity. At this time, viscous losses are already well-accounted for in theoretical seismology and are attributed to the interaction of a viscous pore-fluid with an elastic solid. However, viscous losses do not explain the persistence of frequency-independent energy losses occurring in dry rocks. Born imputes this phenomenon to a second dissipation mechanism, called solid friction, or macroscopic Coulomb friction, a process where Q^{-1} does not depend on frequency but rather scales with the maximum strain amplitude. He suspects it to be primarily responsible for seismic attenuation observed in seismic reflection method, ahead of viscous losses. His interrogation marks the beginning of many decades of feverish investigation to identify the sources of intrinsic attenuation.

Following the paper by Born [1941], similar frequency-independent observations pile up [Knopoff, 1964] as the role of solid friction in seismic wave attenuation is ruthlessly investigated, preferably on oven-dry or air-dry samples in order to minimize the contribution of water. Evidence supporting the importance of solid friction is apparently found when observations conducted on limestone and calcite conclude that attenuation α is one order of magnitude higher for limestone samples constituted of calcite grains, than it is for the plain calcite crystal [Peselnick and Zietz, 1959]. To account for these observations, Mindlin and Deresiewicz [1953] followed by White [1966] discuss a loss mechanism by static friction in granular media involving stick-slip process between grains at the area of contact. Another mechanism proposed by Walsh [1966] is based on frictional dissipation at cracks surface, caused by their sliding relatively to one another as the wave passes. This theory is supported by measurements on crystalline rocks by Gordon and Davis [1968] showing that internal friction increases with strain and decreases with confining pressure. Consecutively, several authors appeal to frictional mechanism to interpret experimental observations where the seismic quality factor appears predominantly frequency-independent (O'Connell and Budiansky [1977], Lockner et al. [1977], Johnston et al. [1979]). According to the chosen frictional model, Q^{-1} is expected to increase slower (grain friction) or faster (crack friction) than the first power of strain.

It is important to note that the role of fluids is still considered, even if it is thought to be secondary. Indeed, should it be in granular or fissured crystalline rock, water addition tends to increase the energy dissipation [Toksöz et al., 1979]: the general view seems to be that once the solid surface is lubricated, the sliding friction that would have been blocked under dry condition is facilitated.

A growing number of authors, however, are sceptical regarding the importance of frictional mechanisms attenuation for actual seismic wave exploration reckoning that the choice of source producing large strain amplitude may have driven the result-interpretation (Winkler et al. [1979], Winkler and Nur [1982]). As a matter of fact, if frequency independency

of Q in dry material seems to hold for any strain, many authors had already observed how strain dependency appeared at strains starting from 10^{-6}. Savage [1969] however is one of the first to note that, by this threshold, most seismic waves would qualify as low-strain. Eventually he questioned the relevance of frictional loss for seismic applications on theoretical basis, as reported by Mavko [1979]. Savage points out that if solid friction occurs at low strains then the maximum slip Δu on a crack of millimetric length l would be proportional to that very strain ϵ, taken inferior to 10^{-6}. According to the formulation $\Delta u = \epsilon l$, it would produce a slip in the order of some nanometers which can probably not be interpreted using macroscopic sliding friction.

Another issue refers to the question of nonlinearity, inherent to frictional mechanism. If cusped stress-strain hysteresis loops provide actual indication of non-linear effects at high-strain [Gordon and Davis, 1968], low-strain behavior appears to be linear [Brennan and Stacey, 1977]. Hence, if Walsh [1966] theory would explain the above-mentioned data at high-strain, possibly compatible with amplitude observations close to the source, for lower strain however another mechanism has to be appealed to [Winkler et al., 1979].

This mechanism should be both linear and mostly frequency-independent in regard of the available collection of data. For dry material, Lomnitz [1957] had already proposed logarithmic creep as a possible low-strain mechanism that complies with the required characteristics, and had it tested for strains up to 10^{-9}. His experimental tests had been endorsed by Pandit and Savage [1973]. An attempt was made by Liu et al. [1976] to propose a Nearly-Constant-Q model by superposing many linear models of distinct characteristic frequencies (an approach that will be more thoroughly explained in coming paragraph on fluid-induced attenuation). But until the theoretical formulation of a constant Q-model by Kjartansson [1979], the notion of a loss mechanism combining strict linearity, causality and frequency-independency was thought nonphysical. This model gave an opportunity to unify observations conducted at both high and low-strain amplitudes.

Biot-Stoll model

Kimura [2007] proposed a simplified version of the Biot-Stoll model dedicated to the fast P-wave, that determines asymptotes to velocity dispersion, attenuation curves and quality factor at both extremities of the frequency spectrum. Complex frame moduli are defined as:

$$K^*_{fr} = K_{fr}\left(1 + i\frac{\delta_l}{\pi}\right) \tag{2.61}$$

$$G^*_{fr} = G_{fr}\left(1 + i\frac{\delta_s}{\pi}\right) \tag{2.62}$$

where $\delta_l = \delta_s = 0.15$, based on a ratio of extensional to shear decrement of 1 for sand [Stoll, 1985] and the value of 0.15 being taken accordingly to results by Stoll [1989]. Modification of the frame moduli will cause Gassmann modulus K^*_G and Biot's coefficients C^*, M^* and H^* to become also complex.

In addition to these poroelastic moduli complex redefinition, Kimura [2007] considers effective pore diameter d_p, a parameter that is not involved in standard Biot's theory, and

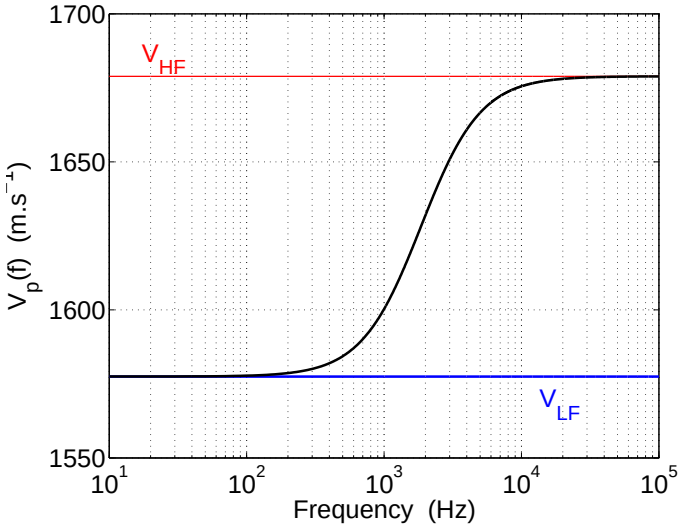

Figure 2.10: Lower and higher velocity bound V_{LF} (blue) and V_{HF} (red) framing the frequency-dependent velocity $\tilde{V}_p$ defined by For a low to middle-frequency approximation of velocity $\tilde{V}_p$, we may resort to Geertsma and Smit [1961].

introduces the added mass m_0 as:

$$m_0 = \alpha_\infty \frac{\rho_f}{\phi} \tag{2.63}$$

P-wave velocities at zero frequency V_{LF} (identical to Gassmann's velocity), and infinitely high frequency V_{HF} (with no more fluid loss) are formulated as:

$$V_{LF} = \sqrt{\frac{H^*}{\rho}} \tag{2.64}$$

$$V_{HF} = \frac{\sqrt{2(C^{*2} - H^* M^*)}}{-(m_0 H^* + \rho M^* - 2\rho_f C^*) + \sqrt{(m_0 H^* + \rho M^* - 2\rho_f C^*)^2 - 4(C^{*2} - H^* M^*)(\rho_f^2 - m_0 \rho)}}$$

(2.65)

For a low to middle-frequency approximation of velocity $\tilde{V}_p$, Kimura [2007] points at Geertsma and Smit [1961] formulation based on combination of V_{LF} and V_{HF} (as shown in figure 2.10):

$$\tilde{V}_p = \sqrt{\frac{\left(\frac{f}{f_{Biot}}\right)^2 V_{HF}^4 + V_{LF}^4}{\left(\frac{f}{f_{Biot}}\right)^2 V_{HF}^2 + V_{LF}^2}} \tag{2.66}$$

Velocities V_{LF} and V_{HF} are then incorporated in the definition of asymptotes to attenuation α for the lower and the upper frequency range, being respectively identified as α_{LF}

and α_{HF}:

$$\alpha_{LF} = \frac{\omega^2}{2V_{LF}}\left(\frac{V_{HF}}{V_{LF}}^2 - 1\right)\frac{m_0\rho - \rho_f^2}{\rho}\frac{k_0}{\eta_f} \tag{2.67}$$

$$\alpha_{HF} = \frac{\sqrt{\omega}}{8\sqrt{2}V_{HF}}\left(1 - \frac{V_{LF}}{V_{HF}}^2\right)\frac{\rho}{m_0\rho - \rho_f^2}\frac{d_p}{k_0}\sqrt{\rho_f\eta_f} \tag{2.68}$$

Similarly, low-frequency and high frequency asymptote to quality factor Q^{-1} are defined by expressions Q_{LF}^{-1} and Q_{HF}^{-1} as:

$$\frac{1}{Q_{LF}} = \omega\left(\left(\frac{V_{HF}}{V_{LF}}\right)^2 - 1\right)\frac{m_0\rho - \rho_f^2}{\rho}\frac{k_0}{\eta_f} \tag{2.69}$$

$$\frac{1}{Q_{HF}} = \frac{1}{4\sqrt{2\omega}}\left(1 - \left(\frac{V_{LF}}{V_{HF}}\right)^2\right)\frac{\rho}{m_0\rho - \rho_f^2}\frac{d_p}{k_0}\sqrt{\rho_f\eta_f} \tag{2.70}$$

Position of the asymptotes intersection may be moderately adapted through the effective pore diameter d_p: indeed all other parameter fixed, α_{HF} and Q_{HF}^{-1} are increasing linearly with d_p. If we consider that d_p variate with the mean grain diameter related to permeability by Kozeny-Carman or Glover-Walker relation (see eq. (2.14) or (2.17)) this effect appears enhanced. Consequently, the bigger the effective diameter of the pore the higher the intersection frequency (as will be seen in figure 2.11). As asymptotes intersection appears to draw the line of a maximal energy loss, we expect the intersection frequency to lie by transition frequency f_{Biot}. For an effective pore diameter $d_p = 60\ \mu m$ compatible with a mean grain diameter of 250 μm (see table 2.3), this maximal loss would be expected by $2-3\ kHz$, at the intersection of red curves in figure 2.11. This would indeed correspond to f_{Biot}, estimated to be of 2 kHz on a fully saturated quartz sand having been attributed a porosity $\phi = 0.42$, tortuosity $\alpha_\infty = 1.65$ and permeability $k_0 = 20\,D$. It appeared that considering frictional losses will increase the initial Biot estimation of attenuation and inverse quality factor by a factor 3.

2.4.2 Adaptation to partial saturation: definition of an effective fluid

Another strong limitation to wide utilization of standard Biot theory concerns the assumption of full saturation of the pore volume by a monophasic fluid. Practically, when imbibing an air-saturated dry porous medium with a liquid phase, full saturation requires imbibition under depressurised conditions. This holds true even if the non-wetting gaseous-phase is replaced by a wetting liquid-phase. Hence, developments on partial saturation constitute an important step in the generalisation of the Biot theory.

For this purpose, the bulk fluid, formed from two immiscible fluid-phases, may be mechanically characterised as an effective fluid. Characteristics of the effective fluid are primarily born by a new definition of fluid density ρ_f, fluid viscosity η_f and fluid modulus K_f. For this last parameter, we will see that the definition is not unique, having to account for different behavior depending on homogeneity degree of the fluid blend and the saturation history of

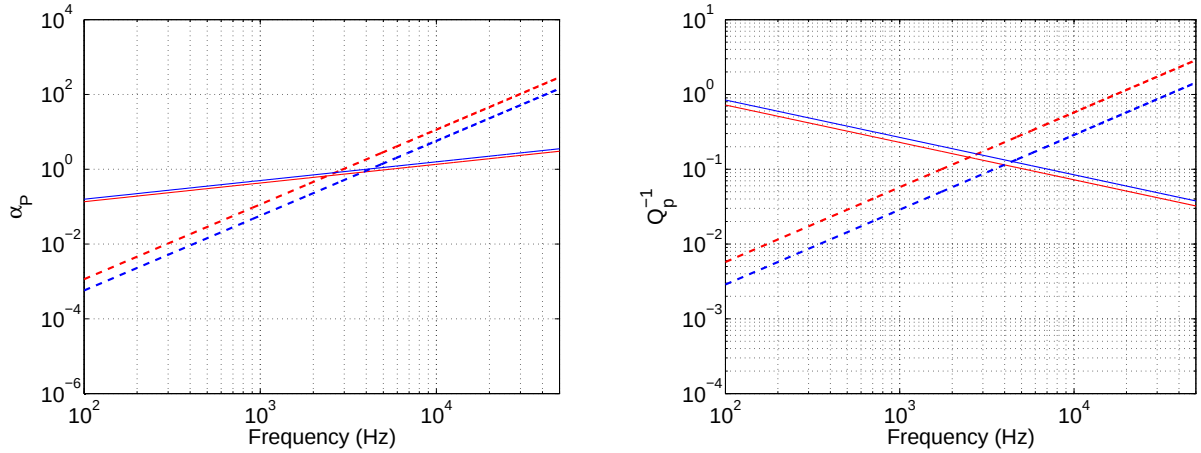

(a) (b)

Figure 2.11: Variation in the position of the asymptotic Biot-Stoll model with changes in the model parameters: for the red lines we considered $k_0 = 20\,D$ $d_g = 250\,\mu m$ and $d_p = 60\,\mu m$, for the blue lines we took $k_0 = 10\,D$ $d_g = 150\,\mu m$ and $d_p = 35\,\mu m$. The agreement between k_0 and d_p was taken accordingly to table 2.1. Dashed line correspond to LF asymptotes while plain lines are HF asymptotes.

the medium. All quantities involving the aforementioned effective parameters will consequently become saturation-dependent. The dependency of Biot critical frequency f_{Biot} on ρ_f and η_f will ensure the subordination of dynamical parameters to saturation.

Density of the effective fluid

Be S_w the water saturation degree, ρ_g the density of the gaseous constituent and ρ_w that of the liquid, in analogy to the definition of the bulk density of a porous medium, the effective fluid density is given by a simple arithmetic average:

$$\rho_f(S_w) = \rho_g(1 - S_w) + \rho_w S_w \tag{2.71}$$

Viscosity of the effective fluid

While density ρ_f is commonly thought to result from an arithmetic mean, dynamic viscosity η_f tends to be overestimated by such an operation. Being aware of this, Teja and Rice [1981] proposed a new relation for viscosity where saturation S_w appears as an exponent (see figure 2.12). Hence for an effective fluid where η_g and η_w are respectively the dynamic viscosity of the gaseous and the liquid constituent, we will have:

$$\eta_f(S_w) = \eta_g \left(\frac{\eta_w}{\eta_g}\right)^{S_w} \tag{2.72}$$

Effective fluid modulus

For characterising the effective elastic moduli of a given mixture, information on volume fraction and elastic moduli of the various phases are generally required, completed by details on phases disposition relatively to another, characterising among others the homogeneity

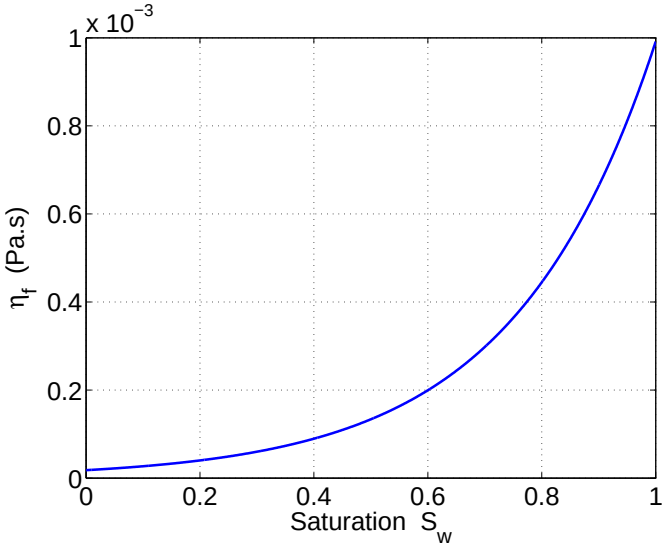

Figure 2.12: Evolution of the effective viscosity of an air + water fluid mixture according to the relation by Teja and Rice [1981].

of the mixture. When lacking that previous knowledge regarding geometric arrangement of a multiphase entity, one can only approach the result by upper and lower bounds Mavko et al. [2003]. In this respect, Voigt-Reuss bounds constitute a common approach for effective medium characterisation.

Considering a fluid mixture of air and gas, of respective bulk moduli K_g and K_w, and a water saturation degree S_w, Voigt upper-bound based on an arithmetic average would be expressed as:

$$K_V(S_w) = K_g(1 - S_w) + K_w S_w \tag{2.73}$$

whereas Reuss lower-bound, more commonly known as the Wood [1955] model, would be calculated as an harmonic average:

$$\frac{1}{K_R(S_w)} = \frac{1 - S_w}{K_g} + \frac{S_w}{K_w} \tag{2.74}$$

The homogeneity of the effective fluid would direct the choice of the averaging method. Indeed while Voigt arithmetic average is characteristic of heterogeneous fluid (where patches of water and gas appear as if putted in series, their size being non-negligible compared to wavelength-scale), Reuss geometric average would correspond to the highest homogeneity level reached by a fluid mixture (valid for miscible constituents or fluid heterogeneities being small compared to wavelength-scale).

Confronted to real data acquired on gas-bearing sands, Brie et al. [1995] proposed an intermediary solution under the form of an empirical power law in saturation S_w:

$$K_{Be}(S_w) = (K_w - K_g){S_w}^e + K_g \tag{2.75}$$

Interestingly, Brie model equals Voigt prediction when taking the exponent to be unity, whereas it tends to jump from air modulus K_g to water modulus K_w, exacerbating Reuss-

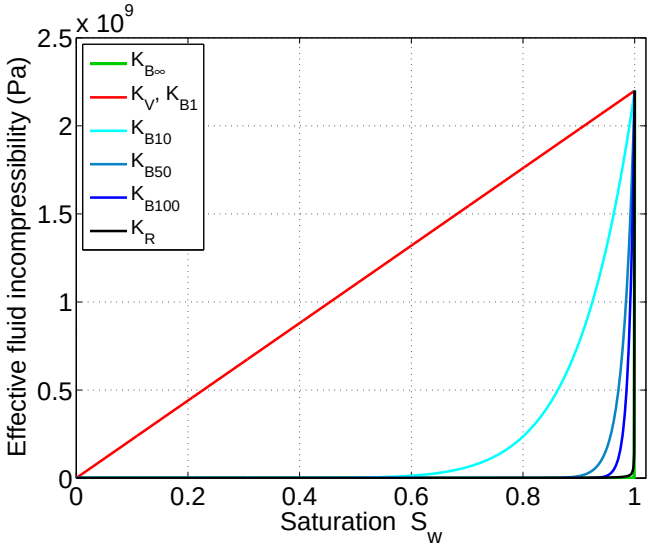

Figure 2.13: Presentation of various model for effective fluid modulus K_f computation of an air+water mixture relatively to water saturation degree S_w. Voigt and Reuss model are respectively noted as K_V and K_R, while a Brie model of exponent $e = n$ will be referenced as K_{Bn}.

like steep variations, when $e \to \infty$. A gather of Voigt, Reuss and various Brie models is presented in figure 2.13; Brie model of exponent $e = n$ will be noted K_{Bn}. We see that, the higher the exponent would be, the steeper and the later will final velocity increase take place, indicating an effective fluid of higher homogeneity. On this figure within the higher saturation range, it appears that $K_{B\infty} < K_R < K_{B100}$; a fairly reasonable approximation of K_R by a Brie model would take place for exponent e taken within $[100 - 1000]$.

Conclusion

This adaptable law for effective fluid modulus is frequently implemented to account for patchy saturation (Johnson [2001], Carcione et al. [2006]), a fluid configuration often experienced during drainage where macroscopic gas patches appears within an otherwise fairly homogeneous effective fluid. Thus, Brie's empirical law, developed to account for patchy saturation, adapts to all possible state as can be seen on figure 2.14 for $S_w = 0.95$. It goes from fully homogeneous K_R, equivalent to K_{B130} at that saturation degree, characterising a fluid having a similar compressibility to air (no matter how fine the scale there will always be some air volume to absorb the compression and dissipate the seismic energy) to highly heterogeneous $K_V = K_{B1}$ representative of a 'stiff' fluid.

With figure 2.15, we measure the tremendous impact of the effective-fluid-model choice on predictions of fast P-wave velocity by Biot. When combined to a Brie model for effective fluid modulus, the brutal increase in velocity occurs all the sooner so as Brie exponent is low. Yet, as observed in figure 2.16 for $K_f = K_{B10}$, velocity dispersion seems not much enhanced by partial saturation. In this same figure we present the evolution of Biot transition frequency with water saturation, varying with saturation-dependent parameter ρ_f and η_f. We note that for this computation adapted to an unconsolidated silica sand, the transition frequency range by 2 kHz at full saturation reaches a minimum of 500 Hz for saturation degree $S_w \approx [0.1 - 0.1]$ before increasing dramatically as the sand approaches the dry state.

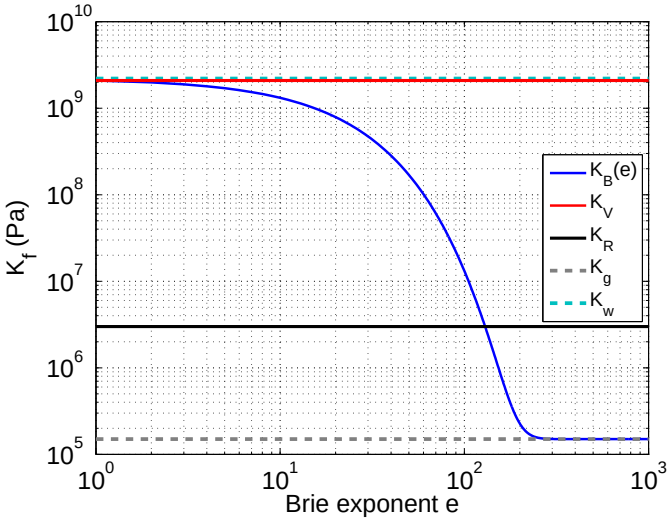

Figure 2.14: Evolution of the empirical effective modulus K_f by Brie K_B with exponent e (blue curve) for a constant water saturation degree $S_w = 0.95$ relatively to the Voigt K_V and Wood-Reuss K_R average and fluid moduli of water K_w and air K_g.

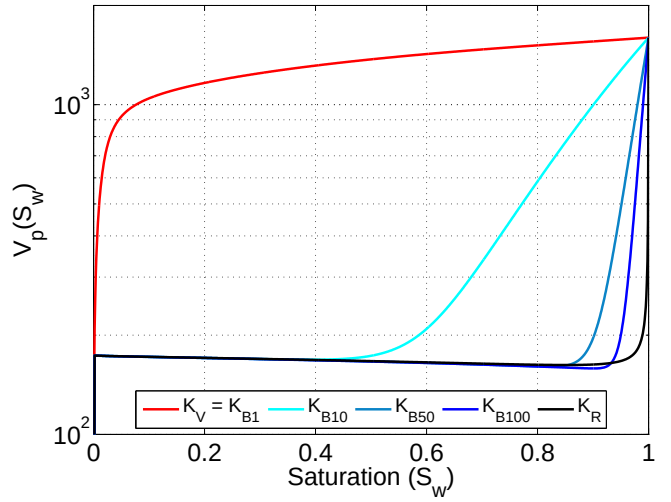

Figure 2.15: Velocities dependency on saturation, obtained by standard Biot theory for various estimations of the effective fluid modulus using Brie models $K_{B1} = K_V$, K_{B10}, K_{B50}, K_{B100} and a Wood model K_R.

2.4.3 Further sources for viscous losses under partial saturation: squirt-flow and patchy saturation

Naturally, fluid inhomogeneities related to partial fluid saturation are given much attention (Gardner et al. [1964], White [1975], Mavko and Nur [1979], Palmer and Traviolia [1980]). On this point, some precisions regarding the effect of mesoscopic heterogeneities as in patchy saturation will be brought. Another matter of interest is the response of compliant saturated cracks to seismic excitation. These cracks, disregarded in the standard Biot theory, notably for the sake of the elasticity assumption, would contribute to losses by local flow dissipation, in a complementary approach to the macroscopic flow aspect treated by Biot.

Concomitantly, with the release of Biot's theory on poroelasticity (Biot [1956a], Biot

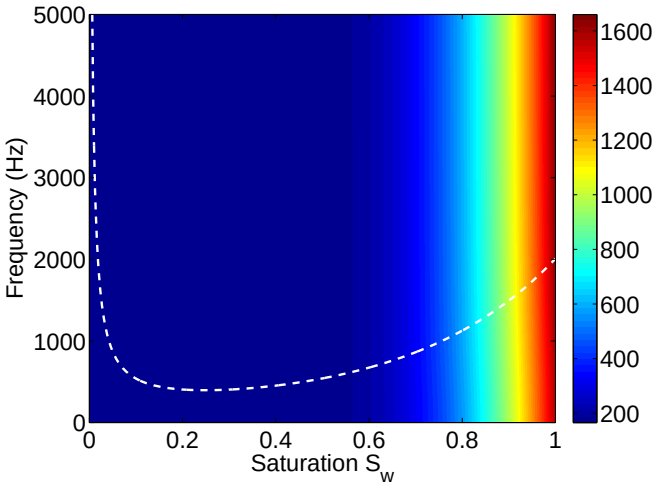

Figure 2.16: Evolution of Biot transition frequency f_{Biot} with water saturation as a white dashed line, while the evolution of the fast P-wave velocity with saturation and frequency is represented as a color scale in the background (for an effective fluid modulus using Brie models $K_f = K_{B10}$).

[1956b]), questions on the role of fluid-flow in viscous damping grow central. More and more authors suspect a determinative contribution to attenuation, especially at seismic frequencies and strains(Wyllie et al. [1962], O'Connell and Budiansky [1977],Winkler and Nur [1979]).

In their paper Winkler and Nur [1982] review all processes possibly implicated in fluid-induced attenuation. Next to the already quoted wetting effect of the liquid phase on sliding boundary, present even at very low fluid-saturation and all the more important so as the wetting phase is more polar [Jones, 1986]; they also mention the thermal relaxation of pore fluids as a possible viscous loss but mostly negligible for temperatures below $100°C$. They subsequently address the possible attenuation mechanisms involving fluid flow at various scales. It ranges from the macroscopic viscous drag first described by Biot [1956a] to microscopic fluid-flows at crack/pore scale [Mavko and Nur, 1975], not to mention attenuation induced by mesoscopic fluid heterogeneities in partially saturated medium.

Attenuation by squirt-flow Squirt-flow is resulting from fluid movements from compliant into more stiffer pores. Hence a good candidate for squirt-flow are porous media containing cracks as secondary porosity. From a theoretical point of view, Mavko and Nur [1975] and O'Connell and Budiansky [1977] agreed that the cracked solid could be represented by a standard Zener model also called "standard linear solid" (see figure **??**). The response of this model is composed of a strict elastic component, represented by a spring, that is associated to a viscous elastic component, represented by a damper and a spring in parallel; all these components participate to define a characteristic frequency for the system. The viscous behavior introduces a delay between stress application and related strain. As a result, modula in viscoelastic context will be complex and the phase will express this delay.

The frequency dependent behavior of cracked rocks was thoroughly described by O'Connell and Budiansky [1977]. Along to the very low frequency case where drained mode is equivalent to frictional sliding at wetted cracks, they presented three other squirt-flow modes

punctuated by two characteristic frequencies. First, a central relaxation frequency f_{squirt}, also acknowledged by Palmer and Traviolia [1980], marks the transition between an isobaric and an isolated mode, respectively named intercrack- and intracrack-flow by Mavko and Nur [1979] and traducing the passage from an incompressible to a compressible flow. Below this transition frequency despite the absence of flow out of the bulk region (local flow) fluid pressure is homogenous, whereas for higher frequencies, the flow will be restricted to the crack (viscous relaxation) causing each crack to fix its own fluid pressure. Second, a no-flow limit frequency f_{lim}, also reported by Murphy [1982], delimits the isolated from the "glued" mode. Under such high frequencies, the fluid is totally unrelaxed and the solid acts as if it were free of cracks. These frequencies are respectively proportional to the third and the first power of the aspect ratio e, a ratio between the aperture and the radius of a circular crack necessarily inferior to unity. Maximal dissipation is expected at relaxation frequency f_{squirt} varying as e^3. Hence, if e varies by one order of magnitude, traducing the existence of a variety of crack dimensions, f_{squirt} would vary by three. A variety of attenuation curves, characteristic of linear relaxation mechanisms, will add on to produce a quasi-constant Q^{-1} on a large frequency-band (see figure 2.17). This argument of continuous aspect ratio distribution was cited by [Liu et al., 1976] to explain the emergence of nearly constant Q-profile, otherwise typical of solid friction, under wet conditions and in the absence of any frictional nonlinear mechanism. In the low frequency approach, meaning frequency condition that ensures Poiseuille flow, Q^{-1} is expected to vary linearly with frequency. In that it agrees with the Biot model. The high frequency comportment at full saturation as predicted by Gurevich et al. [2010] depends on the fluid nature : for a gas-saturated granular rock the decrease of Q^{-1} should be proportional to $f^{-1/2}$; if the saturating fluid is water Q^{-1} will first decrease as $1/f$ before switching to the $f^{-1/2}$ dependency at very high frequency. A model previously developed by Mavko and Nur [1979] for partially saturated rocks with parallel-walled pore had predicted a uniform fall of Q^{-1} proportional to $f^{-3/2}$ for frequencies beyond f_{squirt}. Thus the high-frequency attenuation due to squirt-flow appears to be extremely dependent on fluid-phase composition.

When Mavko and Nur [1975] proposed the squirt-flow mechanism, they also suggested that the impact of round-shaped pore may be marginal. Jones [1986] came to a similar conclusion after having compared attenuation peaks for a wide collection of experimental results on water-saturated rocks. No matter the rock type (sandstones, limestones, granites), maximum attenuation always took place around 2 kHz which indicated that attenuation was dominated by cracks of aspect ratio e by $[10^{-4} - 10^{-3}]$. Thinner cracks would not participate to squirt process for their water content would probably be bounded, whereas, according to the local-flow model, the contribution of rounder pore would not be of much significance. Palmer and Traviolia [1980] who modeled squirt-flow explicitly for granular materials, had to consider aspect ratios greater than 10^{-2} and contact in the sand of water-suspension type in order to fit the prediction to experimental data on gas sands. However, elevated compliance of broken grain contacts remains a possible origin of squirt-flow within granular media, as evoked by Pride [2005].

Complementarity of the Biot model and the squirt-flow, both concerned with opposite

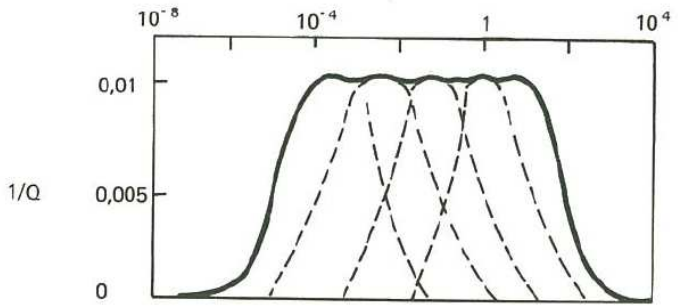

Figure 2.17: Inverse quality factor for Nearly-Constant-Q model (after Liu et al. [1976]).

fluid-flow scales but related by fluid mass balance, has swiftly been assessed [Dvorkin and Nur, 1993]. Ever since, combined models have regularly been adapted and reformulated (Diallo and Appel [2000] and Chotiros and Isakson [2004]).

For Pride and in contradiction with Jones, squirt-flow attenuation is expected in the MHz range, why)

Attenuation in patchy saturation When looking for possible cause of increased attenuation, mesoscopic scale heterogeneity appeared as a good candidate. The heterogeneity may be born by the frame as it would be in a sand/shale mixture or by fingering effect in an unconsolidated material. It may also be related to inhomogeneity within the saturating fluid, resulting in the existence of mesoscopic patches of distinct immiscible fluids. patchy saturation : (White [1975], Dutta and Odé [1979] and Dutta and Seriff [1979],Pride et al. [2004], Müller et al. [2010]) - for Pride [2005], the only mechanism that can account for enhanced attenuation in the seismic band

	Characteristic frequency	Significance	Frequency dependency	f values for geomaterials	
				Berea sandstone	Landes sand
Biot	$f_{Poise} = \frac{\pi \eta_f}{4 \rho_f d_p^2}$	laminar to turbulent flow	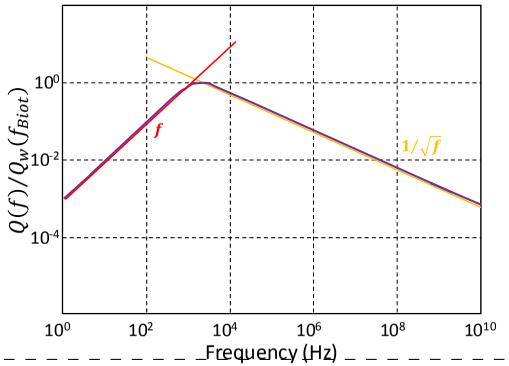	6.5 kHz	50 Hz
	$f_{Biot} = \frac{\eta_f \phi}{2\pi \alpha_\infty \rho_f k}$	viscosity to inertia driven flow		0.1 MHz	1.5 kHz
	$f_\lambda = \frac{H \eta_f}{2\pi M \rho k}$	P_f equilibration in one wave period		1 GHz	50 kHz
Squirt	$f_{squirt} = \frac{K_{fr} e^3}{\eta_f}$	intercrack to intracrack flow	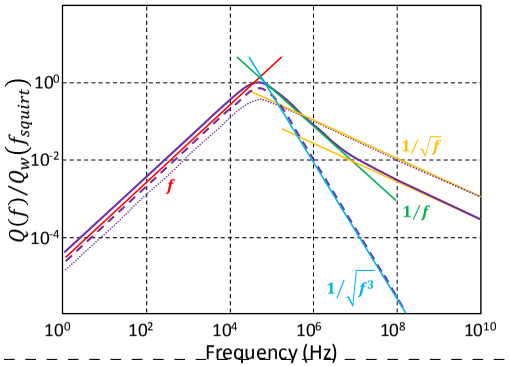	2 kHz	40 kHz
	$f_{lim} = \frac{G_{fr} e}{\eta_f}$	intracrack flow to glued cracks		6 GHz	0.2 GHz
Patchy	$f_{patchy} = \frac{4 k K_w}{\eta_w R_P^2 [S_g^{-1/3} - 1]^2}$	central relaxation frequency	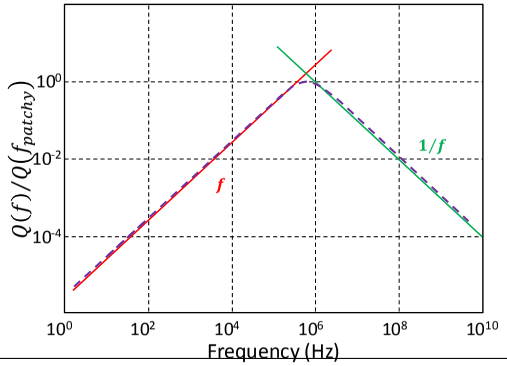	7 kHz	1 MHz

Table 2.2: Recap chart of the expression for all characteristic frequencies associated to dissipative fluid-flow mechanisms. Numerical values were calculated for typical characteristics of an unconsolidated Landes sand and a high porosity Berea sandstone on basis of the effective fluid model for $S_w = 90\%$. For patchy saturation, gas patches were taken centimetric ($R_P = 1cm$). Figures illustrate the dependency of a normalized Q^{-1} on frequency (inspired by work on squirt flow by Gurevich et al. [2010]). Full saturation data are represented by solid ($S_w = 1$) or dotted ($S_g = 1$) lines. Partial saturation corresponds to dashed lines.

2.4.4 Conclusion: expected attenuation-behavior on unconsolidated sand

In previous chapter, we have discussed a variety of viscous loss mechanisms causing intrinsic wave attenuation at length. We will now briefly recall these mechanisms, before questioning their relevance regarding our particular experiment. We hope to define which dissipation processes may intervene in an unconfined uncompacted granular sand, under partial to full water-saturation. This sand will be submitted to an acoustic excitation at sonic frequencies with typical maximum accelerations in the range $1 - 50\ m.s^{-2}$.

In dry rocks, mechanisms for intrinsic losses depend on the strain amplitude. At high strain, the energy loss appears to be dominated by solid friction, a nonlinear process where the inverse quality factor Q^{-1} will directly depend on strain ϵ. At lower strain, Q^{-1} will adopt a linear behavior owed to microscopic processes possibly including logarithmic creep or dislocation. The limit between high and low strains has experimentally been settled at $10^{-5} - 10^{-6}$. For both processes, and as long as the sample remains totally dry, the energy loss represented by Q^{-1} appears essentially frequency independent. Addition of water may facilitate the sliding at cracks or grain boundaries as well as introduce a frequency dependent component.

Besides the friction part played by the frame in viscous dissipation, a multiscale contribution to attenuation of wave-induced fluid-flow (WIFF) has to be considered. Frequency-dependency due to linear behavior is a common feature for viscous losses by WIFF. The typical profile of the inverse quality factor Q^{-1} is a bell-curve centered on a characteristic relaxation frequency for which the system suffers maximal viscous loss. These relaxation frequencies can be seen as indicators of transition in the pore-fluid behavior at macroscopic (Biot), mesoscopic (patchy) and microscopic scale (squirt). Knowing the relative position of the characteristic frequencies would help identifying the viscous effect expected to dominate at a given frequency. For this purpose, we recapitulate the various WIFF-mechanisms and their associated characteristic frequencies as well as their frequency-dependent behavior in table 2.2 and figure 2.18. This table was elaborated using elastic and hydraulic properties either taken from literature or deduced from lab measurement, all to be found in the appendices. Fluid bulk properties, indexed with an f, were calculated on basis of the effective fluid model for a water saturation degree of 90%. Undrained compressibilities K_U and Biot coefficient were estimated using Gassmann relations. For patchy saturation, gas patches were taken centimetric so that the radius of the air patch would be $R_P = 1\ cm$.

The first WIFF-mechanism to be addressed is Biot macroscopic viscous damping. Its importance at seismic and logging frequencies is rapidly questioned by experimental data. Indeed, while transition frequency f_{Biot} is expected to be proportional to fluid viscosity η_f, experimental data tend to show an attenuation peak at characteristic frequencies proportional to $1/\eta_f$. One particular data set addressing kilohertz acquisition within sandstone [Jones and Nur, 1983], for varying frequencies and viscosities, is reported to have shown such characteristics. Namely for various experiment, Q^{-1} repeatedly peaked at a given $f \times \eta_f$

value. As can be seen in table 2.2, under such kilohertz condition the sandstone would qualify for the low frequency limit of the Biot theory for which viscous drag is expected to be negligible. Another WIFF-phenomenon, however, happens to reach its maximal attenuation at 2 kHz. The dependency of the relaxation frequency f_{squirt} on $1/\eta_f$ within this frequency range would indeed identify this as an intercrack squirt-flow effect.

But unconsolidated materials behave quite differently from consolidated rocks, as can be seen when comparing the respective positions of WIFF-characteristic frequencies for sand and sandstone (figure 2.18). So, while squirt-flow prevails in high porosity sandstone at sonic frequencies, many authors expect its effects to be negligible for a sphere pack in a similar frequency band (Mavko and Nur [1975], Jones [1986]). This would be particularly true for a sphere pack composed of equal-sized spherical grains, a description that would usually apply to well-sorted eolian sand as the Landes sand used in our experiment. Reason is that f_{squirt} varies as the third power of the aspect ratio e. Yet, for such arrangement of spherical grains, pores are expected to be rounded shape leading to a high aspect ratio e. As such, for a squirt-flow model developed on sand, e had to be taken greater than 10^{-2} in order to match experimental data [Palmer and Traviolia, 1980]. In our calculation of the characteristic squirt-flow frequencies in sand, we chose to consider this lowest value to be characteristic for sand. By doing so, we determine a lower frequency bound on f_{squirt} from which on we have to be aware of possible attenuation peak induced by the transition regime in squirt-flow. If we go back to table 2.2, the first transition from intercrack to intracrack flow takes place for frequencies about 40 kHz, way above our domain of investigation. Consequently, if we experienced squirt-flow in our laboratory measurements it would be of intercrack nature. In this case the inverse quality factor is expected to depend linearly on frequency, as it does in both Biot and patchy low-frequency domain. The central frequency relaxation for patchy saturation appears to be out of range. On the contrary, Biot transition frequency f_{Biot}, more than two orders of magnitude below the former is expected within our investigation domain at kilohertz range. Hence, if a peak in the inverse quality factor was to be observed it should primarily be considered from the Biot transition point of view.

2.5 Pride's theory

When applying a seismic excitation on a porous saturated medium, one induces a transient relative movement between fluid and matrix, causing an electrokinetic coupling to initiate at the grain-fluid boundary. As we have seen in section 2.2.1, this electrokinetic coupling results from the so-called double layer, previously known from such methods as spontaneous potential or induced polarization. The alternating fluid movement generates a coseismic seismoelectromagnetic field at the scale of the mother seismic-wavelet that propagates with it.

In a complete theorization of the seismoelectromagnetic phenomena, Pride [1994] completed by Pride and Haartsen [1996] provided the governing equations coupling the coseismic seismoelectromagnetic effects to their seismic supports. Pride's theory, as it will be referred

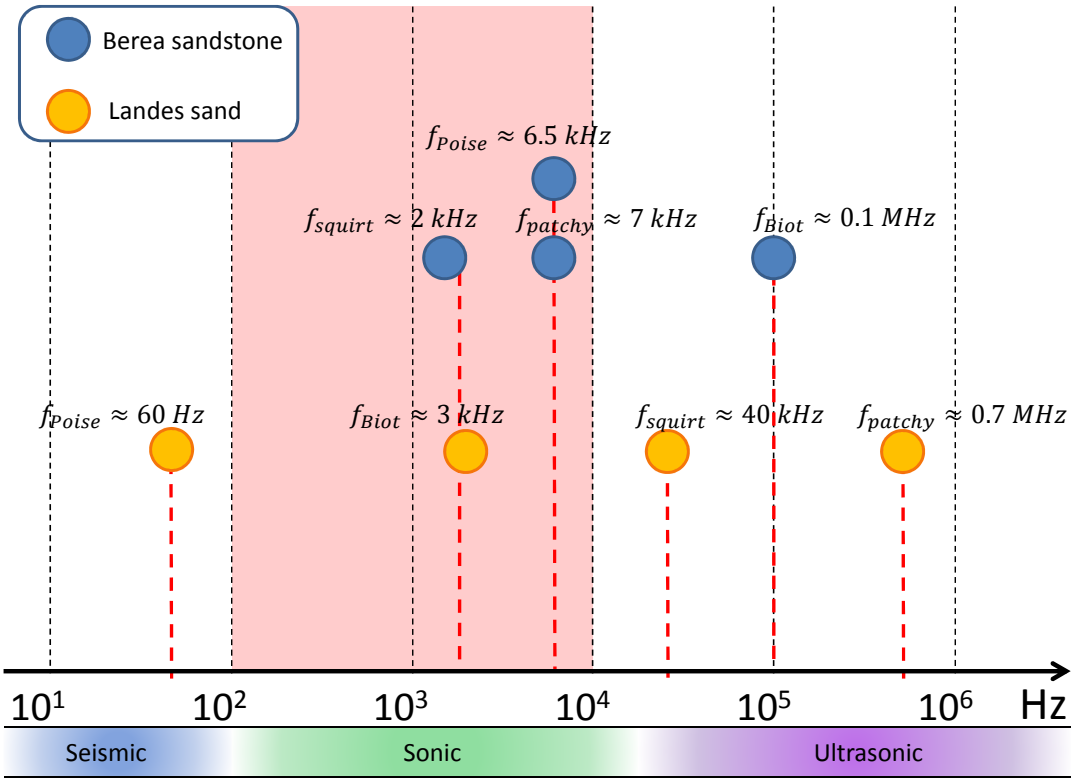

Figure 2.18: Relative position of characteristic frequencies for viscous losses induced by WIFF-phenomena in a Berea sandstone and a Landes sand. Our frequency domain of investigation is highlighted in red.

to, results from the combination of Maxwell's equation to Biot's poroelasticity and to the transport equations of electrokinetics dynamically adapted. In this present description of the coseismic seismoelectric theory, inspired by the works of Bordes [2005] and Warden [2012], we will state the main principles and equations underlying its formulation by Pride.

This model, as well as its reversibility to electroseismic through Onsager reciprocity, are derived from first principles and thermodynamic considerations at microscopic scale (notably through ionic mobilities and intervention of the Boltzmann constant k_B). Macroscopic expressions of Pride's theory are finally obtained through homogeneization methods: the relations relevant at microscopic scale are averaged on a mesoscopic volume V_A, so that its specific length remains large in comparison to the grain size d_g, yet small with regard to wavelength λ. On a given averaging volume V_A the medium is expected to be homogeneous and the medium properties might be taken as constants, so that the averaged value of a microscopic quantity a_ξ associated to phase ξ might be expressed as:

$$< a_\xi >= \int_{V_\xi} a_\xi \, \mathrm{d}V \tag{2.76}$$

where V_ξ represent the volume occupied by phase ξ within averaging volume V_A.

2.5.1 The constitutive equations

The first principles on which Pride's formulation is based are of three sorts: they combine the law of electromagnetics, represented by the full set of Maxwell equations, to the mechanical laws for poroelasticity, involving the full array of elastic and poroelastic moduli. They finally incorporate the electrokinetic transport equations. The theory is built on basis of the 9 equations presented hereafter, on the sole postulates of uniform surface-charge density adsorbed at the surface of the solid grains and of the absence of net charge within the medium prior to the disturbance arrival [Pride, 1994].

Maxwell's equations

Pride was the first to account for the whole set of Maxwell equations, these four equations being:

$$\nabla \times \mathbf{E} = -i\omega \mathbf{B} \tag{2.77}$$

$$\mu_0 \nabla \times \mathbf{B} = (-i\omega\, \epsilon + \sigma_b)\, \mathbf{E} \tag{2.78}$$

$$\epsilon \nabla \cdot \mathbf{E} = Q \tag{2.79}$$

$$\nabla \cdot \mathbf{B} = 0 \tag{2.80}$$

where $\mathbf{E}$ is the electric field $[V.m^{-1}]$, $\mathbf{B}$ is the magnetic induction $[T]$, $\mathbf{J}$ is the current density $[A.m^{-2}]$ and Q is the adsorbed charge density $[C.m^{-3}]$. These four equations, where the $-i\omega$ factor stands for time derivative, traduce the coupling between electric and magnetic fields. Hence eq. (2.77), also called Maxwell-Thomson, shows how a varying magnetic field induces an electric field while eq. (2.78), also called Maxwell-Ampère, shows the reverse effect. The Maxwell-Gauss equation or eq. (2.79) shows how static charges may produce an electric field. Finally, eq. (2.80) of Maxwell-Faraday proves the magnetic field to be purely rotational. It is notably by incorporating this last equation that Pride was able to predict the existence of the seismomagnetic effects that may be generate by a divergence-free shearing wave.

Mechanical equations

To derive generalized Biot's mechanical equation from the original formulation (eq. (2.45) to (2.49)), Pride renamed $\tau_B = \tau^D - P_c I$, where I is the identity matrix. This bulk tensor that may be alternately defined as $\tau_B = \phi\, \tau_f - (1-\phi)\, \tau_s$ with τ_f and τ_s the stress tensor associated to the fluid phase and the solid phase respectively [Pride and Haartsen, 1996]. This mechanical system gathers a first dynamical equation and two coupled constitutive laws of poroelasticity:

$$\nabla \cdot \tau_B = -\omega^2 (\rho \mathbf{u} + \rho_f \mathbf{w}) \tag{2.81}$$

$$\tau_B = (K_G\, \nabla \cdot \mathbf{u} + C\, \nabla \cdot \mathbf{w}) + G_{fr} \left(\nabla \mathbf{u} + \nabla \mathbf{u}^T - \frac{2}{3} \nabla \cdot \mathbf{u} I \right) \tag{2.82}$$

$$-p_f = C\, \nabla \cdot \mathbf{u} + M\, \nabla \cdot \mathbf{w} \tag{2.83}$$

Hence, in eq. (2.81) we do recognise eq. (2.45), while eq. (2.82) combines eq. (2.47) and (2.48). Final eq. (2.83) is the same as (2.49). Equation (2.46) having no equivalent here will be recovered in the transport equations.

Transport equations

The transport equations, that describe electric current flux J and water flow w, do bear the actual electrokinetic coupling. First equation combines conduction currents (first term associated to Ohm's law) to electrofiltration current. Second equation accounts for fluid flow driven electrically and mechanically (second term associated to a generalised Darcy's law):

$$\begin{cases} J = & \sigma(\omega)E + L_{EK}(\omega)\left(-\nabla p_f + \omega^2 \rho_f u\right) \\ -i\omega w = & L_{EK}(\omega)E + \dfrac{k(\omega)}{\eta_f}\left(-\nabla p_f + \omega^2 \rho_f u\right) \end{cases} \tag{2.84}$$

These equations also enclose the frequency-dependency through dynamic permeability $k(\omega)$ previously defined in eq. (2.53), dynamic conductivity $\sigma(\omega)$ and seismoelectric coupling coefficient $L_{EK}(\omega)$ $[m^2.s^{-1}.V-1]$. The last two parameters will be defined in association to the dynamic expression of the transfer function. Yet already we may point out that, similarly to $k(\omega) = k_0\ g(\omega)$, dynamic parameters $\sigma(\omega)$ and $L_{EK}(\omega)$ may each be split as the product of two functions, one being a constant associated to the LF boundary while the other supports the dynamic dependency.

Assumptions and limitations

Pride's theory is based on eight hypothesis [Pride, 1994]:

- Medium is isotropic and fully saturated;
- Seismically induced perturbations are linear, implying that seismic strains are reasonable (below 10^{-6});
- Solid frame is isotropic;
- Grain size is negligible in comparison to wavelength;
- Thermomechanical coupling is disregarded;
- Fluid is monophasic, viscous and newtonian;
- Electrolyte concentration is inferior to 1 $mol.L^{-1}$ in order to consider that ions are moving freely;
- Currents caused by Lorentz forces are negligible in comparison to electrokinetic conduction and convection currents.

Hence, in accordance with previous Biot's theory, the medium is considered fully saturated by a monophasic fluid. In this respect, for adaptation of Pride's theory to partial saturation conditions, aforementioned developments on Biot's theory regarding hydraulic and elastic properties of the effective fluid may be incorporated as such, while saturation-dependency of electric parameters has to be clarified.

2.5.2 The coseismic seismoelectric transfer function

Having define the poroelastic and electrokinetic context, and indicated how both are intertwined by the means of coupled transport equations, we may now proceed to the presentation of the coseismic seismoelectric transfer function. This transfer function, which is occasionally referred to as $E/\ddot{u}$, connects the coseismic electric field E to the point acceleration due to the mother P-wave $\ddot{u}$. We will come to its general formulation after having introduced its frequency-dependent components.

High-frequency dynamic behavior

Earlier in this section, we mentioned dynamic conductivity $\sigma(\omega)$ and seismoelectric coupling coefficient $L_{EK}(\omega)$. The first of these parameter may be expressed as:

$$\sigma(\omega) \quad = \quad \sigma_b \left[1 + \frac{2\left(C_{em} + C_{os}(\omega)\right)}{\sigma_f \, \Lambda}\right] \simeq \sigma_b \tag{2.85}$$

While developed expressions of electro-migration conductance C_{em} and dynamic electro-osmotic conductance C_{os} may be respectively found in equation (7.6) and (7.5) of the appendices, the frequency-dependent factor $2\left[C_{em} + C_{os}(\omega)\right]/(\sigma_f \Lambda)$ appears mostly negligible as for a saturated unconsolidated sand it remains inferior to 0.005 for frequencies up to 20 kHz and fluid conductivities as low as 1 mS/m. Consequently in our model calculation we may consider the approximation (2.85), and if saturation-dependency there is, it will be given by that of σ_b (see Archie's law eq. (2.97)).
Coming to the dynamic expression of the seismoelectric coupling coefficient $L_{EK}(\omega)$, we have:

$$L_{EK}(\omega) \quad = \quad L_0 \left[1 - i\frac{\omega}{\omega_c}\frac{m}{4}\left(1 - 2\frac{\tilde{d}}{\Lambda}\right)\left(1 - i^{3/2}\frac{\tilde{d}}{\delta(\omega)}\right)^2\right]^{-\frac{1}{2}} \tag{2.86}$$

$$L_0 \quad = \quad C_{EK} \, \sigma_b \tag{2.87}$$

where we meet anew with the DC electrokinetic coupling coefficient C_{EK}, while the expressions of Debye length $\tilde{d}$ $[m]$ and pore geometry factor Λ $[m]$ may respectively be found in the appendices under eq. (7.1) and (7.2). Again, the dynamic dependency is restricted to the last factor.
The last electrical parameter showing frequency dependency is the effective electrical permittivity $\tilde{\epsilon}(\omega)$:

$$\tilde{\epsilon}(\omega) \quad = \quad \epsilon(\omega) + \frac{i}{\omega}\sigma(\omega) - \tilde{\rho}(\omega)L_{EK}^2(\omega) \simeq \frac{i}{\omega}\sigma(\omega) \tag{2.88}$$

similarly to $\sigma(\omega)$, $\tilde{\epsilon}(\omega)$ may be simplified as shown in eq. (2.88) under the condition that $\epsilon(\omega) \ll (1/\omega)\sigma(\omega)$. For Earth material, this assumption is verified for moderate frequencies below 10^5 Hz (Garambois and Dietrich [2001], Ward and Hohmann [1987]).

The dynamic behaviour is further conveyed by elastic parameters as the effective density

$\tilde{\rho}(\omega)$ previously defined in eq. (2.51) and complex density $\rho_t(\omega)$ defined as follows:

$$\rho_t(\omega) = \rho - \frac{\rho_f^2}{\tilde{\rho}(\omega)} \tag{2.89}$$

With apparition of the electrokinetic coupling auxiliary parameter γ has to be redefined with inclusion of seismoelectric coupling coefficient L_{EK}:

$$\gamma(\omega) = \frac{\rho M + \tilde{\rho}(\omega) H \left(1 + \tilde{\rho}(\omega)\ L_{EK}^2(\omega)/\tilde{\epsilon}(\omega)\right) - 2\rho_f C}{HM - C^2} \tag{2.90}$$

so do also P-waves slownesses $s_{pf,ps}$:

$$s_{pf,ps}(\omega) = \left(\frac{1}{2}\gamma(\omega) \mp \frac{1}{2}\sqrt{\gamma(\omega)^2 - \frac{4\tilde{\rho}(\omega)\rho}{MH - C^2}\left(\frac{\rho_t(\omega)}{\rho} + \frac{\tilde{\rho}(\omega)\ L_{EK}(\omega)^2}{\tilde{\epsilon}(\omega)}\right)}\right)^{1/2} \tag{2.91}$$

again $'-'$ for fast P-wave, $'+'$ for slow P-wave. Knowing the slowness s_{pf}, we can easily deduce velocity dispersion $V_p(\omega)$, intrinsic attenuation α_p and inverse quality factor Q_p^{-1} from equations (2.56) to (2.58). Finally, pulsation ω also intervene in the mechanical coupling $\beta_{pf,ps}$ identified as the fluid/matrix displacement ratio:

$$\beta_{pf,ps}(\omega) = -\left(\frac{H\ s_{pf,ps}^2(\omega) - \rho}{C\ s_{pf,ps}^2(\omega) - \rho_f}\right) \tag{2.92}$$

This mechanical coupling without dimension, involving the Biot coefficients C and H, quantifies the fluid/frame interaction. In our experimental measurement we will essentially focus on seismic attributes of the fast P-wave, so that beyond this point we will consider $s_{pf} = s_p$ and rename $\beta_{pf} = \beta_P$. We will further dwell on β_P for the specific role it plays under partial saturation.

The coseismic transfer function, to which we may compare our experimental results, is hence fully defined as:

$$\mathbf{E}(\omega) = \frac{i\omega\ \tilde{\rho}(\omega)\ L_{EK}(\omega)\ \beta_P(\omega)}{\tilde{\epsilon}(\omega)}\mathbf{u}(\omega) \tag{2.93}$$

$$\mathbf{E}(\omega) = \frac{\tilde{\rho}(\omega)\ L_{EK}(\omega)\ \beta_P(\omega)}{i\omega\ \tilde{\epsilon}(\omega)}\ddot{\mathbf{u}}(\omega) \tag{2.94}$$

where first expression relates the coseismic electric field E to frame displacement u while second expression, that has been derived twice in time as $-i\omega = \delta/\delta t$, connects E to frame acceleration $\ddot{u}$.

Low-frequency approximation

This transfer function between the coseismic electric field and the seismic acceleration was investigated experimentally and theoretically by Garambois and Dietrich [2001]. They deduced a simplified expression of the coseismic transfer function under low-frequency as-

sumption where $\mathbf{E}$ and $\ddot{u}$ are supposed to be linearly dependent. It actually means that, for frequencies below transition frequency f_{Biot}, the transfer function will first form a plateau, until prevalence of the inertial effects causes the transfer function to adopt a dynamic behaviour, as typically seen in figure 2.19. The low frequency approximation proposed by these authors gives a correct magnitude of this plateau, but we noticed an opposite sign [Bordes et al., 2015]. We consequently corrected the initial low frequency approximation from Garambois and Dietrich [2001] by a factor -1 giving:

$$\mathbf{E} \approx -\frac{1}{\sigma_f} \frac{\epsilon_0 \kappa_f \, \rho_f \, \zeta}{\eta_f} \left(1 - \frac{\rho}{\rho_f} \frac{C}{H}\right) \ddot{u} \tag{2.95}$$

This expression commonly valid at seismic field-frequencies, notably encloses the fluid's electrical conductivity σ_f, viscosity η_f, density ρ_f, relative permittivity κ_f and also zeta potential ζ. This information abundance shows how important coseismic seismoelectric could be if its sensitivity to the involved medium parameters was well understood. For this purpose, next section proposes to test the impact on Pride's transfer function of common hydraulic, electric and mechanical parameters defining a porous medium.

2.5.3 Sensitivity analysis of the transfer function

For this sensitivity analysis, basic parameter to characterize the porous medium will be taken from table 3.3 ; in following figures the red line corresponds to the reference model at full saturation, combining all parameters as defined in table 3.3 with a fluid conductivity of $\sigma_f = 5 \; mS/m$ (with the exception of figures 2.28 and 2.29). As the transfer function is a complex quantity, here we are to represent its absolute value $|E/\ddot{u}|$.

Dependency on hydraulic / transport properties

Hydraulic properties as permeability k_0, porosity ϕ and tortuosity α_∞ are known to intervene in the expression of Biot's characteristic frequency f_{Biot}. They consequently participate in the definition of the transition from LF viscous flow for which the coseismic seismoelectric effect is devoid of any frequency-dependency, to a HF inertial flow triggering dynamic behaviour in the coseismic seismoelectric transfer function $|E/\ddot{u}|$. The sensitivity analysis run on those transport properties will give the opportunity to see how they may affect this transition.

Porosity ϕ and tortuosity α_∞: We chose to decorrelate porosity and tortuosity in our computing, so that one could variate while the other is taken constant. We note that porosity and tortuosity variation impact different frequency domains. Porosity changes have a greater impact in the lower frequency range, as can be seen in figure 2.19 where a variation of $\pm$ 5 % over a mean porosity of 0.42 porosity produces a maximal variation of 3.5 % below the Biot frequency but almost no variation in the upper frequency range. A close look would show that the curve associated to higher porosity is the last to depart the LF constant behaviour. On the contrary, figure 2.20 shows that variation in tortuosity affects more specifically higher

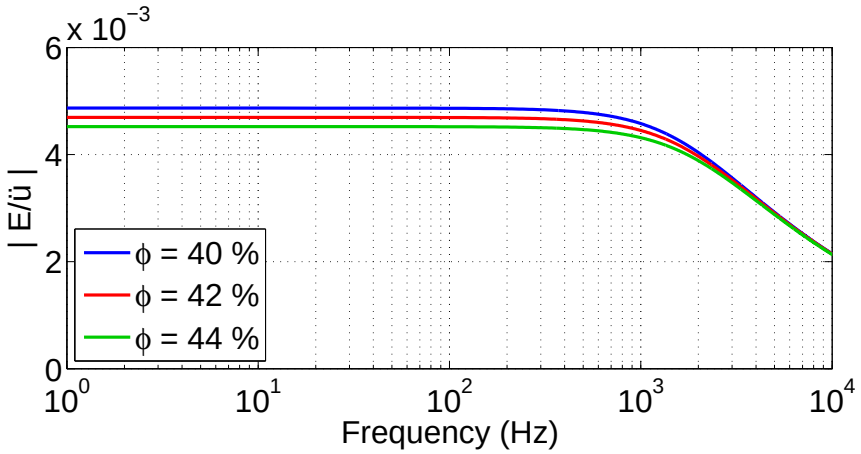

Figure 2.19: Dependency of the dynamic transfer function $|E/\ddot{u}|$ on porosity ϕ

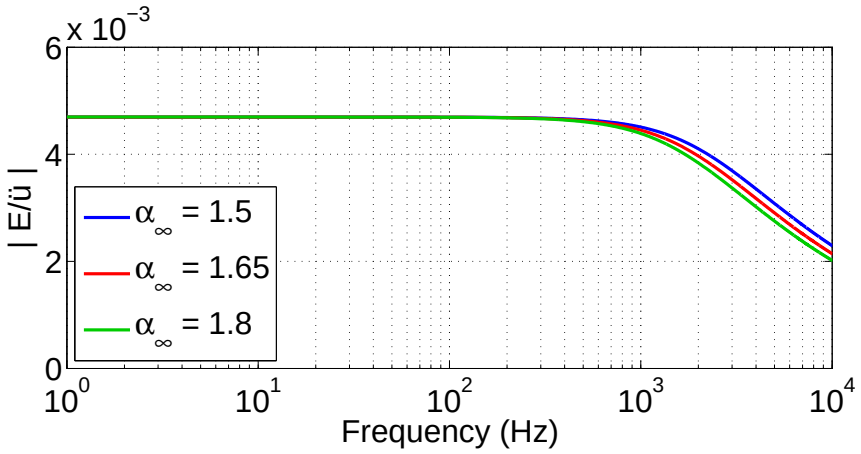

Figure 2.20: Dependency of the dynamic transfer function $|E/\ddot{u}|$ on tortuosity α

frequencies, leaving the transfer function $|E/\ddot{u}|$ at lower frequencies almost unchanged, while the smaller the tortuosity the longest the LF constant behaviour lasts. For a mean tortuosity value of 1.65, an error of $\pm$ 9 % on α_∞ would induce a maximal error of 6.5 % on the transfer function determination.

Intrinsic permeability k_0: As we already mentioned, dependency of the transfer function with permeability is negligible at lower frequencies. For increasing frequencies, the transfer function eventually quit this quasi-constant behavior to decrease with increasing frequencies. The transition frequency, also known as Biot frequency, is all the lower than permeability is higher (for permeability appears in the denominator of the expression for Biot's frequency). Figure 2.21 shows the resolution of the $|E/\ddot{u}|$ transfer function for permeabilities of the same order of magnitude: at a given frequency, the transfer function diminishes with increasing permeability, first importantly then more moderately. The repercussion of a $\pm$ 50 % changes in permeability are a variation of $|E/\ddot{u}|$ by 20 to 25 % in the HF domain. Here, the imposed perturbation on permeability being larger than those previously applied on porosity and tortuosity, we clearly see how an increase in permeability would lower f_{Biot} for an earlier transition to $|E/\ddot{u}|$ dynamic behaviour.

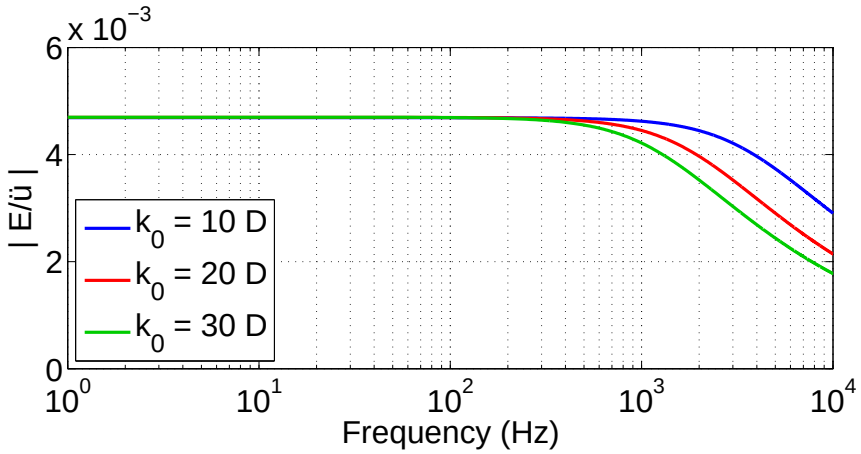

Figure 2.21: Dependency of the dynamic transfer function $|E/\ddot{u}|$ on intrinsic permeability k_0 in darcy ($1D = 10^{-12}m^2$)

Dependency on electric and fluid properties

While hydraulic parameters play a major role in the definition of the Biot transition frequency (see f_{Biot} in eq. (2.50)) marking the switching to frequency-dependency, electric and fluid properties are expected to have a huge impact on the low frequency (LF) portion of the coseismic seismoelectric transfer function. Indeed, according to eq. (2.95), the LF plateau of $|E/\ddot{u}|$ is expected to be inversely proportional to σ_f and η_f, and proportional to κ_f, ρ_f and ζ. We will verify the compatibility of the low-frequency observations with the dynamic Pride formulation, and try to characterize the dependency of $|E/\ddot{u}|$ to identified electric or fluid parameter above f_{Biot} critical frequency marking the transition to a dynamic behaviour of the coseismic seismoelectric transfer function.

Fluid relative permittivity κ_f: In figure 2.22 we display the impact of $\pm$ 6 % variations of the relative permittivity κ_f when taken as an independent parameter (by disregarding its coupling to temperature and fluid salinity). We noticed that the influence of relative permittivity on the transfer function was uniform over the LF and HF domain, and that it was influenced in the same proportion to κ_f variations, says 6 %. Moreover an increase in κ_f produces an increase in the transfer function. Hence the transfer function appears to be proportional to κ_f not only at LF but rather on the whole frequency band.

Fluid dynamic viscosity η_f: The transfer function seems quite sensitive to fluid viscosity, as can be seen in figure 2.23, where an applied change of $\pm$ 5 % in viscosity triggers errors of 5 to 2.5 % on the transfer function. The impact is particularly remarkable in the LF domain, where proportionality is observed accordingly to eq. (2.95).

Zeta potential ζ: In figure 2.24 we display the influence of a zeta potential ζ variation by $\pm$ 14 % when uncoupled from any other parameter (as from fluid conductivity for example). We noticed that the influence of ζ variations on the transfer function was uniform over the LF and HF domain, and being also of 14 % it varied in the same proportion to the zeta potential. Moreover, similarly to the observation made on relative permittivity κ_f, an

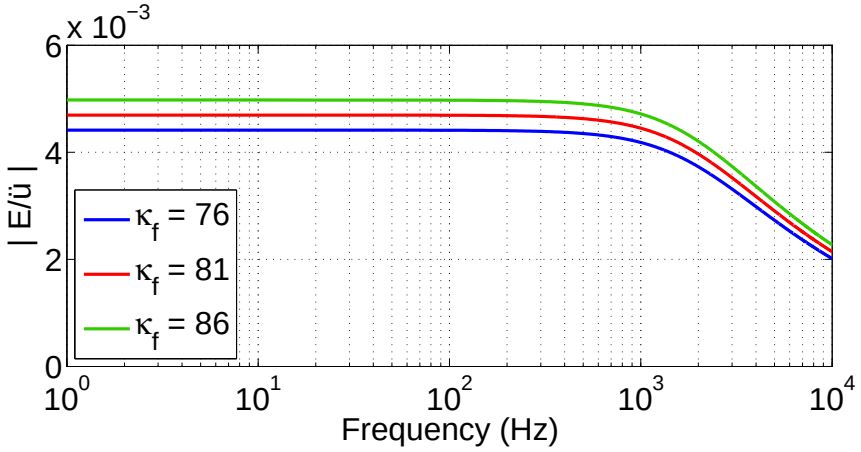

Figure 2.22: Dependency of the dynamic transfer function $|E/\ddot{u}|$ on relative fluid permittivity κ_f

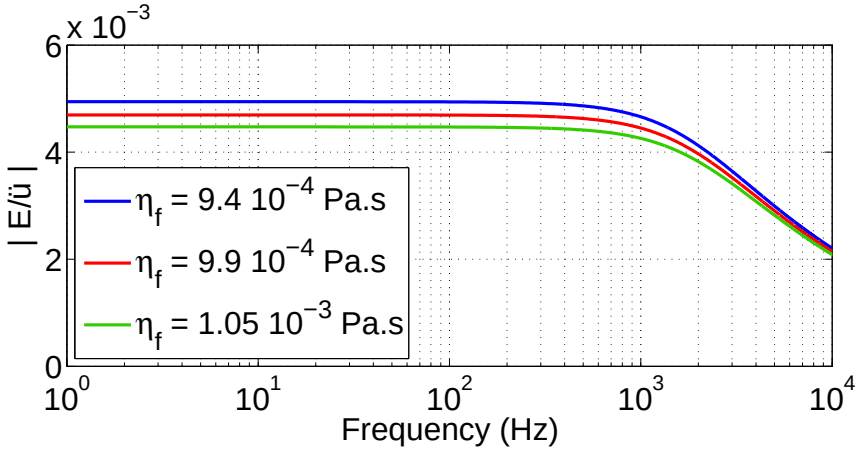

Figure 2.23: Dependency of the dynamic transfer function $|E/\ddot{u}|$ on fluid viscosity η_f

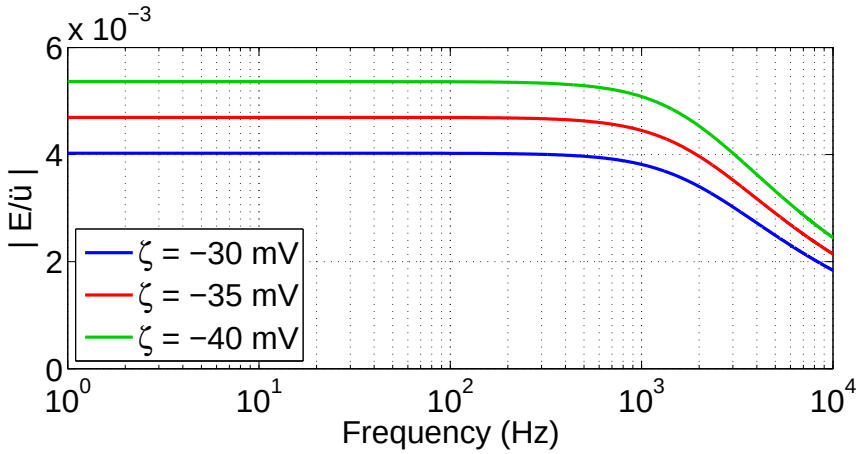

Figure 2.24: Dependency of the dynamic transfer function $|E/\ddot{u}|$ on zeta potential ζ

increase in ζ produces an increase in the transfer function. Hence the transfer function appears also to be proportional to ζ.

Fluid electric conductivity σ_f: In figure 2.25 we see how a variation of $\pm$ 20 % on fluid conductivity σ_f induce a variation of over 21 % on our transfer function. By normalizing the results to a reference conductivity σ_{ref} of 5 mS/m, we ended up with an error on the estimation of $|E/\ddot{u}|$ shrinking to about 1 %.

Such a normalization is not optimal, but seems to give a reasonable idea of the amplitude level to be expected at a given conductivity. However varying salinities may impact further fluid parameters, and if it is expected to have minor effects on density, relative permittivity or fluid viscosity (variations below 1 ‰), the impact on the zeta potential ζ however will range by 1 %. It corresponds to the residual error we observed on the transfer function for the conductivity-normalized case **??**. It may be explained as follows: an increasing σ_f inducing a decrease in ζ, and $|E/\ddot{u}|$ decreasing linearly with increasing σ_f as well as with decreasing ζ, contributions add up to produce a greater decrease in $|E/\ddot{u}|$ than expected when assuming the transfer function to be directly proportional to fluid conductivity. In conclusion, we may get a better error-reduction by combining fluid conductivity and zeta potential in our normalization efforts (see conclusion)

The effect of fluid conductivity σ_f or salinity C_f on the seismoelectric transfer function has been the object of the first parameter-dependent seismoelectric studies conducted in the lab. Among others, Block and Harris [2006] used NaCl electrolytes of varying concentration to show an overall decrease of the seismoelectric potential for increasing salinity (main results of those seismoelectric vs. salinity studies will be discussed relatively to our results in section 5.2.1). With decreasing amplitudes of electric signal, the signal-to-noise ratio drops rapidly. On the other hand, reasonable variations of salinity, leaving the bulk density unchanged, should not influence the seismic. As a result, the $|E/\ddot{u}|$ transfer function will decrease dramatically with increasing fluid conductivity and the signal-to-noise ratio will be terrible.

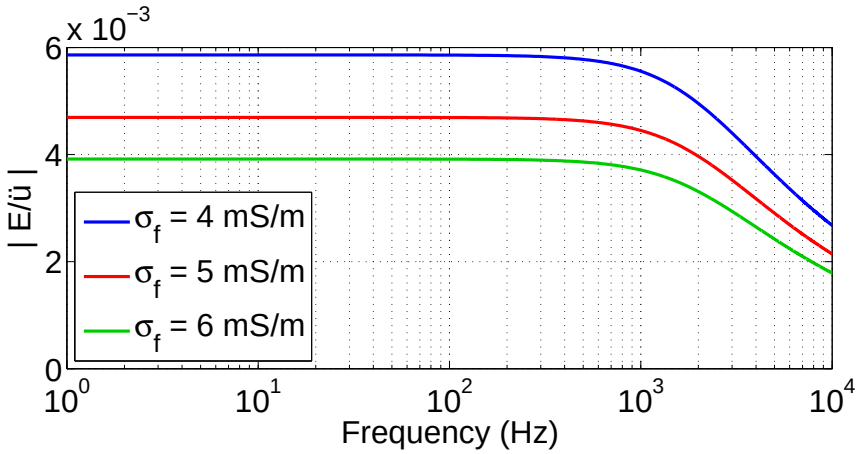

Figure 2.25: Dependency of the dynamic transfer function $|E/\ddot{u}|$ on fluid electric conductivity σ_f

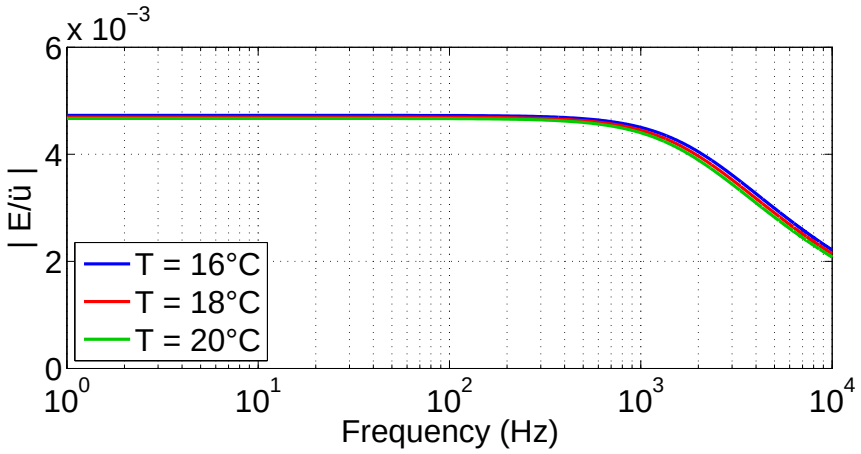

Figure 2.26: Dependency of the dynamic transfer function $|E/\ddot{u}|$ on temperature T_C

Fluid temperature T_C: When considering a temperature change of $\pm$ 2°C around an average of 18°C, a variation of 3 % is observed over the higher frequency part of our transfer function (see figure 2.26). This is mainly due to the impact of temperature variations on fluid viscosity and to a lesser extent on fluid conductivity and relative permittivity.

Such a temperature variation would produce a mean deviation of fluid viscosity η_f by 5.5 %, 5 % for σ_f and a minor variation of κ_f by 1 %. Yet, while viscosity decreases with temperature, conductivity increases, so that both effects tend to counteract one-another. Influence on Pride and Morgan [1991] formulation of a zeta potential ζ would be about 1 %. As the estimated error on fluid density induced by such a variation would lay by 1 ‰, it can be neglected.

Dependency on elastic properties

Frame bulk modulus K_{fr} and associated shear modulus G_{fr}: Considering the link between K_{fr} and G_{fr} for granular medium, we limited our study of transfer function dependency on elastic modula to the impact of K_{fr} variations over $|E/\ddot{u}|$. For large variations of K_{fr} by $\pm$ 50 % (inducing proportional variation of G_{fr}) the impact over transfer function is minimal (below 2 %) as can be seen in figure 2.27. When decoupling K_{fr} and G_{fr} and

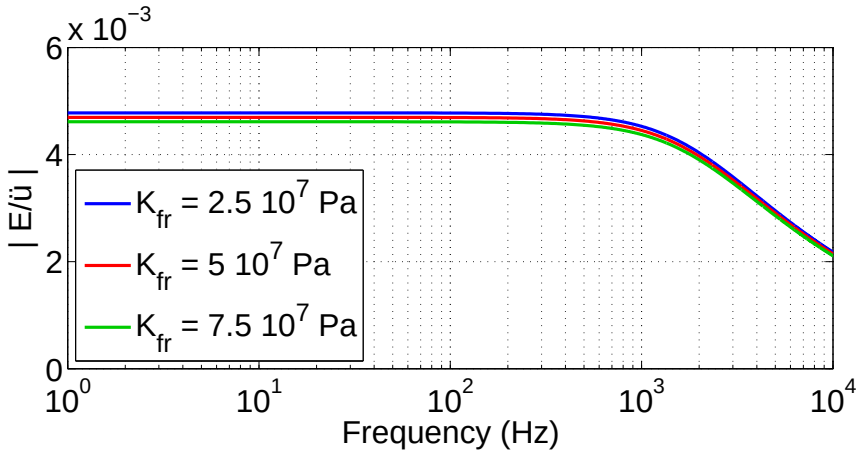

Figure 2.27: Dependency of the dynamic transfer function $|E/\ddot{u}|$ on frame bulk modulus K_{fr}

making one vary by $\pm$ 50 % while the other stays constant, the impact on transfer function $|E/\ddot{u}|$ would stay below 1 %.

Fluid modulus K_f: Particularity of the effective fluid modulus K_f is that is is expected to vary by two orders of magnitude from dry to fully water saturated material. Moreover, model for calculation of the effective K_f will be chosen accordingly to the homogeneity degree of the fluid mixture, as explained in section 2.4.2. Under such circumstances, variation of the $|E/\ddot{u}|$ transfer function relatively to changing K_f will be important. In figure 2.28, we show what impact the choice of a model for effective fluid modulus has on the transfer function: we considered here a water saturation of 0.95. While Voigt K_V and Reuss K_R bound-values are separated by a factor 700, the transfer function are separated by a factor 1.5: hence, if fluid modulus has a small impact on $|E/\ddot{u}|$, its variation range makes its impact significant.

In figure 2.29, we combine a change in saturation to various model for effective fluid modulus : in this figure the reference model, would be the black line obtained by all effective fluid model at full saturation. We see that the sole impact of saturation is non-negligible: an error on saturation estimation by 5% leads to an error of 10% to 20% on the transfer function. In section 2.6.1, we are going to see what parameter, besides $\rho_f(S_w)$, $\eta_f(S_w)$ and $K_f(S_w)$ do influence the transfer function at partial saturation.

2.5.4 Conclusion on parameter sensitivity

This sensitivity study proves the transfer function $|E/\ddot{u}|$ to depend on various parameters ranging from permeability of the medium k_0 to fluid temperature T_C(see table 2.3). These parameters may be classified into three groups.

First group gathers the parameters uniformly impacting the transfer function equally in LF and HF domain in a proportional way. It encloses the fluid salinity, that can be defined by C_f or σ_f and has the particularity to impact $|E/\ddot{u}|$ even in a enhanced proportion (for it also plays a role in η_f, κ_f and ζ). Further parameters of this class are relative fluid permittivity κ_f and zeta potential ζ. For those parameters, we observed that the transfer function may be recalculated to a reference value using following formula :

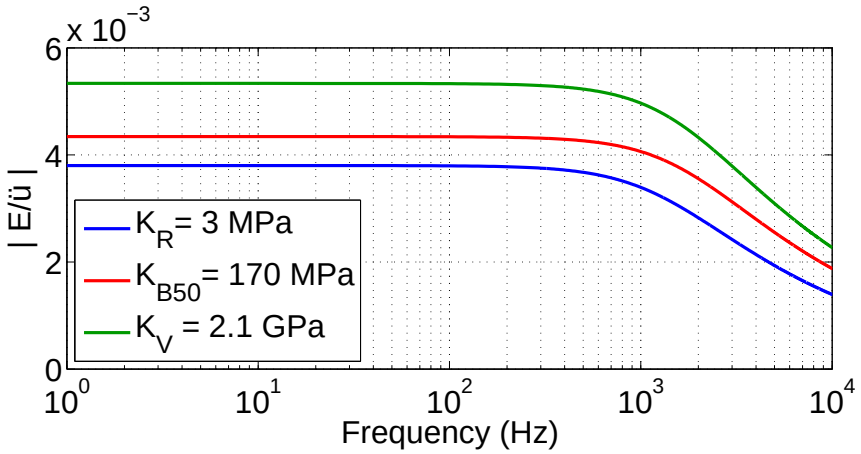

Figure 2.28: Dependency of the dynamic transfer function $|E/\ddot{u}|$ on effective fluid modulus estimated by different models for a given saturation of $S_w = 0.95$.

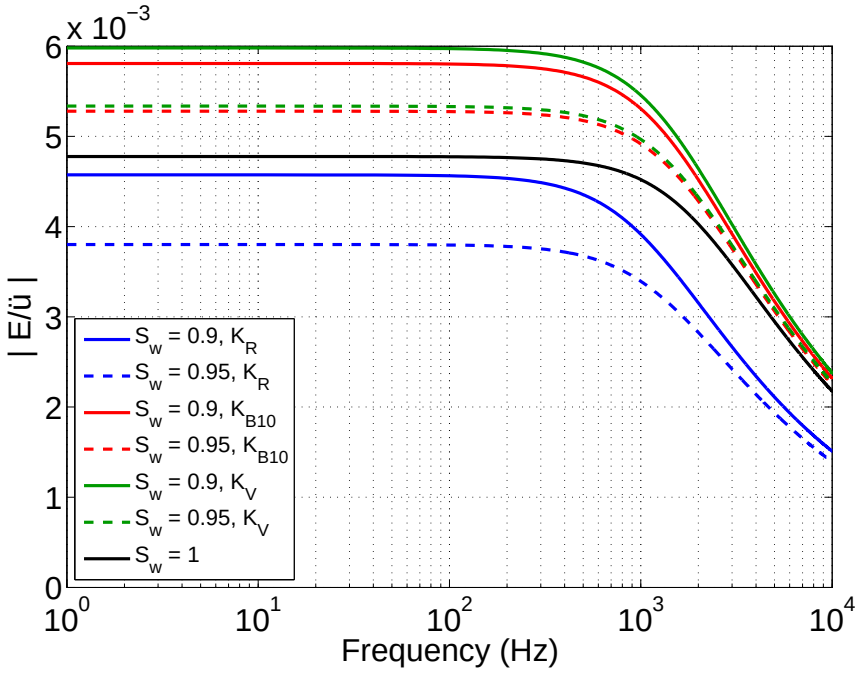

Figure 2.29: Dependency of the dynamic transfer function $|E/\ddot{u}|$ on effective fluid modulus estimated by different models, for saturation degrees S_w at 0.95 or 1.

$$|E/\ddot{u}|_{ref} = \frac{\sigma_f}{\sigma_{ref}} \times \frac{\zeta_{ref}}{\zeta} \times \frac{\kappa_{ref}}{\kappa_f} |E/\ddot{u}| \tag{2.96}$$

This expression might be of use to correct the contribution of electrical parameter for comparison purposes, on a transfer function that would also variate for instance in saturation or hydraulic properties.

The fluid viscosity η_f despite resembling the first group for the extent of its impact on the transfer function proportional to that of its variation, already belongs to the second group characterized by a greater impact in the LF domain. Along with fluid viscosity comes porosity ϕ and temperature T_C.

On the contrary, the third group reunites the parameters having a greater impact in the HF domain showing a dynamic dependency. This is the case of tortuosity α_∞ and permeability k_0.

Surely, not all parameters are perfectly independent. As a matter of fact, accord-

	Parameter	LF	HF	input variation	$\Delta\|E/\ddot{u}\|$ LF		$\Delta\|E/\ddot{u}\|$ HF	
Frame	k_0	-	+	$\pm$ 50 %	0.5 %	$\nearrow$	26.5 %	$\searrow$
	ϕ	+	-	$\pm$ 5 %	3.5 %	$\searrow$	$<$ 0.5 %	$\nearrow$
	α_∞	-	+	$\pm$ 9 %	$<$ 0.5 %	$\nearrow$	6.5 %	$\searrow$
	K_{fr}	-	-	$\pm$ 50 %	$<$ 2 %	$\searrow$	$<$ 2 %	$\searrow$
Fluid	η_f	++	+	$\pm$ 5 %	5 %	$\searrow$	2.5 %	$\searrow$
	σ_f	++	++	$\pm$ 20 %	21 %	$\searrow$	21 %	$\searrow$
	κ_f	++	++	$\pm$ 6 %	6 %	$\nearrow$	6 %	$\nearrow$
	ζ	++	++	$\pm$ 14 %	14 %	$\nearrow$	14 %	$\nearrow$
	T_C	-	+	$\pm$ 2°C	$<$ 1 %	$\searrow$	3 %	$\searrow$

Table 2.3: Sensitivity of transfer function $|E/\ddot{u}|$ to involved poroelastic, hydraulic and electric parameters. A code shows in which frequency domain the transfer function is affected the most and to what extent: '++' for variations of the $|E/\ddot{u}|$ transfer function equalling or surpassing that of the perturbation, '+' for variations of $|E/\ddot{u}|$ by 50% to 75% of the perturbation,'-' if it lays below 10% of the perturbation. Further indications are: $\nearrow$ for an increase of $|E/\ddot{u}|$ when the parameter of interest increases, $\searrow$ for a decrease of $|E/\ddot{u}|$ with parameter increase. The low (LF) and high (HF) frequency domain are defined relatively to the relevant Biot frequency: for our medium the HF variation of the transfer function was taken at 10 kHz.

ing to a starting model involving the 16 parameters listed in the introduction, if we know temperature T_C and fluid conductivity σ_f we get access through equations to three more fluid parameters (namely fluid salinity C_f, permittivity κ_f and viscosity η_f) and may as well get an estimation of the zeta potential ζ. As already known, porosity ϕ can determine tortuosity α_∞, and from frame compressibility K_{fr} one can deduce frame shear compressibility G_{fr}. Further parameters involved and thought to be independent are permeability k_0, fluid and solid phase densities ρ_f and ρ_s, fluid and solid phase compressibilities K_f and K_S and permittivity of solid phase κ_s. The latest happens to be neglected in a reduced formulation neglecting the counteracting electro-osmosis phenomena.

In conclusion, strictly required parameters are T_C, σ_f, ϕ, k_0, ρ_f, ρ_s, K_{fr}, K_f and K_S. According to a similar terminology, we are able to measure T_C, σ_f, ϕ, k_0, ρ_f, ρ_s, α_∞ and

possibly η_f and ζ. Yet, scale changing from centimetric devices filled with compacted material for characterization of decimetric experience on random pack may be of concern. Last, estimations, not to say direct measurements, of required elastic modula may be more complex. In this matter, our main concerns remain for frame compressibility K_{fr}, as well as for the effective fluid compressibility K_f in an unsaturated case.

2.6 Seismoelectric transfer functions under variable saturation

2.6.1 Dependency of electrical parameters of the medium σ_b and C_{EK}

The role of partial saturation in electrokinetics has long been addressed, proposing a variety of theoretical models for saturation-dependent expression of the electrokinetic coupling coefficient C_{EK}. These models are of many sorts: one of the first proposition for high-salinity electrolytes was made by Revil et al. [1999] and generalised by Guichet et al. [2003]: in their domain of validity they predict the decrease of C_{EK} with increasing water saturation S_w. An important class of models are based on the concept of relative permeability as the one initially proposed by Perrier and Morat [2000] to account for a reduced connectivity pattern under partial saturation. Another model by Jougnot et al. [2012] combines it to a flux-averaging approach. Further models by Linde et al. [2007]; Revil et al. [2007] based on a volume-averaging method and still considering relative permeability, were interested in the various wettability pattern. In a capillary approach Jackson [2008, 2010] proposed to distinguish the partial saturation effect with regard to the thickness of the electrical double layer, while Doussan and Ruy [2009] focused on hydraulic conductivity and relative permeability. Yet theoretical predictions are often challenged by experimental data, which promoted the formulation of experimental laws as in the case of Guichet et al. [2003], Revil and Cerepi [2004] or Allègre [2010]; Allègre et al. [2011, 2012]. Eventually, actual extension of partial saturation electrokinetic to seismoelectric has been lately proposed by Warden et al. [2013] and Revil et al. [2013], while experimental investigation on that subject were published by Bordes et al. [2015]. In this section, after a short presentation regarding the impact of partial saturation on basic electrical parameters, we will introduce some formulations of electrokinetic models at partial saturation. As we compare the saturation-dependent parameters relatively to their values at full saturation, we will adopt the notations:

$\sigma_b(S_w = 1) = \overline{\sigma_b}$

$C_{EK}(S_w = 1) = \overline{C_{EK}}$

$L_{EK}(S_w = 1) = \overline{L_{EK}}$

Impact of saturation on further electrical parameters of the medium

When neglecting surface conductivity, Archie's second law for saturation predicts the effective electrical conductivity of the porous medium to increase as a power law of saturation:

$$\sigma_b(S_w) = \overline{\sigma_b}\ S_w^n \tag{2.97}$$

where n is the second Archie's coefficient, with average value $n = 2$. This exponent, also known as Archie's saturation coefficient, characterises the continuity of the water film at the pore surface: it will increase with decreasing continuity of this film depending on wettability issues (oil-wet medium or smooth interfaces poorly holding residual fluid layer will increase n - Suman and Knight [1997]). In the following we will use the value $n = 2.58$ as employed by Doussan and Ruy [2009] and Bordes et al. [2015] [4].

Another electrical parameter of interest is the effective relative fluid permittivity $\kappa_f(S_w)$, a parameter that intervenes in coupling coefficient C_{EK}, dynamic conductivity $\sigma(\omega)$ and effective electrical permittivity $\epsilon(\omega)$. Yet we saw that in our frequency band of interest ($f < 10^5 Hz$) the last two parameters could be simplified according to equations (2.85) and (2.88) so that:

$$\sigma(S_w, \omega) \approx \sigma_b(S_w) \tag{2.98}$$

$$\epsilon(S_w, \omega) \approx \frac{i}{\omega}\sigma_b(S_w) \tag{2.99}$$

As for the saturation-dependency of C_{EK}, the following step will show how various electrokinetic models integrate this effect by directly moderating the saturated $\overline{C_{EK}}$ with a saturation factor. Under such circumstances there is no immediate necessity of correcting κ_f for partial saturation.

Impact of saturation on electrokinetic and seismoelectric coupling coefficient C_{EK} and L_{EK}:

Based on theoretical considerations (Ohm's law), the electrokinetic coupling coefficient C_{EK} was first expected to be inversely proportional to the effective water saturation S_e [Jouniaux et al., 2009], defined as:

$$S_e = \frac{S_w - S_{irr}}{1 - S_{irr}} \tag{2.100}$$

where S_{irr} is the irreducible saturation below which there is no more fluid flow. This was based on the assumption that the decrease of the medium's bulk conductivity σ_b with decreasing water saturation would boost C_{EK}.

Hence, from previous electrokinetic models adapted to the high-salinity domain [Revil et al., 1999], Guichet et al. [2003] had the expression of coupling coefficients relatively to

[4] While first and second Archie exponents m and n are expected to be of the same order [Waxman and Smits, 1968], our reference value of $n = 2.58$ after Doussan and Ruy [2009]; Bordes et al. [2015] is almost twice as large as our estimation of the cementation factor $m = 1.45$.

water saturation S_w and Archie's exponents m and n generalised to:

$$\frac{C_{EK}(S_w)}{\overline{C_{EK}}} = \frac{1}{S_e^n \left(1 + m\left(\frac{F}{S_e^n} - 1\right)\frac{\sigma_s/\sigma_f}{S_e}\right)} \tag{2.101}$$

the relation being only valid for $S_w > S_c$ due to implied model arguments based on the relation of bulk conductivity σ_b to water saturation degree S_w. This threshold defined as S_c marks a turning point in the curve $C_{EK}(S_w)$ as it starts to decrease with decreasing saturation [Revil et al., 1999]:

$$S_c = \left(F\frac{\sigma_s}{\sigma_f}\right)^{1/(n+1)} \tag{2.102}$$

Moreover, for a negligible surface conductivity such as $\sigma_s \ll \sigma_f$ the expression should simplify as:

$$\frac{C_{EK}(S_w)}{\overline{C_{EK}}} = S_e^{-n} \tag{2.103}$$

a formulation that diverges for $S_e \to 0$.

Yet actual experimental observations pointed either at non-dependency or proportionality of C_{EK} to S_w. Thus, while the desaturation of a sand-column by gas injection led by Guichet et al. [2003] gave no clear trend for nitrogen gas, for desaturation by argon-injection the results showed a direct proportionality relation:

$$\frac{C_{EK}(S_w)}{\overline{C_{EK}}} = S_e \tag{2.104}$$

while Allègre et al. [2012] adapted this initial expression by introducing two fitting parameters a_1 and a_2 so that:

$$\frac{C_{EK}(S_w)}{\overline{C_{EK}}} = S_e \ [1 + a_1(1 - S_e)^{a_2}] \tag{2.105}$$

for a sand column experiment on silica sand, they took $a_2 = 0.4$ and adaptable $a_1 = 30 - 90$ that would vary with the receiver offset. By these means they could account for a bell-shaped curve $C_{EK}(S_w)$ reaching a maximum at $S_w = 0.75 - 0.8$, greatly superior to $\overline{C_{EK}}$.

In parallel, using Ampère's law, Nernst-Planck equation and Stokes equation, Revil et al. [2007] developed a further expression of the relative coupling coefficient based on volume-averaged calculation of excess charges per unit of pore volume. They assumed a solid phase of negligible surface conductivity, being wetted by water combined to a second immiscible insulating phase (air or oil) constituting the non-wetting phase. Within this effective fluid,

Model	$f(S_w)$	Reference
High salinity model	$\frac{1}{S_e^n\left(1+m\left(\frac{F}{S_e^n}-1\right)\frac{\sigma_s/\sigma_f}{S_e}\right)}$	Revil et al. [1999]; Guichet et al. [2003]
Linear model	S_e	Guichet et al. [2003]
Volume averaging	$S_e^{\frac{2+3\lambda}{\lambda}} S_w^{n+1}$	Revil et al. [2007]
Capillary tubes	S_e/S_w^n	Jackson [2010]
Experimental	$S_e\ [1+a_1(1-S_e)^{a_2}]$	Allègre et al. [2012]

Table 2.4: List of the various functions $f(S_w)$ used in the electrokinetic coefficient depending on saturation $C_{ek}(S_w) = \overline{C_{EK}} f(S_w)$.

both phases are assumed to remain continuous at any saturation degree:

$$\frac{C_{EK}(S_w)}{\overline{C_{EK}}} = \frac{S_e^{\frac{2+3\lambda}{\lambda}}}{S_w^{n+1}} \tag{2.106}$$

$$\tag{2.107}$$

where λ is a curve-shape parameter characterizing the pore-space distribution, usually taken at 1.7 for sands [Bordes et al., 2015].

Finally, Jackson [2010] described the multiphase streaming potential coupling coefficient following a capillary approach with reference to relative permeability. The excess of charge is born by the water phase, mixed to a second insulating fluid-phase (air or oil), while surface conductivity of the rock is neglected. For a water-wet frame under a thin double-electrical-layer assumption the model predicts:

$$\frac{C_{EK}(S_w)}{\overline{C_{EK}}} = \frac{S_e}{S_w^n} \tag{2.108}$$

This model allows for $C_{EK}(S_w) > \overline{C_{EK}}$, a phenomenon experimentally observed during drainage experiments on silica sand by Allègre et al. [2010, 2012], and theoretically predicted by an alternate model from Jougnot et al. [2012] also based on a bundle of capillary tubes [Bordes et al., 2015]. It supposes that the electric conductivity decreases more rapidly than the effective water saturation. For instance, such effect may arise if the integrity of the water film is locally corrupted: a small loss in effective saturation would come with the full loss of the capillary contribution to effective conductivity. A further particularity of this model is to move the linear dependency of C_{EK} upon S_e to L_{EK}. This may be observed in figure 2.30, where the presented $C_{EK}(S_w)$ and associated $L_{EK}(S_w)$ are represented. A recap of these various model is to be found in table 2.4.

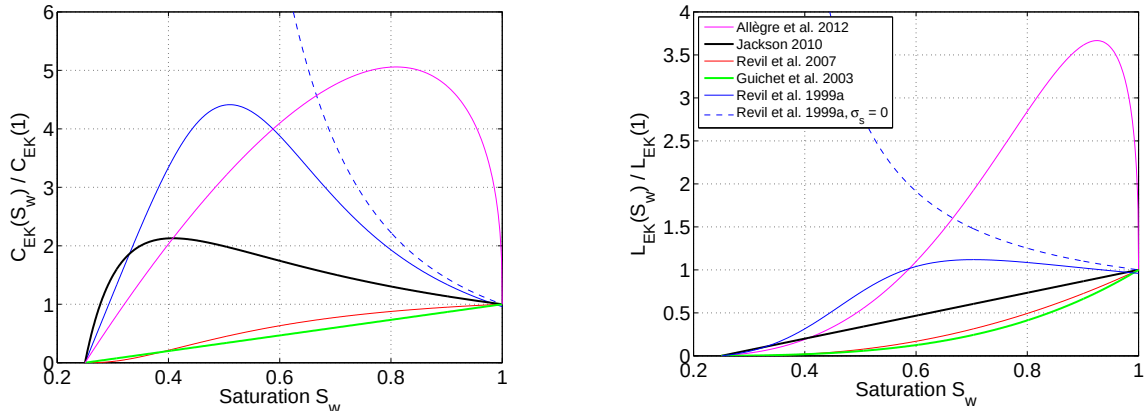

(a) (b)

Figure 2.30: Representation of normalised values of $C_{EK}(S_w)/\overline{C_{EK}}$ and $L_{EK}(S_w)/\overline{L_{EK}}$ coupling coefficients as a function saturation S_w for various electrokinetic models considering partial saturation conditions. The values of L_{EK} are taken at the zero frequency. Model were computed on parameters relevant for silica sand (see table 3.3), with residual saturation $S_{irr} = 0.25$. Additional parameters were taken as: $\sigma_f/\sigma_s = 100$ for Revil et al. [1999], $a_1 = 10$ and $a_2 = 0.4$ for Allègre et al. [2012] and finally $\lambda = 1.7$ for Revil et al. [2007].

2.6.2 Global shape of transfer function

Applying the effective fluid properties defined in sections 2.4.2 and **??** to all variables involved in the transfer function expressed by equation (2.94), we can compute some $E/\ddot{u}$ as typically expected by the Pride's theory generalised to an effective fluid (Warden et al. [2013] and Bordes et al. [2015]). Using the model of Jackson [2010] for electrokinetic coefficient, we performed some computations for a silica sand which properties are those of the sample presented in next chapter (figure 2.31). This figure obviously shows the strong dependency of transfer functions to the effective fluid modulus $K_f(S_w)$ as defined by Reuss (figure 2.31a - eq. (2.74)) or Brie's models (figure 2.31b- eq. (2.75)). Moreover, we notice a change in the sign of transfer functions occurring at a saturation clearly depending on the chosen mechanical model. This change in sign might generate a sign inversion of seismoelectric field and merits to be discussed and better understood before any measurements.

Here this phenomenon appears to be related to a change in the behavior of the computed modulus of the effective fluid coinciding with a change in velocity behaviour. We show the respective behaviour of the coseismic transfer function at two selected frequencies of 100 Hz (black) and 2 kHz (red). For both frequencies, the phase remains mainly constant until it flips by an angle of π rad for a given saturation, of approximately 0.995 for the Reuss model and 0.544 for the selected Brie model of exponent 8 $K_f = K_{B8}$. In each case, these saturations correspond to the point for which the effect of water addition or subtraction becomes visible on monitoring of velocity and effective fluid modulus with saturation (see figures 2.31e and 2.31f).

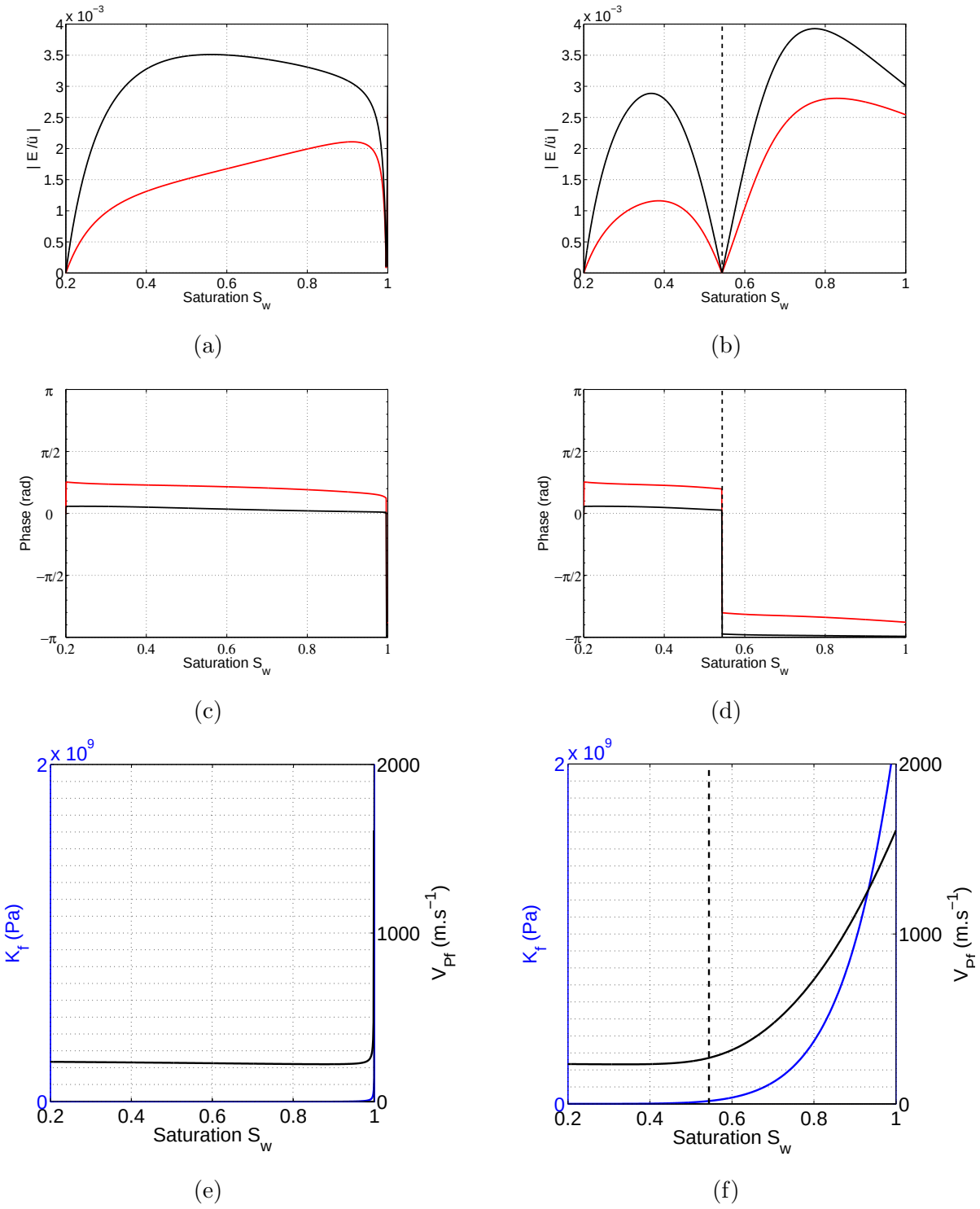

Figure 2.31: Evolution with water saturation S_w, for an air-water mixture, of the absolute value of coseismic transfer function $|E/\ddot{u}|$ (a and b) as well as its phase information (c and d) according to Pride's model. Double ordinate graphics e and f show the saturation dependent curve for effective fluid modulus (blue) and fast P-wave velocity at 500 Hz (black). Calculations were conducted for an effective fluid either compatible with Reuss average (a,c and e) or following the empirical law of Brie for modulus calculation with exponent 8 (b,d and f). Data in red are estimated at a frequency of 2 kHz whereas black curves correspond to phase behaviour at 100 Hz. The black dashed line marks the saturation at which the sign inversion of the $E/\ddot{u}$ ratio occurs using a Brie model.

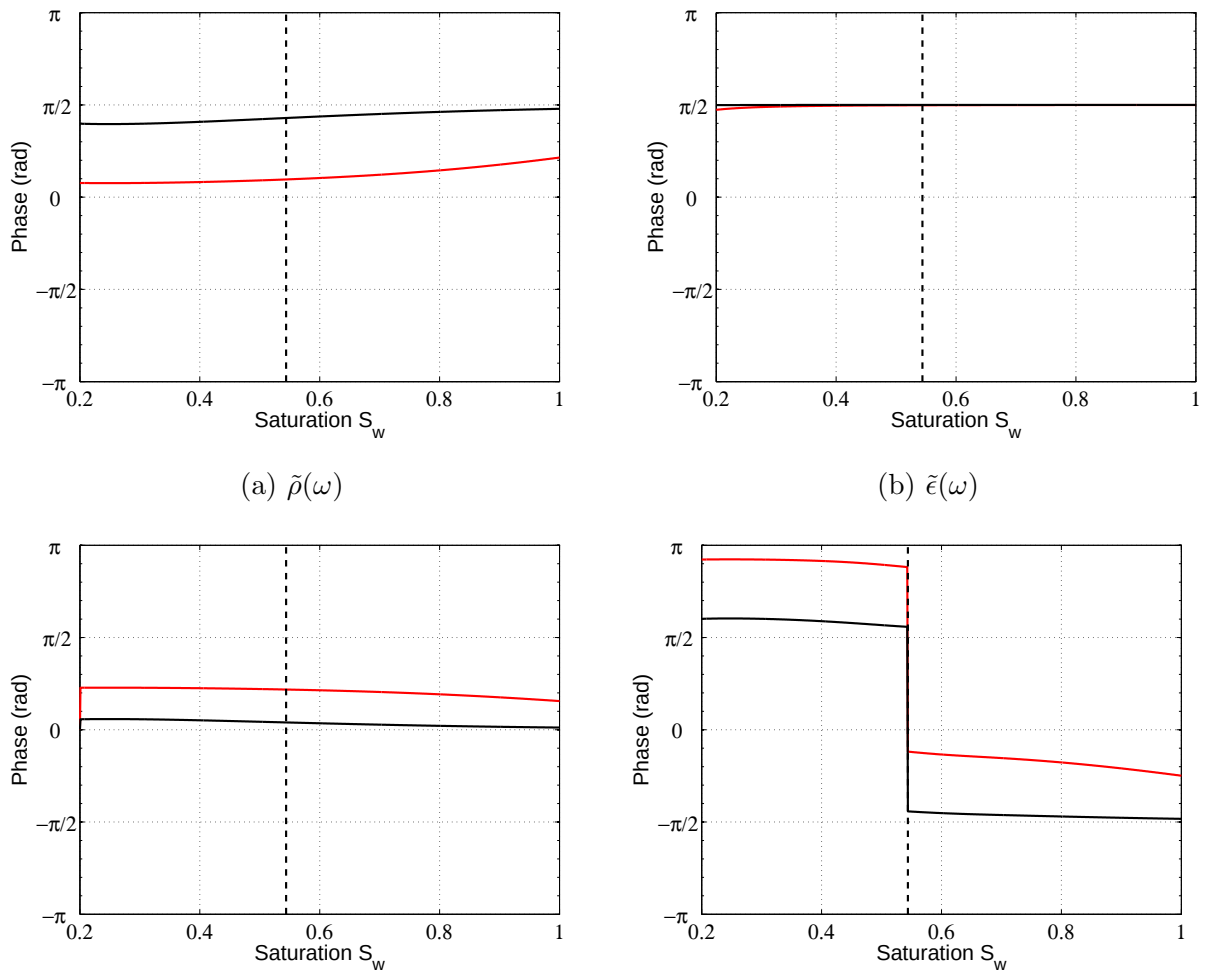

(a) $\tilde{\rho}(\omega)$ (b) $\tilde{\epsilon}(\omega)$

(c) $L(\omega)$ (d) $\beta_P(\omega)$

Figure 2.32: Evolution with water saturation S_w, for an air-water mixture, of the phase information given by the four factors intervening in the dynamic transfer function according to Pride's model. These calculations were conducted for an effective fluid following the empirical law of Brie for modulus calculation (exponent 8). Data in red are estimated at a frequency of 2 kHz whereas black curves correspond to behaviour at 100 Hz. The black dashed line marks the saturation at which the sign inversion of the $E/\ddot{u}$ ratio occurs.

Preliminary theoretical investigation

We chose to investigate this change of sign, under the light of phase reversal relatively to the spectral expression of the transfer function. The dynamic expression by Pride and Haartsen [1996], previously defined as eq. (2.94), states that:

$$\mathbf{E} = \frac{\tilde{\rho}(\omega)\ L(\omega)\ \beta_P(\omega)}{i\omega\ \tilde{\epsilon}(\omega)}\ddot{\mathbf{u}}$$

We decided to test all four factors intervening in the dynamic definition of the transfer function against phase reversal, for an effective fluid model of Brie exponent 8. Results are to be found in figure 2.32. In light of this figure, we conclude that the sole factor displaying such a phase reversal as to explain a sign change of the $E/\ddot{u}$ ratio is the mechanical coupling β_P.

Considering now that the sign change appears to be born by the factor β_P, we will document how this factor appears in Pride and Haartsen [1996], then we will interpret the

possible expressions available.

For longitudinal plane waves propagating in an isotropic, homogeneous wholespace one can express the frame displacement $\mathbf{u}$, relative fluid displacement $\mathbf{w}$ and propagating electric field $\mathbf{E}$ relatively to the associated amplitudes $\mathcal{U}$, $\mathcal{W}$ and $\mathcal{E}$ as :

$$\mathbf{u} = \mathcal{U}\exp(i\mathbf{k}\cdot\mathbf{r})\hat{\mathbf{u}} \tag{2.109}$$

$$\mathbf{w} = \mathcal{W}\exp(i\mathbf{k}\cdot\mathbf{r})\hat{\mathbf{w}} \tag{2.110}$$

$$\mathbf{E} = \mathcal{E}\exp(i\mathbf{k}\cdot\mathbf{r})\hat{\mathbf{e}} \tag{2.111}$$

with $\mathbf{k}$ being the wave vector such that $\mathbf{k} = \omega\, s_P(\omega)\hat{\mathbf{k}}$, where s_P is the complex slowness of the P-wave. For longitudinal waves, the unit vectors are all collinear to $\hat{\mathbf{k}}$, giving $\hat{\mathbf{k}} = \hat{\mathbf{u}} = \hat{\mathbf{w}} = \hat{\mathbf{e}}$. When combining the frame equation for poroelastic coupling to Newton's second law of motion under such circumstances, Pride and Haartsen [1996] obtained an equation linking amplitudes of the relative fluid displacement to that of the frame displacement:

$$\mathcal{W} = -\frac{Hs_P^2 - \rho}{Cs_P^2 - \rho_f}\mathcal{U} \tag{2.112}$$

with Biot coefficients C and H, both analogous to incompressibility. By rewriting eq. (2.92) for the fast P-wave, we get:

$$\beta_P = -\frac{Hs_P^2 - \rho}{Cs_P^2 - \rho_f} \tag{2.113}$$

which directly implies the expression:

$$\beta_P = \frac{\mathcal{W}}{\mathcal{U}} \tag{2.114}$$

This expression gives a more discernable interpretation of physical parameter β_P and of the origin of the sign change : it would proceed from a change of the fluid displacement direction relatively to the solid displacement.

Concomitantly we decided to investigate and decompose the initial expression of β_P into absolute value and phase of its denominator and numerator, as presented in figure 2.33, for two frequencies of 100 Hz and 2 kHz flanking the transition frequency f_{Biot} estimated at coarsely 1.5 kHz. Singularly, the denominator and numerator of parameter β_P go to zero for the same saturation value, generating no singularity in β_P. This very particular value of the saturation also marks the sign inversion of the transfer function and does not depend on frequency. As a result, the sign inversion of the coseismic seismoelectric transfer function appears as a sheer mechanical effect.

Thank to this analysis, the sign of the seismoelectric coseismic dependency is circum-

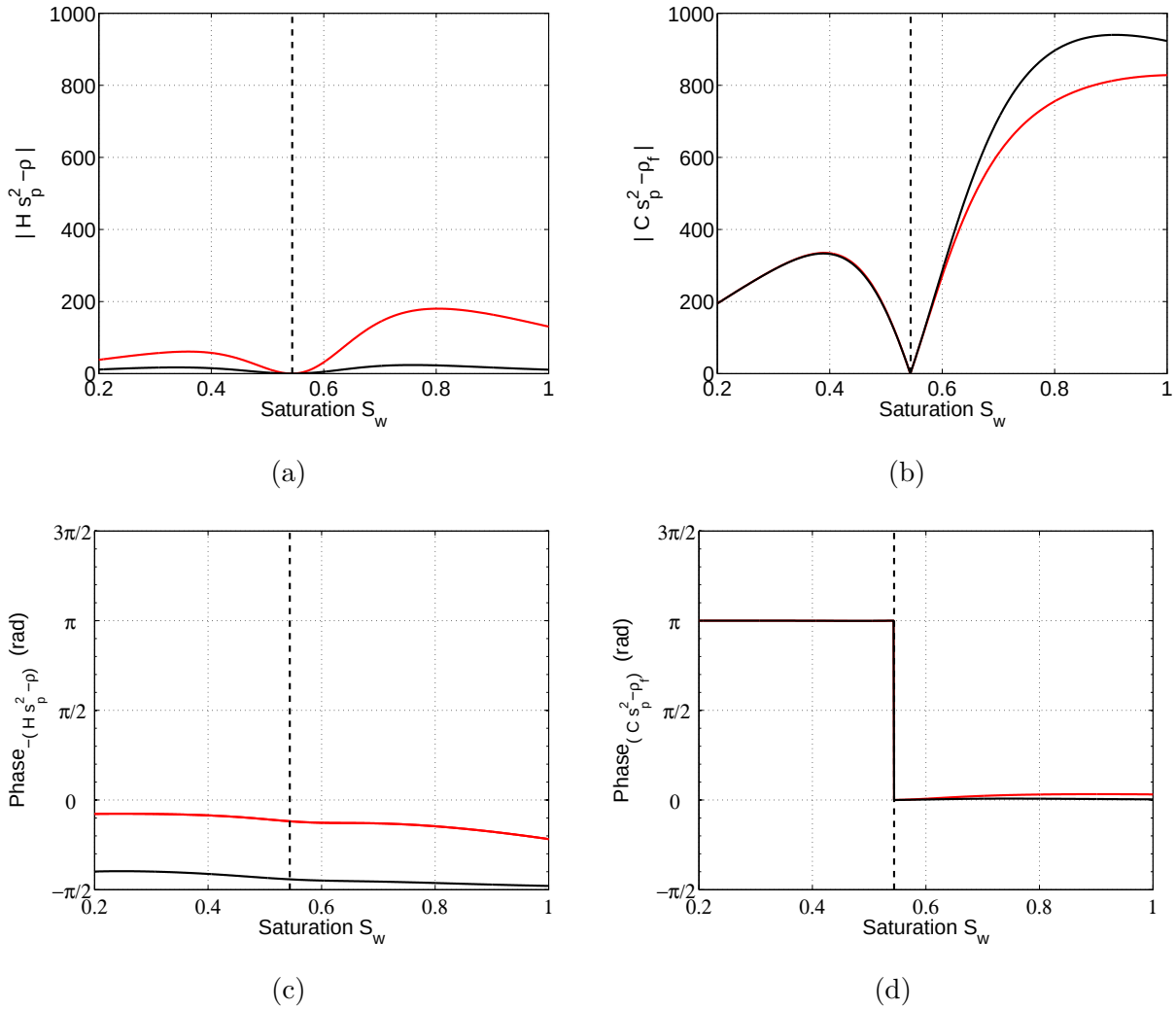

Figure 2.33: Evolution with water saturation S_w for an air-water mixture, according to Pride's model, of the absolute value and phase of β_P's numerator defined as $-[H.s_P^2 - \rho]$ (respectively a and c), as well as of its denominator of expression $[C.s_P^2 - \rho_f]$ (respectively b and d). Calculations were conducted for an effective fluid which modulus was defined as $K_f = K_{B8}$, inducing a phase shift of β_P at $S_w = 0.544$. Data in red are estimated at a frequency of 2 kHz whereas black curves correspond to behaviour at 100 Hz. The black dashed line marks the saturation at which the sign inversion of the $E/\ddot{u}$ ratio occurs.

cised to the sign of expression $Cs_P^2 - \rho_f$. Moreover the transition occurs precisely when the numerator equals zero, meaning when $s_P^2 = \rho/H$. As a conclusion the exact localisation of the phase shift is obtained for :

$$\frac{C}{\rho_f} = \frac{H}{\rho} \tag{2.115}$$

all densities and Biot coefficients depending on the water saturation degree S_w. A visualisation of the C/ρ_f vs H/ρ intersection agreement with the phase shift will be given in figure 2.34i obtained on synthetic analysis basis further in this section.

Investigation on partial saturation for various synthetic porous media

Indeed, in order to visualise the effect of the saturation-dependent seismoelectric transfer function on a simple computed seismic waveform we produced synthetic data, with a special focus on the phase behaviour of β_P as an indicator of relative displacement between fluid and solid. This time, the Gaussian waveform was taken as the solid displacement U created by the passing P-wave. Acceleration $\ddot{u}$ was obtained as the second derivative of solid displacement U; by construction, the input values U and $\ddot{u}$ were equivalent to all models and had no dependency on saturation S_w. Knowing U and $\ddot{u}$, it was then possible to formally calculate the coseismic component of the electric field E (eq. (**??**)) as well as the induced fluid displacement W (eq. (2.114)) for the employed air-water mixture in a sand frame. It was subsequently possible to generalize our calculation to further synthetic geomaterials by changing the saturating fluid for an oil-water mixture of low fluid incompressibility contrast (with an effective fluid modulus still taken as $K_f = K_{B8}$). Another perspective was to model the results obtained on a limestone frame, which happens to have a very stiff structure (frame bulk modulus K_{fr} being about 50 times higher than that of our experimental medium) while other parameters stay pretty close to that of unconsolidated sand.

We finally computed four cases on basis of two frame and two fluid compositions with the parameters presented in table 2.5. The associated illustrations, disposed in four columns matching the four cases, are presented in figures 2.34 and 2.35. The first row of figures in 2.34 shows the phase of the β_P-term, conducting the sign of the transfer function. Second figures row presents the evolution of frame and fluid incompressibilites with water saturation degree S_w. Finally, the third row pictures the evolution of quantities C/ρ_f and H/ρ with S_w for each virtual medium.

We observe that our experimental case of study, combining a sand frame saturated by an air-water mixture, is the sole example involving a phase shift in $\beta_P(S_w)$, here for a transition saturation S_{w_t} of 0.544. It also presents us with the one and only occurrence of curves intersection in figures 2.34e and 2.34i, location of the latest conforming exactly with the transition saturation. Correspondingly, as exposed in figure 2.35, the 'sand-water-air' medium is the sole example of our benchmark showing a sign reversal in the computed coseismic seismoelectric response when water saturation decreases from 0.8 to 0.35. This change of sign apparently combines to a similar sign inversion on fluid displacement W, obtained from

	Case 1		Case 2		Case 3		Case 4	
Frame	Sand		Sand		Limestone		Limestone	
ϕ	0.42		0.42		0.25		0.25	
$k\ (m^2)$	2.10^{-11}		2.10^{-11}		5.10^{-12}		5.10^{-12}	
α_∞	1.65		1.65		1.8		1.8	
$\rho_s\ (kg.m^{-3})$	2650		2650		2650		2650	
$K_{fr}\ (Pa)$	5.10^7		5.10^7		26.10^9		26.10^9	
Fluid	air+water		oil+water		air+water		oil + water	
$\rho_f\ (kg.m^{-3})$	1.2	1000	800	1000	1.2	1000	800	1000
$\eta_f\ (Pa.s)$	18.10^{-6}	1.10^{-3}	445.10^{-3}	1.10^{-3}	18.10^{-6}	1.10^{-3}	445.10^{-6}	1.10^{-3}
$K_f\ (Pa)$	15.10^4	22.10^8	10.10^8	22.10^8	15.10^4	22.10^8	10.10^8	22.10^8
$\sigma_f\ (mS/m)$	0	7.2	0	7.2	0	7.2	0	7.2

Table 2.5: Matrix and fluid parameters used in the study of computed coseismic field behaviour presented in figure 2.34. Solid parameters were obtained on one hand by experiments on our Landes Sand, on the other by considering Mount Gambier Limestone as presented by Toms-Stewart et al. [2009]. For the effective fluid, density $\rho_f(S_w)$ was taken as the arithmetic average, viscosity $\eta_f(S_w)$ was determined according to the formulation by Teja and Rice [1981] while saturation-dependent fluid modulus was calculated as $K_f = K_{B8}$.

the spectral product of solid displacement U by β_P. The possibility of such behaviour had already been addressed while evoking the general definitions of parameter β_P.

Yet these computations also arise some concerns regarding the causality of the synthetic signal: if the fluid might bear a displacement information preceding the solid displacement at some distance from the source, the earliness of the computed air-water fluid displacements seen on figure 2.35a seems non-physical. This behaviour shows especially through for fluids with high air-content (see also figure 2.35c), and its initiation time is all the more challenging that permeability of the medium is high. If we are unable to either to restrain or explain what appears as a numerical effect, it seems however that this earliness is restrained to fluid displacement W and does not propagate to electric field E.

Moving to the cases of the benchmark, by changing the fluid composition for an oil-water mixture, the coseismic electric becomes monotonically in-phase with seismic excitation : the sign change disappears. If, on the contrary, we return to the high incompressibility-contrast of the air-water fluid, but give a much stiffer frame to the model by entering limestone values, all electric curves flip in phase opposition to the seismic with no sign change respectively to variations in water saturation. Finally, if we combined the very stiff limestone with a stiff oil-water mixture, we still get no sign change with saturation and a phase opposition between electric and seismic. For all this case there is no intersection neither of the compressibility curves nor of the Biot coefficient curves normalised by densities.

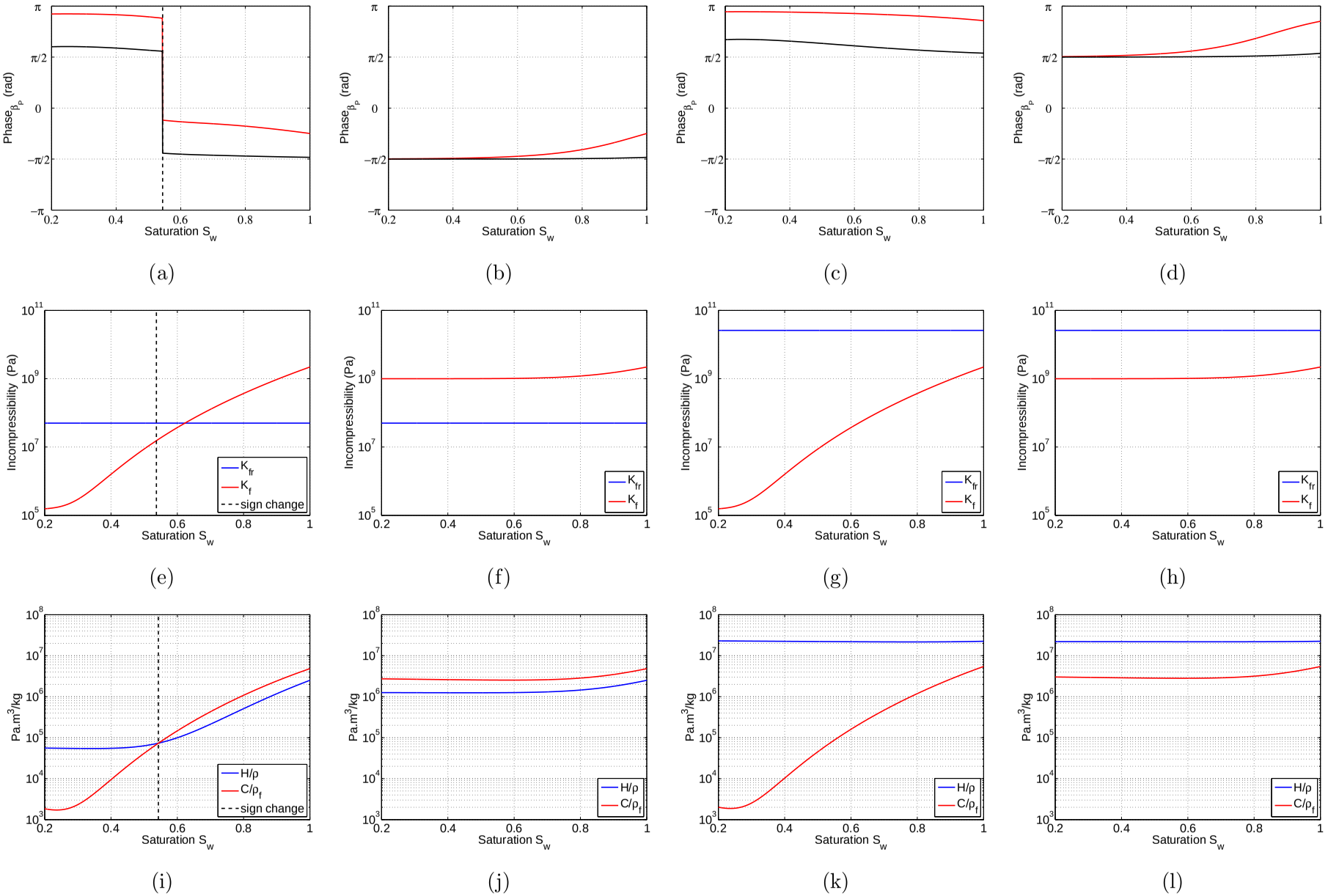

Figure 2.34: Effect of matrix nature and fluid mixture on the phase of the sign-controlling parameter β_P (a to d) for 100 (black) and 2000 Hz (red) and on the relative position of moduli (e to h) or Biot coefficients normalised by densities (i to l) for the fluid and the frame. Effective fluid modulus, represented in red on figures e to h, is calculated for $K_f = K_{B8}$ while frame bulk modulus stands in blue. First column concerns our case study on a sand frame filled by a mixed air-water fluid; the black dashed line marks the saturation at which the sign inversion of the $E/\ddot{u}$ ratio occurs. Second column takes the same frame but considers an oil-water fluid. Third and fourth column involve a limestone frame respectively filled by an air-water fluid and an oil-water fluid. These last three cases involve neither a phase-shift, nor a sign inversion.

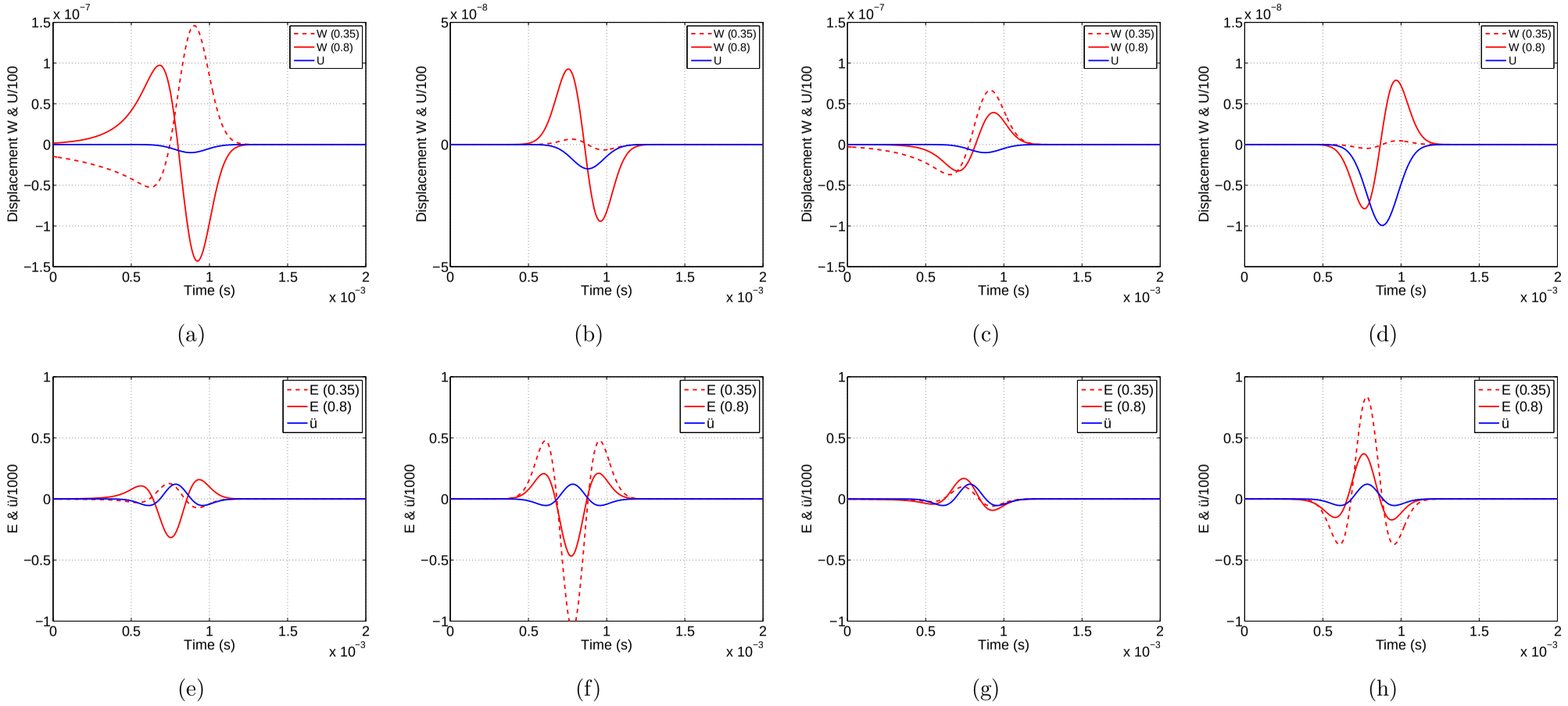

Figure 2.35: Effect of matrix nature and fluid mixture on the relative behaviour of solid and fluid displacement (a to d) as well as seismic excitation $\ddot{u}$ and its related coseismic electric effect E (e to h) at a 9 cm offset; water saturation degree is taken at 0.35 for red dotted lines and 0.8 for plain red lines. First column concerns our case study on a sand frame filled by a mixed air-water fluid. Second column takes the same frame but considers an oil-water fluid. Third and fourth column involve a limestone frame respectively filled by an air-water fluid and an oil-water fluid.

2.6.3 Theoretical conclusions on the sign inversion in the transfer function

Hence, the specificity[5] of the 'sand-air-water' example (embodying our experimental case) relatively to the other synthetic cases is to present an equivalence of factors C/ρ_f and H/ρ for a given saturation degree S_{w_t}.
If we note:

$$\Delta_{C,H} = 1 - \frac{\rho}{\rho_f}\frac{C}{H} \tag{2.116}$$

then, on basis of our observations run on figures 2.34 and 2.35, regarding relative positions of C/ρ_f to H/ρ curves and the resulting sign of the $E/\ddot{u}$ ratio, we propose that:

- the sign inversion of the $E/\ddot{u}$ ratio is experienced when

$$\Delta_{C,H} = 0 \tag{2.117}$$

- E and $\ddot{u}$ are in phase $(-\pi/2 < \psi < 0)$ when

$$\Delta_{C,H} > 0 \tag{2.118}$$

- E and $\ddot{u}$ are in phase opposition $(\pi/2 < \psi < \pi)$ when

$$\Delta_{C,H} < 0 \tag{2.119}$$

The sign dependency of the $|E/\ddot{u}|$ ratio on $\Delta_{C,H}$ is confirmed by Pride [2005] first order approximation of the fast P-wave β_P as:

$$\beta_P = \frac{i\omega\rho_f k_0}{\eta_f}\Delta_{C,H}\left[1 + O(\omega\rho_f k_0/\eta_f)\right] \tag{2.120}$$

Indeed in Pride's approximation, that should apply within frequencies inferior to 10 kHz for permeabilities compatible with unconsolidated sand such as $\omega\rho_f k_0/\eta_f \ll 1$, the sign of β_P, bearing the sign change, is given directly by that of the expression $\Delta_{C,H}$. Factor $\Delta_{C,H}$ can also be identified within the low-frequency approximation of the coseismic seismoelectric transfer function as expressed by Garambois and Dietrich [2001] (eq. (2.95), rewritten here):

$$\mathbf{E} \approx -\frac{1}{\sigma_f}\frac{\epsilon_0\kappa_f\rho_f\zeta}{\eta_f}\Delta_{C,H}\ddot{u} \tag{2.121}$$

Hence in both expressions, should it be this frequency-independent formulation relevant for the LF domain, or the frequency-dependent formulation by Pride for intermediate frequency,

[5]The perception of Biot coefficients relative position is not straightforward. In a first approximation, the chance to observe a sign change of the coseismic seismoelectric ratio with evolving saturation can be increased by choosing properly the saturating fluid mixture (two distinct fluid-phases relatively to the medium frame properties, so that $K_{f_1} < K_{fr} < K_{f_2}$. If $K_{fr} \gg (K_{f_1}, K_{f_2})$ the electric field and the acceleration should be in phase ; on the contrary it appear that they will be in phase opposition for $(K_{f_1}, K_{f_2}) > K_{fr}$.

the sign change is directed by same factor $\Delta_{C,H}$, endorsing the frequency-independency of this sign change to frequency and supporting its mechanical nature.

Finally, we would like to recommend caution against too hasty a treatment of $\Delta_{C,H}$. Indeed, in most situations the medium is expected to show $C \ll H$ causing $\Delta_{C,H}$ to approach unity. Consequently, according to the equation here above, the most common coseismic field observation should be in phase with seismic acceleration. Such assumptions are mainly true for consolidated media as we can see in figures 2.35g and 2.35h obtained on limestone, where K_{fr} remains monotonically superior to K_f despite varying water content. For unconsolidated media however the term $\Delta_{C,H}$ should be carefully taken into account, for there is great chance that Biot coefficient C be comparable to or even greater than coefficient H. On that account, for a large portion of our experimental data (those with highest water saturation degree) electric field and acceleration were actually close to phase opposition.

Chapitre 3

Conception of the experimental setup

Sommaire

This laboratory investigation comes after the respective works by Barrière et al. [2012] and Bordes et al. [2015] regarding saturation-dependent behaviour of seismic attenuation and coseismic seismoelectric field relatively to the theory of poroelasticity. Our ambition is to complete both studies, first by widening the frequency domain of investigation, second by extending the saturation-dependent observations to full saturation conditions. Our object of studies concerns the coseismic seismoelectric phenomenon; as such, precision of electric and seismic measuring do wear equal importance. Our purpose is to experimentally investigate, in a controlled environment of limited dimensions, the validity and observability of certain phenomena predicted by the extended Biot theory and a saturation adapted Pride theory.

We will start by a global introduction to our experimental setup presenting main characteristics of the sandbox and its instrumentation. In continuation to this section, the characteristics of the medium will be detailed, by resorting to literature, granular models or laboratory measurements.

In a more technical section, we will pursue with the presentation of the different seismic sources considered for the experiment before explaining our choice. We will then focus on seismic and electric captors while paying great attention to questions regarding measurements localisation and spacial resolution, before eventually giving a quick overview of the acquisition chain.

Having introduced the acquisition's main protagonists, description of the experiments will be broached, giving a detailed account of experimental proceedings for conductivity-dependent and saturation-dependent monitoring.

Finally, before moving to the next chapter developing signal processing aspects, preprocessing processes will be exposed, mostly relying on data reproducibility. We will question the validity and utility of data stacking and will ultimately explain how data reproducibility helped reconstructing larger data sets from separate acquisitions.

3.1 General description of the experiment

3.1.1 Global overview

We conceived a cubic sandbox from sealed plywood elements, accessible by the open top. A hole was arranged on one side of the box to let the punch of the source through. We disposed 3 cm thick acoustic foam slabs at the bottom as well as on the opposed and lateral walls to the source to prevent boundary reflection effects (see figure 3.1b). This acoustic foam (Strasonic, Paulstra) made of melamine resin was designed to absorb acoustic waves within the kilohertz range (attenuation of -10 dB at 2.5 kHz, -20 dB at 5 kHz).

As a result of this acoustic insulation, the dimension of the sandbox came to a 53×50 cm^2 basis, expected to be filled by a 50 cm high sand-layer for a total sand volume of approximately 130 l; the source emission point will be located at the center of a 50×50 cm^2 panel. We finally placed four injection wells, one at each corner of the sandbox, to allow for bottom imbibition. These wells were connected to elevated barrels in an attempt to improve saturation degree by an increased water column. The average quantity of water required for

initial imbibition was about 60 l. A global view of the experiment is given in figure 3.2.

Since preliminary seismoelectric measurements had convinced us that the coseismic seismoelectric E field could not be identified for offsets much larger than 20 cm, we decided to regroup all our captors within a distance of 30 cm to the source. By this choice of offsets, we notably differed from previous seismic [Barrière et al., 2012] and seismoelectric [Bordes et al., 2015] analysis realized on the same material within our laboratory.

With regard to the volume of each accelerometer, to combine a wanted captor density of 20 accelerometers to be placed within $[3 - 30\ cm]$ to the source required to dispose the transducers on two parallel lines. A thin central space, aligned with the source, was left free to host the electrode array. Accelerometers were implanted on either side of this central line with a centimetric lateral offset (see figure 3.4).

The electrode array of 30 electrodes and 27 cm length, created in concordance to the specific offset requirement, was placed on the central line between offsets of 3 cm and 30 cm. Accelerometer were systematically placed in regard to an electrode (see figure 3.1b).

For recollection of saturation information, the sandbox was further equipped with moisture sensors as to surround the measurement line. Some of this capacitance probes were arranged vertically, at horizontal planes located 10 cm beneath and 10 cm above the measuring plane in the purpose of informing us of nearing saturation changes (figure 3.1a). Others were disposed within the measuring plane at a distance of approximately 10 cm from the measuring line, as indicated in figure 3.1b. A detailed description of all captor types may be found in section; further in this section, the precise positioning of those captors is more thoroughly described.

In completion to moisture sensors, acquired separately, the instrumentation of the sandbox dedicated to coseismic seismoelectric measurements eventually implicated a total of 21 accelerometers and 29 electric dipoles controlled by a dynamic signal acquisition module. As these 50 captors exceeded the 31 available acquisition channel, we had to split the acquisition according to two distinct configurations. Section 3.4.2 will show how we proceeded to reconstruct a full data set from partial recordings.

3.1.2 Description of our unconsolidated porous medium: Landes sand

For our experiments we used the same granular material as had been described by Barrière et al. [2012], namely pure silica sand of SiO_2 content superior to 98 % and unidisperse granulometry of 250 μm. The supplier estimates its grain density by $2635 - 2660\ kg.m^{-3}$. This eolian rounded sand was extracted from a quaternary sandpit in the South-West of France (Landes).

While hydraulic properties (as porosity, formation factor and permeability) were directly measured on small sand probes and are to be shortly exposed in the followings, other pa-

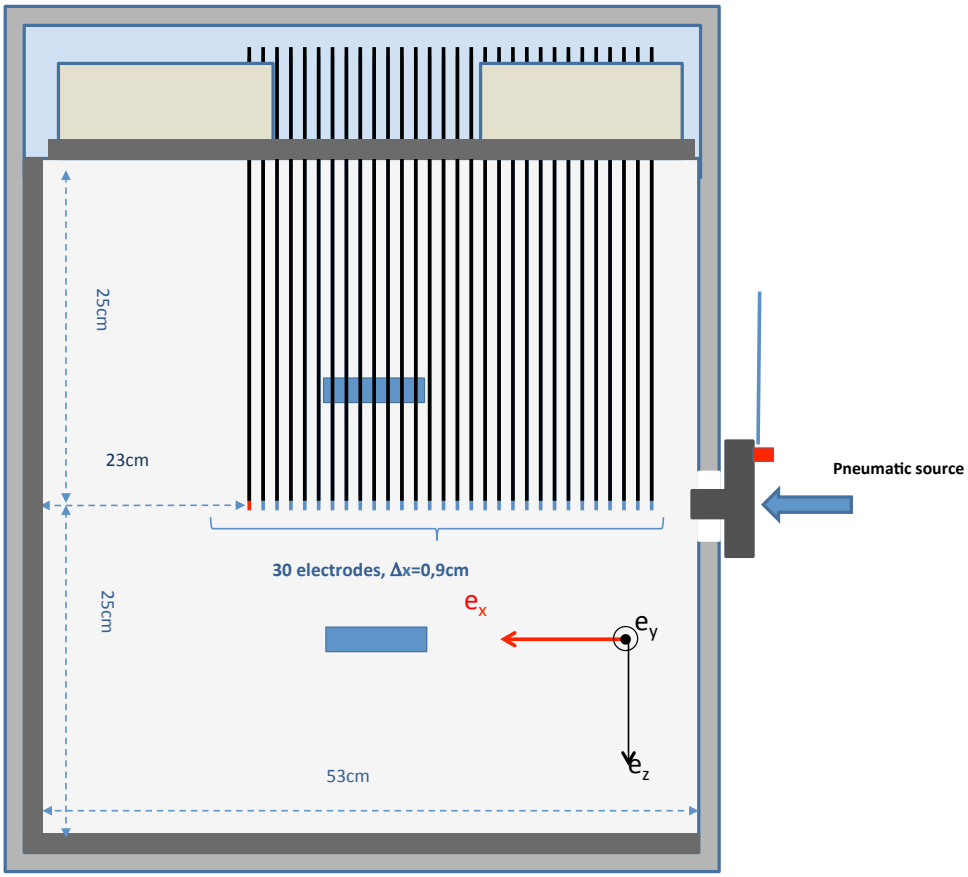

(a) Side view

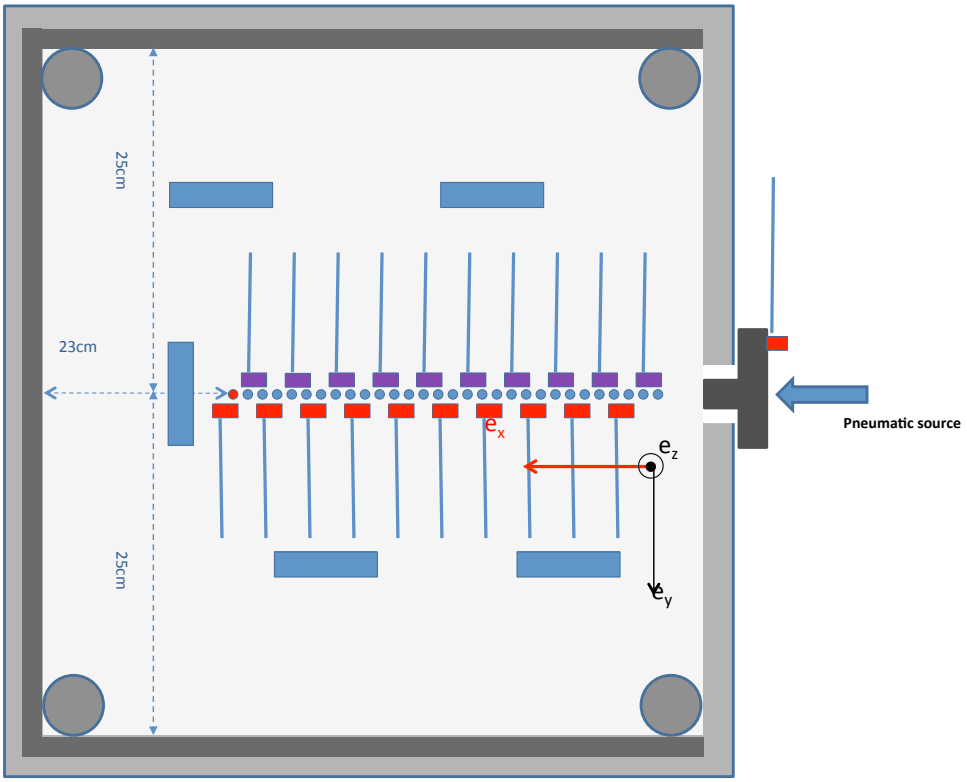

(b) Bird view

Figure 3.1: Side (a) and bird (b) view of the sandbox instrumentation and dimensions. The electrodes array is shown as series of 30 rods on (a) and aligned circles on (b), saving the red color for the common reference electrode. The 20 accelerometers disposed on two parallel lines are visible as small rectangles in (b) only. A last accelerometer, visible in (a) and (b), is placed on the punch for direct recording of source acceleration. The 7 water sensors, including 5 within the measuring plane (b) and 2 disposed vertically (a), are represented as blue rectangles.

Figure 3.2: Global view of the sandbox, the pneumatic source and the water injection system.

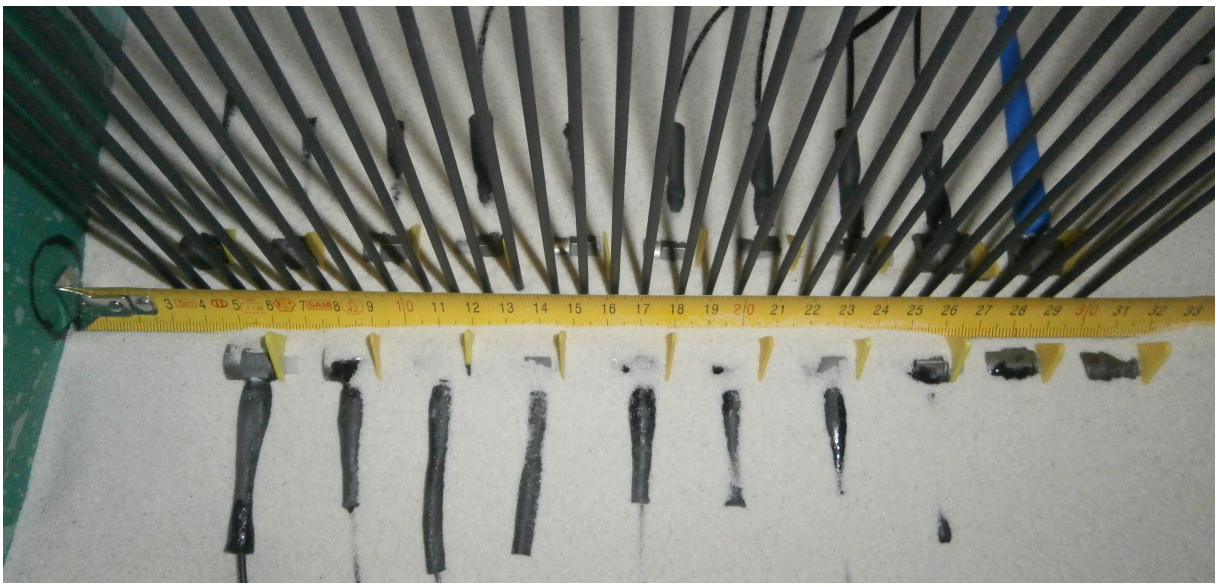

Figure 3.3: Picture of accelerometers and electrodes position within the measuring plane. The black circle marks the location of the source punch; the central line of the sandbox is materialised by the tip of the electrode array. It is framed by two parallel accelerometer lines shifted laterally by 1 *cm*.

Figure 3.4: Partial emptying of the sandbox after measuring campaign: half of the measuring plane is visible while the other half is covered by a 25 cm thick sand-layer. Rigidifying blocks are placed well off the measuring plane.

rameters, of electric or elastic nature, have been inferred from literature or models. Hence, frame bulk modulus K_{fr} and shear modulus G_{fr} are taken respectively to be of 25.5 MPa and 15.3 MPa, after the work by Barrière [2011] on the very same material. These values were obtained by the author, having given extensive consideration to unconsolidated grain contact theory by Kjartansson [1979] and Walton [1987].

Zeta potential ζ of the Landes sand was estimated at -35 mV accordingly to electrokinetic measurements realised by Nazarova Cherriere [2014] on this same material for a fluid of $pH \approx 7 \pm 2$ and $\sigma_f \approx 8.5$ mS/m (obtained by NaCl dilution 0.05 $g.l^{-1}$), using an apparatus developed by Bouriat [1997] and exposed in Bouriat et al. [1999]. In fact, while empirical models by Pride and Morgan [1991] and Guichet et al. [2003] would account for opposite evolution of ζ with conductivity σ_f (see section 2.2.2), predicting for the first on our conductivity range we chose to consider a constant zeta potential. The value we take is intermediate to the $-69mV$ prediction by Pride and Morgan [1991] and the $-19mV$ estimation by Guichet et al. [2003] at $\sigma_f \approx 10mS/m$. However, experimental values of zeta potential of $-24mV \pm 4$ deduced by the later from direct C_{EK} measurements on similar silica sand for conductivities comparable to our upper bound of $9 - 10$ mS/m, corroborates the ζ of -35 mV experimentally measured on our material.

Experimental determination of hydraulic parameters on Landes sand and unconsolidated glass bead samples

For measuring hydraulic properties on granular material, we disposed of a small cylindrical cell (see figure 3.5) of dimensions $\oslash = 0.056\ m$ and $L = 0.07\ m$, connected to a suspended water canister and equipped with fine metallic sieves on its whole section at both ends. These sieves would allow for water circulation while serving occasionally as electrodes, in order for the apparatus to be worked either as a permeameter to determine permeability k, or as a porosimeter to measure formation factor F. This last approach would eventually lead to tortuosity α_∞. As for porosity it would systematically be inferred from the mass of the dried material reported to the volume of the cell.

Greatest attention was given to the filling of the cell, compacted by vibration, and to subsequential sample saturation. To enhance the saturation process and prevent air-trapping within the mesh of the sieves, the cell was depressurized before being connected to the water arrival. The device was alternatively used as a permeameter or as a porosimeter. Indeed, after moving the reservoir to apply a new differential pressure, the system was given 15 min for water circulation to equilibrate, before measuring permeability. Water circulation was then momentarily interrupted, to allow for a measurement of the sample electric conductivity. After that measurement, fluid conductivity was modified within the supplying reservoir, before this reservoir being put to a new position, water circulation to be reestablished and the whole cycle to be rerun.

In this section we rapidly present the experimental points measured for Landes sand in both configuration of the device, along with further results obtained on sorted glass beads. Furthermore, these results will be completed by permeability measurements performed on Landes sand within a column of medium size (diameter $\oslash = 0.08\ m$ and length $L = 0.3\ m$) and on glass beads for a column of larger dimension (diameter $\oslash = 0.1\ m$ and length $L = 0.5\ m$) , following exactly the same principles as the small cell, but filled without any compaction.

Formation factor measurements Resistivity measurements for formation factor characterisation were made on the small cell once water circulation had been interrupted. The resistance R_Ω was measured at the sample extremities using an impedancemeter at frequency 1 kHz. It was then corrected by the sample section S and length l to finally express the bulk conductivity of the medium as:

$$\sigma_{bulk} = \frac{l}{R_\Omega . S} \tag{3.1}$$

Formation factor was then estimated knowing its electric definition after Archie [1942] as $F = \sigma_f / \sigma_{bulk}$, eventually giving access to tortuosity thanks to the hydraulic definition of the formation factor as $F = \alpha_\infty / \phi$ after the capillary model from Brown [1980] (see section 2.1.1). Measurement points associated to resistivity investigations on Landes sand are to be found in figure 3.6, while all values for resistivity measurements on compacted unconsolidated media have been recapitulated in table 3.1.

Figure 3.5: Cell of the permeameter / porosimeter apparatus equipped with electric connections for measuring the bulk conductivity of the medium and with tube derivations to monitor differential pressure at sample extremities.

For our Landes sand we deduced tortuosity from formation factor values ; these parameters are respectively of 1.65 ± 0.05 and 4.8 ± 0.1. Though porosity shows appreciable variation on the sample proposed in table 3.1, tortuosity α_∞ remains rather stable around a value of 1.6. Inspite of this stability, we chose to conserve the value of 1.65, experimentally obtained on compacted Landes sand, to characterise our unconsolidated medium (though possibly less compacted).

Permeability measurements Within the small cell, permeability measurement were run on compacted samples by imposing differential pressures ranging from 90 to 180 $mbar$, obtained by establishing a water column of approximately 1 up to 2 m. Intrinsic permeability k_0 was estimated after Darcy's law, which states the linear dependency of fluid flow Q to

	F	ϕ (%)	α_∞	m
GB 125 − 160 μm	3.5 ± 0.6	40.1 ± 0.2	1.4 ± 0.25	1.37
Landes Sand $\bar{d} = 250$ μm	4.8 ± 0.1	34.7 ± 0.2	1.65 ± 0.05	1.48
	$3.65 \pm 0.1^*$	$40.9 \pm 0.4^*$	1.5 ± 0.02	1.45
GB 250 − 355 μm	4 ± 0.05	38.7 ± 0.2	1.55 ± 0.03	1.46
GB 355 − 500 μm	4.2 ± 0.2	38.1 ± 0.2	1.6 ± 0.1	1.49
	4.2 ± 0.1	37.8 ± 0.2	1.6 ± 0.05	1.475

Table 3.1: Formation factor F, porosity ϕ, tortuosity α_∞ and cementation factor m data acquired on Landes sand and glass beads (GB) of sorted granulometry. Data with en asterisk (*) were obtained on a medium-size column, while further results were obtained on the small cell.

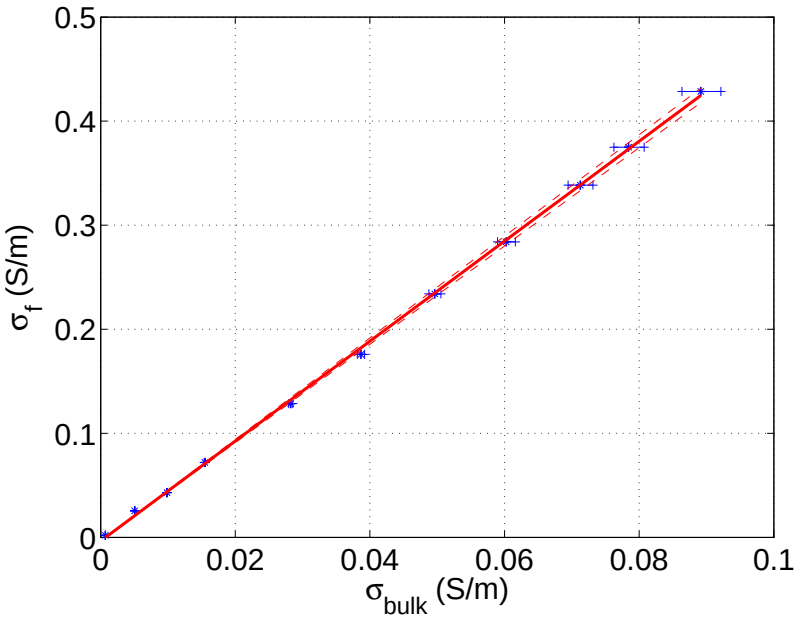

Figure 3.6: Resistivity measurements conducted on unconsolidated compacted Landes sand. The formation factor, given by the slope of the plain red curves, is of 4.8 ± 0.1. The dashed curves give the slope with errors on basis of linear regression with a confidence interval of 80%. Error bars on the measurement point were deduced from assumed error readings to be of ± 1 s on time, ± 1 g on quantity of recollected water, ± 2 $mbar$ on differential pressure.

the applied gradient of fluid pressure after the relation 2.12. Measurements were made after a 15 min equilibration time over a fixed duration of 60 s, the average amount of collected water would be of 80 g to 160 g.

Taking the smaller cell into consideration, permeability measurement were conducted twice on compacted samples of Landes sand (see figure 3.7). Both results converge toward an average permeability value of 5.5 D. First measurement estimated the permeability to be of 6 ± 0.4 D, the second $4.7 \pm 0.4D$. Yet, considering the compacted state of the sample, this experimental value for permeability and porosity must rather be taken as lower bounds.

Indeed while further experiments on a larger and uncompacted volume of Landes sand, within the medium cell, gave a permeability estimation of $k_0 = 22 \pm 7$ D, measurements run on the largest column for a previous experiment showed permeability of 28.4 ± 2 D for the $250 - 355$ μm glass-beads fraction. For this granulometry only slightly larger than that of our experimental medium, permeability estimation within the compacted small cell averaged 7.5 D. Supported by estimations given by the Kozeny-Carman and Glover-Walker permeability models presented in section 2.1.1 and by the permeability measurements on uncompacted sand, we settled our intrinsic permeability of reference for the medium at 20 D.

For porosity, in addition to measured values giving the lower bound, we calculated a porosity value after equation (2.2). This empirical relation by Hamilton [1974], developed for marine sediment, only requires the mean grain diameter as preliminary knowledge. For a mean grain diameter of 250 μm porosity would be expected to lay by 0.42. As this estimation appears conceivable with regards to porosity values observed within the uncompacted medium size cell, we adopted a porosity value of 0.42 ± 0.02 for our uncompacted sand within

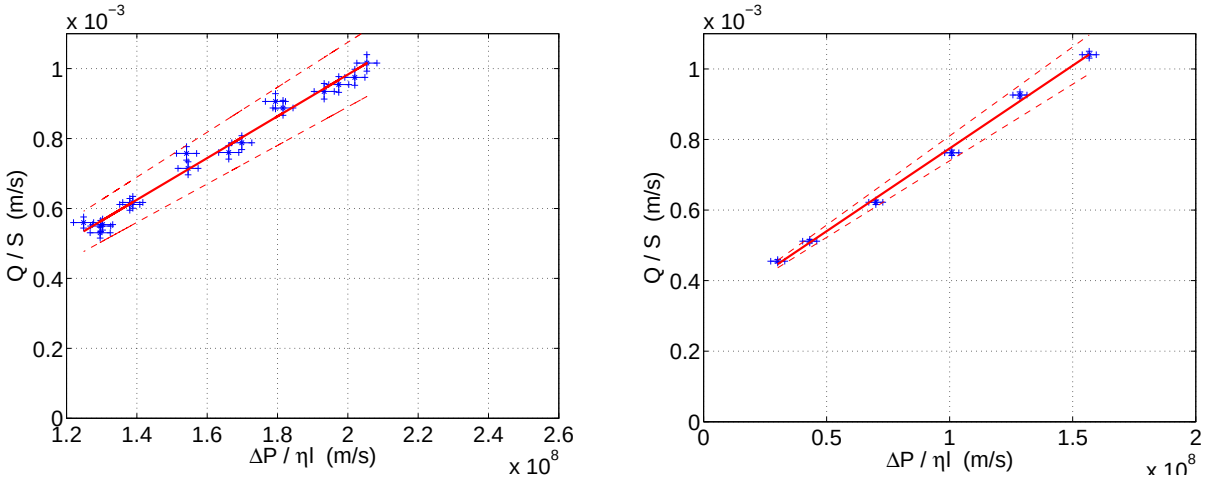

(a) $k = 6 \ \pm 0.4 \ D$ (b) $k = 4.7 \ \pm 0.4 \ D$

Figure 3.7: Permeability measurements conducted on unconsolidated compacted Landes sand. The permeability, given by the slope of the plain red curves, is of 6 ± 0.4 D for figure (a) and 4.7 ± 0.4 D for figure (b). The dashed curves give the slope with errors on basis of linear regression with a confidence interval of 95%. Error bars on the measurement point were deduced from assumed error readings to be of ± 1 s on time, ± 1 g on quantity of recollected water, ± 2 $mbar$ on differential pressure.

the larger 130 l sandbox.

Conclusion

All grain-, frame- and fluid-parameters characterising the porous medium are gathered in table 3.3. The last two fluid parameters, namely fluid conductivity σ_f and water saturation degree S_w, were made to variate and accordingly monitored within the indicated span. The evolution of principal effective fluid properties with water saturation degree S_w may be found in figures 2.13 and 2.12 of section 2.4.2, while future observations will show that it might be relevant to consider an increase of bulk modulus K_{fr}, compatible with additional compaction , when the medium has long been in place (see section 5.1.3).

For the material described in table 3.3, Biot transition frequency f_{Biot} is expected to lay by 2000 Hz when fully saturated, evolution of this transition frequency on the whole saturation range being shown in figure 2.16. The unconsolidated nature of the Landes sand causes it to act as a low-pass filter: literature reports a difficulty to observe frequencies greater than 3 kHz within such material [Barrière et al., 2012; Bordes et al., 2015], as may also be observed on the noise-spectra in figure 3.8, letting pass a certain amount of noise up to 2 kHz before dropping. Yet, we will try to extend our restricted frequency domain of investigation by stacking. Legitimacy and contribution of this process will be discussed further in coming section 3.4.1.

	d_g (μm)	d_p (μm)	Cell size	k_0 (D)	ϕ (%)	k_{KC} (D)	k_{GW} (D)
Glass beads 125 − 160 μm	114	35	S	0.3 ± 0.2	42.8 ± 0.2	9.6	10.7
			L	4.3 ± 0.4	37 ± 1	5.1	8.6
Landes sand	250	60	S	6 ± 0.4	34.5 ± 0.2	14.1	22.8
			S	6.1 ± 1.9	34.5 ± 0.2	14.1	22.8
			S	4.7 ± 0.4	32.6 ± 0.2	11.2	20.9
			M	22 ± 7	37 ± 1	18.8	25.3
Glass beads 250 − 355 μm	304	70	S	3.2 ± 0.8	35 ± 0.2	24.4	30
			S	11.2 ± 4.3	39.4 ± 0.2	40.1	35.7
			S	8.1 ± 1.1	37.3 ± 0.2	31.8	32.9
			L	28.4 ± 2	38.8 ± 1	37.5	34.9
Glass beads 355 − 500 μm	406	90	L	52.3 ± 4	37.3 ± 1	52.2	57.7

Table 3.2: Permeability k_0 and porosity ϕ data acquired on Landes sand of mean diameter 250 μm and glass beads of sorted granulometry, within column of various sizes (S = small $\oslash = 0.056$ m and length $L = 0.07$ m, M = medium $\oslash = 0.08$ m and length $L = 0.3$ m, L = large $\oslash = 0.1$ m and length $L = 0.5$ m). Data noted with an asterisk (*) were taken from permeability measurements conducted on a large sand column of diameter 0.1 m and length 0.5 m using glass beads.

	Parameter	Notation (Unity)	Values	Comments
Frame	intrinsic permeability	$k_0\ (m^2)$	2×10^{-11}	measured
	porosity	ϕ	0.42 ± 0.02	"
	formation factor	F	4 ± 0.5	"
	tortuosity	α_∞	1.65 ± 0.15	deduced from measured F and ϕ
	cementation factor	m	1.45 ± 0.1	Archie's law
	2^{nd} Archie parameter	n	2.58	Bordes et al. [2015], Doussan and Ruy [2009]
	bulk modulus	$K_{fr}\ (Pa)$	2.55×10^7	Barrière [2011] from Walton [1987]
	frame shear modulus	$G_{fr}\ (Pa)$	1.53×10^7	"
	undrained modulus	$K_G\ (Pa)$	5.4×10^7	eq. (2.27) from Gassmann [1951]
Grain	grain diameter	$d_g\ (m)$	250×10^{-6}	measured by supplier
	solid phase density	$\rho_S\ (kg.m^{-3})$	2650	"
	grain modulus	$K_S\ (Pa)$	36×10^9	reference silica value
	grain shear modulus	$G_S\ (Pa)$	44×10^9	"
	grain rel. permittivity	κ_S	4	"
	zeta potential	$\zeta\ (mV)$	-35	measured by Nazarova Cherriere [2014]
Pore	pore diameter	$d_p\ (m)$	100×10^{-6}	Glover and Walker [2009]
	water density	$\rho_w\ (kg.m^{-3})$	998	reference water value
	water modulus	$K_w\ (Pa)$	2.2×10^9	"
	water viscosity	$\eta_w\ (Pa.s)$	$9.91^{-4} \pm ‰$	eq. (2.34) by Phillips et al. [1978]
	water rel. permittivity	κ_w	$80.8 \pm ‰$	eq. (2.33) by Sen and Goode [1992]
	air density	$\rho_g\ (kg.m^{-3})$	1.2	reference air value
	air modulus	$K_g\ (Pa)$	1.5×10^5	"
	air viscosity	$\eta_g\ (Pa.s)$	18×10^{-6}	"
	air rel. permittivity	κ_g	1	"
	electrolyte conductivity	$\sigma_f\ (mS.m^{-1})$	$1.7\ -\ 10$	measured
	water saturation degree	S_w	$0\ -\ 1$	"

Table 3.3: Properties of the experimental porous medium constituted of Landes sand saturated by an air + NaCl electrolyte mixture. Those parameters all intervene within the model computation of the coseismic seismoelectric phenomena by Pride [1994]. Origins of the estimations are indicated.

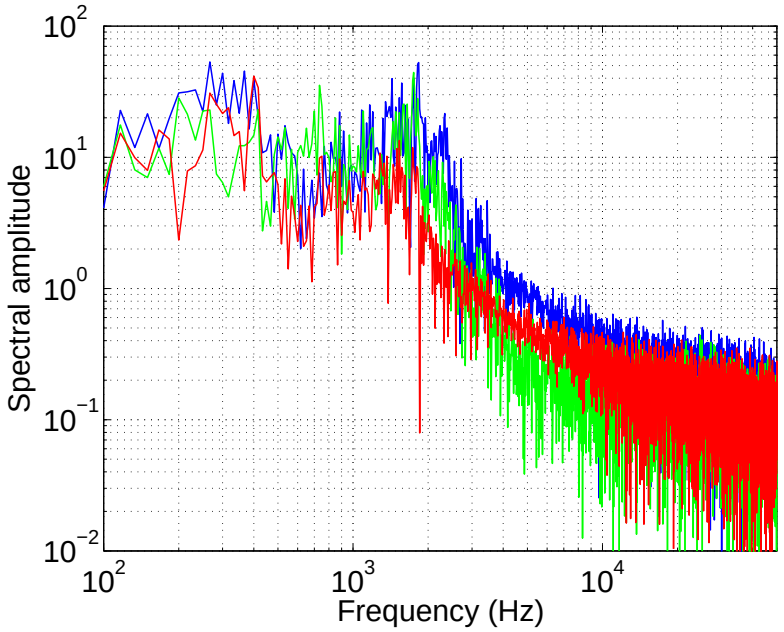

Figure 3.8: Noise spectra for seismic receivers at 3 *cm* (blue), 10.4 *cm* (green) and 18.8 *cm* (red) obtained on the signal preceding the activation of the pneumatic source.

3.2 Characteristics of the experimental devices

3.2.1 The seismic source

Domain of investigation

When considering the theory of poroelasticity, behaviour of the porous medium is expected to show a certain stability at low frequencies, while becoming frequency-dependent when entering its high-frequency domain; the transition domain is evidently of particular interest. The progression from one behaviour to the other is caused by the overtaking of inertial forces over viscous ones, the tipping point having been attributed a characteristic frequency already introduced as f_{Biot}.

For unconsolidated material this transition frequency is expected to lay within the kilohertz range; we consequently aimed for seismic sources exciting the medium at acoustic frequencies. Most fortunately, frequencies within $[0.1 - 5\ kHz]$ appear particularly favourable to coseismic electric observations, as supported by Block and Harris [2006] in a previous laboratory work on unconsolidated sand and glass beads (see figure 3.9).

To investigate such high frequency within our medium we have two options on the source. First, we may approach the ideal dirac function by a short seismic pulse having wide frequency spectrum. Or, we may apply a long signal of single frequency content, namely a continuous sinusoid, to produce a dirac-like spectrum. Since spectra are expected to be monochromatic, this last method would greatly simplify the signal processing part. As a further advantage, this approach would offer greater chances of observing frequencies greater than 3 kHz by imposing them repeatedly and exclusively.

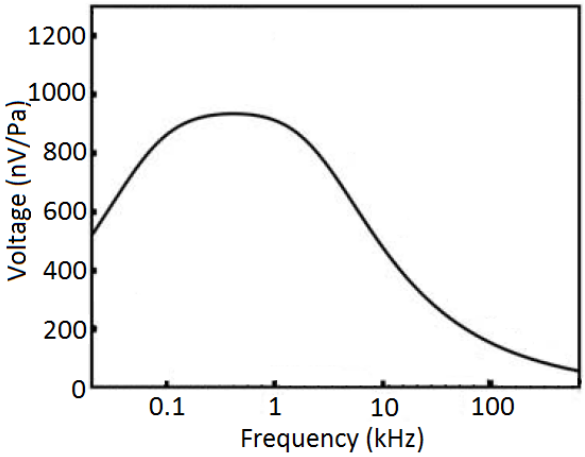

Figure 3.9: Amplitude of the coseismic seismoelectric response in sand with frequency (from Block and Harris [2006]).

Attempt to work with a piezoelectric source

We first considered analysing one isolated frequency at a time. Aim was to have seismic and electric spectra resembling a dirac in order to calculate the ratio of both spike-spectra as the value of the coseismic transfer function at that precise frequency. To provide an akin monochromatic signal, a continuous sinusoid is needed. Yet generation of such a maintained signal necessarily involves a piezoelectric source.

In this prospect, a piezoelectric source (International Transducer Corp.) meeting our frequency requirements was collected. This omnidirectional source, also usable as an hydrophone, was made from a piezoelectric device encapsuled in a 15 cm polyurethane sphere. The frequency band of use extended from 10 Hz to 20 kHz, with a resonance frequency and maximal efficiency of the source at 11.5 kHz. The delivered acceleration would depend on the excitation frequency, yet it would range from $1 - 10$ $m.s^{-2}$ at the source. The piezoelectric element could be used as a pulse or as a sweep: to achieve continuous sinusoids we imposed mono frequency sweeps. When used as a 10 kHz sine-wave pulse (i.e. in its most favourable frequency band), maximal acceleration would be of ± 600 $m.s^{-2}$ and the signal is concentrated at frequencies of 10 ± 5 kHz (see figure 3.10). In this configuration, the source shows admirable reproducibility.

Yet, we encountered two major problems while using this source, one affecting the electric the other one the seismic. The first issue, to be expected when using a piezoelectric source, is that emitted EM noise synchronous to the source will spoil the electric record. This effect was particularly clear on dry sand, for which no coseismic response is expected: electric records, apart from being uniformly plagued by a coherent 550 Hz noise of amplitude ± 2 mV, are tremendously affected by the activation of the source to an extent of over 0.1 V for the dry sand and twice as less when saturated (see figure 3.11a). By wrapping the source within an aluminium foil, noise on records in dry sand was clearly reduced (figure 3.11b). Yet water introduction within the medium would partly disable the protection (figure 3.12): noise level at the nearest offset would be comparable to that observed on saturated sand in the absence of an aluminium foil (on a captor that was unrelated to the source). As a more permanent and complete solution, one would cover the source in impermeable metallic

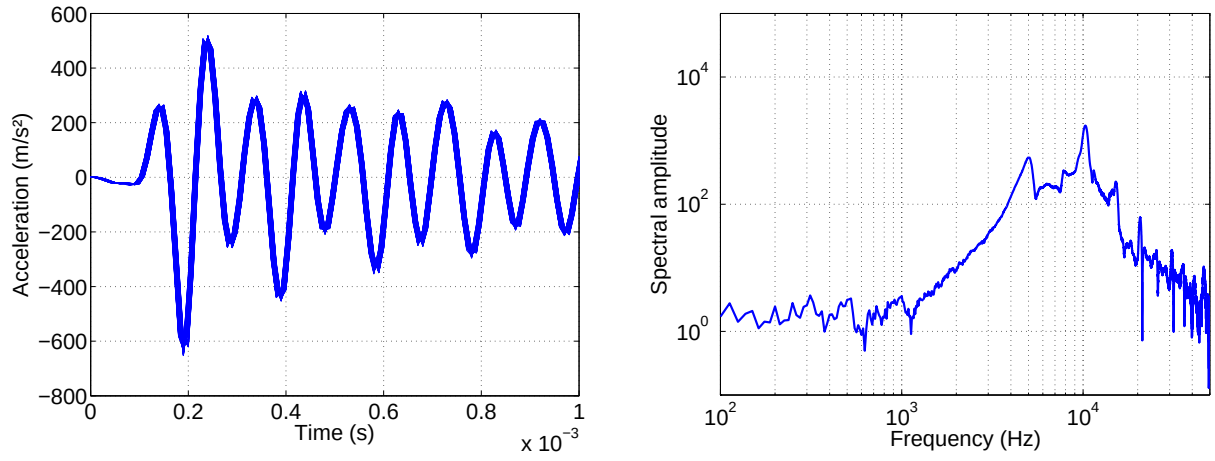

(a) (b)

Figure 3.10: Reproducibility of the piezoelectric (PZ) source (a) with superposition of 75 shots obtained during measurement row '20130607' and spectrum associated to a 10 kHz sine-wave pulse as a single shot (b).

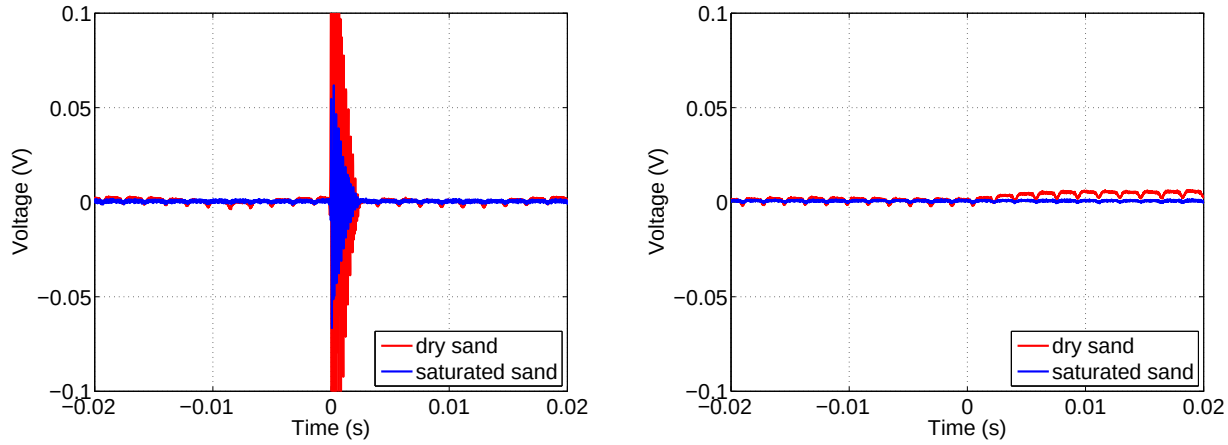

(a) Source without aluminium foil (b) Source in aluminium foil

Figure 3.11: Electric recordings acquired within dry (red) and saturated (blue) sand while activating the piezoelectric source. In case (a) the source is unaltered while in case (b) it has been wrapped in an aluminium foil to simulate a Faraday cage. Each dipole is in a separate bucket having no direct contact to the source: no sign of propagation is expected in any electric records, we pick only EM noise.

painting to create a Faraday cage. In spite of the second less expected problem however, we did not alter the source.

Origin of the second issue affecting the accelerometers is not fully solved: it appears that the continuous sinusoidal excitation of the accelerometer caused them to enter a resonance mode affecting their amplitudes rather than their spectral signatures. Evidence of this phenomenon was given by the observation of erratically distributed amplitudes as experienced in figure 3.13: the receiver closest to the source was not necessarily the one showing the highest amplitudes while the amplitude ranking of the receivers would change with changing frequencies and acquisition history.

As we could neither fully explain the origin, nor fix the aberration on seismic amplitudes observed while using the source as a monochromatic sweep, some attempts were made to employ the piezoelectric source as a pulse of wide frequency spectrum. Yet, acknowledging

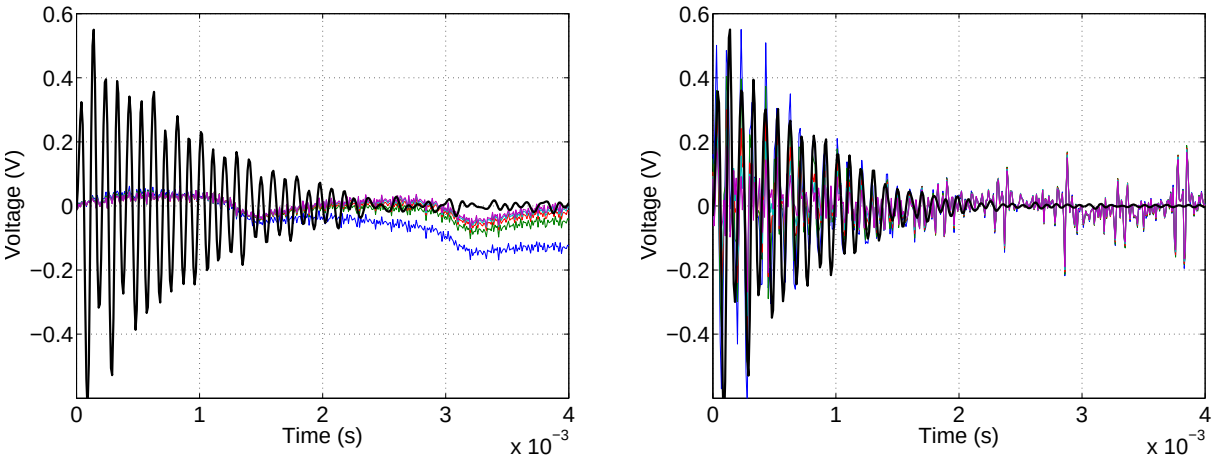

(a) Dry sand

(b) Moist sand

Figure 3.12: Electric records on the five dipoles closest to the source compared to the normalised signal of the seismic excitation at the source (thick black curve). In this experiment the dipoles are in the same box as the source wrapped in aluminium foil: for dry sand (a) there is now source noise on the electric records, but introduction of water weakens the protection.

the persistence of source-associated EM radiations and the global weakness of high-frequency components now that the signal was a large-band pulse, the piezoelectric source became obsolete. As an alternative we chose to use a high-energetic air-gun pneumatic source devoid of any EM noise.

Final choice: a home-made pneumatic source

The pneumatic source appeared as a the better option for being used as a pulse. This source is made of two separate elements:

- a piston supplied with compressed air, which valves are commanded by a Labview programm that controls how rapidly the air chamber is filled or emptied (general view of the source in figure 3.2). The punching end may be approached from the hitting plate by adjusting the source-plate distance.

- a fixed frame that maintains the steel hitting plate by four screws equipped with shock-absorbers. The rectangular plate ($8 \times 8\ cm^2 \times 4cm$) ends as a short cylinder acting as a source to the experimental medium (see figure 3.14).

A hole was arranged on one side of the sandbox to let the hitting punch through, the punch showing by 5 mm on the other side of the wood slab to transmit the impulsion from the pneumatic source to the medium. In order to prevent the material from pouring out of the box, the hole and punch were then covered with a strong green canvas sheet of dimension $15 \times 15\ cm^2$ (see figure 3.15b), coupled to the punch by acoustic gel. The whole structure was then covered in a second protecting transparent canvas, coupled to the green canvas at the punch location by more acoustic gel (see figure 3.15c). If the presence of this two sheets of canvas does not jeopardize the measurement to the very high energy of the source, it will altere the coupling of the medium to the source. Accelerations observed at the hitting plate are consequently only indicative of the global energy of the source and its reproducibility but are by no way of the order of magnitude that will be observed within the sand.

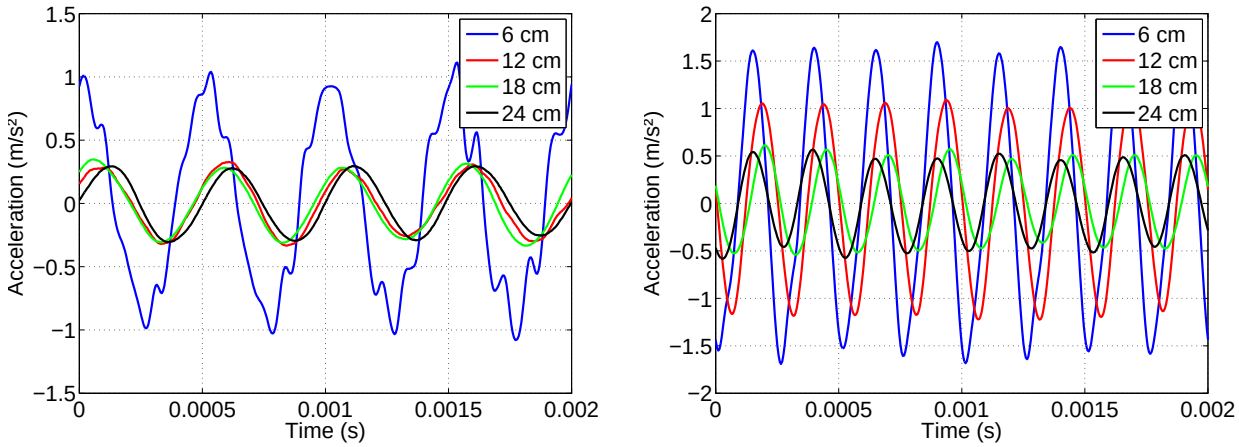

(a) Monochromatic sweep at 2 kHz.

(b) Monochromatic sweep at 4 kHz.

Figure 3.13: Seismic records obtained at offsets ranging between 6 cm and 24 cm under monochromatic sweep excitation of the medium using the piezoelectric source. Amplitudes at seismic receivers appear not to follow common attenuation patterns, utilisation of these data appears hazardous.

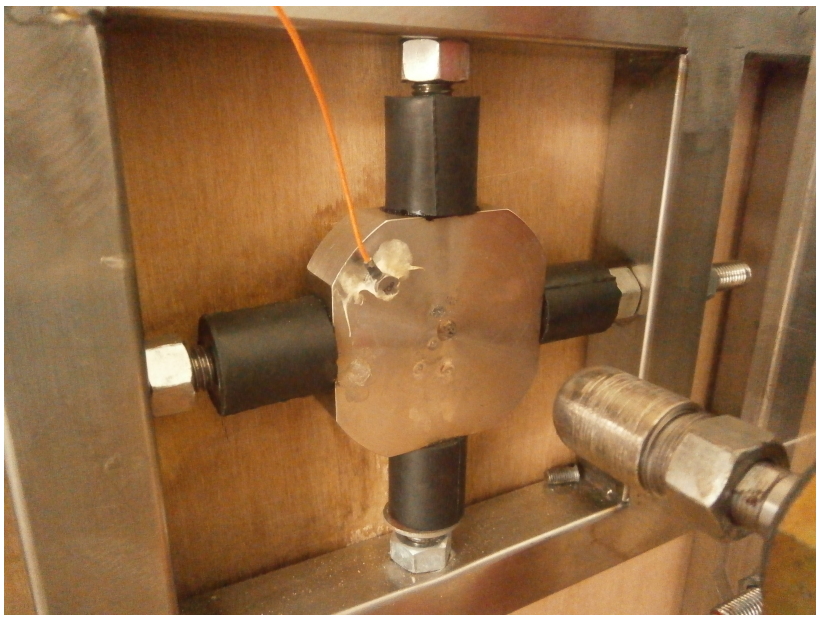

Figure 3.14: Detail of the pneumatic source: the hitting plate with corresponding transducer giving the acceleration at the source (b).

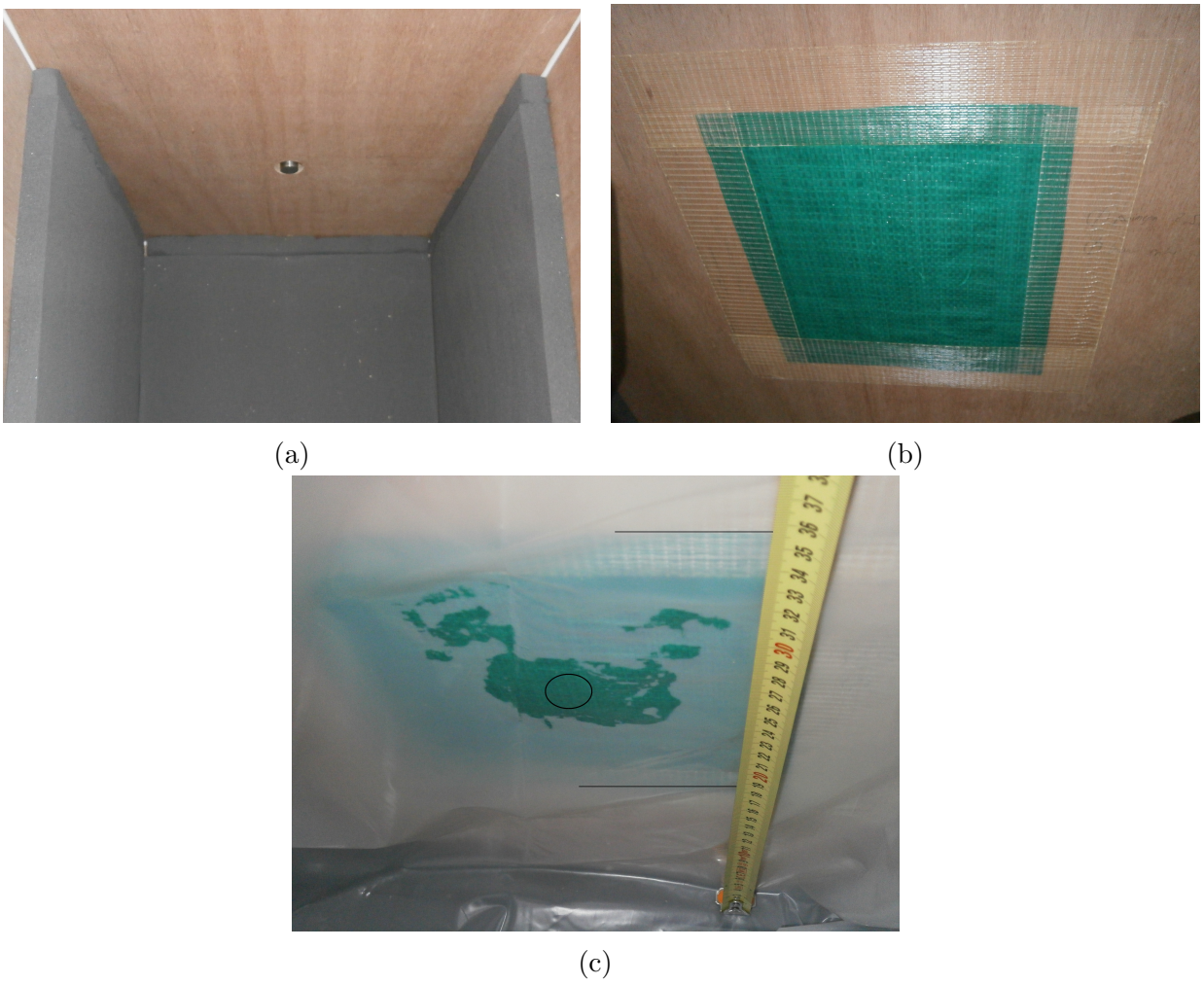

Figure 3.15: Pneumatic source configuration (a) source punch (b) covered by a piece of strong green canvas sheet of $15 \times 15\ cm^2$ coupled to the punch by acoustic gel. (c) To preserve the wood casing, the experimental medium is then placed in a second thinner canvas, coupled to the green canvas as well. The position of the punch behind the 2-ply canvas is identified by a black circle; black lines materialize the side-length of the green canvas patch.

The quality of this high-energetic pneumatic impact, in both form and amplitude, is controlled by the valves activation times, the distance from the punching head to the hitting plate, as well as the screw tightening of the hitting plate. By way of example, all these elements will contribute to prevent the source to bounce back, causing a secondary excitation of the medium and a second P-wave arrival to stain the records. The multiplication of these fitting parameters may eventually question the reproducibility of the source during prolonged acquisition. Yet for a given measurements row the reproducibility is satisfying (see figure 3.16a for a typical series of 75 shots).

If the piezoelectric source offered better reproducibility than the pneumatic source, the delivered acceleration of the last is greatly superior. Acceleration values at the hitting plate stretch from a minimum of 1000 $m.s^{-2}$ up to 5000 $m.s^{-2}$. Hence, when comparing spectra of both sources, one can note the frequency band $[0.1 - 10]kHz$ of the pneumatic source being much wider, and the amplitudes at any given frequency being much larger, than the ones provided by the piezoelectric source (figures 3.16b and 3.10b). We also note on figure 3.16b the presence of a resonance frequency at approximately 19 kHz possibly related to a characteristic frequency of the source system. Though all the energy is not

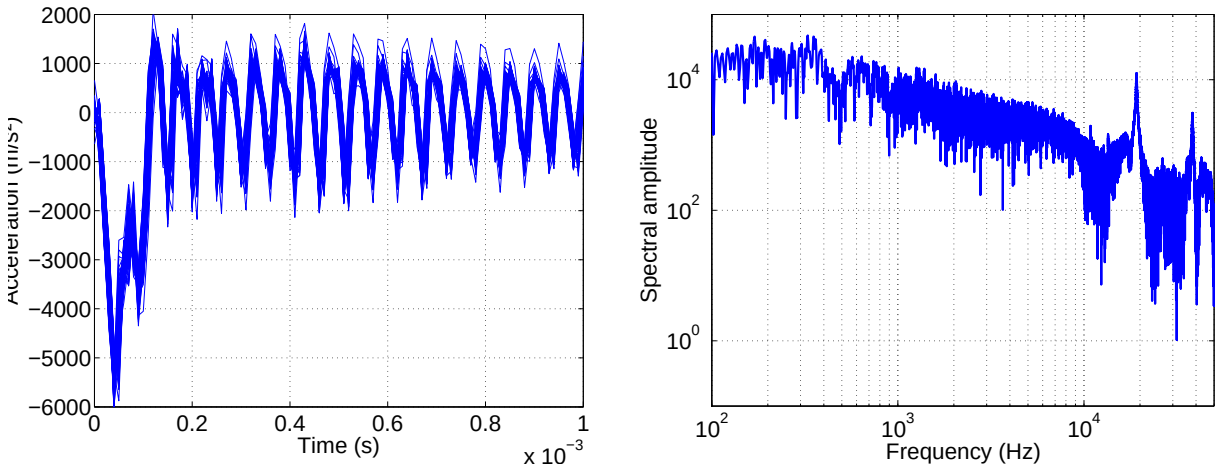

(a) (b)

Figure 3.16: Reproducibility of the pneumatic source (a) with superposition of 75 shots obtained during measurement row '20140305' and spectrum associated to a single shot (b).

fully transmitted to the medium due to the coupling at the punch, acceleration values at comparable offsets within the sand, for receivers submitted to either source types used as a pulse, clearly demonstrated the superiority of the pneumatic source.

3.2.2 The captors

The seismic captors and moisture sensors we used have previously been employed in the experiment by Barrière [2011], also reported in Barrière et al. [2012] and Bordes et al. [2015]. For our presentation of the experimental material, we reproduce part of their descriptions of the experimental setup here.

Moisture sensors

Our moisture sensors were capacitance probe $Waterscout\ SM100\ Soil$ delivered by Spectrum. One probe encloses two separate electrodes acting as a capacitor, the soil playing the part of the dielectric lagging. As represented in figure 3.17, the measurements will be sensitive to the medium dielectric permittivity within a distance of 1 cm from the captor. The relative permittivity of air and water being respectively of 4 and 80, with higher water content comes higher dielectric permittivity and an enhanced facility for the capacitor to increase its charge causing the probe response to be accordingly elevated. Alimentation of the electrodes requires a power support of $3-5\ V$ at an amperage of $6-10\ mA$.

Estimation of the water content being deduced from a capacitance measurement of the surrounding medium, these probes have to be calibrated relatively to the medium of interest. Calibration was realised by Barrière [2011]: the capacitance probe was placed within a beaker of water-saturated sand at full saturation. A measurement was made at known saturation, the medium was then slowly desaturated thanks to a hot plate. The measured values would then linearly decrease with saturation, down to a water saturation degree of about 0.015. Having corrected the measurement from a possible temperature drift, he could ultimately

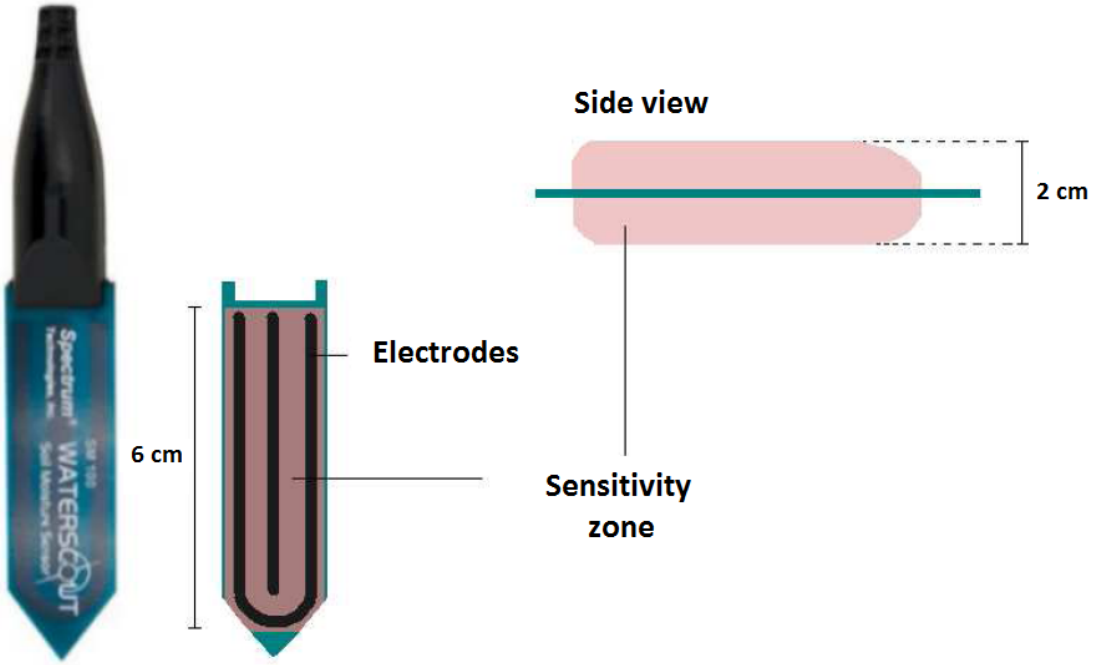

Figure 3.17: Waterscout SM100 moisture sensor

define a linear relation between the volt measurement of the probe and the saturation S_w of the medium, and evaluate the error on the measurement to be of $\pm\ 3-5\ \%$ for saturation degree comprised between 0.3 and 0.9.

Accelerometers

For our main experiments, two distinct types of accelerometers have been involved. On the one hand, a single DJB accelerometer, was glued to the punching plate for measuring acceleration at the source. To prevent overloading the acquisition device, a low sensitivity of approximately 1 $mV.m^{-1}.s^{-2}$ was chosen. Its main task was to monitor the repetitiveness of the source and the quality of the impulsion.

On the other hand, we used Brüel & Kjær IEPE accelerometers of type '$4513-001$' and '$4513-002$' for the sandbox instrumentation. A full calibration chart is to be found in the appendices for a transducer of each kind, while we report here the most important characteristics. These accelerometers claim average sensitivity of respectively 10 $mV.m^{-1}.s^2$ and 50 $mV.m^{-1}.s^2$ within the $[0.1-10\ kHz]$ frequency range; the voltage response should remain within $\pm 5\ V$. The use of type $4513-001$ accelerometers, showing lower sensitivity, was restricted to a 5 cm radius to the source. The experiment eventually counted 2 accelerometers of that first type and 18 of second type '$4513-002$', amounting to a total of 20 accelerometers.

Sensitivity drift for frequencies below 5 kHz is supposed negligible, averaging 2 % in amplitude and being inferior to a 10° phase (see figure 3.18 taken from a '$4513-002$' calibration chart). Each accelerometer presents a plane surface supporting the receiver reference and a screw thread on the opposite face; cable connector are located on the side. Transducer

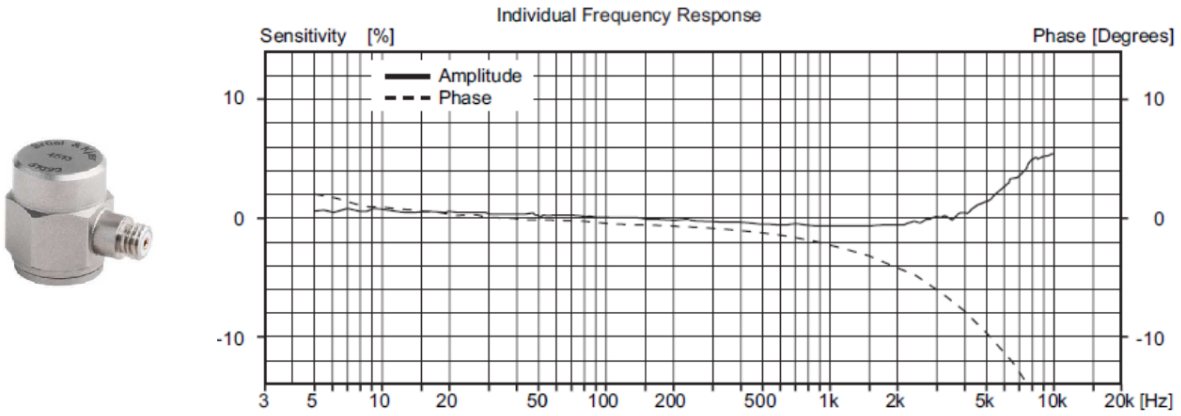

Figure 3.18: Brüel & Kjær IEPE accelerometers of type '4513' and associated spectral sensitivity (extracted from a Brüel & Kjær characterisation document).

dimensions are a 12.7 mm diameter and a 15.65 mm length.

These accelerometers give oriented response: when submitted to a compression, first lobe of the recorded signal will be negative if the plane surface (upper surface from accelerometer in figure 3.18) is presented to the source, positive otherwise. Transducer responses of either polarity are to be seen in figure 3.19. With this same figure, we ran a series of test regarding the location of the sensing surface within the receiver of non-negligible length: upper part of this figure represents schematically various sensor positions, for which the plane surface is identified as a black line. On the one hand, if transducers are in opposed direction while their plane surface or their screw thread coincide respectively, amplitudes and arrival time will differ. On the other hand if the position of both transducer coincide, only they are opposed, arrival times and amplitudes will grossly match and will be comparable to the control test. Explanation is as follows: as P-wave propagation velocity in steel amounts to 6000 m/s, the signal would need approximately 3 μs to propagate from one extremity of the receiver to the other. This duration is inferior to the shortest achievable sampling time on our measuring device. Hence, the closest surface to the source should be considered as the rightful offset. As seismic acceleration is conventionally taken to be negative for a compression, we chose to place the accelerometers such as to orient the plane surface toward the source.

Electrode array

In our attempt to compare seismic data to their corresponding coseismic electric, special attention was given to spacial precision of respective measurements. This concern, already reflected by our questioning regarding accelerometer positioning, utterly steered the conception of a suitable electrode array, designed to improve precision on electrical measurement localisation.

The electrode array was home-made using 30 stainless steel rods of equal length as electrodes. We used terminal blocks to stabilize the inter-trace of our electrode array to 0.9 cm. In order to keep the rigidifying terminal blocks away from the measurement plane, as to prevent them from acting as a waveguide, chosen rods were of 50 cm length. Each rod was

then covered with a heat shrink tube on its whole length except for 5 mm at each of its ends, one end being the measuring tip, the other allowing for the electric potential to be transmitted to the acquisition device. The ending of the cable sleeve was finally sealed to the rod by some varnish at the measuring end to prevent water from intruding beneath the sleeve and change the actual measuring length. All these preparation stages are resumed in figure 3.20. Rods were then assembled on rigidifying blocks as presented in figure 3.21. We consequently made sure that both ends of each electrode were properly connected while the integrity of the insulation along the rods was controlled, as to prevent the electric signal to come from anywhere but the measuring plane (no secondary current entry through damaged cable sleeve).

Control measurement showed that the acquisition unit would reject the DC component of the electric field (due to the already mentioned high-pass filter cutting below 10 Hz). As another observation, when measuring a potential V_A relatively to the ground V_{com} we record the potential difference Δ_A, as:

$$\Delta_A = V_{com} - V_A \tag{3.2}$$

Hence, if we consider the convention according to which, voltage U_{AB} oriented, as in figure 3.22, from point A to B is given by:

$$U_{AB} = V_B - V_A \tag{3.3}$$

then, with point C being the common reference V_{com}, knowing voltages Δ_A and Δ_B measured relatively to this point, we would reconstruct U_{AB} as follows:

$$\begin{aligned} U_{AB} &= U_{AC} - U_{BC} && (3.4)\\ U_{AB} &= (V_{com} - V_A) - (V_{com} - V_B) && (3.5)\\ U_{AB} &= \Delta_A - \Delta_B && (3.6) \end{aligned}$$

so that, due to our connection system, we finally end up having:

$$V_B - V_A = \Delta_A - \Delta_B \tag{3.7}$$

As for issues regarding suitable dipole reconstruction and spacial localisation of the measured electric dipole, in the prospect of quantitatively measuring the coseismic electric field $\mathbf{E}$, they will be extensively treated in section 4.5.1 of following chapter. Yet we can already mention a series of choice which were made in order to enable adjustable measuring of electric potential difference. First, we decided to record each potential difference relatively to the last electrode of the array taken as a common reference; this procedure validated by Bordes [2005], would ultimately facilitate the reconstruction of dipoles of any given length. Second, we took as small an electrode intertrace as we could manage in order to allow for very small dipoles, the smallest dipole being here of 9 mm. Finally, the relative position of accelerometers and electrode was anticipated as to match the offset of each accelerometer

either with the center or with the tip of an electric dipole.

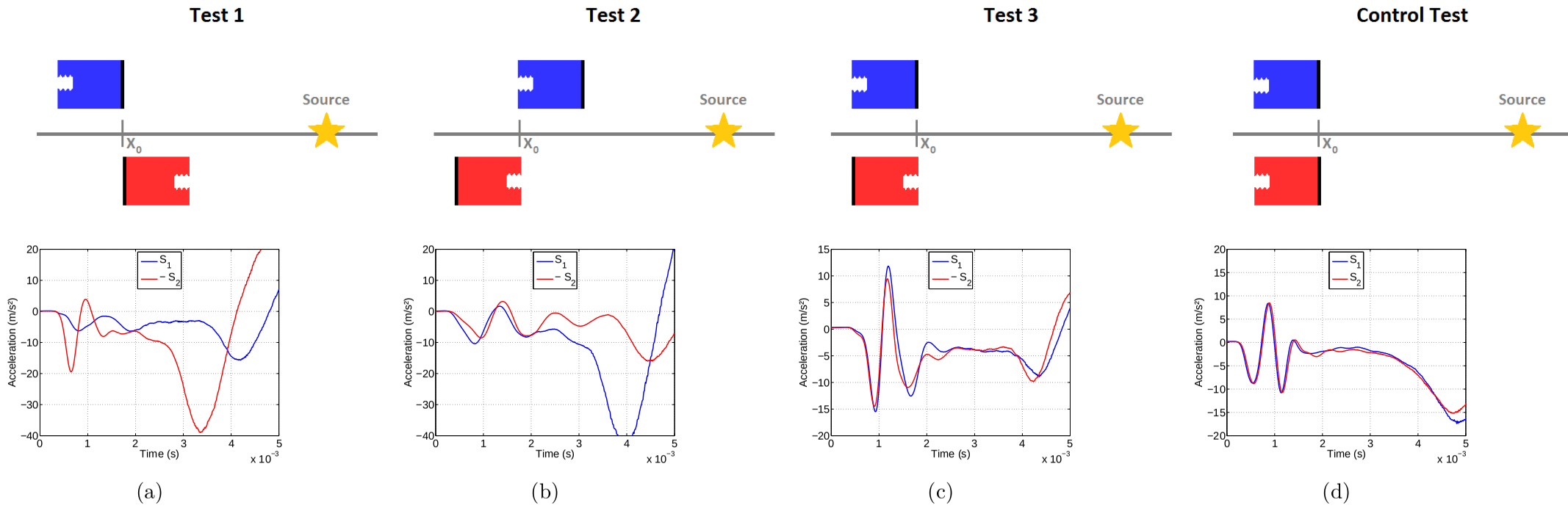

Figure 3.19: Calibration of the Brüel & Kjær accelerometer orientation. Accelerometer color matches that that of the corresponding record. The reference bearing surface of the transducer is identified in black: when surfaces are in opposition, as in (a) or (b) or (c), signals are of opposed polarity. Delays in the accelerometer response however does not depend on the relative position of the identified black surface, but rather on the position of the whole captor relatively to the source. Hence, results of test 3 and the control test, though opposed in polarity are comparable in amplitude: in sand there is no evidence of identified sensing surface, offset of the accelerometer is given by its closest point to the source, polarity by its orientation.

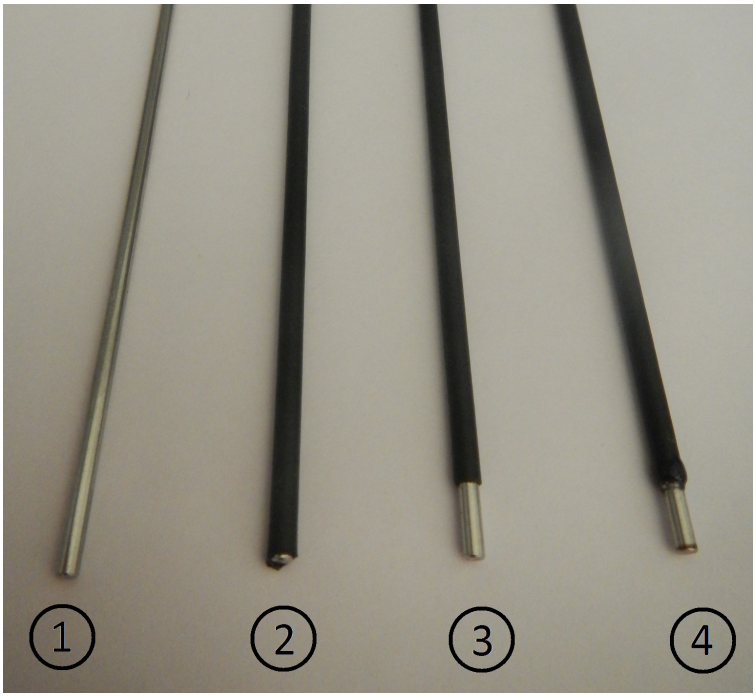

Figure 3.20: Successive stages for the preparation of a single electrode: 1) the bare rod. 2) covering with a heat shrink tube. 3) freeing the 5 *mm* tip. 4) sealing the end of the cable sleeve to the rod using varnish.

Description of captors positioning

As exposed in section 3.1.1, all captors were to be placed within 30 *cm* to the source, the coseismic seismoelectric signal having been witnessed to faint very quickly with increasing offsets within our medium.

Transducer length being of 15.65 *mm*, we decided to space our accelerometers by 36 *mm*. Combining our wanted captor density of 20 receivers (to be located within 30 *cm* to the source), to the minimum spacing of 36 *mm*, we had to place the accelerometers on two parallel lines. A central space of 2 *cm* width, aligned with the source, was left free to host the electrode array. Accelerometers were implanted on either side of this central line with a lateral offset of 1 *cm* (see figure 3.4). For precise positioning, the transducer were planted within the sand by being screwed to plastic shaft of approximate length 5 *cm*.

The electrode array of 30 electrodes and 27 *cm* length, created for that limited offset range, was placed on the central line between offsets of 3 *cm* and 30 *cm*. The relative position of accelerometers and electrode was anticipated as to match the offset of each accelerometer either with the center or with the tip of an electric dipole, by necessarily putting the accelerometer top in regard to an electrode (see figure 3.1b). Assistance was required to maintain the electrode array in position whilst pouring sand to complete the sandbox filling.

Within the sandbox, we also counted 7 water sensors disposed as to surround the measurement line: as we already mentioned, 2 captors were arranged vertically at the middle of the horizontal planes located 10 *cm* beneath and 10 *cm* above the measuring plane (figure 3.1a) while 5 further captors were disposed within the measuring plane at a distance of approximately 10 *cm* from the measuring line, as indicated in figure 3.1b.

The seismoelectric instrumentation of the sandbox eventually implicated a total of 7 moisture sensors connected to an auxiliary recording device, as well as 21 accelerometers

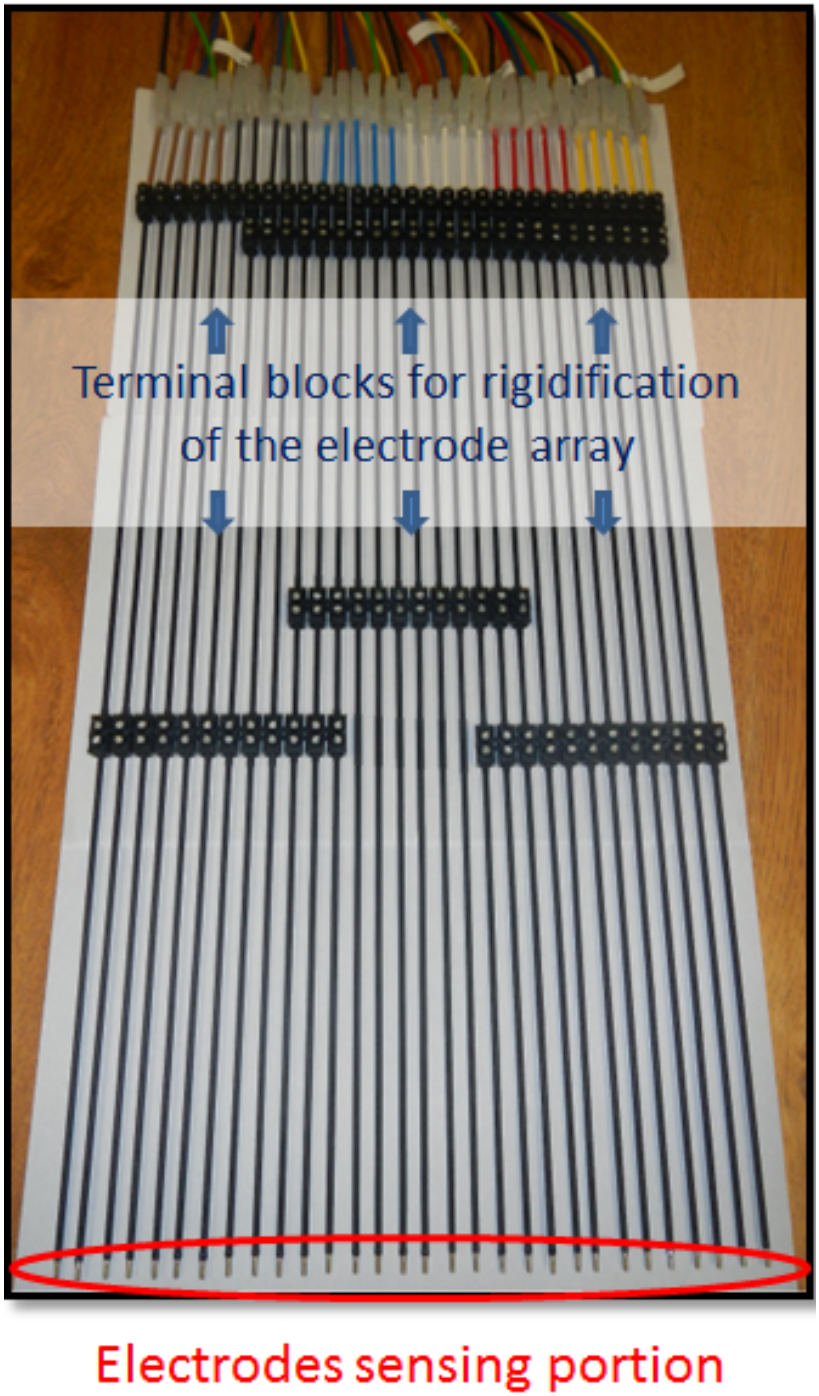

Figure 3.21: Custom build electrode array composed from 30 steel rods of length 50 cm, spaced by 0.9 cm. The sensing portion is limited to the 5 mm portion identified by a red mark at one end of the rods. Rigidity of the device and consistency of the inter-trace is achieved by the use of electric terminal blocks.

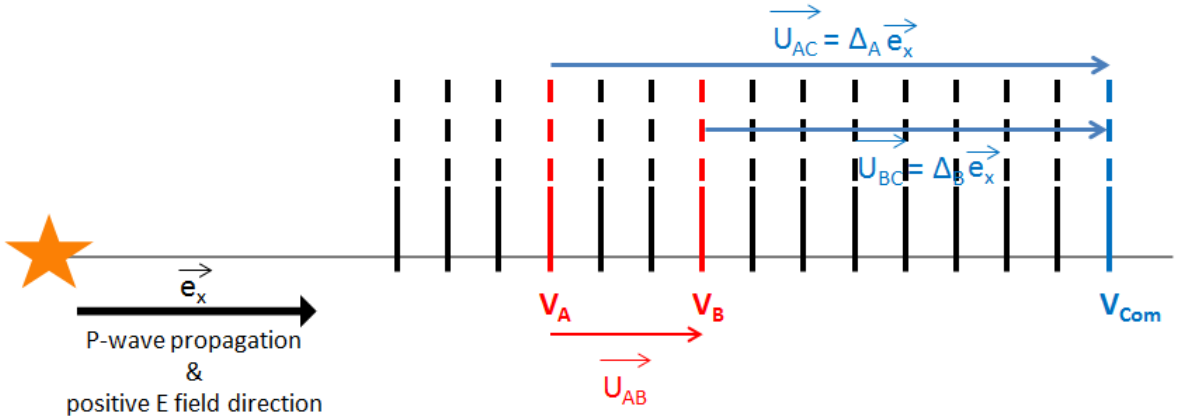

Figure 3.22: Explanation of the sign convention when reconstructing an electric dipole from original voltage measurements relatively to the common reference.

and 29 electric dipoles controlled by the dynamic signal acquisition module. As we could not record all these channels at once, acquisition were split according to two distinct configurations A and B. Section 3.4.2 will present what choice were made to distribute the captors into those two configurations, before showing how to reconstruct a complete data set from partial recordings A and B. An alternate acquisition-configuration concentrated on the 12 accelerometers and the 18 dipoles closest to the source for a maximal offset of 19 cm (the common reference electrode being still located at 30 cm). This more ergonomic 'near-offset configuration' was primarily used for rapidity preliminary observations. Saturation information was recorded on an auxiliary device.

3.2.3 The acquisition chain

The acquisition chain is composed of a dynamic signal acquisition device PXI-4498 from National Instruments having 16 simultaneous 24-bit analog inputs per module (acquisition capacity of 204 $kbit/s$). Our acquisition device was equipped with two modules: the first module being divided into 13 channels dedicated to seismic while the last 3 channels and the totality of the second module were meant for electric acquisitions.

The whole system is triggered by a Labview program, commanding both the source and the acquisition start. Seismic and electric channels are clearly identified within the Labview interface. For the data of first category the calibration may be entered in $V.s^2.m^{-1}$ or $V/|\vec{g}|$ the entry range being automatically chosen at 10 V, while electric acquisitions will be given adapted resolution by choosing the relevant scale between 10 V to 316 mV. In the case of seismoelectric measurements this last value is generally chosen.

The acquisition chain is completed by an home-made pre-amplifier of input impedance 1 $G\Omega$ and gain 1. This pre-amplifier was meant to adapt input impedance for reliable electric potential measurements; it applies a high-pass filter cutting at 10 Hz to the recordings. The voltage sign of the acquired dipole will be the subject of a discussion in section 3.2.2.

3.3 Proceedings of the variable parameter experiments

In preparation of the continuous set of experiments presented here, the medium had to be put in place. After having placed a canvas sheet, to prevent water from lately pouring from the sandbox, sand was cautiously sieved in. To prevent the wells from being in direct contact with the plastic canvas and improve water circulation, wells were actually placed after having sieved a 5 cm sand-layer into the sandbox. Sand sieving would then resume until reaching the source marker located at 25 cm height (representing an introduced sand volume of approximately 75 l). At that point we placed the captors within the measurement plane before sealing the experiment by sieving about the same amount of sand than previously used, up to a height of 50 cm. Finally, we placed pieces of acoustic foam overloaded by buckets full of sand at the top. Aim was on the one hand to avoid creation of an sand-air reflecting boundary, on the other to prevent the light acoustic foam from floating around after water imbibition.

3.3.1 1^{st} Protocol: Measurements under variation of fluid conductivity σ_f

The experiment started on dry sand. Series of acquisitions were run in order, first, to define seismic characteristics of the dry medium, second, to prove the absence of EM noise and state the electrokinetic nature of the seismoelectric phenomenon from absence of coherent signal in electric records. Following a rapid imbibition phase, we then equilibrated the fluid conductivity with the medium by continuous circulation of originally demineralized water for a couple of hours.

First measurement row was conducted within the day of primary imbibition, having stabilized the fluid conductivity at 1.7 mS/m. This conductivity strictly arose from solubilizing elements of the medium. We then diluted the electrolyte by adding demineralized water before adding small quantities of NaCl salts. Aim of this procedure was to dilute the contribution of unknown solubilized species and obtain an electrolyte which conductivity was overwhelmingly owed to identified Na^+ and Cl^- ions. Within the week following initial imbibition, this operation was renewed many times as to equilibrate the saturating fluid at conductivities ranging from 2.5 mS/m to 10 mS/m. A precise recap of the full experimental round is to be found in the appendices 7.1.1.

Before beginning any acquisition the saturating fluid was made to circulate; conductivity was tested until it equilibrated within the four injection wells and matched that of the free water at the top. For a given conductivity the measuring procedure usually combined the acquisition of 25 shots in configuration A and B, as well as 25 shots in 'near-offset configuration'. According to the offset of interest, a total of 25 to 50 stacks could be reached. Towards the end of the conductivity experiment, a rather elevated fluid conductivity restricted our electric observation within the first 15 cm: the 'near-offset configuration' was accordingly chosen and maintained through the rest of the experiment. In the absence of full saturation, a 100 kHz sampling rate would suitably keep track of the P-wave propagation.

Pressure conditions within the sandbox were not monitored. Yet we may estimate the

differential pressure at the measurement plane on basis of water column estimation. Indeed, during the experiment, the measurement plane was overloaded by about 27 ± 2 cm of unconsolidated sand of porosity $\phi = 0.4$ and a 34 ± 1 cm water column (for both saturated and sub-saturated data). Knowing the equivalence 1 $cmH_2O = 1$ $mbar$ for fluid pressure, we might similarly deduce that 1 cm of sand should produce a confining pressure of 1.6 $mbar$. As a consequence, the differential pressure at the measurement line should be of approximately 10 $mbar$.

3.3.2 2^{nd} Protocol: Measurements under variation of water saturation degree S_w

Saturation monitoring during drainage

After a long resting time of several weeks, repeated tests on the evolution of P-wave propagation velocity finally revealed the saturation completion of the medium. As we reached a P-wave velocity superior to 1500 m/s, the monitored seismoelectric drainage experiment was launched. For this experiment we abandoned connection switching and adopted the 'near-offset configuration' (see section 3.2.2). We focused on a stable pool of 31 receivers (including one accelerometer at the source) regrouping the 12 accelerometers and the 18 dipoles closest to the source, having selected the receivers still-responding after being immersed over one month. In this captor configuration, the electric measurements were still acquired relatively to the common reference electrode located at offset 30 cm, while other electrodes were regrouped between $3 - 19$ cm offsets. The considered seismic receivers were located on a 20 cm line starting at an offset of about 5 cm.

The first step was to lower the fluid conductivity of the medium electrolyte to allow for exploitable electric data. The electrolyte was tediously re-equilibrated at a rather high value of 7.2 mS/m. To do so, we extracted the pore fluid while avoiding desaturating the medium, diluted it to an inferior conductivity value by pouring in demineralised water, before putting in some $NaCl$ to ensure that the new conductivity of the electrolyte was foremost due to this identified salt specie. We then re-injected an electrolyte of conductivity 70 mS/m and repeated the process until the extracted water was of satisfyingly low conductivity and matched that of the electrolyte at the sand top and within the four wells.

To improve the observation of wave propagation, the sampling rate was increased to 200 kHz. Yet, the corresponding time resolution was almost insufficient for acquiring data at full saturation. Indeed, due to high propagation velocity, arrival times at consecutive seismic offsets spaced by 1 cm would often differ by a single time sample.

Before starting the drainage process, over hundred shots were recorded on the fully saturated medium. As presented in figure 3.23, here for a seismic receiver at offset 4.8 cm, full-saturation data would present a very high-frequency content relatively to the seismic waveforms commonly encountered in partial saturation (see later figure 3.24a). After completion of the data set acquisition at full saturation ($'F - 20140408'$), we activated the water-pump and started monitoring the water saturation while recording seismic and seis-

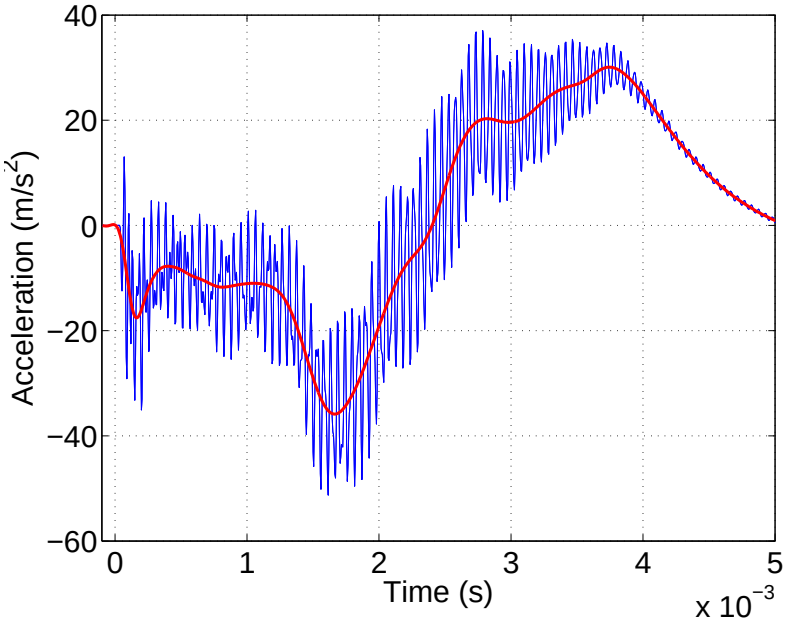

Figure 3.23: Seismic record obtained on water filled sand at offset 4.8 cm, under its raw form showing a strong 19 kHz component (blue) and after being applied a low-pass Butterworth filter (red).

moelectric data as packets of five consecutive shots, giving the possibility to get at least a stack 5 for each recorded data.

Drainage method kept evolving throughout the monitoring. The initiation was rather tedious, as we pumped into the four wells alternately before pausing for the wells to equilibrate with the medium and replenish. Measurements were made every 15 min during approximately 8 hours: despite some observable variations of the seismic waveform, water saturation within the measurement plane remained almost complete with $S_w > 0.95$. At this point, our pumping method started having trouble recovering water from the injection wells. The pumping system was then adapted as to pump simultaneously within the four wells, while a vacuum pump was added to the system to help initiating the water-pump. This system proved very efficient, but was sadly put in place at a very critical moment: within minutes the saturation at the measuring plane dropped from 0.95 to 0.6. After that the monitoring was continuous during 3 hours and required a measurement about every minute. After that duration, final saturation degree was estimated at approximately 0.3; we concluded to a residual saturation degree of $0.25 - 0.3$.

As a conclusion, our 11-hours drainage experiment provided us with about 150 experimental points (each with stack 5), 60 of them obtained for saturation degrees comprised between 1 and 0.95, 80 more acquired for saturations between 0.6 and 0.3. The $[0.95 - 0.6]$ saturation range is unfortunately under-represented.

Saturation monitoring during imbibition

After documenting a drainage cycle, choice was made to monitor an imbibition phase. Yet in an effort to restore full saturation, as to swiftly reproduce the drainage phase starting from $S_w = 1$ while sparing a month waiting, the medium was re-imbibed massively right after

completion of the drainage experiment. This failed attempt caused our monitored imbibition cycle to be discontinuous from the aforementioned drainage experiment, separated by a unrecorded imbibition-drainage complete cycle. As a notable consequence, a discontinuity in residual saturation degree was observed between both monitored cycles, residual saturation having reached 0.23 during the second unrecorded drainage.

We respected the same stable captor configuration as the one described for drainage acquisition. Water re-introduction was made stepwise at a stable conductivity of 5.5 mS/m. We hence intended to compensate the conductivity increase of the trapped water to reach a final fluid conductivity of $6.5 - 7$ mS/m comparable to the one imposed to the medium previously to the drainage monitoring. Quantities of 0.33 l were introduced at once through 1, 2 or all injection wells (for a total increase of water of 0.33 l to 1.32 l between two measurements). Injection wells were alternately selected as to favour the creation of a horizontal planar imbibition front. Between an injection and the corresponding measurement, a waiting time of $15 - 30$ min was observed to allow for fluid/medium equilibration. A typical measurement sequence begun with five consecutive saturation measurements, followed by the seismoelectric recording of a five shots series, concluded by renewing the five saturation measurements.

Within 8 hours, 20 measurements and the injection of 15 l water, saturation within the measuring plane was of approximately 0.8. Three days later, for a total water injection of 30 l, the water front came up to the surface. At this stage the re-imbibing process provided us with 40 measurement points and a saturation degree of approximately 0.88 within the instrumented plane.

The following phase consisted in a slow process of saturation increase by water circulation and stagnation hopefully chasing the trapped air. Despite regular water circulation, an evolution check of the saturation over 6 weeks showed that it would not go past 0.92. Since achieving full saturation seemed out of reach, the experiment was eventually terminated.

3.4 Pre-processing

3.4.1 Reproducibility and stacking

Satisfactory reproducibility of the source should lead to a similarly satisfying reproducibility of the data. In this section we will verify this assumption, before discussing the contribution of stacking to measurements optimisation.

Figure 3.24 superposes a collection of data associated to 25 single shots, relatively to an average of this 25 data into a light blue curve at stack 25. While the good reproducibility of seismic acquisitions throughout the record matches that of the pneumatic source, questioning the utility of such processing, the stacking operation tends to smooth out the otherwise very noisy electric records. The same effect may be appreciated for a stack 50 in figure 3.25, where seismic and electric receivers positioned within the first 19 cm offsets have been reported. For readability's sakes, some of the receivers at approximate offsets of 3 cm, 11 cm and 18 cm have been identified in blue, green and red colors. While the seismic remains

mostly unchanged, stacking enabled the suppression on electric data of the 550 Hz EM-noise inherent to the acquisition chain (yet not connected to the source triggering).

When analysing the effect of stacking in terms of spectral amplitude evolution, the advantage of stacking, so clear on electric time records, is hardly observable on electric spectra (see 3.26b). The sole appreciable effect would be the disappearance from stacked records of the amplitude peak at $[500 - 600\ Hz]$, corresponding to previously mentioned EM noise, that may otherwise be observed at larger offsets on single shots. Besides a global lowering of the noise level within the higher frequency band, the effect on seismic spectra is as little noticeable (see 3.26a).

Spectra observation being not fully conclusive, we considered the evolution of the signal to noise ratio. To do so, an average noise value was given to each channel, based on spectral values on the frequency range $[15-50\ kHz]$ where no signal is expected. We then represented the ratio of the spectrum to the average noise level. For seismic, the evolution in signal to noise ratio is clear, it increases with increasing stack and is all the more important than the receiver is furthest from the source. The relative increase is due to the lowering of the global noise level, yet the limit $S/N \geq 10$ is pushed by 1 kHz to 2 kHz towards higher frequency when a stack 50 is taken instead of a single shot (see figures 3.26c and 3.26e). The effect on electric appears grossly similar, especially in the lower frequency domain, yet the evolution is not as monotonous as for seismic. In particular, at offsets superior to 15 cm the S/N ratio does not support frequency investigation in the kilohertz range (see 3.26d), while for smaller offsets the same ratio would allow for extending the investigation domain by 1.5 kHz thanks to stacking (see 3.26f).

As a conclusion, the reproducibility of the seismic data supports the stacking. The gain on seismic through stacks is overwhelmingly due to an automatic decrease of the background noise level with increasing data quantity. A stack of 25 to 50 shots may differ the entering of the noise level domain by 1 kHz to 2 kHz.

For electric records, the most profiting effect of stacking is the reduction of the acquisition-bound 550 Hz EM-noise. Yet this is achieved with a reasonably low number of 25 shots. The exploitable frequency domain may be extended by about 1 kHz. However for offsets larger than 15 cm, signal above noise level appears to lay below the kilohertz.

3.4.2 Partitioning of data acquisition and reconstruction of a whole data-set

As we instrumented the sandbox, we equipped it with a total of 50 captors including 20 accelerometers within the box plus one at the source and 30 electrodes forming 29 dipoles. Yet the acquisition system can only record 31 channels at a time: we consequently had to split the acquisition according to two distinct configurations A and B. Among the 31 channel available, 13 are dedicated to seismic acquisition and 19 are calibrated for electric recordings; the acquisition of seismic and electric had therefore to be run concomitantly.

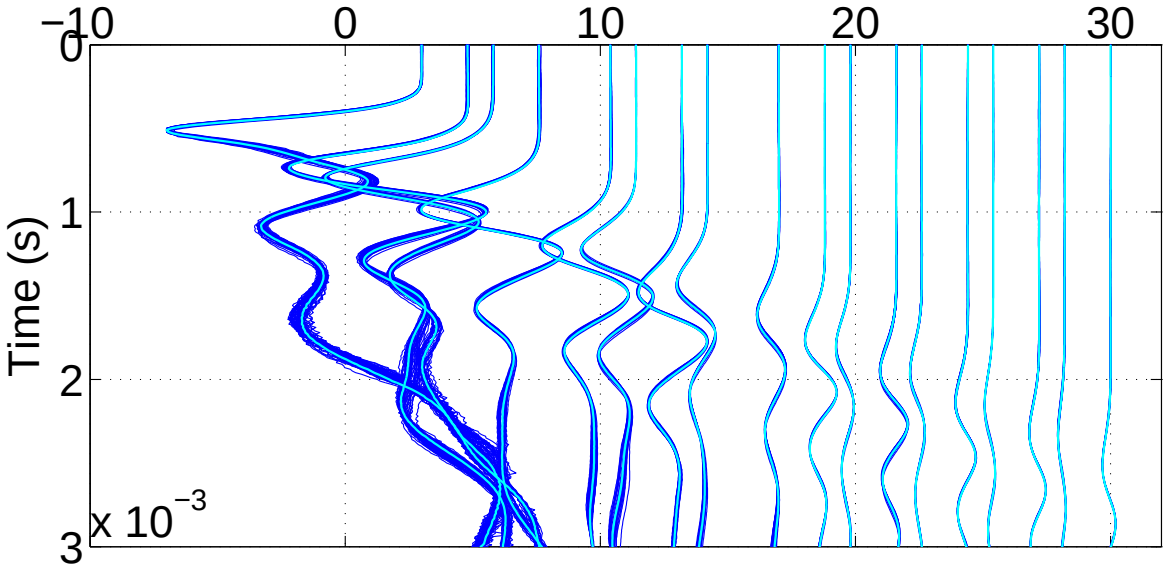

(a) Seismic

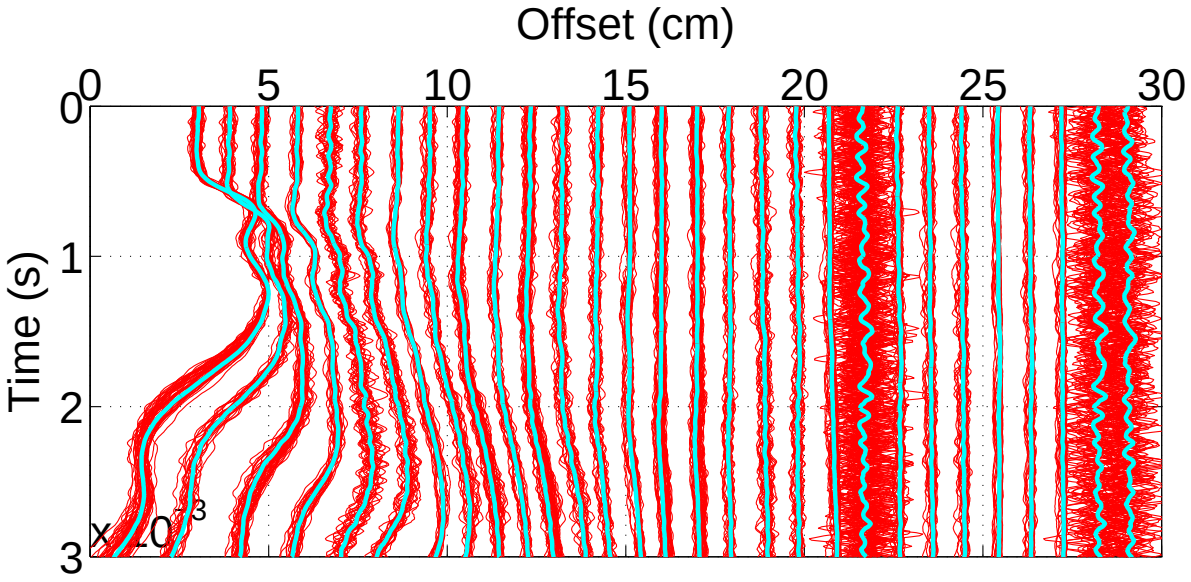

(b) Electric

Figure 3.24: Superposition of 25 single shots for seismic receivers (a) and electric dipoles acquired relatively to the common reference (b) from experiment ′20140305′. Result of the stacking of the 25 shots is given by the curves in light blue.

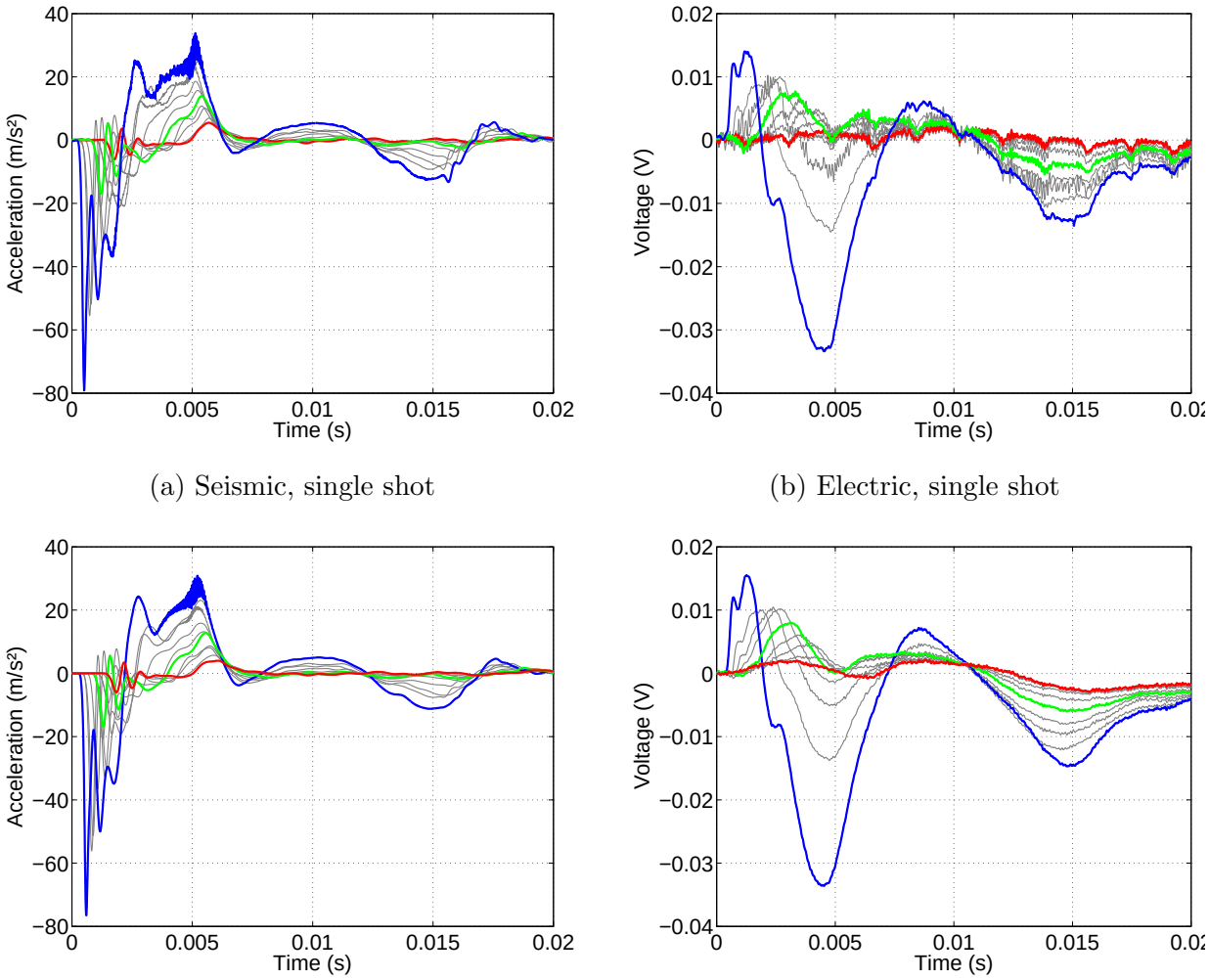

(a) Seismic, single shot

(b) Electric, single shot

(c) Seismic, stack of 50 shots

(d) Electric, stack of 50 shots

Figure 3.25: Available seismic and electric data at offsets inferior to 19 *cm* (one dipole selected every 2 *cm* approximately). Seismic (a) and electric (b) are obtained on a single shot; seismic (c) and electric (d) are the result of a stack 50. Data were taken from the ′20140305′ data set.

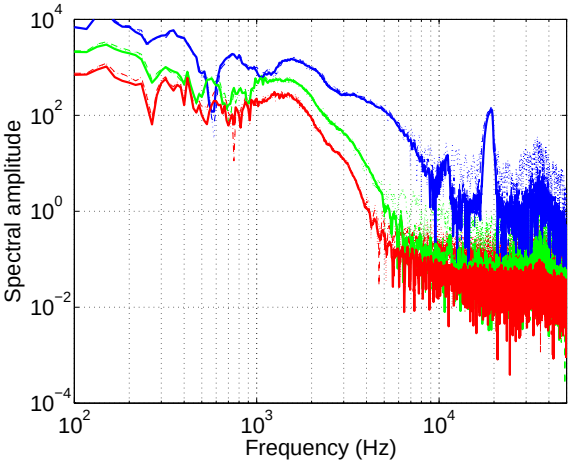

(a) Seismic

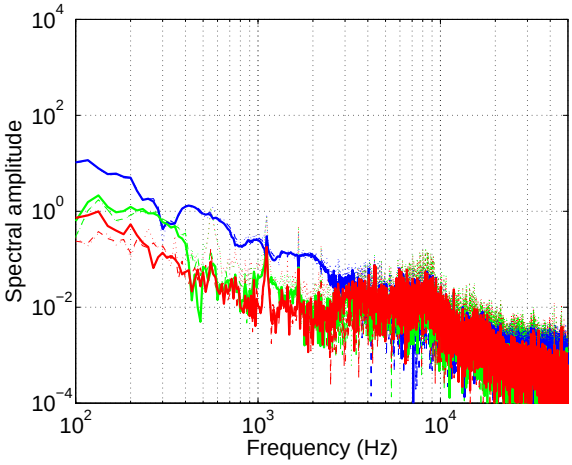

(b) Electric

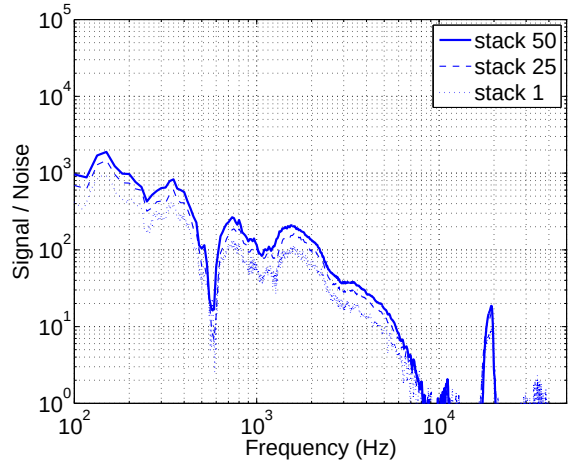

(c) Seismic at offset 3 *cm*

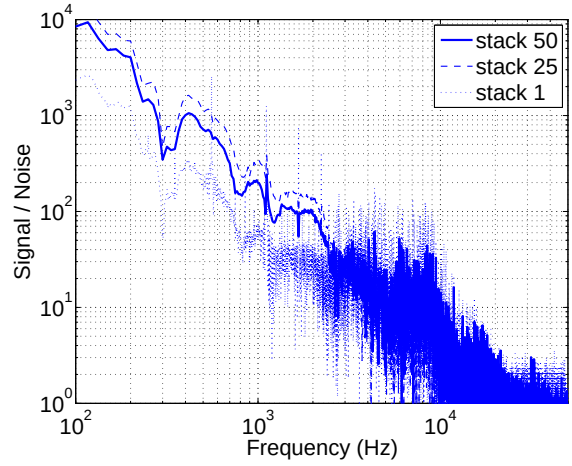

(d) Electric, 1^{st} electrode at offset 3 *cm*

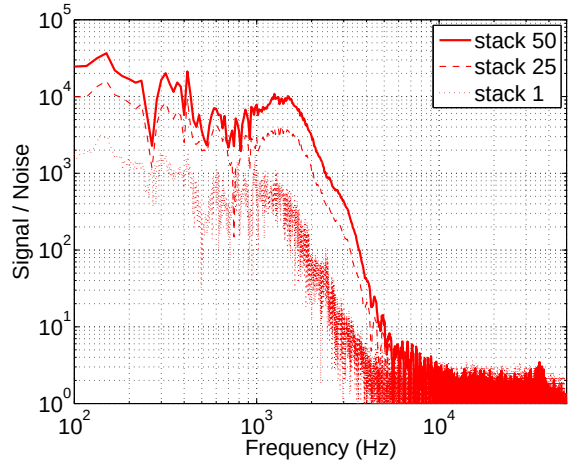

(e) Seismic at offset 18.8 *cm*

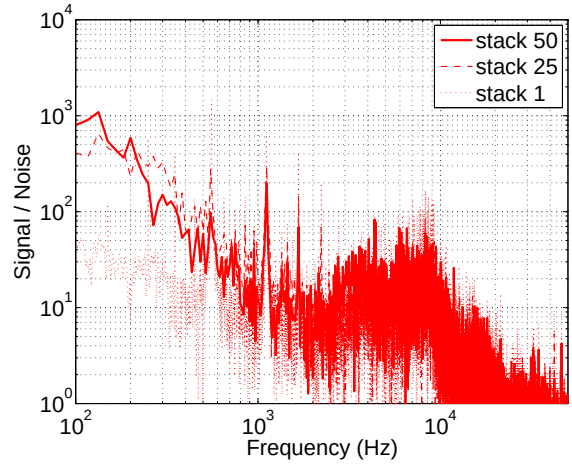

(f) Electric, 1^{st} electrode at offset 17.9 *cm*

Figure 3.26: Impact of stacking on spectra (a, b) and signal to noise ratio (c, d, e, f) of selected seismic and electric channels. Blue, green and red colors represent respectively channels at 3 *cm*, 11.4 *cm* and 18.8 *cm* for seismic (a) vs. 3 *cm*, 10.4 *cm* and 17.9 *cm* for electric(b). Dotted, dashed and thick plain lines stand respectively for a single shot, a stack 25 and a stack 50.

As the most logical division, we chose to attach each configuration to one line of 10 accelerometers, we added the source accelerometer and chose two further receivers at the front and the middle of the second accelerometer line. We ended having a total of 13 accelerometers, 5 of which were systematically shared by both A and B configurations, in order to check whether comparable accelerations at shared accelerometers supported the reconstruction of the full data set.

We proceeded similarly to attribute the 19 respective electric channels of configuration A and B. For a considered configuration with its corresponding seismic receivers, any dipoles sharing first electrode offsets with one of the seismic would be automatically taken in, the 6 to 7 remaining electric channels were allocated between both configurations as to permit full record recovery when being combined.

We finally covered the full seismic and electric receiver array thanks to two distinct configurations having 5 seismic and 7 electric recordings in common, in order to test the reconstruction legitimacy. This reconstruction process is exposed by figure 3.27, showing the different acquisition geometries while pointing out the redundant channels, and figure 3.28 illustrating the reconstruction in itself. In this last figure the overlapping of redundant channels, the seismic as well as for the electric, supports the reconstruction legitimacy.

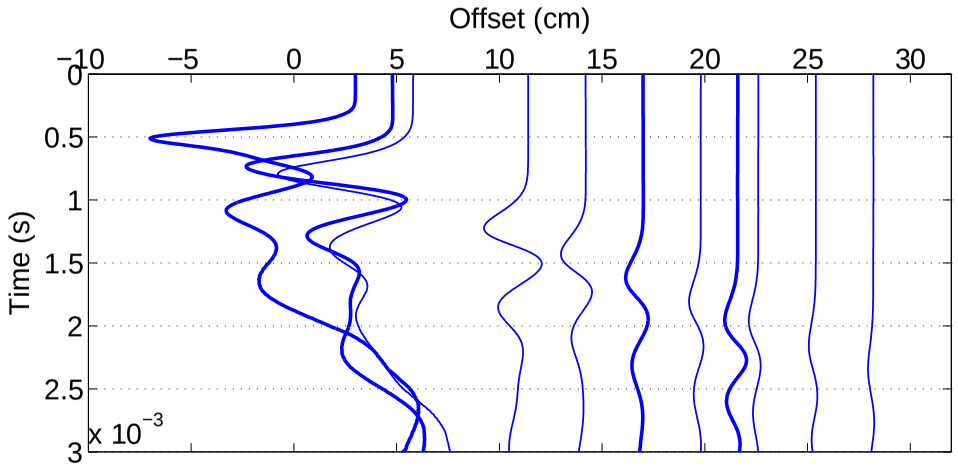

(a) Seismic in configuration A

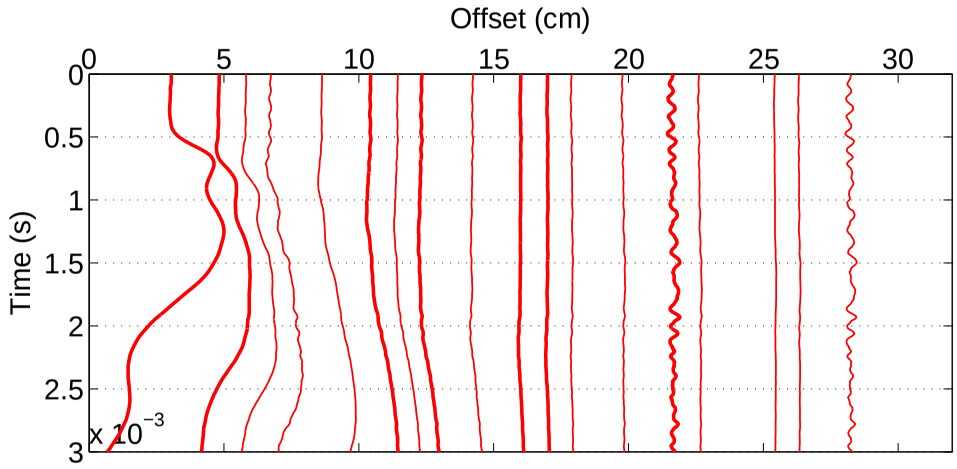

(b) Electric in configuration A

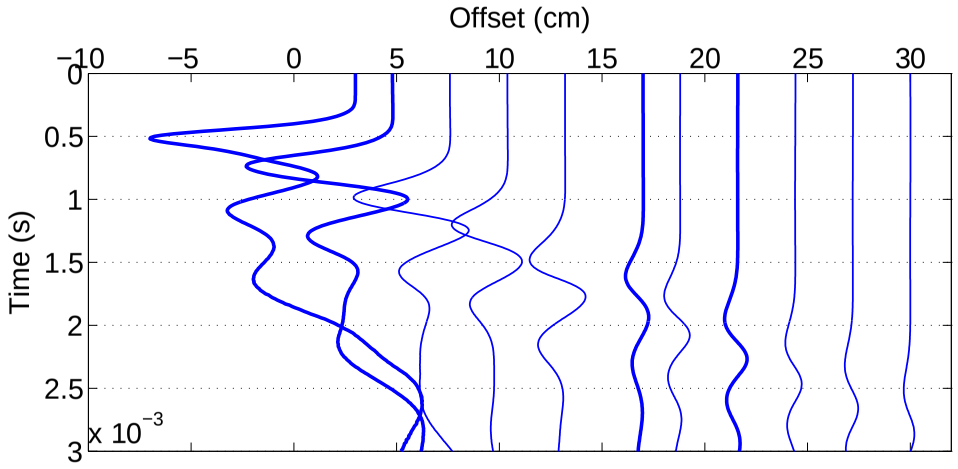

(c) Seismic in configuration B

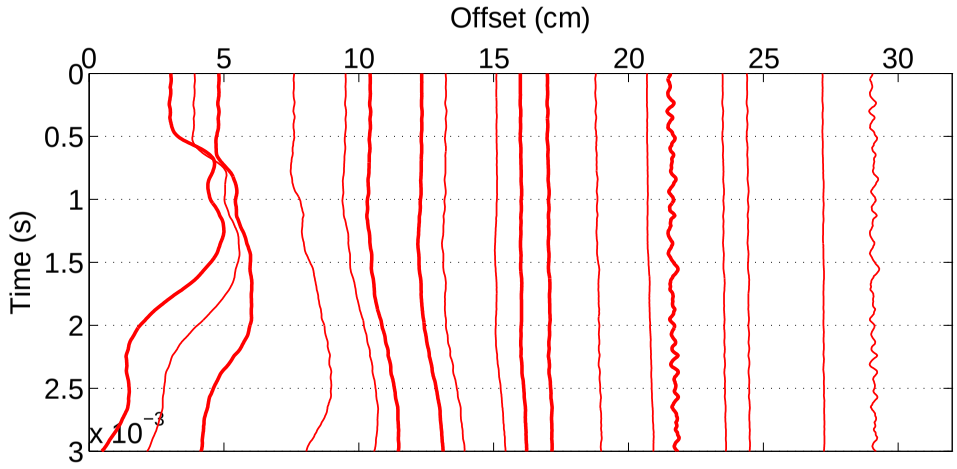

(d) Electric in configuration B

Figure 3.27: Raw seismic and electric data obtained after 25 stack for both A and B acquisition configurations. Channels in bold lines are shared by both configurations. Data were taken from the '20140305' data set.

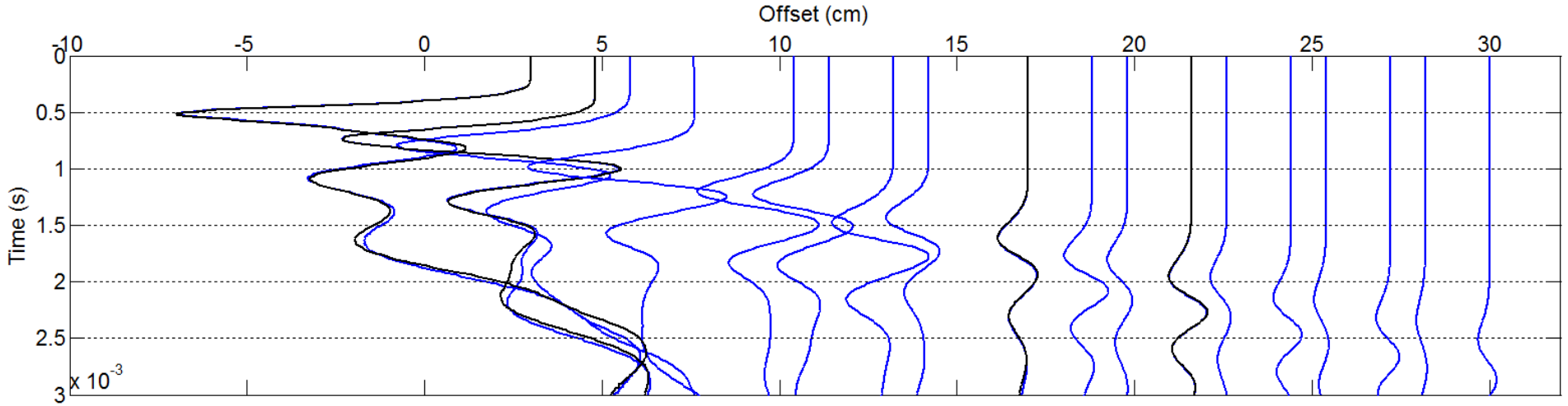

(a) Full seismic record

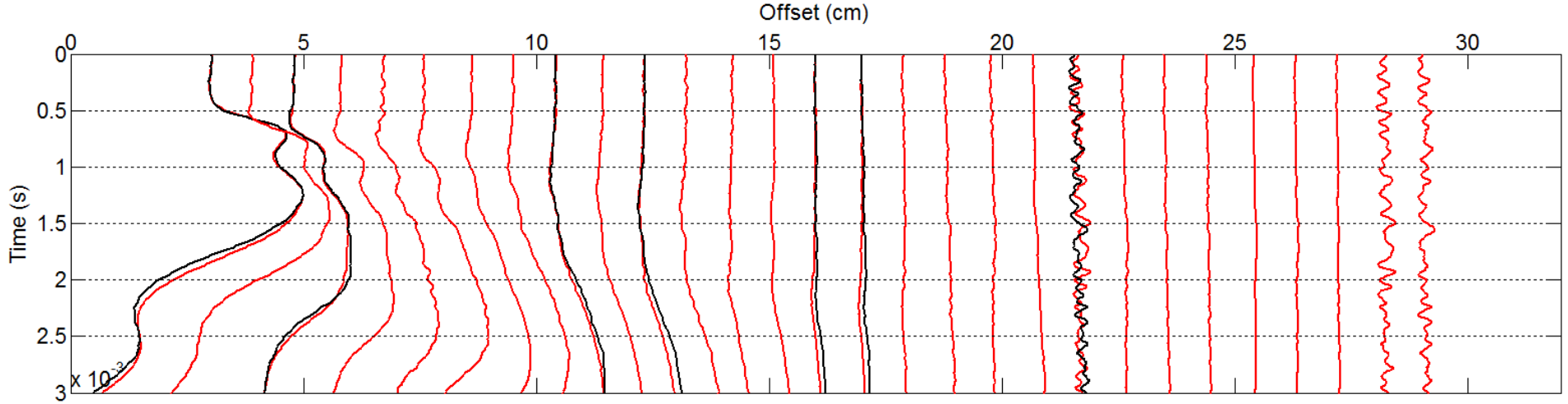

(b) Full electric record

Figure 3.28: Reconstruction of a full data set from seismic and electric data in configuration A and B. The redundant channels of configuration B, checking the legitimacy of the data reconstruction, are represented as thick black lines.

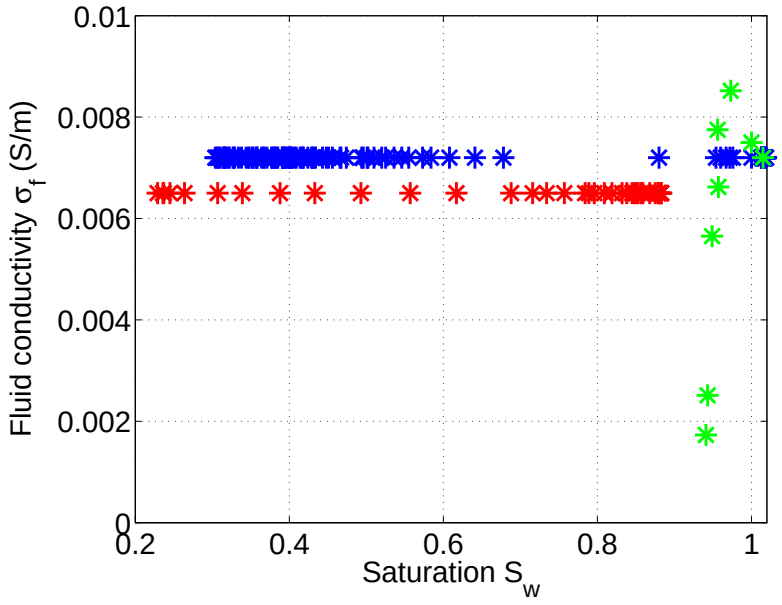

Figure 3.29: Summary of all experiments realized under variable fluid conductivity and saturation. Three distinct experimental rounds are gathered: primo-imbibition data in green, drainage data in blue and re-imbibition data in red.

3.5 Conclusions

This experimental set-up was specifically designed to facilitate the observation of the direct P-wave and its associated coseismic electric wave, under high density of precisely positioned accelerometers and electrodes. For EM-noise reduction, the source was chosen to be pneumatic. As the impulsive shots guarantee large spectral bandwidth, they will also demand tedious signal selection (as will be seen in section 4.1) for spectral recovering of the coseismic seismoelectric information

Seismic and electric fields were synchronously recorded. Experimental conditions separately varied fluid conductivity spreading from 1.5 mS/m to 10 mS/m and water saturations ranging from 0 to 1 (see figure 3.29). By stacking, electric records would get cleared from acquisition EM-noise of 550 H, while background noise on already neat seismic records would be mechanically lowered. The frequency domain of investigation, centered on the kilohertz, would eventually extend to cover a $[0.5 - 5\ kHz]$ maximal range.

F

Chapitre 4

Towards a quantitative analysis of seismic and seismoelectric observations

Sommaire

The experimental set-up presented in previous chapter was especially designed to facilitate the recording of direct waves and prevent the apparition of secondary sources. But all these precautions are no guarantee for full integrity of the first arrival, closely followed by further wave packets. The scope of this study being the characterisation of coseismic seismoelectric phenomenon specifically identified in relation to the direct P-wave, extraction of relevant information becomes critical.

Consequently, one aim of this chapter is to provide us with generic processing tools identifying major wave-attributes (as velocities and amplitudes), on which basis a procedure for first arrival retrieval will be assembled. About this topic we will discuss some windowing function and time-frequency transforms. Once the relevant signal has been isolated, a second stage concerns the spectral valorisation of the retrieved information as velocity dispersion, attenuation and quality factor curves. All suggested procedures will be tested for efficiency on a simple propagating synthetic of known characteristics.

The second purpose of this chapter is to define the best-suited dipole geometry for coseismic seismoelectric observations. The difficulty here is to approach a punctual value of the transitory electric field on basis of potential difference measurements. The elected dipole geometry should provide satisfactory waveform analogy to the mother seismic wave and electric field stability. Investigations will be mostly conducted on real data, as our experiments were designed to allow for a multitude of dipole reconstructions, before being eventually supported by a simple propagating synthetic.

4.1 Selection of the first seismic arrival

As previously defined, the coseismic seismoelectric field we are investigating appears under longitudinal excitation of the porous medium. Resulting from this excitation, a compressive P-wave is generated that constitutes the first arrival in the seismogram. It is correlated to a coseismic first arrival in its associated electrogram. Hence, to achieve a quantitative analysis of the coseismic seismoelectric effect, we will have to extract and compare the information related to first arrivals from both records.

A first approach, which we will refer to as the 'time-domain approach', consists in picking major features of the first arrival within its first lobe. In this view, the major characteristics will be the maximal amplitude, the arrival time of this maximum as well as the associated first break.

A second and more complete approach relies on the spectral analysis of the first arrival. This 'frequency-domain approach' would allow for a dynamic characterization of the electric coseismic dependency on seismic excitation. However it requires to select first arrivals, of possibly varying bandwidth with respect to the receivers offsets, without distorting their spectra.

Within this chapter, both approaches are to be developed and tested on synthetics. Eventually, they will be applied to our seismic and electric data sets in our next chapter.

4.1.1 A time-domain approach

Signal processing, required for the selection and extraction of relevant information out of the experimental records, usually implies to move on to spectral analysis. But before manipulating and altering the data sometime permanently, it seems only natural to take the time-domain acquisition into consideration. Our object of study being the first arrival, we focus on the first lobe to determine its starting time and local extremum. The compressive nature of the P-wave generated by the source appears as a first negative arch on figure 4.1. On this figure, we also displayed the first-break and local-extremum marks for successive seismic receivers. Such information enables us to estimate the propagation velocity of the P-wave V_p as well as a punctual value of the wave attenuation α. This last specific term characterizes the ability of the medium to dissipate the seismic energy as heat while the seismic wave propagates, each wave-type having a specific dissipation-pattern (Winkler and Nur [1979], Toksöz et al. [1979]). This notion will be described further in this chapter.
Direct velocity measurement of P-wave were performed by semi-automatised first-break picking. To achieve this, we had to identify the first local extremum as the peak amplitude of the first arrival. Being A this amplitude located at t_{max}, we then went backwards on the time-vector checking the amplitude against a settled threshold value, most commonly 2% of amplitude A. For the first amplitude below $0.02A$ threshold, the corresponding time t_{1st} was picked as being the first break. This rather empirical method demanded eye-control as this threshold value may need to be adapted for noisy records. If this method does not pretend to perfect picking, we expect the systematical aspect to provide a more robust estimation of first-arrival velocity than hand-picking does. When applied to our synthetic, the velocity estimation for the first arrival laid by $230 \pm 1\ m.s^{-1}$ showing good agreement with the expected $230\ m.s^{-1}$ (see green crosses on figure 4.1 for our synthetic from offset 3 to 13 cm). On this figure we see that the picking of t_{1st} is somewhat overestimated by our procedure: indeed identification quantity $0.02A$ necessarily differs from zero and will be all the more important than maximum A is large. Yet, the error being systematic on all channels, we expect very little impact on velocity estimation. On our synthetic case the error would range by 0.5%.

In the following section, we will explain how we proceeded to associate a nominal frequency to our time-domain-picked data.

Main frequency of the first arrival

In order to associate the punctual attenuation value α obtained by time-domain analysis to a more commonly-used quality factor Q, or even to allow for literature comparison, this attenuation needs to be related to a nominal frequency.

As reported by Bourbié et al. [1986], an amplitude decrement in time records can possibly be attributed to an apparent nominal frequency when considering reasonable attenuation

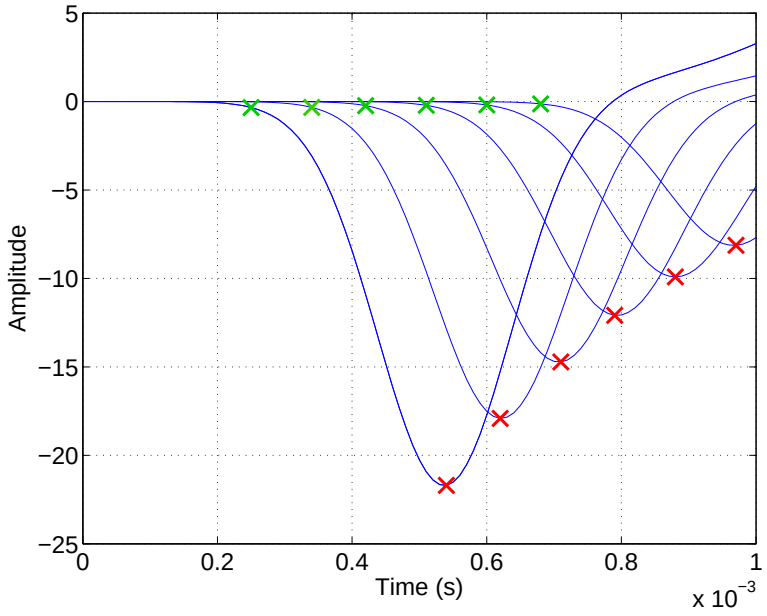

Figure 4.1: Example of first-break (green crosses) and first extremum (red crosses) automatic-picking on a synthetic, constituted by two distinct arrivals, the first propagating at 230 $m.s^{-1}$. Synthetic was calculated at 6 receivers with offsets starting at 3 cm and a 2 cm intertrace. This picking will enable us to calculate the P-wave velocity V_p and estimate the P-wave attenuation α.

level and limited propagation distance. Under such conditions phase velocity equals group velocity in first approximation. Then for a given event, the decrement of the maximal value -or punctual attenuation- stands for the attenuation at the event central frequency, with this central frequency displaying as the overall period of the analysed arrival.

To determine our nominal frequency, we relied on easily identifiable characteristics of the first arrival. Indeed, for each seismic receiver, our time-domain analysis provides us with one first-break and one first-extremum time, respectively referred to as t_{1st} and t_{max}, that covers what could appear as the fourth of a complete period of a sine wave. With this definition, our nominal frequency f_{nom} would be:

$$f_{nom} = \frac{1}{4(t_{max} - t_{1st})} \tag{4.1}$$

Yet, we expect this nominal frequency to be a gross estimation of our signal central frequency: on the one hand, each receiver will give a more or less different value, the calculated frequency being all the lowest so as the receiver offset increases; on the other hand, the frequency spectrum associated to a single sine-curve does not peak at the apparent nominal frequency as a continuous sine-wave does, but rather below. The nominal frequency f_{nom} should be taken as the average of the calculated frequencies at each considered receiver. In the present example having no velocity dispersion, first break and maximum pickings shown in figure 4.1 would lead to $f_{nom} = 875 \pm 15\ Hz$ for the first arrival.

4.1.2 Towards the frequency domain: window functions

To each record conducted in the time-domain corresponds an equivalent expression in the frequency domain, containing exactly the same information amount. The reversible transition from one domain to the other is enabled by the Fourier transform (FT) and its associated inverse Fourier transform (IFT). The Fourier transform is a major tool when dealing with signal analysis. It basically scans the original time-signal to detect any oscillating pattern (to be understood as 'periodic' events) and identify their frequencies, eventually decomposing the signal into its frequency components. Concretely to calculate the spectral component $H(f)$ at frequency f, it correlates the signal $h(t)$ with a complex sine-wave of that same frequency $exp(-2i\pi ft)$.

$$H(f) = FT[h(t)] = \int_{-\infty}^{\infty} h(t)e^{-2i\pi ft}\,\mathrm{d}t \tag{4.2}$$

$$h(t) = IFT[H(f)] = \int_{-\infty}^{\infty} H(f)e^{2i\pi ft}\,\mathrm{d}f \tag{4.3}$$

It eventually associates a complex number, defined by its modulus (or amplitude) and phase, to each frequency. The amplitude registers the energy associated to this periodic oscillation whereas the phase contains all information regarding time localization.

Therefore, if we move to the frequency domain in order to look at the spectral amplitude for a specific frequency, we should be aware that every contribution of that given frequency throughout the record will add into one single amplitude value. This frequency component may appear in various wave-types (resulting from a wave conversion for example) but the information will indistinctly sum up in one single spectral component. Thus, the Fourier transform does not enable local analysis of the signal. Knowing that each wave type possesses its own attenuation mode, the direct use of the full-record spectrum constituted of mixed arrivals is prohibited.

Since we are interested in calculating the attenuation of the P-wave, also referred to as the direct wave or the first arrival, we need to identify the information of interest and to find a tool to mute the irrelevant part of the record. For our coming study, we will refer to a set of synthetic signals displayed on figure 4.2. These synthetics were obtained from assembling two propagating Gaussian functions according to following expression:

$$G(x,t) = -A_0\left(e^{-\alpha_1 x}e^{-\frac{(t-x/V_1-4\sigma_1)^2}{2\sigma_1^2}} - e^{-\alpha_2 x}e^{-\frac{(t-x/V_2-4\sigma_2)^2}{2\sigma_2^2}}\right) \tag{4.4}$$

These Gaussians propagating as a plane-wave have in common a starting amplitude $A_0 = 30$, but they differ in width, velocity propagation and attenuation. The first Gaussian of characteristic width $\sigma_1 = 0.1\ ms$, propagates at $V_2 = 230\ m.s^{-1}$ and is linearly attenuated by a factor $\alpha_1 = 10$. The second Gaussian, four time as wide as the first so that $\sigma_2 = 0.4\ ms$, propagates at velocity $V_2 = 150\ m.s^{-1}$ and is attenuated by a factor $\alpha_2 = 5$. In figure 4.3 we see the detailed construction of the double gaussian synthetic at offset 15 cm as well as

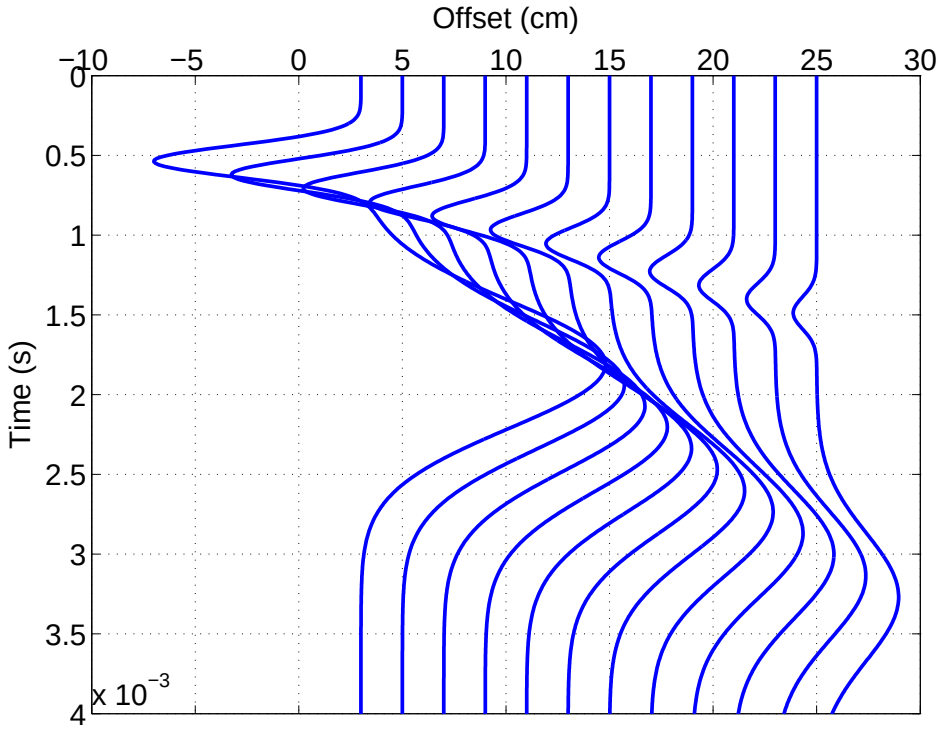

Figure 4.2: Synthetic signal constituted of two Gaussian curves, propagating at two distinct velocities. Our first arrival selection and frequency processing will be developed on this case of study

the spectral contribution of each gaussian to the whole spectrum. Since, the characteristic width of the second Gaussian equals four time that of the first, we expect the second cutting frequency to be a quarter of the first. The synthetics were sampled at 100 kHz over 50000 samples.

Being supplied with a synthetic wave, mimicking a rapid first seismic arrival of rather low energy and high frequency content followed by a slower second arrival of higher energy and lower frequencies, we can now measure the spectral effect of our first-arrival selection tools. The first selection method presented hereafter, named door function, is an arbitrary muting of the 'late' signal using a rectangular $[0, 1]$ window. The second method, using Gabor atoms, can be applied as a windowing tool or as a time-frequency analysis. It will lead to the next step of our spectral approach, namely the time-frequency analysis.

Door function

As a first windowing tool, we tested the most basic door function, a rectangular binary window build of $[0, 1]$ values. In our particular case, we selected an early portion of the signal we thought was due to the sole P-wave first arrival, represented in our synthetic by the first recorded lobe. Having chosen the portion to be preserved, we muted the rest of the signal as soon as the record changed sign by putting all following samples to zero. In practice, the door function was computed to equal unity from the first sample to the first or second change in sign following the first local extremum. By preserving the initial length of

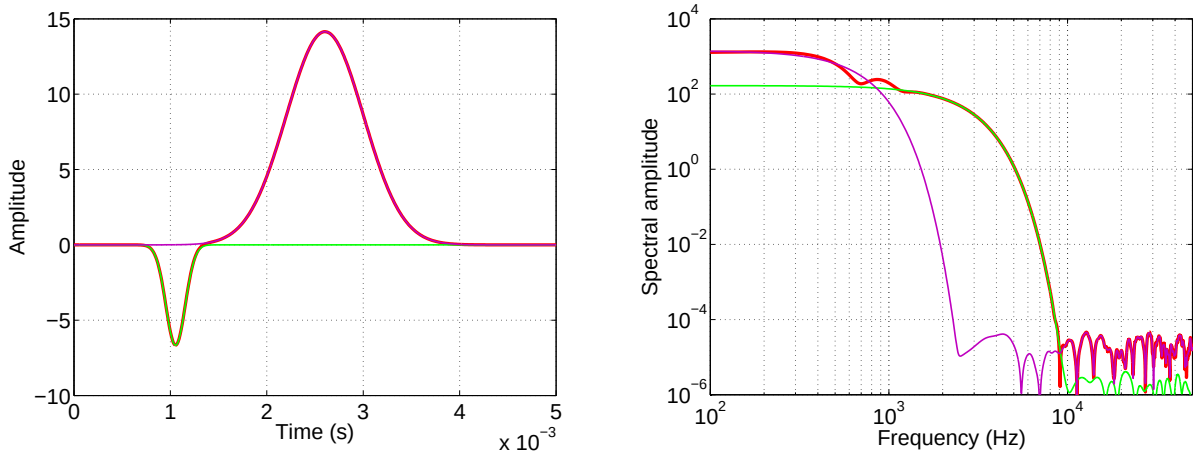

(a) (b)

Figure 4.3: Decomposition of the synthetic construction from two Gaussian curves, calculated here for the receiver at 15 cm: (a) in the time-domain, (b) in the frequency-domain. Curves in green represent the first arrival from the narrower gaussian propagating at 230 $m.s^{-1}$. Curves in purple stands for the second arrival at 150 $m.s^{-1}$ from the wider Gaussian. The addition of the two Gaussian motives gives the red curves

the record, we kept our initial frequency resolution.

Result of this operation applied to our synthetic at offset 15 cm can be seen on figure 4.4. At first sight, the time-selection appears successful. However, the spectral result of our selection in black, initially fully superposable to the isolated first arrival spectrum in green, dramatically deviates from this same curve starting from about 6 kHz. It eventually displays a unrealistically high frequency-content up to 50 kHz with no link to initial data. Indeed, the door function induces a brutal cut from signal to zero-line, resulting in systematically forming an angle at the transition with the muted part of the signal. To adapt to this brutal transition in the time-domain, the frequency spectrum suffers from a virtual increase of higher frequencies, an effect even more remarkable when we trade the smooth Gaussian for a more dynamic sine curve. The resulting artifacts hence prevent the use of a rectangular door-function as a first arrival selection tool.

Gabor atoms

Searching for a window function of smoother features than the door function, so that it would be more respective of the signal spectrum in the higher frequencies, we investigated the Gaussian functions of general expression:

$$g(t) = e^{-(t-\tau)^2/2\sigma^2} \tag{4.5}$$

giving the a Gaussian $g(t)$ centered at time τ of characteristic width determined by the parameter σ.

Knowing the position of the first max t_{max} and that of the first break t_{1st} for each channel, we multiplied the original signal by the Gaussian centered at t_{max} and of ideal width $\bar{\sigma} = (t_{max} - t_{1st})$. We found this method to be a marked improvement over the door function application. Arrival times t_{max} and t_{1st}, previously calculated on the raw record for defining

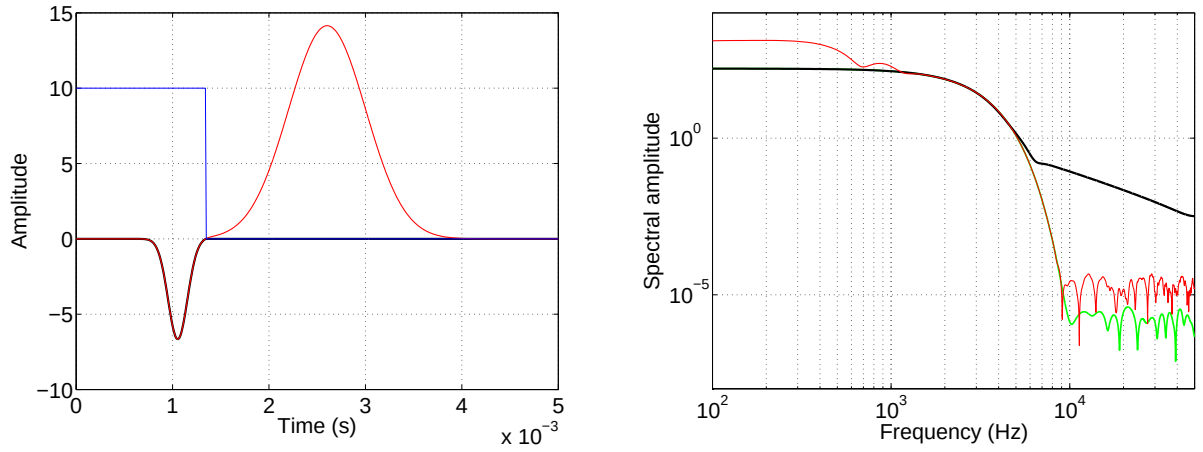

(a) (b)

Figure 4.4: Selection process of the first arrival in the time-domain. (a) The original synthetic signal at offset 15 *cm* (red) multiplied by the Door function (enlarged 10 times in blue) gives the selected first arrival (black). (b) View of the associated spectra for the original signal (red), the result of the first-arrival selection process (black) and the isolated first Gaussian arrival (green).

the appropriate Gaussian window, are preserved in their initial form as they would be using a door function. The amplitudes being pondered by the Gaussian window are mainly preserved but not as completely as with previous process. Notably, the first arrival may appear narrower, meaning of higher frequency content. But this procedure will not cause further errors on velocity estimation.

In figure 4.5 we notice indeed how the black selection spectrum seems to slightly overestimate spectral amplitude ideally represented by the green curve, visible on figure 4.5b, starting from about 2 kHz. Between 2 kHz and 4 kHz, the overestimation would lay by between 5% and 30%. Yet this windowing process is more gradual: if spectral amplitudes are moderately overestimated, the decreasing trend is respected so that it prevents the creation of fully virtual high frequencies as was previously the case. Note that we may reduce this overestimation at high frequency by enlarging the Gabor atom through increasing the parameter σ. Yet, this would be at the expense of the lower frequency-band, that is presently as well-preserved by the Gabor atom than it was by the door function.

In conclusion, the Gaussian of width directed by the delay $t_{max} - t_{1st}$ and centered on the first extremum manages a better extraction of the first-arrival spectral-signature than the previously mentioned door function. It appears to us that it qualifies as a satisfactory first-arrival selection tools to our purpose.

4.1.3 A frequency-domain approach: time-frequency analysis

Our first aim has been to isolate the first arrival using adapted windowing tools. This operation seems to be managed by the aforementioned Gabor atoms. Yet we can push a little further the use of our window function by sliding it along the time-axis to achieve a Short Time Fourier Transform (STFT), thus gaining further insights into the frequency distribution over time. The STFT, also known as the sliding window Fourier transform, involves a window function $w(t)$ of fixed width that is shifted along the time axis by a delay

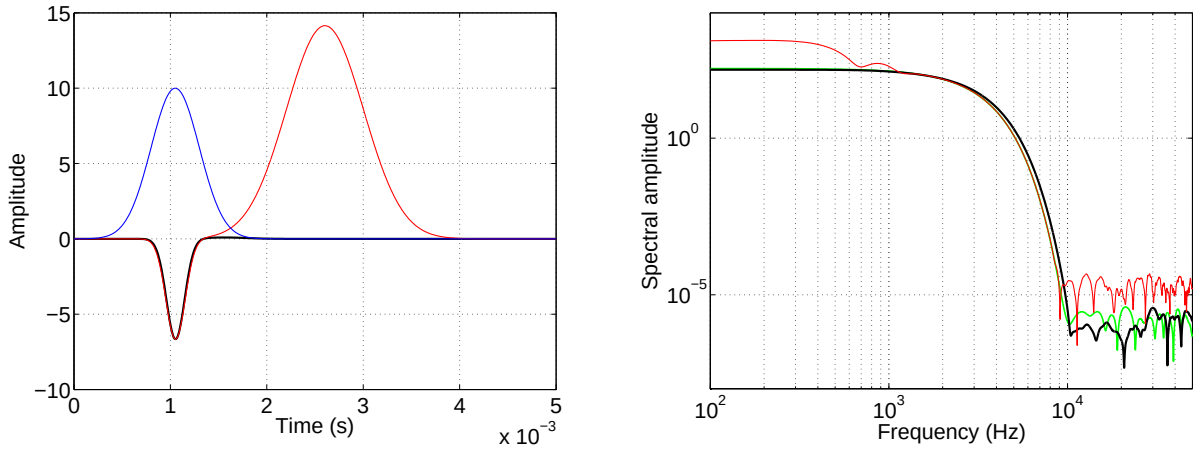

(a) (b)

Figure 4.5: Selection process of the first arrival in the time-domain. (a) The original synthetic signal at offset 15 *cm* (red) multiplied by the Gabor window of standard deviation $\bar{\sigma}$ centered on t_{max} (enlarged 10 times in blue) gives the selected first arrival (black). (b) View of the associated spectra for the original signal (red), the result of the first-arrival selection process (black) and the isolated first Gaussian arrival (green).

time τ. Its general expression is:

$$H_W(\tau, f) = \int_{-\infty}^{\infty} w(t-\tau)h(t)e^{-2i\pi ft}\,\mathrm{d}t \tag{4.6}$$

Representing H_W produces a time-frequency plot: examples are to be seen further in this section. This time-frequency diagram enables to observe the signal decomposition into its major arrivals and to distinguish the main frequencies involved in each of them, however with some limitation. Indeed, because of the time-frequency duality we cannot expect the signal energy to be perfectly located in both time and frequency. As an illustration of this phenomenon, a dirac function, infinitely precise in time will be totally delocalized in frequency whereas a continuous sinusoid, going on indefinitely, will show a unique peak extremely well-defined in the frequency-domain.

This has been theorized by Heisenberg [1927] as the uncertainty principle: there is an unshrinkable inaccuracy in our knowing the respective position of two parameters that are complementary variables. As a fact, the product of the standard deviation on frequency and time $\sigma_f \times \sigma_t$ is necessarily superior or equal to $1/(4\pi)$. This was a well-known fact to Gabor as he intended to investigate the science of communication in such a way that "time and frequency play symmetrical parts" [Gabor, 1946].

Gabor transform

The Gabor transform is a specific expression of the STFT obtained when the signal $h(t)$ is convoluted to the previously mentioned Gaussian window $g(t)$ (see eq. (4.5)). This transform noted $H_G(\tau, f)$ will be written as:

$$H_G(\tau, f) = \int_{-\infty}^{\infty} e^{-\frac{(t-\tau)^2}{2\sigma^2}} h(t)e^{-2i\pi ft}\,\mathrm{d}t \tag{4.7}$$

This transform is the most popular STFT, for it is unique in providing the best possible time-frequency resolution [Harris, 1978] by equaling the uncertainty threshold value of $1/(4\pi)$, as intended by Gabor [1946]. But as a STFT, it also has the drawback of being a fixed time window support, resulting in the impossibility of correctly representing low as well as high frequencies simultaneously[1].

Application of the Gabor transform to our synthetic, previously to any first arrival selection, can be seen in figure 4.6. It was obtained for a Gaussian windowing function characterised by $\sigma = \bar{\sigma}$ (as that previously used for extraction of first arrival information), and shifted throughout the record by changing τ. Although this window function should be adapted to detect the first arrival, the amplitude contrast between the first and the much more energetic second event is so unfavourable that we barely detect our first arrival of interest. The diagram maximum, located by a white cross, is in good time-agreement with that of the second event (located here at $t = 2.58\ ms$ when expected at $2.6\ ms$). Frequency location however is very poor as it is drawn to $0\ Hz$. An earlier local maximum corresponding to the maximum of the first arrival, barely identifiable, is marked by a black cross at the point $t = 1.02\ ms$ (when expected at $1.05\ ms$) and $f = 150\ Hz$. This time-frequency diagram provides good time-localisation of maximal events but no valuable frequency information can be extracted and poor overall resolution makes it unadapted to our general purpose. Complementary information regarding Gabor-transform resolution may be found in section 7.3.4 of the appendices.

S-transform

In the 1980's, to face the time-frequency resolution problem observed with STFT, a group of researchers (Morlet et al. [1982], Grossmann and Morlet [1984]) developed a new class of time-frequency transforms involving scalable window functions. The flexibility of this so-called continuous wavelet transform (CWT) enabled constant resolution throughout the analysis. For, by dilating or compressing a sliding mother-wavelet $\Psi(t)$ thanks to the scale parameter a, it is possible to have a fixed number of wavelet cycles per period, the period being described by its scale a rather than by its frequency f. The expression of the sliding dilated wavelet would then be:

$$\Psi_{\tau,a}(f) = \frac{1}{\sqrt{|a|}}\Psi\left(\frac{t-\tau}{a}\right) \tag{4.8}$$

When replacing the usual $e^{-2i\pi ft}$ Fourier factor by the conjugate expression of the wavelet $\Psi_{\tau,a}(t)$, one obtains the CWT of signal $h(t)$ at scale a and position τ.

$$C(\tau,a) = \frac{1}{\sqrt{|a|}}\int_{-\infty}^{\infty} h(t)\bar{\Psi}\left(\frac{t-\tau}{a}\right)\,\mathrm{d}t \tag{4.9}$$

[1]Hence, for a very defined information in time, one would take a very narrow window. But this window will not be able to encompass full-cycles of the lower frequency band causing frequencies to be poorly characterized. Conversely, for a precise information in frequency, one should take a large window, but then the time-localization will be uneasy.

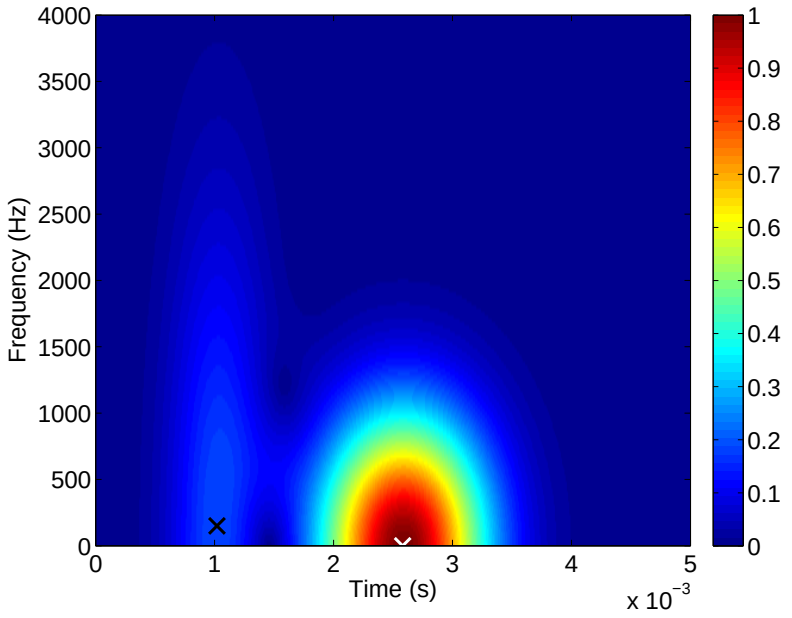

Figure 4.6: Synthetic signal at offset 15 cm treated by the Gabor transform for a fixed window-width controlled by a standard deviation of $\sigma = \bar{\sigma} \approx 0.3ms$. This standard deviation was calculated to be optimal relatively to the synthetic first lobe. The two Gaussian events are identifiable as a first event (black cross at $t = 1.02\ ms$) corresponding to a frequency of 150 Hz while the maximum of the more energetic second event (white cross at $t = 2.58\ ms$) is identified as being a continuous signal. In the original time synthetic maxima were located at 1.05 ms and 2.6 ms respectively. Spectra amplitudes have been normalised to the interval [0,1].

But in the expression of $C(\tau, a)$ there is no direct reference to frequency f and phase information is hard to recover. To get round this problem, Stockwell et al. [1996] proposed the S-transform as the "phase-correction" of the CWT[2]. This S-transform is obtained by taking a Gaussian windowing function that will scale with frequency through its σ-parameter determining its standard deviation. It consequently shares the CWT ability for multiresolution while speaking in common 'frequency'-term by determining an adaptative parameter σ as:

$$\sigma(f) = \frac{1}{|f|} \tag{4.10}$$

Once $\sigma(f)$ has been defined the expression of the S-transform logically stems from the Gabor-transform, with addition of a normalizing factor proportional to frequency f, that authorizes the invertible transform.

$$H_S(\tau, f) = \frac{|f|}{\sqrt{2\pi}} \int_{-\infty}^{\infty} e^{-\frac{(t-\tau)^2 f^2}{2}} h(t) e^{-2i\pi f t}\, \mathrm{d}t \tag{4.11}$$

$$\int_{-\infty}^{\infty} H_S(\tau, f)\, \mathrm{d}\tau = H(f) \tag{4.12}$$

[2]Other authors (Simon et al. [2007], Sahu et al. [2009]) rather saw the S-transform as an extension of the Gabor STFT with characteristics of the CWT

As a consequence of this invertibility and unlike the CWT, the S-transform maintains a direct link to the Fourier transform and to the absolute phase of each frequency component. In fact, it can promptly be obtained by summing the S-transform over the τ-axis. Another convenience is its amplitude conservation, as reported by Ventosa et al. [2008]: for sine-waves having various frequencies but a same amplitude in the time domain, the S-transform will impart them equal amplitude in the (τ, f) domain independently of the frequency.

However, this goes with some drawbacks. As a counterpart of its amplitude conservative behavior, the S-transform fails to be energy-conservative [Ventosa et al., 2008]: an equal energy modification on different (τ, f) localizations will cause impact of same amplitude but different energy in the original domain. For this reason, the Gaussian functions supporting the S-transform would not strictly qualify as a mother wavelet for CWT [Stockwell et al., 1996]. Finally, the plain S-transform does not fully resolve the issue of poor energy concentration in the time-frequency domain [Sahu et al., 2009]. Indeed, the use of frequency-adapted windows by investigating lower frequencies with wider windows than those inspecting high frequencies will produce a time-smearing in the lower frequency-band and a frequency-smearing in the upper frequency-range. Yet,this weakness is shared by any CWT function. To this respect, Reine et al. [2009] compared four transforms belonging to two distinct classes of time-frequency analysis: the Hamming STFT and the Gabor-transform represented the fixed-window support, while the S-transform and CWT illustrated the multiresolution ability of variable-window. They concluded that is was more relevant to compare classes of transforms, i.e. fixed- or variable-window, rather than individual transforms themselves. For even if in each cases, small changes in the transform parameters can induce small benefits from one transform over the other, the big picture would remain unchanged. For resolution sake they advocated for the use of variable window-function. They added that their preference goes to the S-transform for, unlike the CWT, it directly shows the result as a function of frequency rather than scale while preserving the time reference for the phase information. These accessibility and comfort of use were key arguments in our decision to move to the S-transform.

We tested the S-transform on our initial synthetic of assembled Gaussian curves (see figure 4.7). Using this transform, both arrivals were identifiable. Yet, the maximum amplitude of the second arrival (white cross) being much higher than that of the first (black cross), the color scale denies good contrast for the latter. While the first arrival shows a central frequency of 1600 Hz, the second centers on 375 Hz. It approaches the ratio 1/4 initially computed regarding the respective Gaussian width, with a minimal resolution of 25 Hz associated to the frequency-pace. Time location of the black cross perfectly coincides with the maximum of the direct arrival at offset 15 cm occurring at 1.04 ms. As for the white cross it is located at 2.36 ms when expected at 2.6 ms from the maximum location of the second arrival in the time-record. This time-shift may be related to the previously mentioned time-smearing at low frequencies (for complementary information regarding Stockwell-transform resolution please report to section 7.3.4in the appendices).

Observation of time-frequency analysis on synthetics confirms the superiority of the S-

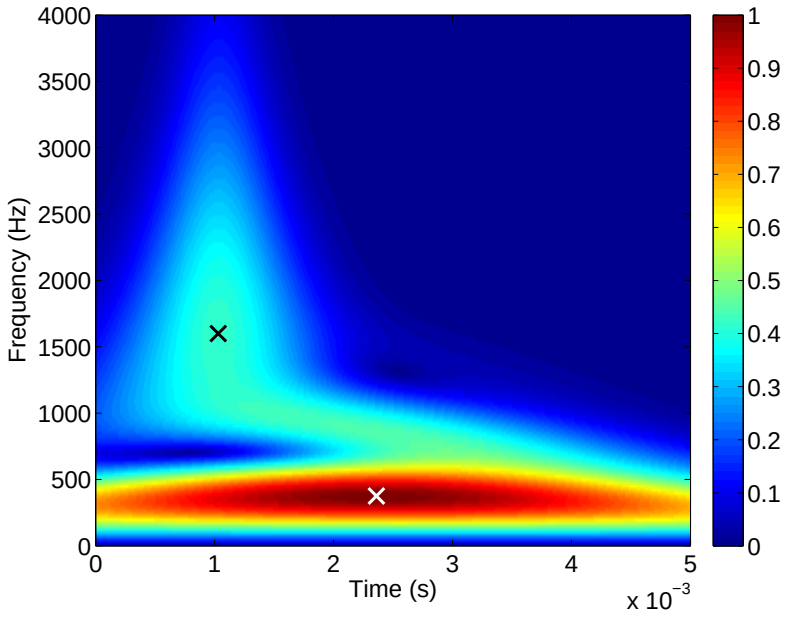

Figure 4.7: Synthetic signal at offset 15 cm treated by the S-transform. The two Gaussian events are identifiable. The local maximum of the first event (black cross at $t = 1.03\ ms$) corresponds to a frequency of 1600 Hz while the maximum of the more energetic second event (white cross at $t = 2.36\ ms$) shows a central frequency of 375 Hz. Spectra amplitudes have been normalised to the interval [0,1].

transform over the Gabor transform. Thus, despite the fact that the Stockwell-transform comes with a tremendous increase in computation time, it gains our preference for time-frequency analysis. We will consequently resort to the S-transform whenever a time-frequency analysis is needed, should it be for a full comparison of seismic and seismoelectric records or as an help in identifying receivers showing unmingled first arrivals.

4.2 Seismic velocity analysis

Seismic velocity analysis is an essential tool in the characterization of porous media. Velocities are indeed intimately related to the arrangement of the frame as well as the presence and circulation of fluid within it. Since fluid behaviour is very sensible to frequency as it can accordingly behave in a relaxed or unrelaxed mode, having a lubricating or a stiffening effect on the frame, it appears clear that seismic velocities may depend on frequency. This phenomenon is called 'velocity dispersion'. Beyond the straightforward determination of seismic velocities by picking, as presented in section 4.1.1, we discuss intercorrelation as a further method for velocity determination on time records before proposing a tool for characterization of P-waves dispersion.

4.2.1 Estimation of first arrival velocity by intercorrelation

To determine first arrival velocities, we thought of an alternate less empirical method by maximising the correlation between two receivers. By reporting the time-shift, corresponding to the best fit, to the receivers separation, we could deduce a velocity value. But when employed, intercorrelation inclined to underestimate P-wave velocities. There may be two

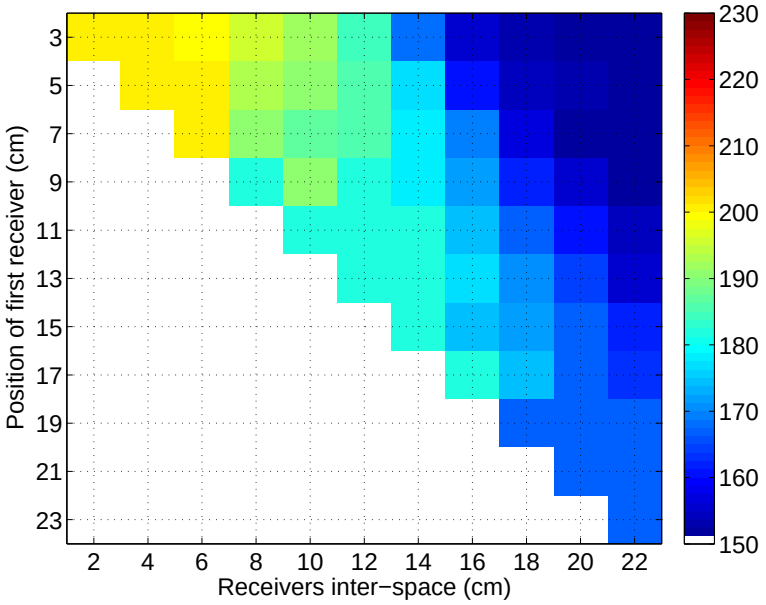

Figure 4.8: Results of velocity estimation by intercorrelation on the synthetic of Gaussian propagating waves. Each possible pair of receiver is represented by the position of the first considered receiver (between 3 and 23 cm) and its position relatively to the second receiver of the pair (inter-space from 2 to 22 cm). The first Gaussian propagates at 230 $m.s^{-1}$, the second at 150 $m.s^{-1}$ but no estimated velocity trespasses 200 $m.s^{-1}$.

explanation to this. On occasions, it selected the low-frequency high-energy tail of the signal, correlating on late arrivals usually propagating at lower velocities. But more regularly, it tended to fit the curves with respect to their first maximum locations thus introducing dispersion bias. Despite this bias, picking of the first maximum for P-wave estimation was sometime applied by default for equivocal first breaks, as sometimes encountered in SE acquisitions.

When testing velocity estimation by intercorrelation on our synthetic Gaussian curves (figure 4.8), we see that they highly depend on the relative position of receiver-pair. The greater the distance between the receivers, the more the estimated velocity tends to converge towards a velocity of 150 $m.s^{-1}$ corresponding to the second less attenuated Gaussian event. As for closely positioned receivers (corresponding to the diagonal), the velocity will be all the higher than their offsets is closer to the source. But the highest estimated velocity of 200 $m.s^{-1}$ still underestimate that of the computed first arrival by 30 $m.s^{-1}$. When the same procedure is applied on the synthetic after first arrival selection we recover a velocity of 230 ± 8 $m.s^{-1}$. However, our first arrival selection requires to know the first-break position, meaning that we already have a reliable first arrival velocity at that early processing-stage. As such, we do not need to re-determine velocities by intercorrelation.

4.2.2 Estimation of velocity dispersion by phase unwrapping

Besides this preliminary time treatment, we chose to investigate velocity dispersion of the P-wave by phase unwrapping. For this purpose, we have to rely on records for which first

arrivals have been selected by adaptable Gabor-windowing, as described in previous section.

If we consider that our selected first arrival is truly representative of a single event then, by moving to the frequency domain, phase information should enable the determination of the phase velocity at a given frequency f. By repeating this operation for each frequency, we would estimate velocity dispersion. If we consider a wave propagating along the x-axis, its expression in the Fourier domain would be:

$$S(f,x) = S_0(f,x)e^{-i\frac{2\pi fx}{v(f)}} \tag{4.13}$$

where $S_0(f)$ gives the spectral amplitude, whereas phase information is encompassed in the last factor. Phase depends on offset x, frequency f and phase velocity $v(f)$. In order to free ourselves from possible bias in the position of the source, we can consider a spectral ratio between two captors. Let the first captor at offset x_0 be the reference to all other receivers. Hence we can write a spectral ratio (El Mouhtadi [2011], Ploix [2006]):

$$R_{x,x_0} = \frac{S(f,x)}{S(f,x_0)} = \frac{S_0(f,x)}{S_0(f,x_0)}e^{-i\frac{2\pi f}{v(f)}(x-x_0)} \tag{4.14}$$

Be ψ the argument of this ratio, on the one hand we formally have:

$$\psi = -\frac{2\pi f}{v(f)}(x-x_0) \tag{4.15}$$

on the other hand we can determine this phase experimentally:

$$\psi = \arctan\left(\frac{\Im[R_{x,x_0}]}{\Re[R_{x,x_0}]}\right) \tag{4.16}$$

The use of the arctangent function necessarily gives a result within the $[-\frac{\pi}{2},+\frac{\pi}{2}]$ interval. The resulting discontinuities have to be removed by phase unwrapping. In this case, it would consist in subtracting π each time a discontinuity is encountered (see figure 4.9a). For high noise level, phase as well as amplitude will be distorted [Kim and Park, 2002]: the result of such noise effect can be seen in figure 4.10. Under such condition, the phase reconstruction by simple discontinuity search may be insufficient.

Once the phases have been reconstructed (see figure 4.9 obtained on our synthetic data set), and as long as the frequency is not to noisy, it is possible to estimate $v(f)$ from the slope obtained by linear regression on the corrected offset $(x-x_0)$ depending on ψ. An additional advantage of linear regression is to allow for a robust calculation of uncertainties [Rouaud, 2012]; this will be further explained in a coming section.

Such a result obtained on our synthetic can be seen in figure 4.11 for frequencies of 100 and 650 Hz, giving respective velocity of about 170 $m.s^{-1}$ and 120 $m.s^{-1}$. If those velocities seem in disagreement with the original computed velocities of 230 $m.s^{-1}$ and 150 $m.s^{-1}$, we will see in coming full dispersion curves that they can be explained by the mixing of the two Gaussians possibly producing some interferences.

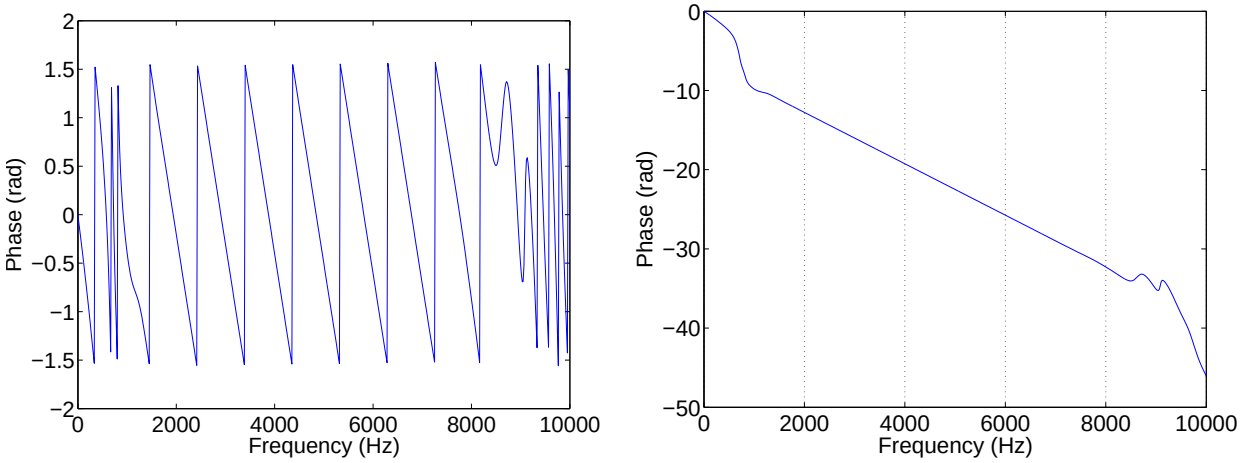

(a) (b)

Figure 4.9: (a) Raw phase data for the Gaussian synthetic curves at offset 15 *cm* relatively to the reference at 3 *cm* and (b) same phase data after phase unwrapping.

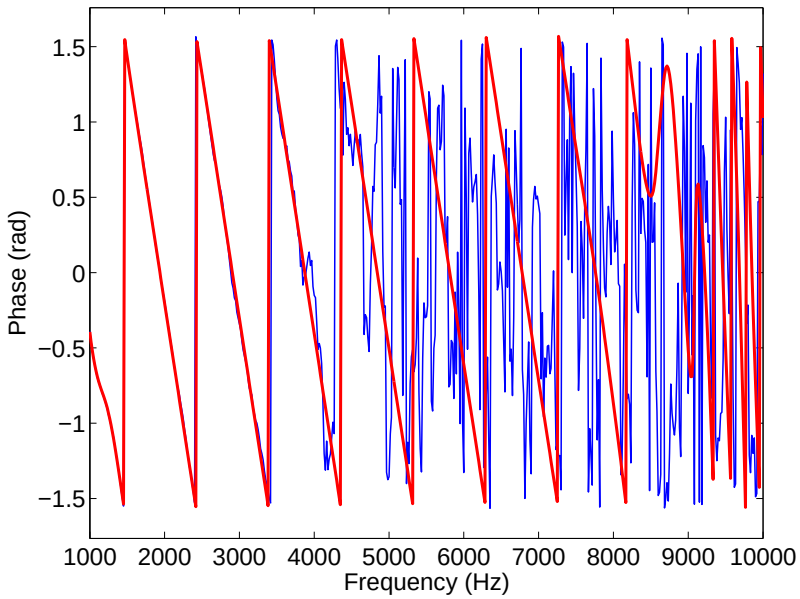

Figure 4.10: Phase spectrum of the synthetic Gaussian signal with (blue) and without (red) addition of noise.

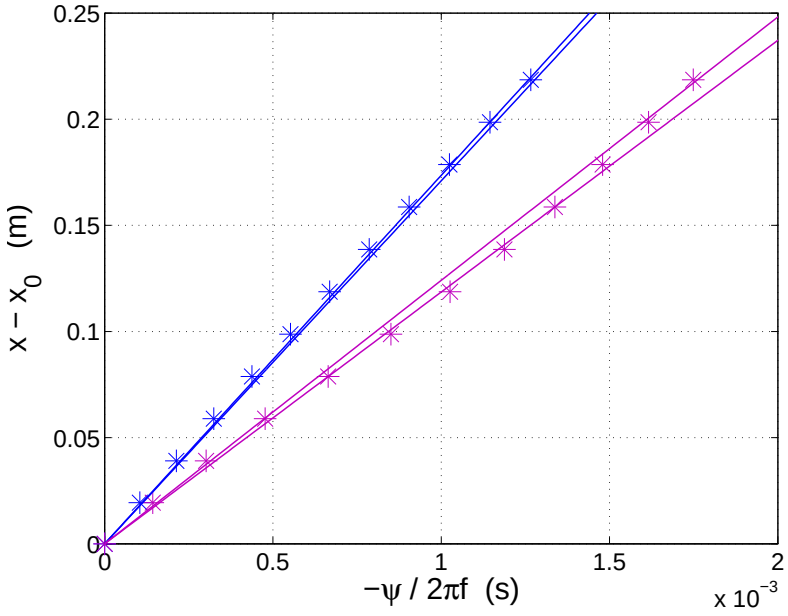

Figure 4.11: Velocity determination on unwrapped phase by linear regression for the complete synthetic of propagating Gaussian waves. Velocity with error bars were evaluated about $172 \pm 1.5\ m.s^{-1}$ at 100 Hz (blue) and $121 \pm 3\ m.s^{-1}$ at 650 Hz (purple).

4.2.3 Estimation of velocity dispersion on synthetic

To validate our approach on estimating velocity dispersion by phase unwrapping, a last test is run on our synthetic of propagating Gaussian waves. Velocity dispersion was calculated on the complete record (figure 4.12a) as well as on the first arrival extraction (figure 4.12b). For comparison, we display a reference line (green) obtained for the sole first Gaussian arrival at fixed velocity of 230 $m.s^{-1}$ with no frequency dispersion. As a first result, we observe how this green dispersion curve is in fact testifying from an exact 230 $m.s^{-1}$ velocity up to 8 kHz ; above this limit we approach the noise level and loose in stability to finally enter noise about 9 kHz (see green curve on figure 4.5b)[3]. Observing the figure on the left side, we understand that the presence of a second Gaussian propagating at 150 $m.s^{-1}$ greatly deviates the dispersion curve from the green reference line. By first arrival selection on the right side, however, the calculated dispersion curve almost overlaps the green reference line starting from an estimation at 220 $m.s^{-1}$ at 100 Hz to reach $230 \pm 0.5\ m.s^{-1}$ starting from about 1 kHz, the error being calculated on the linear regression as exposed in appendices 7.3.3. This result corroborates both our processing for first arrival extraction and our estimation of velocity dispersion by phase unwrapping.

4.3 Seismic attenuation and quality factor analysis

The seismic attenuation basically informs us on the evolution of the seismic amplitudes as the seismic wave propagates. When characterizing a seismic wave, attenuation comes as one

[3]Abrupt terminations of further dispersion curves are also related to entering noise level, which occurs first on full record, then on sole first propagating Gaussian and finally on extracted first arrival as seen on figure 4.5b. This ordering explains the shift observe between curves termination at frequencies about 8 to 10 kHz.

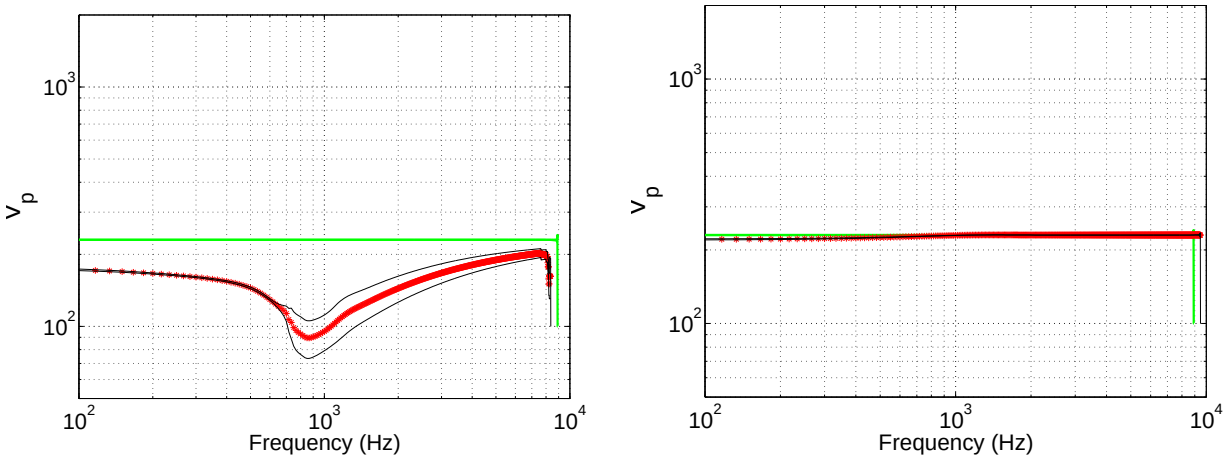

(a) (b)

Figure 4.12: Estimation of velocity dispersion on the synthetic propagating Gaussian waves either for the complete signal (a) or after first-arrival selection (b). In each figure, the dispersion curve obtained for the sole first Gaussian arrival of fixed velocity of 230 $m.s^{-1}$ is shown in green. In figure (b), maximal deviation of synthetic relatively to the green reference line is 10 $m.s^{-1}$.

of the first attribute of importance along with seismic velocities, for both information pieces are closely linked to the structure and composition of the medium (Toksöz et al. [1976] and Klimentos and McCann [1990]). However, under this general term of seismic attenuation three different causes may be distinguished [Born, 1941]:

- a geometric effect or 'geometrical spreading' resulting from the evolution of the seismic energy distribution on a spreading wavefront.

- reflection and scattering effects due to existent discontinuities or inhomogeneities within the propagative medium.

- an intrinsic damping, that will be referred to as the intrinsic attenuation α, depending exclusively on the medium characteristics and featuring its aptitude to preserve the seismic energy while propagating.

Conversely to this last effect that is of dissipative nature and conveys information about the medium, the first two effects, where the total energy of the wave is fractionated but conserved, will be referred to as extrinsic attenuation.

Since our experiment has been designed to avoid major discontinuities and to prevent the spoiling of the first arrival by any reflection, we consider attenuating contributions of the second kind to be negligible. Under this assumption, we will have to account for the sole geometrical spreading before being capable of any estimation of attenuation α. Eventually, we will merge information on seismic velocities and attenuations to draw conclusions on the seismic quality factor Q.

4.3.1 Intrinsic attenuation and geometrical spreading

Attenuation calculation by short-period amplitude spectral ratio

Various methods are available to measure seismic attenuation on a sample: it ranges from stationary vibrating systems, including the widely used resonant bar method (Born [1941], Gardner et al. [1964] and Winkler and Nur [1979]), to stress-strain phase-shift observations [Spencer, 1981]. We choose to measure the seismic attenuation on a propagating wave according to the method of short-period amplitude spectral ratio.

Mathematically, when considering a plane-wave propagating within an isotropic media, thus freeing ourselves from any geometrical or scattering effects, signal amplitude variation with offset $s(x)$ should be expresses by an exponential decrease, for it should suffer the same percentage reduction in amplitude for each unit of distance traveled [Born, 1941]:

$$s(x) = s_0 e^{-\alpha x} \tag{4.17}$$

Yet, when speaking of attenuation, there is also a notion of loss per cycle of oscillation. In this regard, if considering two oscillation modes of respectively 100 Hz and 1 kHz and assuming a non-dispersive velocity, for the higher frequency the absolute offset value $'x'$ will correspond to 10 times as many oscillation-cycles as for the lower frequency. This fact would explain a preferential loss of higher frequency components while propagating, and would consequently account for a frequency-dependent attenuation. This evidence advocates for a spectral approach of the attenuation calculation, in agreement with the chosen method. On this subject, Ward and Toksöz [1971] offer an expression for spatial evolution of spectral amplitude $A(f)$ at offset x showing a very similar structure to previous formulation 4.17:

$$A(f,x) = A_r(f)\, G_x\, exp\,[-\alpha(f)x] \tag{4.18}$$

where:

- α is the linear attenuation coefficient expressed in $Np.m^{-1}$ convertible to $dB.m^{-1}$ ($1Np \approx 8.7dB$)

- $A_r(f)$ represents the spectral response of the seismic receiver as to compensate the possible filtering effect of the sensor

- G_x accounts for the geometrical spreading due to the proper propagation geometry. This parameter will be extensively discussed in the next section.

If we assume $A_r(f)$ to be identical for our whole set of factory-made receivers, the amplitude ratio between any pair of receivers enables to get rid of this corrective term. Consequently, if we consider $A(f,x)$ relatively to a captor at reference offset x_0, where the geometrical spreading is G_{x_0}, the relation becomes:

$$ln\left(\frac{A(f,x)}{G_x}\right) = ln\left(\frac{G_{x_0}}{A(f,x_0)}\right) - \alpha(f) \times (x - x_0) \tag{4.19}$$

Hence for the correct geometric factor G_x and for a given frequency, the quantity $ln(A(f,x)/G_x)$ should depend linearly on offset x with a negative slope that equals $-\alpha$. Consequently, our next task will be to investigate the effect of choosing the adapted geometrical spreading.

Focus on geometrical spreading

As previously introduced, the geometrical spreading G_x is a correcting factor traducing how seismic energy is distributed on the wavefront as it propagates. If considering a point source within the medium, the seismic energy should spread across a spherical wavefront that goes growing as the wave propagates further in any direction. Considering that at a distance x from the source point, the initial energy would be spread on a sphere of $4\pi x^2$, the seismic energy appears to decrease as $1/x^2$ causing seismic amplitudes to geometrically decrease as $1/x$. For a 2D propagation geometry, typically associated to line sources the seismic energy would strew on a circle of perimeter $2\pi x$ so that the associated amplitudes would fall off as $1/\sqrt{x}$. Finally, in a 1D propagation we would have no geometrical spreading. This scenario would reflect the plane-wave case. Such propagation geometry may be assumed when the observation is conducted at far offsets from the source and the length of the receiver-array is small in comparison to the offset. If the considered offset lays within a one-wavelength distance to the source, we will have to consider the highly attenuating near-field geometry decreasing as $1/x^2$.
In short, according to the propagation geometry we will consider:

- $G_x = 1/x^2$ if the propagation is in near-field
- $G_x = 1/x$ if the propagation is 3D
- $G_x = 1/\sqrt{x}$ if the propagation is 2D
- $G_x = 1$ if the propagation is 1D.

Estimation of attenuation α on synthetic

We tested our spectral treatment for attenuation on our synthetic of propagating Gaussian waves; this synthetic was computed as a plane wave with a 1D propagation geometry. It was composed of a first arrival characterised by a linear attenuation $\alpha_1 = 10$ while the second arrival was computed with an attenuation $\alpha_2 = 5$. Results can be seen in figure 4.13. Again, the characteristic feature of the sole first arrival is represented by a green reference line: it stays expectedly constant and equals 10 over the whole kilohertz range. When considering the complete signal, in the left-hand figure we observe that at low frequencies, dominated by the second wider Gaussian arrival, attenuation starts at a value close to 5. From 600 to 1000 Hz impressive variations due to a bump in the spectra (see red curve on figure 4.5b), related to overlapping frequency content from the first an the second Gaussian, take the attenuation back and forth. For frequencies superior to 1.5 kHz, the first arrival of higher frequency eventually prevails and attenuation finally stabilises at 10. By selecting first arrivals, the effect of the second Gaussian is barely noticeable: variations of attenuation in the lower frequency range are fully smoothed out as to reach a nearly constant α at 9.8 ± 0.3 in the $[100 - 1000\ Hz]$ frequency range.

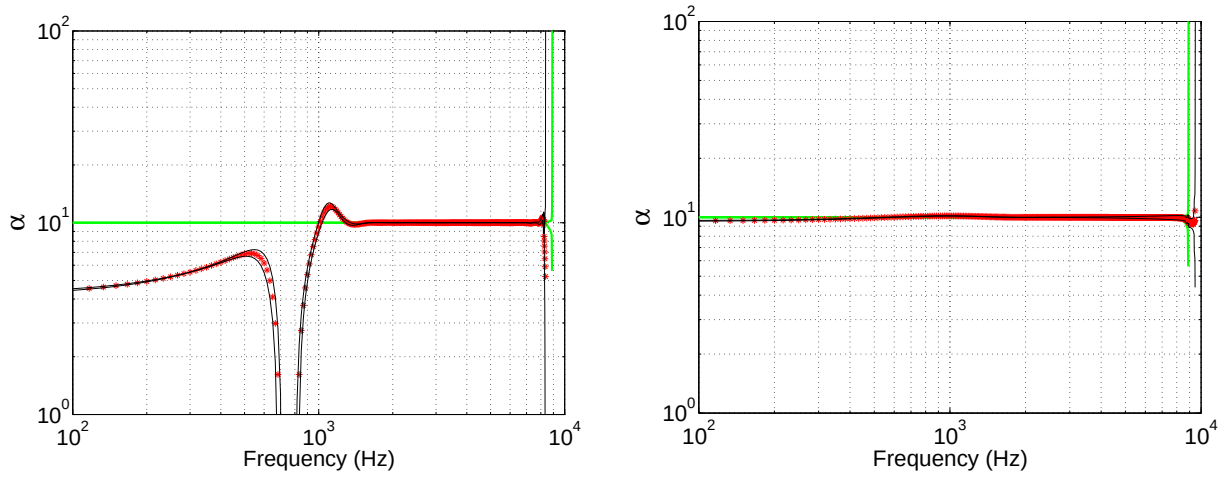

(a) (b)

Figure 4.13: Processing run on the synthetic Gaussian propagating waves. As it has been computed, the attenuation set at 10 appears constant and is estimated at 9.94 by linear regression.

These results support again the first arrival selection by a Gaussian window as well as the attenuation calculation by short-period amplitude spectral ratio.

Possible bias from misinterpreted geometrical spreading

Our synthetic was computed having a predefined 1D propagation geometry. But determination of the appropriate propagation geometry on actual data may be uncertain. Our synthetic data set provides the opportunity to investigate the bias introduced by having mistaken the propagation geometry. What happens in case a 2D or 3D geometrical spreading has been accounted for, when the 1D equivalent would have been needed? To get a first glimpse on that subject, we processed our complete plane-wave synthetic data for attenuation estimation implying 1D, 2D and 3D propagation geometries. We present the three obtained curves in a single figure 4.14. If the upper curve in green is associated to the correct 1D propagation geometry, curves for 2D (blue) and 3D (red) geometries appear simply as a vertical shift of the original green curve. A possible meaning is that attenuation calculated with a 2D or 3D geometrical spreading may be expressed as the attenuation at 1D propagation geometry modulated by a constant.

To prove this true, we need to focus on the term $ln(A(f,x)/G(x))$. For any propagation geometry, this factor may be developed as:

$$ln\left(\frac{A(f,x)}{G_x}\right) = ln\left(A(f,x)\right) + (c \times ln(x)) \tag{4.20}$$

where constant c equals 1 for 3D, 1/2 for 2D and 0 for 1D geometrical spreading. Thus, each point appears as the sum of the 1D expression of $ln\ A(f,x)$ and a weighted contribution of $ln(x)$. For our acknowledged 1D propagation, we may write:

$$ln\left(A(f,x)\right) = -\alpha_{1D} \times x + \beta \tag{4.21}$$

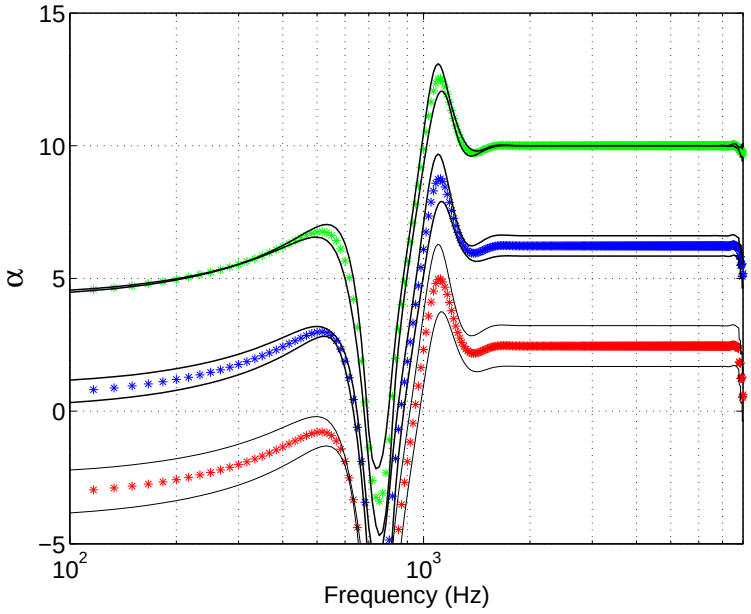

Figure 4.14: Calculation of attenuation on the synthetic data set by considering a 1D- (green), 2D- (blue) or 3D- (red) propagation geometry.

where α_{1D} is our estimated attenuation coefficient for 1D propagation geometry and β is a constant. If we could approximate the evolution of $ln(x)$ as a linear function of offset x, typically:

$$ln(x) \approx a \times x + b \tag{4.22}$$

we might give a first gross approximation of estimated 2D or 3D attenuation values from the available α_{1D} calculated for plane wave. Re-evaluated attenuations may then be:

$$\alpha_{3D} = \alpha_{1D} - a \tag{4.23}$$

$$\alpha_{2D} = \alpha_{1D} - \frac{a}{2} \tag{4.24}$$

On figure 4.15, we see how $ln(x)$ varies with respect to offset x: if we try to force a linear regression on these points, the slope will strongly depend on the offset-range considered. In table 4.1, we give an overview of what this correcting slope could be when considering offset-range varying from $[10cm - 15cm]$ to $[5cm - 30cm]$. In our synthetic case, attenuation calculations have been run considering a minimal offset to the source of 5 cm up to a maximum offset of 25 cm. Hence, a first gross approximation according to table 4.1 would be:

$$\alpha_{3D} \approx \alpha_{1D} - 7.5 \tag{4.25}$$

$$\alpha_{2D} \approx \alpha_{1D} - 3.7 \tag{4.26}$$

These theoretical translation constants echo our observation both for spectral and local estimation of attenuation. Indeed when comparing the three plateau at figure 4.14, we report

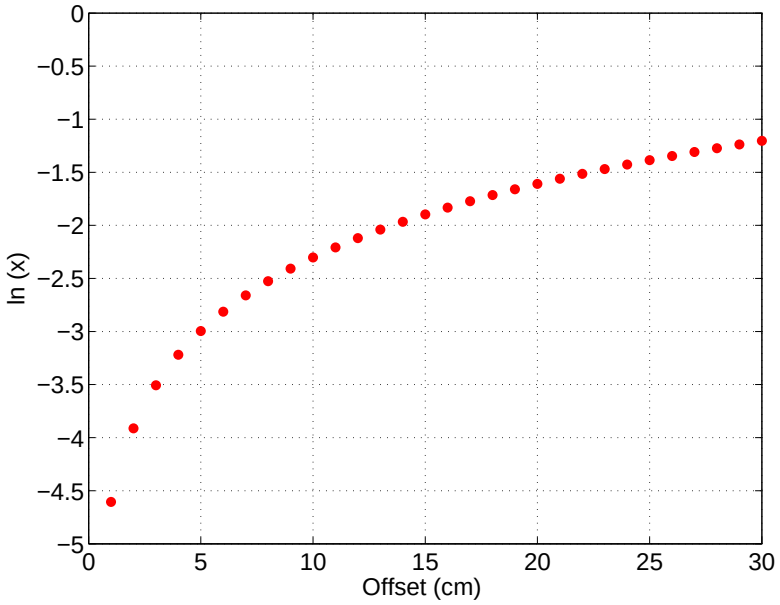

Figure 4.15: Evolution of the term $ln(x)$ with offset x.

Starting offset \ Ending offset	15 cm	20 cm	25 cm	30 cm
5 cm	10.7	8.8	7.5	6.6
10 cm	8.1	6.8	6	5.3

Table 4.1: Slope obtained for the fitting of $ln(x)$ as a linear function of x depending on the range of offset considered.

$\alpha_{1D} = 9.97 \pm 0.05$, about a constant 3.8 below $\alpha_{2D} = 6.2 \pm 0.4$ and a constant 7.6 below α_{1D} we find $\alpha_{3D} = 2.4 \pm 0.8$. Enlargement of the black error bars as geometrical spreading gains a dimension is easily understood when looking at figure 4.16: to obtain this figure, we picked the first extremum A_{max} on every captor in the time domain and represented $ln(A_{max}/G_x) = f(x - x_0)$. If linear regression is adapted to the green 1D-curve, when applied forcing it to the blue 2D-curve and even more so the red 3D-curve one perceives the increasing bias on slope determination. Nevertheless the determined slopes coincide exactly to those determined at the spectral plateau.

Thus it explains why, for a fixed range of offsets, the transition from any propagation geometry to another would mostly consist in an amplitude shifting of the attenuation curve. In consequence, the relative attenuation variations would remain interpretable over the complete experimental set with the quite restrictive limitation of keeping the same offset coverage throughout the experiment. In practical it means that we have to choose a reference offset range for our processing, knowing which captors eventually felt out and what constrains it puts on our offsets selection. For similar geometrical reasons we cannot compare result obtained on different setups or with different seismic sources.

In conclusion, interpretation of attenuation and inverse quality factor will need to check carefully the propagation geometry, *i.e.* estimating a realistic geometrical spreading.

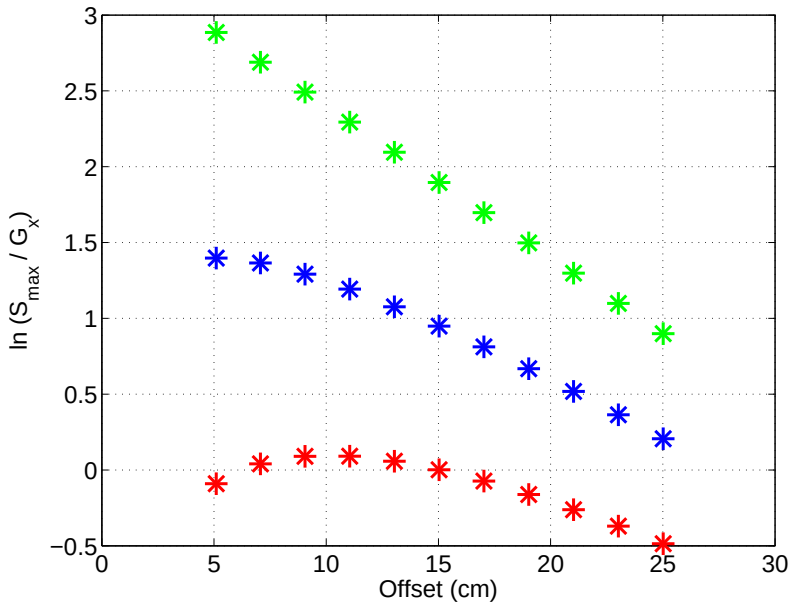

Figure 4.16: Punctual calculation of attenuation by first extremum picking on the synthetic data set by considering a 1D- (green), 2D- (blue) or 3D- (red) propagation geometry.

4.3.2 Determination of quality factor Q and analysis of its frequency dependency

Equivalent definitions of quality factor Q

In their handbook, Mavko et al. [2003] propose many equivalent definitions for quality factor Q, which is from habit rather taken under its inverse form Q^{-1}. For example, Q^{-1} can be seen as the tangent of the phase-shift between the applied stress and its resulting strain (a result that would be associated to the already mentioned stress-strain phase-shift observation). For our purposes, we will focus on two further interpretations, the first of which conveys a clear physical implication, the second linking Q^{-1} to attenuation α.

De facto, in common physical language, Q^{-1} can be defined in terms of energy:

$$\frac{1}{Q} = \frac{\Delta W}{2\pi W} \tag{4.27}$$

and will appear as the ratio of the energy dissipated per cycle of oscillation, to the peak strain energy W. Obviously, the bigger the factor Q^{-1}, the more it will be affected by attenuation (fast amplitude decay). Another convenience of this formulation is to clearly demonstrate that the quality factor does not depend upon the mechanism by which energy is dissipated [Knopoff and MacDonald, 1960].

Finally, in our attempt to quantify Q^{-1}, we will resort to the definition involving attenuation α:

$$\frac{1}{Q(f)} = \frac{\alpha(f)V(f)}{\pi f} \tag{4.28}$$

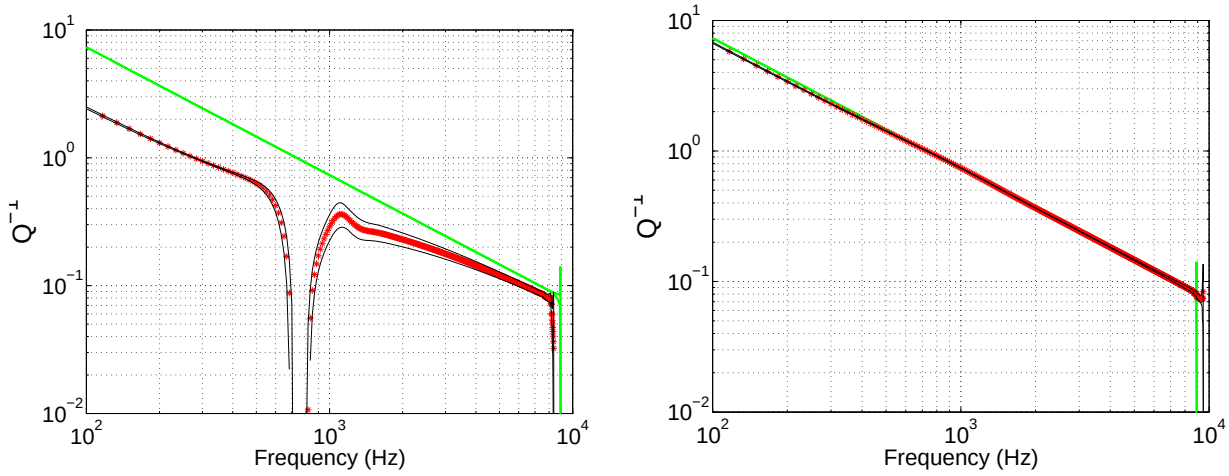

(a) (b)

Figure 4.17: Processing run on the synthetic Gaussian propagating waves. $Q^{-}1$ appears inversely proportional to frequency, as it is expected for constant, frequency-independent, attenuation and velocity.

In this last equation, we introduce frequency-dependent attenuation, velocity and quality factor. As we are to see in the coming section, a given attenuation mechanism gives a particular frequency signature. Hence by comparing theoretical frequency evolution to actual attenuation data, we may recognize the dominant attenuation mechanisms at work and eventually try to model them. In this view, we subsequently present the principal attenuation mechanisms reported in literature.

4.3.3 Estimation of the inverse quality factor Q^{-1} on synthetic

To check the validity of our approach for quality factor determination, a final test is run on our synthetic of Gaussian propagating waves. Again, in figure 4.17, we present two cases, the complete synthetic and the synthetic after first arrival selection, relatively to the ideal case of a sole first arrival presented as a green line. For this ideal case, characterised by constant velocity and attenuation, the inverse quality factor Q^{-1} is expected to be inversely proportional to frequency. And indeed, Q^{-1} decreases by one decade when frequency is increased by one decade. The inverse quality factor resulting from the product of dynamic attenuation and velocity, there is no surprise in recognising similar variations as those affecting attenuation, and more particularly those encountered for the complete synthetic below kilohertz range. The global trend however remains very linear, meaning that the decrease is inversely proportional to a power of frequency, here slightly greater than 1. As for the quality factor obtained after first-arrival selection, it superimpose to the ideal green line of slope $1/f$ as awaited.

4.4 Further information on the actual processing

In order to get interpretable results, our processing programm developed for spectral analysis demanded auxiliary treatments. This went from simple data filtering to the recognition and consecutive discrimination of captors entering their noise level. We rapidly present some

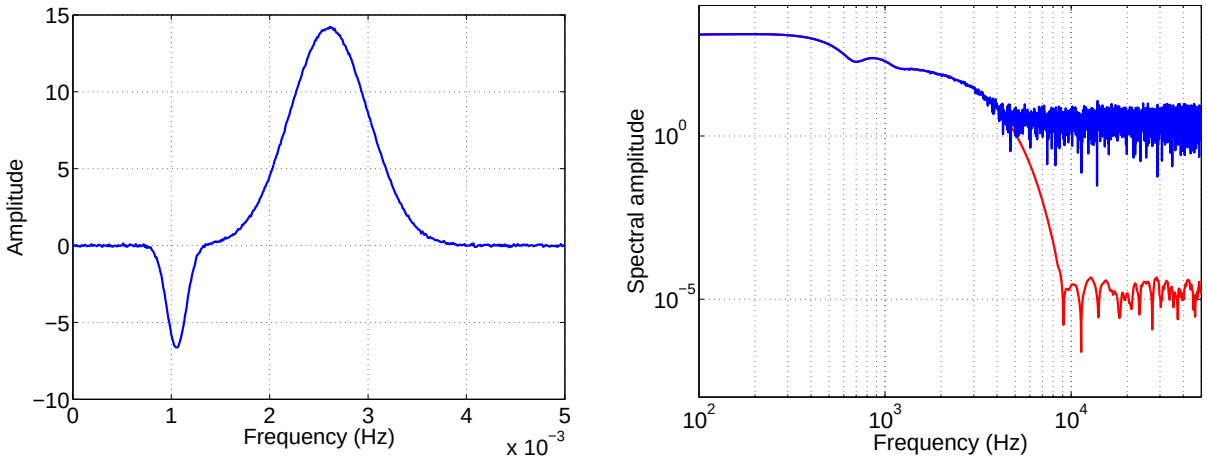

(a) (b)

Figure 4.18: (a) Time record of Gaussian synthetic affected by random noise at offset 15 *cm* and (b) corresponding frequency spectrum (blue) comparatively to the initial noiseless spectrum (red).

specific features of these aspects of the processing.

For this purpose, we added a random noise to our synthetic Gaussian curves, obtained by normal distribution of random numbers, with zero mean and standard deviation 0.05. For the synthetic curve calculated at offset 15 *cm*, the result of noise addition in both time- and frequency-domain can be seen on figure 4.18. In figure 4.18a noisy time-record appears barely different from the original curve (red curve in figure 4.4a). When moving to the frequency domain, while the spectrum with noise addition (blue) does superpose to the original spectrum (red) at lower frequencies, the difference between the two curves at higher frequencies corresponds to a factor 10^5 (see figure 4.18b). Average spectral noise in the original data laid by 10^{-7} to 10^{-5} depending on the receiver position whereas in the noisy synthetic it reached approximately 0.3 ± 0.01 at any offset.

4.4.1 Definition of a water-level

In our processing, the water-level works as a gauge measuring the average noise-level on frequency spectra in order to extract captors approaching the noise level from the computing process. The water-level criteria determines until which frequency a captor can be considered as reliable by calculating the average spectral amplitude on the noise-dominated frequency band [20-50 kHz]. This average noise value is then multiplied by 100 to give the confidence threshold value. If a captor shows a spectral amplitude below this threshold for a given frequency f, it is considered to be within the noise range for any following frequency. It is consequently suppressed from the processed captor-ensemble for increasing frequencies starting from f[4]. Calculation can proceed as long as we can rely on a minimum of 3 'informative' captors. As soon as this condition fails, the calculated quantity is put to zero.

The effect of the water-level application on our synthetics can be seen in figure 4.19. We

[4]Note that for our calculation we usually relied on a series of captors of increasing offsets. Since high frequencies are the first attenuated, the further the receiver, the narrower the exploitable frequency-band. Hence as frequency increases, error bars tend to enlarge as the number of exploitable captors shrinks.

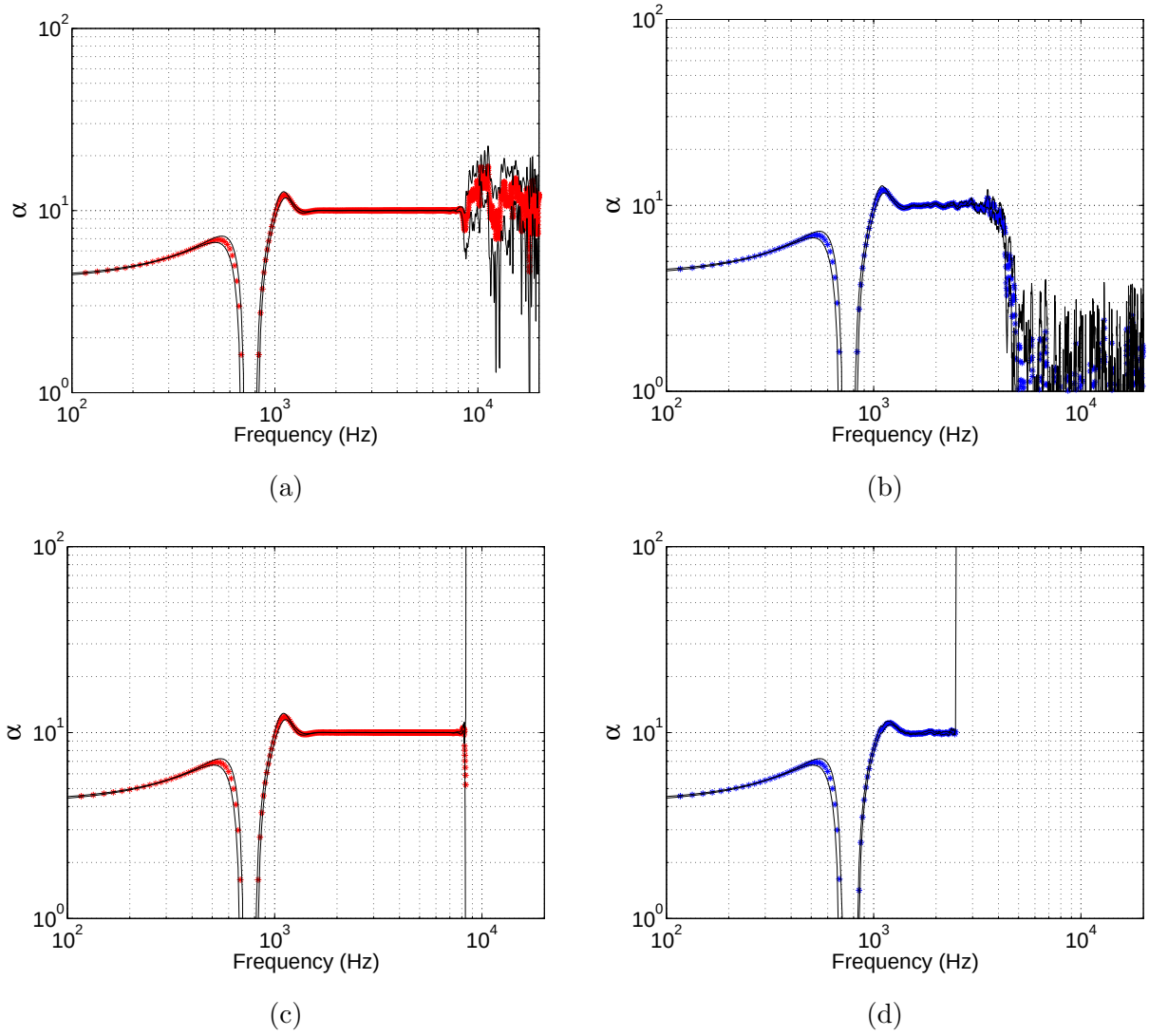

Figure 4.19: Effect of water-level application to attenuation calculation on the original (red) and noisy (blue) synthetic data: (a) and (b) show attenuation calculation with no consideration of water-level whereas (c) and (d) take the water-level into account.

present attenuation calculation related to the original synthetic data (red) next to that obtained after noise addition (blue). In the absence of a water-level (figure 4.19a and 4.19b), for each frequency the programm calculates an attenuation value over the whole set of captors with no concern regarding the quality of its information. Once the water-level applied, calculation is cut as soon as reliable captors are too few (figure 4.19c and 4.19d), corresponding to frequency levels for which calculated values started being unstable in the upper records. As expected noise introduction lowers this limit ; in our example the cutting frequency passes from about 8 kHz to 2.5 kHz.

4.4.2 Spectral smoothing by moving average

In order to smoothen the effect of possible discontinuities in the amplitude and phase spectra due to residual noise, we chose to apply a moving average to spectral data before any further processing. By doing so, every estimation of attenuation or velocity dispersion at a given frequency f has been calculated on spectral value averaged on $[f - 50Hz\ ,\ f + 50Hz]$ the frequency range.

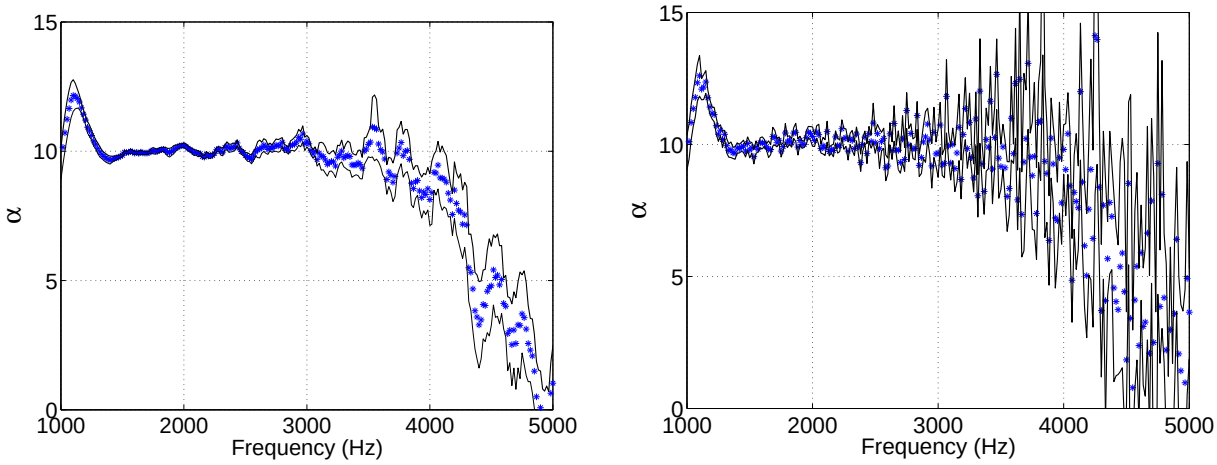

(a) (b)

Figure 4.20: Repercussion on attenuation calculation of moving average treatment on spectral data for synthetic Gaussian waves affected by random noise. (a) Treatment including spectral averaging on the interval $[f-50Hz\ ,\ f+50Hz]$ at each frequency f. (b) Same processing with no moving average treatment.

To illustrate this treatment, we present in figure 4.20 attenuation estimations conducted on our noisy synthetic for both cases. In order to facilitate the observation of moving average effects, dynamic attenuation is represented on a limited frequency band with linear scales. We note that in absence of spectral averaging, singularities in the spectra cause the attenuation curve 4.20b to become hacked and hard to interpret starting from about 2.5 kHz while it would remain interpretable up to 3.5 kHz when a moving average has been applied.

Thus, by stabilising the spectra moving average mitigates noise effects and offers the chance to see a little higher in our available frequency band.

4.4.3 Uncertainty calculation on basis of linear regression

Many of our results (velocities, attenuations, seismoelectric transfer functions) were determined as linear regressions. In a first attempt to evaluate the error on the calculated slope we first resorted to a bootstrap method.

Principle is as follows: from N data-points available noted $n_1, ...n_N$, we would randomly select one out of N before putting it back for possible re-selection. We would repeat this procedure N-times and would eventually dispose of N points, some n_i being possibly redundant, to calculate a slope. The only restrictive intervention would be to avoid selecting N-times the exact same data since slope determination by linear regression demands a minimum of two distinct points. By repeating this whole procedure a number of times, we would dispose of a vast variety of slope estimations. Averaging them with regard to mean-square deviation, would give an estimation on the slope and on its associated error. In our case, for $N \approx 10$, we would reach stable error estimations after averaging the results over 1000 repeated random draws. This procedure was robust, but very time-consuming.

For uncertainties estimation on linear regression Rouaud [2012] proposed an alternate method based on least-square principles. Calculation was more straightforward and very robust. For our data estimation we will rely on this method reported in the appendices

under section 7.3.3.

4.4.4 Filter characteristics

Low-pass filtering was often employed on noisy seismoelectric data and occasionally applied to seismic data obtained under full water-saturation showing a strikingly high frequency content. When in need to get rid of high-frequency components, we applied a classic Butterworth low-pass filter of order 8 with cutting frequency at 15 kHz. By applying this filter onwards and backwards, it was possible to mimic a minimal phase filter in order to preserve the phase spectrum.

4.5 Measuring the electric field: Determination of the optimal dipole geometry

4.5.1 Dilemma of approaching a punctual value of the transient electric field by measuring a potential difference

One specificity of the electric field, is that it can not be measured directly at a single point. As a matter of fact, the most common way of measuring a transient electric field is to appeal to Maxwell-Faraday relation linking $\mathbf{E}(t)$ to the time variation of magnetic induction $\mathbf{B}(t)$. Under static conditions, the Maxwell-Faraday equation simplifies to $\nabla \times \mathbf{E} = 0$. As a consequence $\mathbf{E}$ may be written as the gradient of a potential, giving the well-known relation $\mathbf{E} = -\nabla V$. Hence in electrostatic, the electric field is experimentally deduced from a potential difference measured between two electrodes forming a dipole.

In our present case, we are dealing with a transient electric field, propagating concomitantly to his seismic support. In our experiment, involving a fair volume of sand, measuring the associated induced magnetic field would prove both from logistic and physics point of view even more difficult to measure than the electric field [Bordes, 2005]; we consequently fall back on the usual electric measurement by potential differences. But if this method is approved of to determine static electric field, its relevance for characterizing a propagating time-varying coseismic field is questionable. Observational coseismic seismoelectric has been well-aware of this issue as it ordinarily speaks of raw or normalised potential differences (Garambois and Dietrich [2001], Chen and Mu [2005] and Block and Harris [2006])[5]. Yet, in our attempt to quantify this effect, we must compare our observations to model predictions for which the electric field is ideally determined from the amplitudes of mother seismic waves via a dynamic transfer function. For this purpose, we have to force an estimation of the coseismic electric field out of our static voltage measurements.
This however raises two questions:

- first, how do we associate an electric dipole measurement of non-negligible length, to a punctual seismic acceleration? That is: where should we put the electrodes relatively to the associated seismic receiver?

- second, how does the electric field depends on the dipole-length: can we somehow obtain some stable values of the electric field?

Our experiment was especially designed to investigate these issues. While electric acquisition with common reference enabled us to reconstruct dipoles of any possible length, supernumerary electrodes offered the chance to shift a dipole of given length relatively to its corresponding accelerometer.

[5] A notable exception is the paper by Mikhailov et al. [2000], where the coseismic electric field induced by a Stoneley wave was measured for two dipole lengths, converted into two versions of the electric fields that proved to be in good agreement. However, information regarding the position of the electrodes relatively to the hydrophone location is not to be found in the paper. Consequently we can draw no parallel between this paper and our work.

To identify which dipole geometry was most appropriate, we checked characteristics of the obtained potential differences against two attributes of the inducing seismic wave. First, as it is coseismic, electric first-arrival times should be in good agreement with first arrivals observed on corresponding seismic. Second, we expect analogous frequency contents for seismic and coseismic seismoelectric arrivals for the same reasons, though the proportionality of the electric field spectra to acceleration spectra is not guaranteed on the whole frequency-band due to dynamic dependency. Indeed, major frequency components in seismic should appear in the coseismic electric field even if energy distribution between one and another could be modified. Since, in our experiment, the coseismic event corresponds to the first arrival, comparison of frequency contents could consist in first lobes width analysis completed by time-frequency diagrams.

Finally, while the first two characteristics are best observed on normalised curves, nullifying as such the distinction between voltage and electric field, our last concern specifically refers to the stability of the electric field. Indeed for robustness sake of our quantification process our estimation of the electric field should ideally not depend on the dipole-length. As a consequence, we will favour dipole geometries for which potential differences linearly increase with dipole-length.

The coming sections show the result of this 3-point investigation on electric fields obtained for variable dipole-length and shifting accelerometer/dipole relative localisation.

4.5.2 Evolution of the tension under dipole-length variation

The effect of dipole geometry on the measurement of seismoelectric fields has been a pending issue ever since this phenomenon regained attention in the 90's. A thorough investigation was led by Beamish [1999]. Among other geometrical considerations, he studied the variation of the potential difference recorded for dipoles of increasing length whilst the first electrode was being maintained in a fixed position (see figure 4.21). His observations on metric dipoles tend to show that the observed voltages were mainly controlled by the position of the electrode closest to the source. Voltages were mostly independent of the dipole-length whereas coherent noise components (such as anthropogenic noise) tended to scale with it. Similar observation were made by Strahser et al. [2007] using 2 m and 4 m dipole during field measurements: in the absence of coherent noise however, better signal to noise ratio were obtained for longer dipoles. At this point, dipole-length selection appeared more of an empirical choice to ensure the best signal to noise ratio: shorter dipole-length would be required by high coherent noise component whereas longer dipoles should be favoured when random noise prevails [Strahser, 2006].

As observations reported in literature apparently confront our requirement for a stable coseismic electric field, we propose to check the independency of voltage on dipole-length, already observed at field scale, on our lab-scale data set with the benefit of important electrode density and highly adjustable dipole geometry. For this purpose, we will investigate the potential difference observed for dipole geometry as represented on figure 4.22: supernumerary

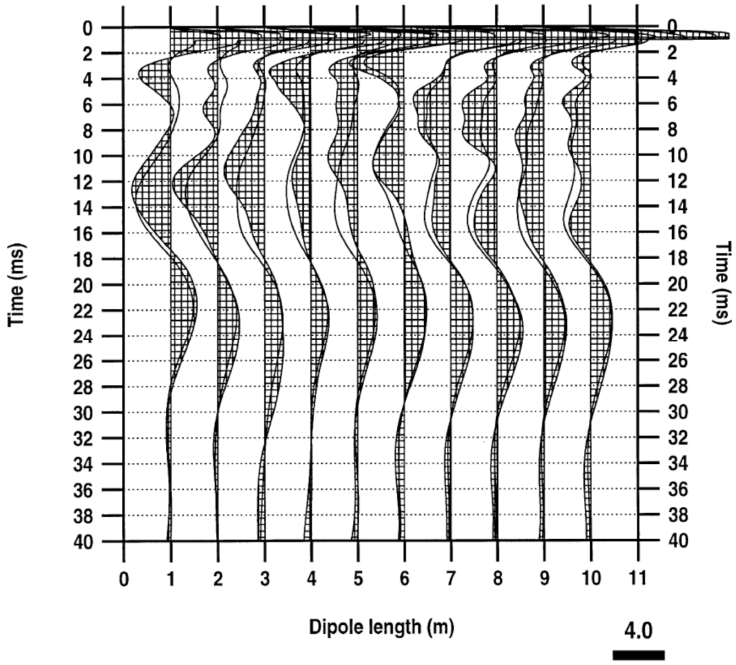

Figure 4.21: Comparison of results obtained by keeping the inner electrode at a fixed location (0.5 m from the shot) and expanding the outer electrode position to provide dipole-length from 1 to 10 m. Channels symmetric to the shot-point are jointly displayed as a single line trace and an infilled trace. Data are true amplitude and can be reported to the yardstick [Beamish, 1999].

electrodes allow to investigate both the effect of dipole-length and dipole geometry relatively to the associated accelerometer which position would coincide with electrode e_N. Regarding dipole geometries, we will distinguish the dipole reconstructions at common first electrode (all dipoles having the electrode e_N in common as pictured in red), from that involving common mid-point geometry (reconstructed symmetrically to the mid-point electrode e_N as pictured in green). The offset of all those dipoles will be taken equal to that of electrode e_N and they will subsequently all be compared to the seismic recorded at e_N position.

Our coming analysis of the effect of dipole geometry on robust measurement of the coseismic electric field will be divided into two sections with complementary purpose: first we will discuss the correspondence between seismic and associated seismoelectric waveforms before focusing on the issue of the stability of the measured electric field.

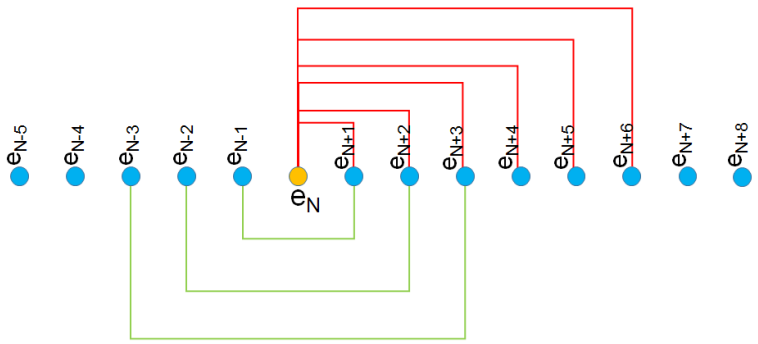

Figure 4.22: Representation of the two geometries of dipole reconstruction at a given offset marked by the N^{th} electrode in yellow. Dipoles in red share e_N as a common first electrode whereas those in green, centered on e_N, are representative of the mid-point geometry.

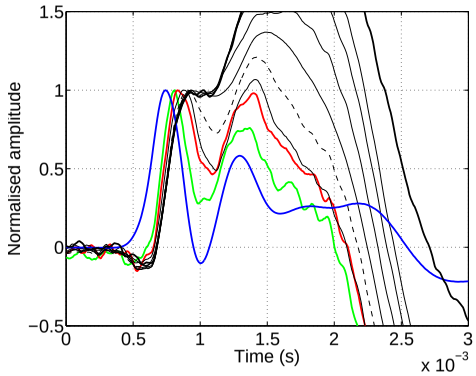

(a) 1^{st} electrode at 4.8 cm

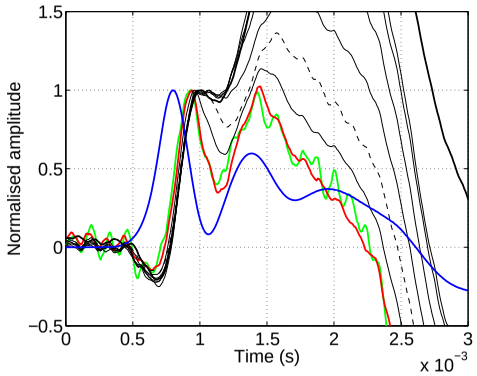

(b) 1^{st} electrode at 5.8 cm

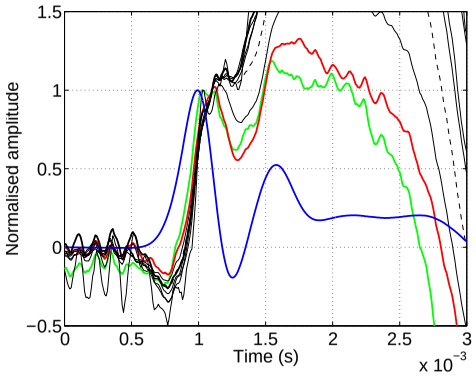

(c) 1^{st} electrode at 7.6 cm

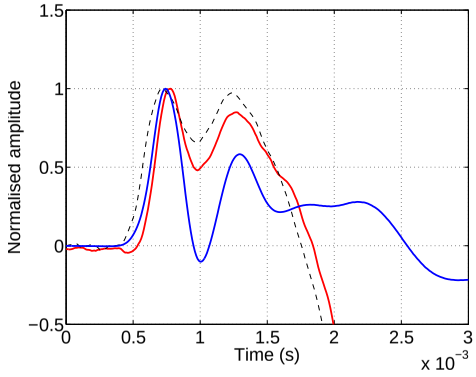

(d) dipole mid-point at 4.8 cm

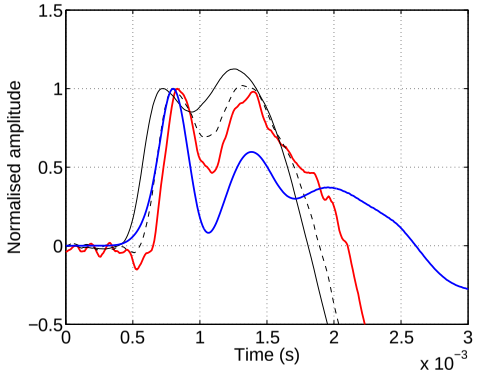

(e) dipole mid-point at 5.8 cm

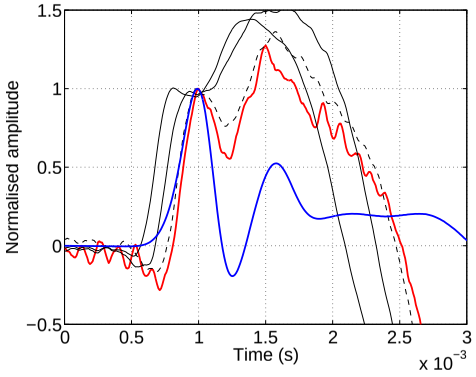

(f) dipole mid-point at 7.6 cm

Figure 4.23: Normalised seismic and seismoelectric data obtained for the experiment '20140305' at offsets 4.8 cm, 5.8 cm and 7.6 cm for both common 1^{st} electrode and common mid-point geometries. Blue curves stand for seismic, green and red curves represent dipole-lengths of respectively 9 mm and 18 mm. Larger dipole-lengths, between 27 mm and 108 mm are represented as thin black lines ; a dotted line materialized the 36 mm dipole-length as it marks the apparition of a clearly identifiable first lobe. Within figures dedicated to common 1^{st} electrode geometry, raw dipoles acquired relatively to the common reference electrode are pictured in thick black lines.

Coseismic electric field likeness to first seismic arrival

Our first task is to identify whether the seismic first arrival is best reproduced by coseismic acquisitions recorded on long or short dipoles. To this effect, we compare seismic and seismoelectric waveforms stemming from real experimental data. As similar waveforms give evidence for similar frequency content, we choose to match curves shape and consider normalised seismic and seismoelectric for various dipole-lengths. By focusing on the morphology of the electric signal we may split up the investigation and momentarily dodge the question of the electric field stability with dipole-length variation. On figure 4.23, we observe normalised data obtained for the sub-saturated experiment '20140305' at offsets 4.8 cm, 5.8 cm and 7.6 cm for both common 1^{st} electrode and common mid-point dipole geometries. Seismic curves are in blue while green and red curves represent the smallest dipole-lengths available, of respectively 9 mm and 18 mm. Further available dipole-lengths from 27 mm up to 108 mm are represented by a variety of thin black lines. The raw dipoles acquired relatively to the common reference electrode, which is located at offset 30 cm, are pictured as thick black lines in the upper figure row.

As we compare characteristic arrival times, it appears that, when considering common 1^{st} electrode geometry, dipole-length has no great effect on the position of the first extremum. In comparison increasing dipole-length at common mid-point dipoles tend to reduce that arrival time, as the first electrode of the dipole concomitantly grows nearer to the source. Hence the relevance of common mid-point geometry would reasonably restrain to the shortest dipole-lengths as to preserve the first break consistency relatively to seismic first arrivals. Yet at this stage, seismic first extremum arrival times appear more consistent with the 18 mm mid-point dipoles than with any reconstruction at common 1^{st} electrode. Determination of the most relevant dipole geometry by first-break comparison is not conclusive: indeed the initial depression in electric records, announcing the coming coseismic arrival, complicates the localisation of the first break. The origin of this often observed electric signature, which importance visibly depends on position of the first electrode rather than on dipole-length, remains unclear. The only conclusion from first-break observation concerns again the warning regarding restricted use of mid-point dipole geometry to short dipole-length. Indeed, first-breaks will shift indefinitely towards earlier times as dipole-length increases, having in the end no direct connection to the seismic field arriving at mid-point location e_N.

When comparing the overall shape of reconstructed potential differences to the original electric measurement relatively to the common reference, we observe that they almost overlap until dipole-length has shrunk down to 36 mm (black dotted lines). From this moment on, the first electric arrival starts to divide into two lobes. The smaller the dipole-length, the more marked the first lobe will be, the more the electric waveform will match that of the seismic first arrival.

This observation is endorsed by time-frequency analysis displayed in table 4.2. In this table, where we restrict ourselves to common first electrode geometry for a question of reconstructed dipoles availability, we compare normalised time-frequency analysis for seismic (on the first line) to those obtained for electric at offsets 4.8 cm, 5.8 cm and 7.6 cm according

to increasing dipole-lengths ranging from 9 mm to 54 mm. Despite the fact that the energy of the coseismic electric arrival rapidly fades away as dipole-length increases, we clearly recognize an equivalent to the seismic first arrival on all electric records; on all time-frequency records, the central arrival time and central frequency of first arrival are reported and indicated by crosses. We attempted to associate a propagation velocity to these markers, yet with some caution, as the maximum energy is associated to the center of the event, often distinct from its local maximum[6]. While seismic first-arrival showed a velocity of about 100 m/s in the time-frequency diagram, first-break time-picking gave $V_p = 170 \pm 12$ m/s. The trade-off might be attributed to the widening of the waveform with propagation possibly due to velocity dispersion. Yet if the comparison between first-break velocity and time-frequency velocity-picking seems hazardous, the comparison of seismic and electric velocity-picking within time-frequency analysis should be comparable. For 9 mm dipoles we evaluated it at approximately 140 m/s, for 18 mm dipoles rather at 110 m/s, while fainter data at larger dipole-length 36 mm and 54 mm showed respective velocity of approximately 210 m/s and 170 m/s. It appears that again on this point, smaller dipole are more consistent with seismic observations.

When looking specifically the electric at offsets 4.8 cm and 5.8 cm we may actually identify two further arrivals on shortest dipole-lengths: first a low-frequency highly energetic signal covering the entire first milliseconds of the record, second, a late arrival of intermediate frequency content. On the same approach as before, we evaluated the its velocity on the time-frequency diagram: it approximates 70 ± 10 m/s. If we assume a similar trade-off as for the first arrival, this event is too fast to be the Biot slow-wave; but it might be associated to a possible S-wave affecting the area close to the source.

[6]Hence, if the time-frequency information associated to a single Gaussian event will center on the Gaussian maximum in the time-axis, that associated to a single period of a sine wave will center at the location of the half-period of the signal where it typically passes by zero.

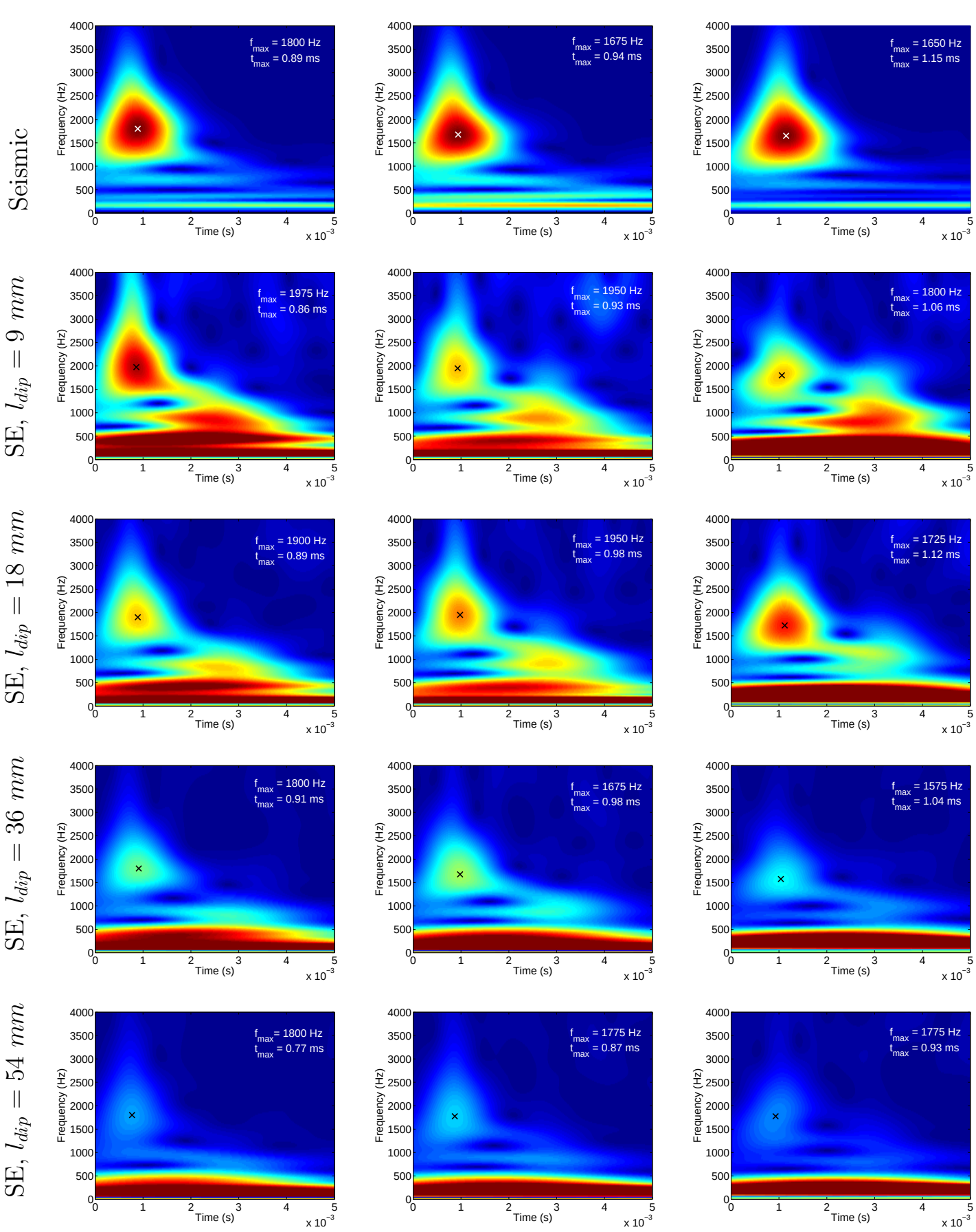

Table 4.2: Frequency content analysis of normalised seismic and SE curves. Left-hand column shows normalised curve for seismic (in blue) and associated SE for mid-point dipoles of 18 mm (in red). Middle column shows seismic time-frequency analysis for normalised values from dark blue (0) to red(1). Right-hand column shows SE time-frequency analysis, here normalised between 0 and 0.6. In each case, the energy maximum attributed to the first arrival is located in frequency f_{max} and time t_{max} by a cross. Note that higher energy is associated to the first arrival in seismic whereas for SE it is poorly located in time and of lower frequency content.

As a global view, central frequency of the first electric arrival tends to decrease with increasing offset of the first electrode. For dipole-length up to 36 mm the electric arrival times are in good agreement with that of the seismic; this consistency is lost for large 54 mm dipoles. Surprisingly the electric coseismic signal appears to be higher frequency than the corresponding seismic which peaks at $1.65-1.8\ kHz$ and shows no clear dispersion for offsets ranging from 4.8 cm to 7.6 cm. This frequency effect may be related to the occurrence of the already mentioned electric signal preceding the arrival of the coseismic signal, as observable in figure 4.23. This often observed signal could contribute to the thinning of the coseismic lobe and the subsequent elevation of its frequency content.

From these observations we conclude that the coseismic electric response better matches the seismic waveform (testifying of comparable frequency contents) for smaller dipole-length. In addition, as the dipole-length exceeds 18 mm, the energy repartition between the electric coseismic effect and the low frequency contribution grows unfavourable: interpretation of seismoelectric records on time-frequency diagrams becomes equivocal. Regarding characteristic arrival times, the observation of electric first breaks is inconclusive and rather rises the question whether first-break reading should take the preliminary depression into account. As for first maximum location, while it appears mainly stable using common first electrode configuration, location agreement with seismic is greater for small mid-point dipoles sharing the same offset. However evolution of such mid-point potential differences as dipole-length increases, eventually leading to anticipated electric field with stretched connection to the seismic field at dipole mid-point location, should prevent the use of mid-point configuration at large dipole-length.

Stability of the electric field

Our second task is to investigate the effect of dipole geometry on the evolution of potential differences with dipole-length. In a first approach we reproduce the geometry investigated by Beamish [1999]: the potential difference is measured on dipole of increasing length for which the position of the first electrode remains unchanged. We will then resume this investigation on an alternative common mid-point geometry (see figure 4.22). Aim of this inquiry is to determine whether a dipole geometry may favour stability of the electric field, or if this stability may be obtained over a limited range of dipole-length.

Observations were again run on the sub-saturated data set $'20140305'$. In a first empirical approach, we superposed voltage curves in real physical units obtained at nearest offsets for either common 1^{st} electrode or common mid-point geometry (see table 4.3). We note that for the first geometry, the voltage waveform does not evolve for l_{dip} dipole-length greater than 18 mm. The maximum amplitude is also barely influenced by the dipole-length. These preliminary observations support literature conclusions stating the major influence of first electrode position on the characteristics of recorded voltage. Conversely, for common mid-point geometry, both the voltage and the location of the maximum appear length-dependent, as hinted in previous section.

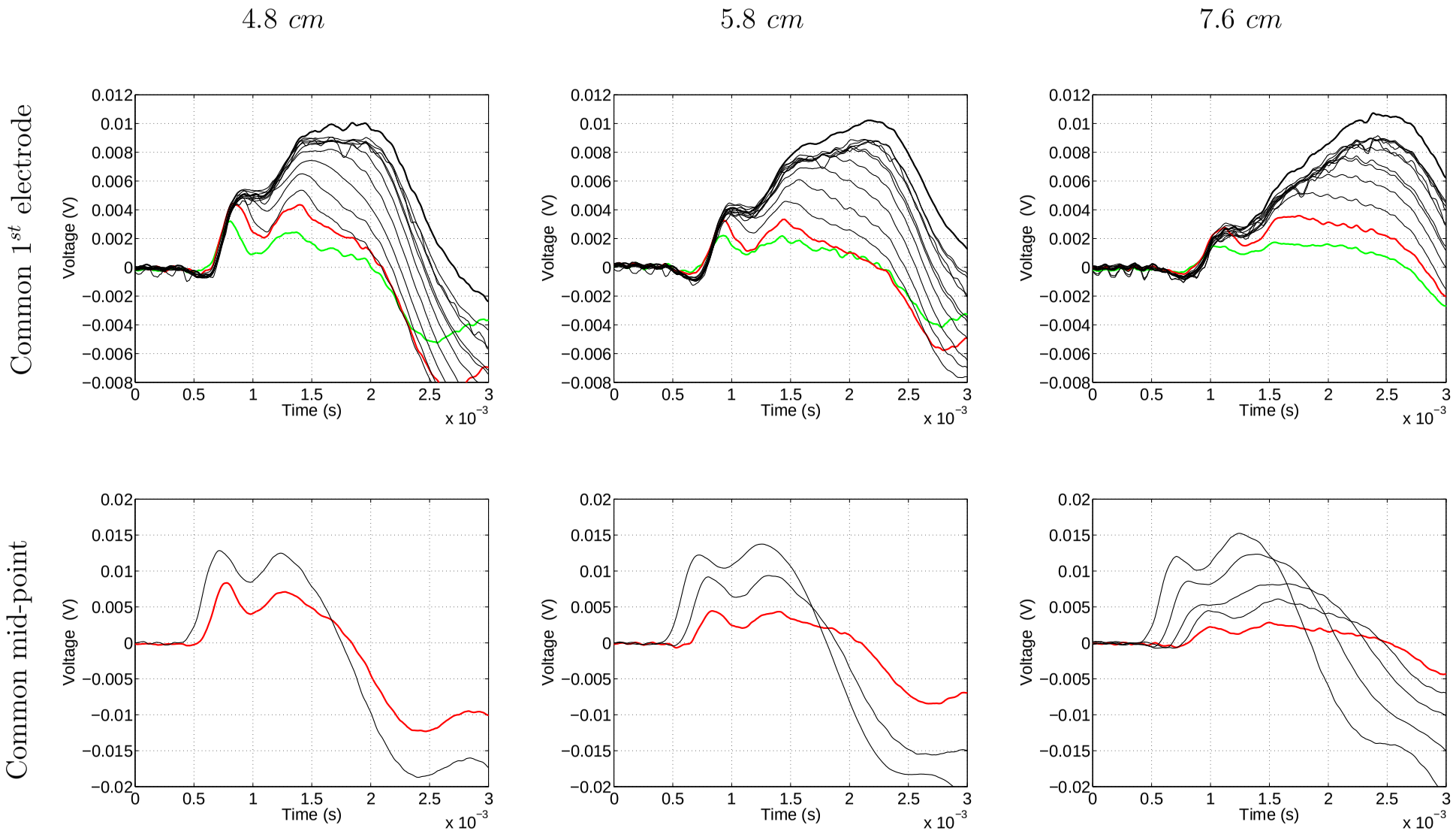

Table 4.3: Potential differences observed at offsets 4.8 *cm*, 5.8 *cm* and 7.6 *cm* for common 1st electrode and common mid-point geometries. Green and red curves represent dipole-lengths of respectively 9 *mm* and 18 *mm*. Larger dipole-lengths, from 27 *mm* and 108 *mm* are represented as thin black lines. For the common mid-point geometry, available curves are in limited number for the electrode array starts at 3 *cm*.

To get a clearer picture, we systematically picked the first maximum at offsets between 3 and 6.7 cm, for dipole-length ranging from the mere electrode spacing of 9 mm to a l_{dip} of 12 inter-traces amounting to 112 mm. For purpose of generalisation, we expressed the varying dipole-length l_{dip} relatively to a local wavelength value λ estimated from the seismic first-break velocity V_p and the central frequency of the first electric lobe for each considered dipole:

$$\lambda = V_p / f_{nom} \tag{4.29}$$

The averaged wavelength λ for our sub-saturated experiment approximates here 17 ± 3 cm.

Results for common first electrode geometry (figure 4.24) appear consistent with field-scale observations. Indeed, for dipole length as little as $\lambda/5$ the potential difference appears mainly independent of dipole-length. According to this observation, we calculated the average voltage on all potential differences associated to dipole length greater than 0.2 λ, and materialised the 5% deviation of this average value at each offset as dotted lines. This constant trend is particularly verified at the two nearest offsets. As the offset increases, lower signal-to-noise ratio intensify the relative disparity, but voltage stability remains clear. This behavior suggests that the coseismic perturbation should be restricted within a distance of 0.2 λ ahead to the seismic wavefront. Note that if stability of the electric field can be reached using common 1^{st} electrode dipoles, then it has to happen within the $[0 - 0.2\ \lambda]$ dipole-length interval. In this portion, the potential difference seems to evolve linearly with the dipole length. Before long, this peculiar linear behaviour of shorter dipoles will be addressed in relation to the stability of electric field estimations

We consider now the mid-point dipole approach. For figure 4.25 we repeated the maximum-amplitude picking-operation while considering a series of dipoles sharing the same mid-point localisation. Again the voltages for offsets spreading from 4.8 cm to 7.6 cm were represented relatively to their l_{dip}/λ ratio. This time however, we restricted our analysis to a maximal dipole-length of 0.4λ. To make this choice, we based ourselves on previous argument regarding the extend of electric field perturbation up to 0.2 λ from the seismic wavefront arrival at mid-point electrode. Having to form symmetrical dipoles relatively to this same mid-point electrode, we came to a largest dipole length of 0.4λ.

For mid-point configuration, potential difference seems to depend linearly on dipole-length, as required to use the linear expression $E = -\Delta V / l_{dip}$. As a result of Ohm's law, stating that a punctual dipole should give no potential difference, we added the point (0,0) to all curves, and traced the best fitting linear dependency of potential difference on the interval $[0 - 0.4\ l_{dip}/\lambda]$. But if linearity seems provided, does it really express the stable value of the electric field? Or is it just a geometrical effect due to proportional increase of the potential difference dipole-length increases and the first electrode of the mid-point dipole approaches the source?

To conclude on the question of the stability of coseismic electric field, we need further elements demanding a more theoretical approach. Yet to do so requires an improved under-

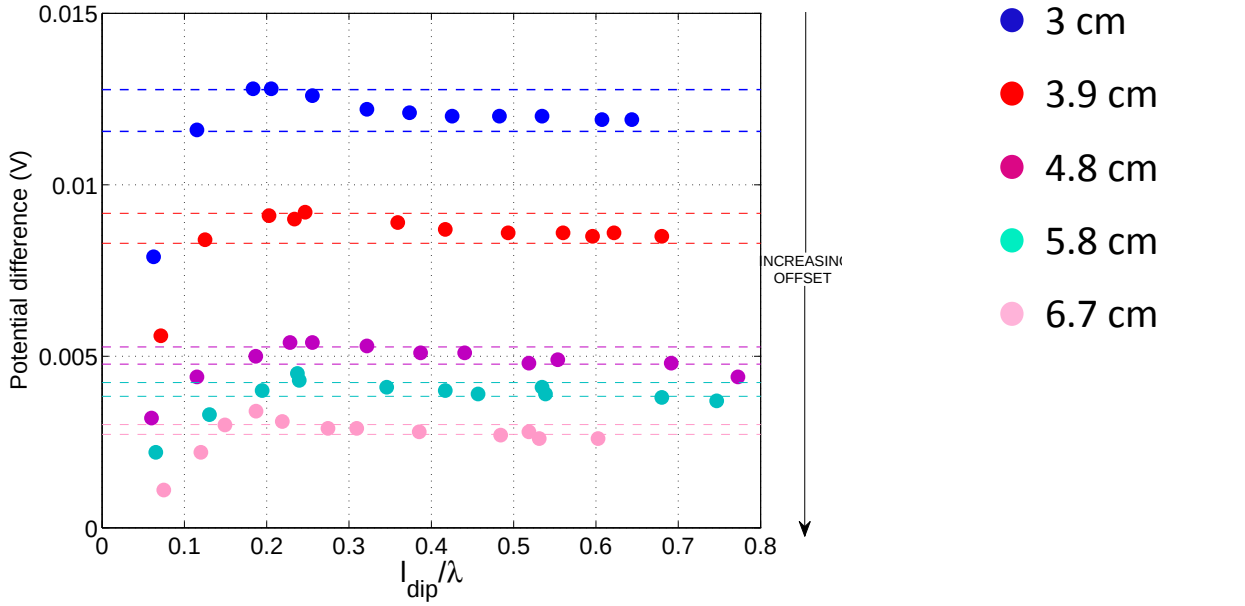

Figure 4.24: Evolution of potential difference with dipole length when position of the first electrode remains unchanged (this position is referenced as the dipole offset). Dipole lengths l_{dip} ranging from 18 mm to 112 mm have been divided by the dominant wavelength associated to their respective first arrivals. Average wavelength λ was grossly estimated at 17 ± 3 cm. We observe that for a dipole length superior $\lambda/5$ the measured voltage appears mainly constant in concordance with field observations previously mentioned. For each offset, a pair of dashed lines mark a deviation of $\pm 5\%$ relatively to an average voltage value estimated from $l_{dip} > 0.2\ \lambda$.

standing of the coseismic electric field. As a prior conclusions, if the stable coseismic field was to be observed, then it would necessarily be on dipole-length smaller than 0.2λ in the common 1^{st} electrode configuration, or on comparably small dipoles for mid-point geometry, for which potential difference does change with dipole-length.

Simple simulation of a coseismic propagating electric field

Observation of constant voltage at common 1^{st} dipole geometry for larger dipole-length may give some indication on the coseismic field behaviour. But before heading in that direction, investigation regarding the dependency of voltage stabilisation on wavelength λ has to be given a larger scope.

For this purpose, we came back to common 1^{st} electrode dipole geometry and investigated further data sets. We gave special attention to records correlated to a velocity increase (due to a moderate rise in water saturation). The directing idea was based on the assumption that the signal central frequency would be mainly determined by the sand bandpass and remain stable, causing wavelength to increase with velocity.

The resulting compilation of first maximum picking, on numerous data for varying wavelength, can be shown in figure 4.26. Dipoles, respectively located at offset 3 cm (blue) and 3.9 cm (red), show again a stabilisation of the voltage for dipole-length approaching $\lambda/5$. The analysis considered wavelength ranging from about 15 cm to 120 cm as saturation in-

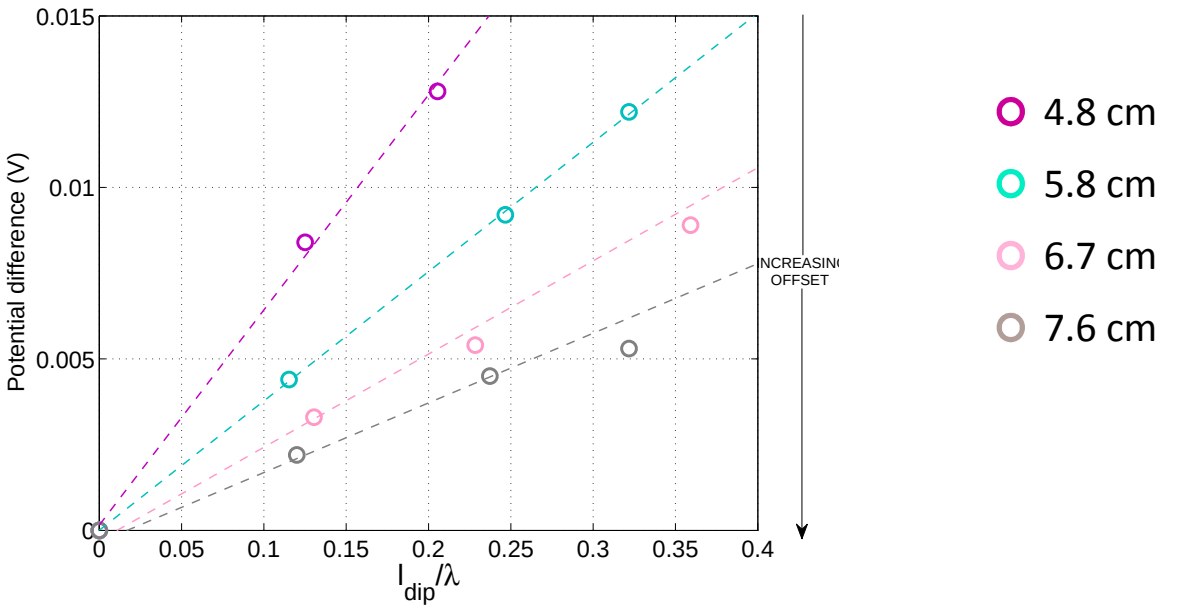

Figure 4.25: Evolution of potential difference with dipole length for mid-point dipoles having common offset (mid-point referenced as the dipole offset). Dipole lengths l_{dip} ranging from 18 mm to 54 mm have been divided by the dominant wavelength associated to their respective first arrivals. Average wavelength λ was grossly estimated at 17 ± 3 cm. Conversely to previous figure, for a given reference offset the voltage seems to depend linearly on the dipole length.

creased from 90% to 100%. All data were acquired during the same imbibition-stabilisation round spread over one month, except for the large blue dots at offset 3 cm, from a previous experiment '20131118' having similar instrumentation but distinct filling. Despite the fact that these last data set do not totally blend into the others, again stabilisation of the voltage occurs for a dipole-length approaching $\lambda/5$. Hence, data cross-checking tend to point a general result that should have a general cause.

The simplest explanation comes from considering that the voltage is calculated as a potential difference between two propagating waves. On this elementary notion, we computed a simple propagating synthetic of central frequency 1 kHz, propagation velocity 230 $m.s^{-1}$ and resulting wavelength of 23 cm. Each signal, standing as a potential difference relatively to a remote common reference, was constituted of two symmetrical Gaussian curves assembled as a sine-wave and computed for offsets ranging from 3 to 20 cm; questions of far and near-field were not taken into account. Finally, a computed electrode spacing of 1 mm allowed for millimetric dipole-lengths in order to get a denser l_{dip}/λ dipole-length array.

This propagating synthetic is presented in figure 4.27 for a selection of offsets between 5 and 15 cm, spaced by a distance of $\lambda/16 \approx 1.4$ cm. First break at each offset is located at the signal intersection with the black line. The first maximum on the upper signal is spotted by a red cross located at t_{ref}. The red dotted line points the amplitudes at further offset for corresponding time t_{ref}. According to this scheme, a voltage plateau should be reached for dipole length starting from $\lambda/4$, as for greater offsets t_{ref} coincides with or precedes the respective first breaks. This critical dipole-length is strikingly comparable to our experimental deduction of $\lambda/5$. Poor resolution on the first-break would explain our underestimating this

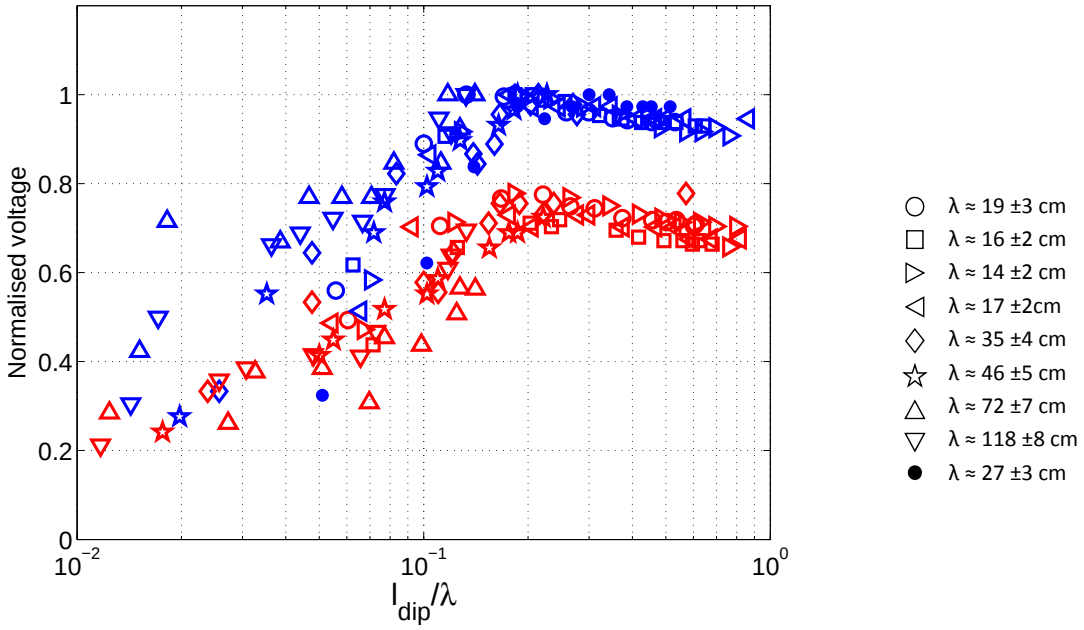

Figure 4.26: Compilation of normalised voltage data for 1^{st} electrode configuration at offsets 3 *cm* and 3.9 *cm* (respectively red and blue signs), obtained for saturation between 90 and 100%. As saturation is under completion the velocity drastically increase and so does concomitantly the wavelength. Red stars ($*$) represent data from a previous experiment round (20131118), all others were acquired during last experiment round. Caption on the right identify the dominant wavelength for each symbol. Voltage seems to stabilise for dipole lengths greater than 0.15 to 0.2 λ

ratio by 0.05 λ on real data basis. This model should also account for the relative stability of the first extremum and first-break locations under variable dipole-length.

We push the analysis forward by calculating potential differences (figure 4.28a) and associated electric field (figure 4.28b) at virtual offsets of 5 *cm* (blue) and 8 *cm* (red), for dipole-length increasing with a 1 *mm* pace up to 0.4λ. Both dipole geometries are considered, common 1^{st} electrode and common mid-point dipoles being respectively represented as dots and circles. As expected, the potential difference at common 1^{st} electrode dipoles stabilises for dipole-length exceeding 0.25λ. On the contrary common mid-point voltages keep increasing indefinitely, though not proportionally to dipole-length as we first considered. Voltages measured by both geometries show good agreement for dipole length inferior to 0.1λ; within that range the voltage increase appears essentially linear.

When moving to synthetic electric field, however, it appears that complete stability is never achieved. Fortunately, for both configurations the electric field converges towards an identical value, say E_0, as dipole-lengths become infinitely small. Hence, for small dipoles both approaches should give very similar results. Yet, an even more interesting observation is the asymptotical convergence of the common mid-point electric field towards this E_0 value as dipole-length nears zero (asymptote materialised as an arrow). In that sense, E_0 appears as the closest approximation of a stable value of the coseismic field.

Particular implication of that mid-point asymptotic convergence, is the slower decay of the mid-point electric field as dipole length increases. As a numerical example, for comparable dipole-length of 0.15λ, deviation of the mid-point measured electric field from E_0 would

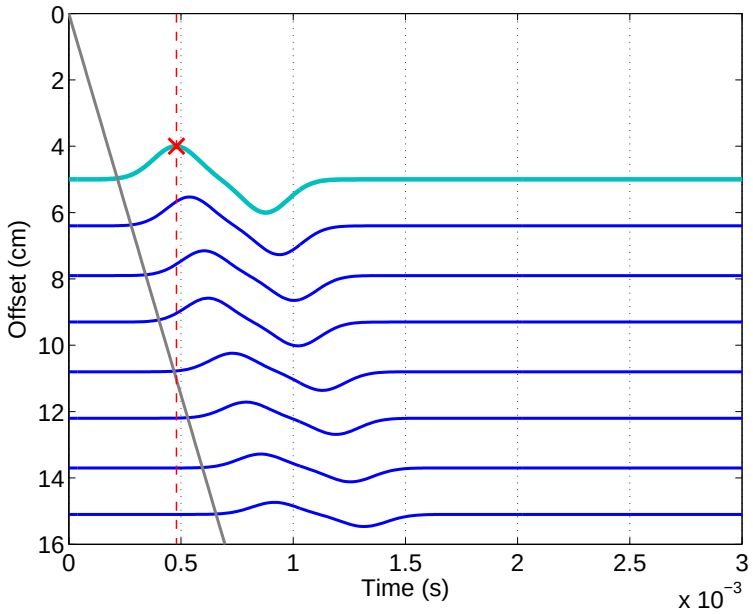

Figure 4.27: Propagation of a synthetic sine wave at 230 $m.s^{-1}$, constructed from two assembled Gaussian curves, with corresponding first arrival line in black locating first break at each offset. Associated wavelength λ being estimated at 23 cm, the represented curves have an inter-trace offset of $\lambda/16 \approx 1.4$ cm. Arrival time of the first extremum at considered offset 5 cm was marked by a red dotted line. Red and black lines meet at a distance of $\lambda/4$ from the considered offset.

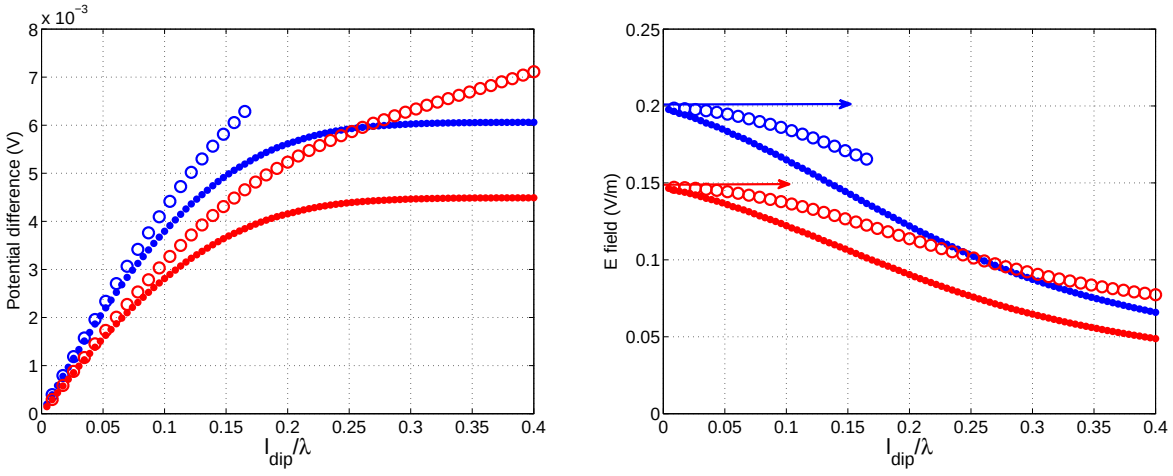

(a) (b)

Figure 4.28: (a) Potential difference calculated on a propagating Gaussian synthetic for either 1^{st} electrode (dots) or mid-point (circles) dipole configuration, relatively to dipole length normalised by wavelength $\lambda =$ 23 cm and (b) associated electric fields. Arrows of corresponding color mark the reached asymptotes for infinitely small dipole length. The dipole offset is considered to be at 5 cm for blue signs and 8 cm for red signs.

be about 14% while it would be twice as important if considering a 1^{st} electrode geometry. Yet for any available mid-point dipole, we can find a 1^{st} electrode dipole twice as small, and for dipole-length of 0.075λ deviation of the electric field measured by 1^{st} electrode dipole is estimated by 12%, being hence comparable to previous smallest deviation ratio. This equivalence between electric fields at small 1^{st} electrode dipoles and twice as large mid-point dipole is documented by figure 4.29 using the synthetic. For a given dipole length l_{dip}, we represented the ratio of the electric field $E_{1_{st}}(l_{dip})$ calculated on first electrode dipole of that given length to the value $E_{MP}(2l_{dip})$ obtained on corresponding mid-point dipole of length $2l_{dip}$. We verified that for very infinitely small dipole that ratio tended towards 1. We then materialised a 5% deviation from unity of this ratio, and noted that this deviation was respected until dipole-length of approximately 0.09λ for 1^{st} electrode geometries or 0.18λ for mid-point geometries.

Coming back to our experimental data and with regard to figure 4.25 it appears that, for a fairly small wavelength of 17 cm, our smallest available 1^{st} dipole of actual length 9 mm is comprised within a interval $[0.05 - 0.08\ \lambda]$. Wavelength of that dimension being at the lower end of our experimental wavelength-range, we note that dipoles of 9 mm length should never exceed 0.08λ. Hence, we should remain within the validity range of satisfactory 1^{st} to mid-point dipole equivalence using smallest available dipoles. We tested this assumption on our data (see figure 4.30). We compiled first arrival maxima of the electric field obtained over a variety of experiment and represented the values recorded for 18 mm mid-point dipoles respectively to that obtained on 9 mm 1^{st} electrode dipoles. As a general trend, these points gather along the identity slope over two orders of magnitude of electric field variations. It accordingly support theoretical observations hinting at the correspondence between 1^{st} electrode dipole and twice as large mid-point dipoles for very limited dipole-length.

Under these circumstances, it seems equivalent to measure the electric field on the smallest available dipole of 1^{st} electrode geometry or on the smallest mid-point dipole, twice as large. Yet, in the absence of coherent electric noise a larger dipole could help enhancing the signal-to-noise ratio. For this reason we would favour smallest dipoles of mid-point geometry.

4.5.3 Characteristics of the chosen characteristic dipole

From previous section we draw following conclusions regarding the characteristic dipole geometry:

- best approximation of the stable coseismic electric field should be equally provided by the smallest 1^{st} electrode or the twice as big smallest mid-point dipoles, but concerns regarding signal-to-noise ratio should favour the largest dipole in the absence of coherent seismic noise.

- the best match between seismic and seismoelectric waveforms is obtained for relatively small dipole-lengths of any geometry, yet characteristic arrival times in seismic seem in better agreement with that observed for the smallest mid-point dipoles.

Shape and stability arguments separately see a small advantage in using the smallest available mid-point dipole. We accordingly selected this configuration, the smallest dipole-length

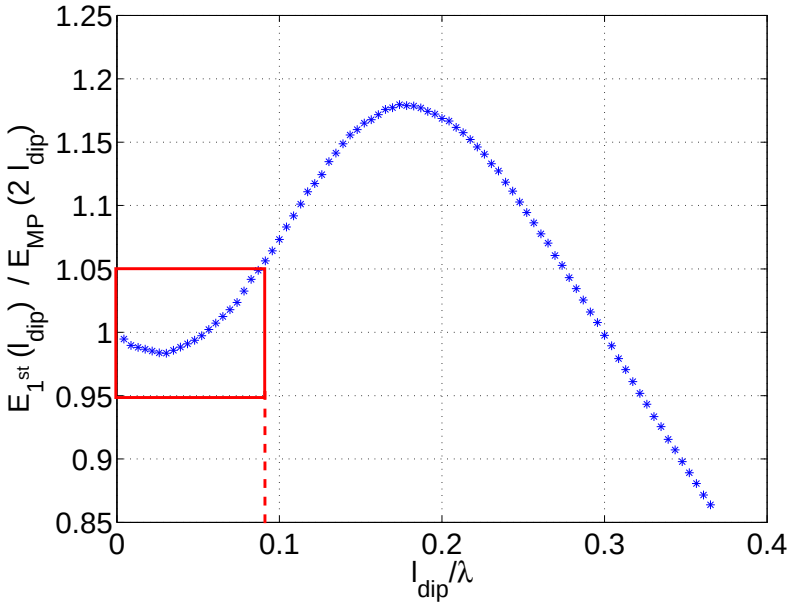

Figure 4.29: Synthetic-based calculation of electric field ratios relatively to the reference dipole length l_{dip}/λ. The ratio is calculated by taking the first-arrival maximum at 1^{st} electrode dipole of length l_{dip} and reporting it to that of the mid-point dipole at same offset of length 2 l_{dip}. The red frame marks the domains for which this ratio stays within a 5% deviation of unity.

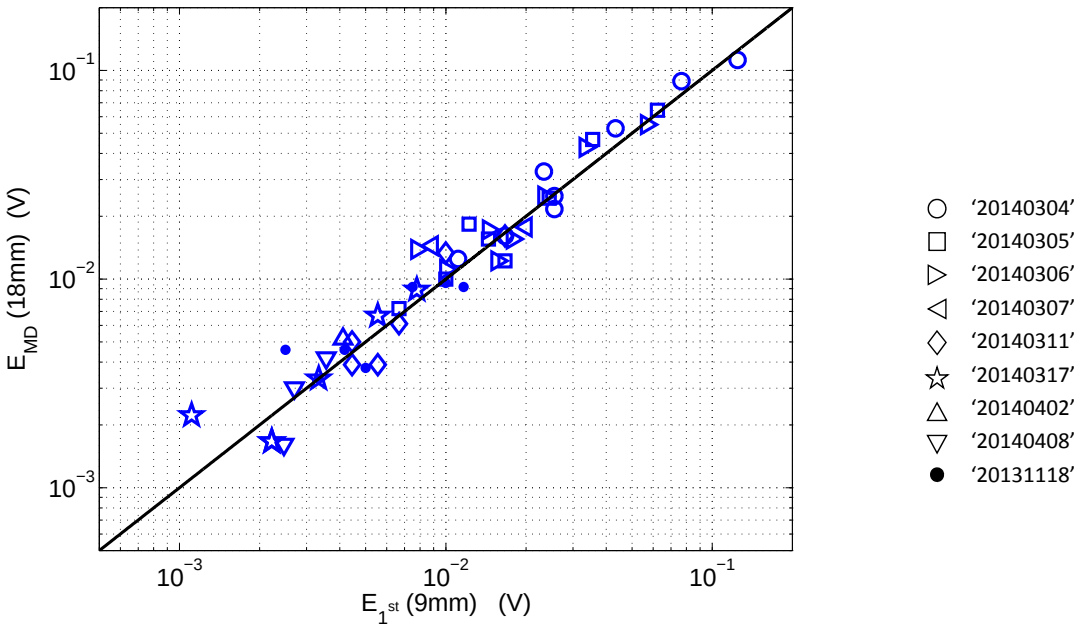

Figure 4.30: Compilation of first-arrival maxima of the electric field stemming from a variety of experiment referenced on the right. Field values calculated on mid-point dipoles E_{MP} of length 18 mm are put in connection to field values $E_{1_{st}}$ obtained on 1^{st} electrode dipole of 9 mm length at corresponding offset. Points tend to gather along the identity line of slope equalling 1.

available for mid-point geometry being of 18 mm for most of our experiments.

In table 4.4, we display normalised curves along with time-frequency analysis for a selection of this seismic-SE pairs distributed every 3.8 cm between offsets of 4.8 cm and 13.2 cm. On the seismic, we see that the t_{max} associated to the maximal energy in the $t-f$ domain, better coincides with the end rather than the maximum of the first lobe: this would indeed correspond to the central point of a complete sine-wave. In electric, this sine-wave first-arrival being rapidly caught up by a second more energetic arrival, its time signature may slightly differ from the corresponding seismic information apparently less altered. In the left column for offsets 4.8 cm and 7.6 cm we notice perfect coincidence between seismic and electric first maxima, matching a reasonable agreement in the time-frequency diagrams, though as noticed before central frequencies of the coseismic electric systematically surpasses that of the associated seismic. For the last offsets we lack a clear detached first arrival on the electric time-records. Conversely time-frequency observation of the electric coseismic signal seems more robust: time-frequency diagrams keep clear track of the coseismic signal, comparable to seismic first arrival in both arrival-time and frequency-content, even when its time-domain signature becomes equivocal. Hence, at offset 13.2 cm, though being hardly noticeable on the time record, a faint first-arrival signature may be recovered in the time-frequency analysis.

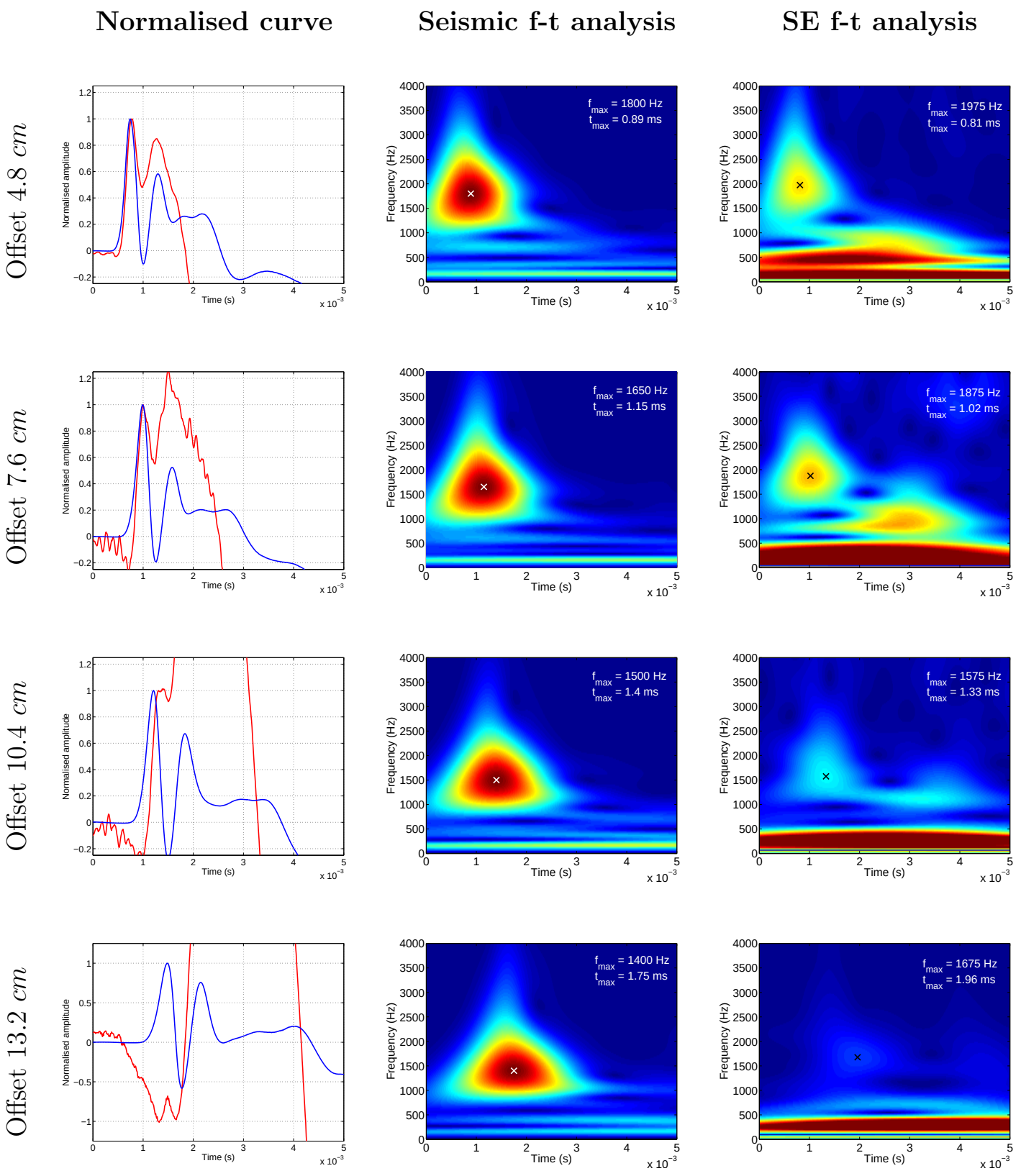

Table 4.4: Frequency content analysis of normalised seismic and SE curves. Left-hand column shows normalised curve for seismic (in blue) and associated SE for common mid-point dipole of 18 mm (in red). Middle column shows seismic time-frequency analysis for normalised values from dark blue (0.2) to red (1). Right-hand column shows SE time-frequency analysis, here normalised between 0 and 0.6. In each case, the energy maximum attributed to the first arrival is located in frequency f_{max} and time t_{max} by a cross. Note that higher energy is associated to the first arrival in seismic whereas for SE it is poorly located in time and of lower frequency content.

4.6 Conclusions

In this methodological chapter we began by introducing and testing signal selection tools developed on seismic to enable the recovering of direct wave information. Tests on a synthetic data set showed that selection of the first arrival by a custom-made Gaussian window permitted to retrieve the spectral signature of the first arrival. But a Gaussian treatment of the time-frequency analysis was unsatisfactory. For this purpose the S-transform, constructed from a Gaussian which width scales with the investigated frequency with analogy to continuous wavelet transforms, would give a better resolution.

Having defined our selection tools, we developed our approach for dynamic investigation of common seismic attributes. We focused on velocity dispersion and attenuation determination that eventually enables to characterise the quality factor. These processing were validated on our synthetic data set, both before and after first arrival selection, and compared to the ideally isolated first arrival. Good agreement between computed and observed attributes of the synthetic signals supported our spectral processing as well as it sustained our first arrival selection process.

In parallel, we investigated the question of the electric field dependency on dipole geometry in order to determine the optimal dipole geometry for coseismic electric field observation. We checked various electric dipole configurations against characteristic features of the mother seismic wave, as central frequency and characteristic arrival times. This analysis pointed a general advantage of small dipoles.

We concomitantly addressed stability issues of the coseismic seismoelectric field. We first verified an observation, previously made at field-scale and reported in literature, stating that the first electrode controls the maximum voltage of the coseismic arrival at any dipole indifferently to its length. On our experimental data, this appeared true for any dipole of length greater than $\lambda/5$. As we looked for a general cause to this repeated observation, a basic calculation of signal difference at two captors for a propagating sine-wave proved consistent with strict stabilisation of such obtained signal for considered captors spacing greater than $\lambda/4$. From similarly computed signal differences, we deduced that, as dipoles grew infinitely small, electric field tends to stabilise towards a finite value E_0 independently from the dipole geometry.

As all criteria spoke in favour of small dipole-length but no real conclusion was given regarding the advantage of one configuration upon the other, we finally chose the shortest mid-point dipole on empirical fit observations and signal-to-noise ratio arguments. Electric measurement were accordingly reconstructed. Finally a good agreement between first arrivals of our original seismic and our reconstructed electric, both in time and frequency, gave fair evidence of our observing the coseismic seismoelectric arrival.

Chapitre 5

Quantitative analysis of seismic and seismoelectric fields

Sommaire

In this chapter we are to perform on real data the methodology previously defined on synthetics in order to conclude on the validity of our experimental process for quantitative coseismic measuring on the one hand, and to discuss the agreement of experimental data with computed projections on the other.

We will start with an attempt at defining the propagation geometry relevant to our experiment on basis of seismic recordings at various saturations. A quick verification on electric records will be made to ensure that data may be accounted for by the same propagation geometry. A subsequent overview of the seismic and seismoelectric spectra will enable us to define our frequency range of investigation.

Once those points cleared, we will be at liberty to run a spectral analysis as to generate velocity dispersion and dynamic attenuation curves. This will be done for three chosen saturation stages, from dry sand to sub-saturated and fully saturated sand. In the sub-saturated case, we will be able to implement spectral analysis on both seismic and seismoelectric, in the other case the analysis will be limited to seismic. By matching experimental curves to poroelastic models in amplitude and shape, we will gain an insight as to the way energy is lost within the system, should it be by strict elastic macroscopic dissipation as acknowledged by Biot poroelasticity, by multi-scale fluid processes or with a viscous contribution of the frame as in the Stoll model.

Then, with the support of seismic data acquired during monitored drainage and imbibition phases, we will engage in refining our poroelastic model. We will see how the observed velocity and attenuation hysteresis may be related to questions of effective fluid homogeneity. These last model refinements will enable us to investigate the evolution with saturation of time-picked velocity, attenuation and inverse quality factor data.

We will eventually broach the quantitative study of the coseismic transfer function. First, we will approach it by local calculation of the $E/\ddot{u}$ ratio on first arrival basis, with regard to its dependency on conductivity. The adaptability and the high impact of parameter σ_f on the coseismic seismoelectric effect will enable testing the reliability of our quantitative measuring process.

Consecutively to this testing, we will tackle the second aspect of our work regarding characterization of the coseismic seismoelectric dependency on water saturation. We will see how the evolution of the $|E/\ddot{u}|$ ratio correlates to that formerly exposed of seismic attributes under varying saturation. Finally, we will conclude on the observability of the dynamic variation of the coseismic seismoelectric transfer function and on leads for possible improvements.

5.1 Attenuation and dispersion of seismic and seismoelectric signals

As shown by the Biot's poroelastic theory, Pride elastodynamic formulation or Stoll model for frictional loss, attenuation and dispersion of seismic waves always stand in connection to petrophysical properties of the medium (porosity, permeability, viscosity, mechanical properties...). These parameters quantifying energy losses may be extracted from the data, using

the different methods presented in previous chapter (as phase unwrapping for estimation of velocity dispersion or amplitude spectral ratio for quantification of the attenuation, both requiring preliminary first arrival selection).

We use here the classical definition of attenuation in the expression of amplitudes $A(f, x)$ for each frequency f and offset x, as described in equation 4.18 from section 4.3.1 reproduced here:

$$A(f, x) = A_r \, G_x \, exp\left[-\alpha(f)x\right] \tag{5.1}$$

where A_r is the typical response of the receiver (already corrected in our data sets), $G_x = 1/x^n$ is the geometrical spreading depending on the propagation geometry, and $\alpha(f)$ the attenuation coefficient. Indeed, the assessment of seismic properties on our experimental data-sets requires the preliminary identification of propagation geometry. This will enable us to isolate the intrinsic seismic attenuation α by accounting for geometrical spreading.

5.1.1 Geometrical spreading estimation on time signals

Propagation geometry should equally affect the data in both frequency and time-domains. Thus, we chose to consider raw seismic record taken in the time domain, in order to determine which geometry of propagation would best explain our data.

We picked maximum amplitudes S_{max} of the first seismic arrival and compared them to expected decays for 1D, 2D, 3D and near field propagation geometries. Geometrical spreading involved in laboratory measurements are generally 1D (waveguides, cores) or 3D (larger scale experiments). Nevertheless, when the receivers are located at offsets shorter than $\lambda/2\pi$, some near field effects can occur (Aki and Richards [2002], Barrière et al. [2012]). Though our experiment was initially designed to avoid these near field effects, in fluid filled medium ($S_w = 1$), P-wave velocity trespasses 1500 m/s, leading to a metric wavelength λ. Since measuring seismic and most especially seismoelectric signals at offsets larger than 1 m would be very difficult due to strong attenuation of seismic waves, we propose to identify data sets affected by near-field propagation to adapt geometrical spreading for attenuation measurements.

For this purpose, in figure 5.1 we tested four data sets illustrating four distinct saturation-scenarios against 1D, 2D, 3D and near-field propagation behaviour. In the upper part of this figure, we show the original seismic data for dry sand ($S_w = 0$), partially saturated ($S_w = 0.50 \pm 0.03$, $S_w = 0.95 \pm 0.03$) and saturated sand ($S_w = 1 \pm 0.03$), along with their first-extremum automatically picked in time-domain. Lower part of figure 5.1 represents the quantity $ln(S_{max}(x)/G_x)$, $S_{max}(x)$ being the local extremum at offset x associated to the first arrival. When the correct G_x is applied, the curve is expected to vary linearly with offset x, meaning a very high R^2 in the linear regression. Black data are related to a near-field behaviour for which geometrical spreading evolves as $G_x = 1/x^2$. For the data in red we consider a 3D propagation for which $G_x = 1/x$ is inversely proportional to the offset, whereas data in green correspond to a 2D propagation with $G_x = 1/\sqrt{(x)}$. Finally data in blue stand for a plane-wave type 1D propagation without any geometrical attenuation ($G_x = 1$).

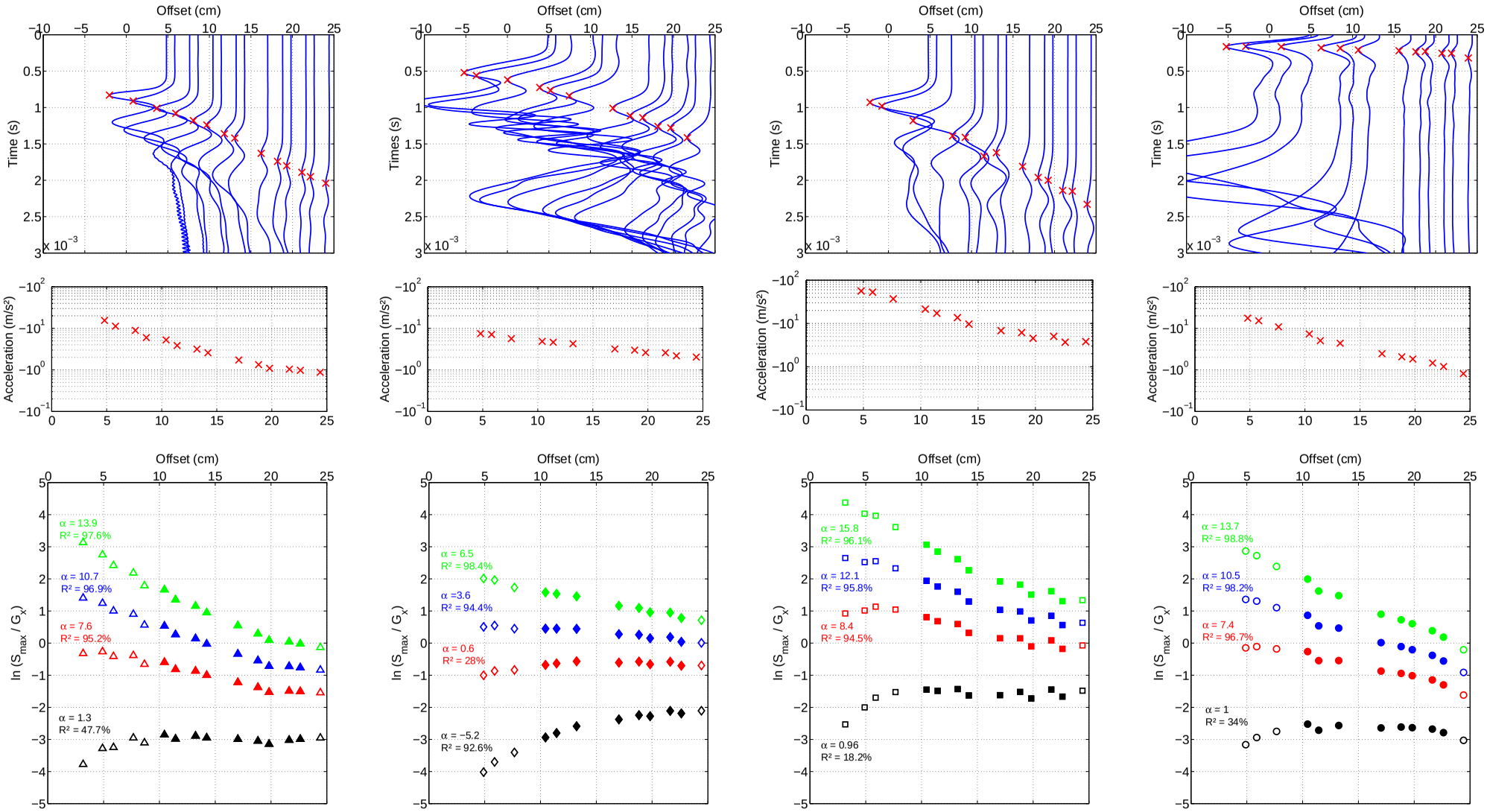

(a) $S_w = 0$ (b) $S_w = 0.5 \pm 0.03$ (c) $S_w = 0.95 \pm 0.03$ (d) $S_w = 1$

Figure 5.1: Test of the quality of linear regression regarding the evolution of $ln(S_{max}/G(x))$ as a function of offset x with respect to different propagation geometries: 1D in green, 2D in blue, 3D in red and near-field in black. The analysis presents different data sets exhibiting variable water-saturation S_w ranging from dry to fully saturated sand, all data acquired with the pneumatic source. Original seismic data and picked accelerations are visible in the upper figure section.

Geometrical spreading in dry and partially saturated sand

A remarkable point is the little dependency from dry sand to sub-saturated sand ($S_w \leq 90\%$) on factor G_x: in this saturation range, the highest R^2 are always obtained for the 1D propagation assumption ($G_x = 1$). This was an unexpected conclusion we sought to clarify by checking the behaviour of the first seismoelectric arrival. In a very similar way, we picked the maximal amplitude of the coseismic direct-wave on experiment '20140305' (figure 5.2) for offsets ranging from 3.9 cm to 11.4 cm (mid-point dipole). We subsequently considered the dependency of the quantity $ln(E_{max}/G_x)$ on the offset, with G_x for 1D, 2D and 3D propagation geometries. A particularity of this data set is the leap observed in the electric field starting from offset 8.6 cm that appears as a general shift of the four last receivers. This feature was found again for similar acquisition geometry in further experiment of the same imbibition round. We tested the processing on a synthetic similar to that use for seismic purpose and can only ensure that this leap is no artifact from the programm. Eventually, the determination coefficient R^2 measuring the quality of the linear regression in seismoelectric data sustains again the hypothesis of a 1D propagation.

As a first explanation, the 1D propagation might have been caused by a specific organization of the sand in the sandbox and along the receivers being not necessarily identical, so that we might have created a waveguide. As a matter of fact, the sand was sieved in the box until it reached the punch, captors where then cautiously placed, sometimes after several attempts. The experiment was then sealed with about the same amount of sand as previously added. In the end, the sand organization might have been more disturbed along the measurement line than anywhere else in the box.

However, there is a second more believable explanation that would implicate the source. As can be seen on figure 3.15a, in the section dedicated to the presentation of the experimental set-up, in order to prevent the sand from pouring out of the box through the hole arranged for the punch of the pneumatic source we covered this hole and the punch with a strong green canvas sheet of 15 $\times$ 15 cm^2. The punch and canvas sheet were coupled by acoustic gel and we expected a good coupling once the box had been filled with sand. Hence, by activating the pneumatic source, the sand possibly saw the whole green canvas sheet as a source. This source dimension being comparable to the size of the experiment and large in regard to the receivers dimensions, the emitted wave may have been perceived by the medium as a plane-wave. Under this assumption, the 1D geometry propagation would not depend on the setting and evolution of our granular medium, but would rather appear as a persistent feature of this experiment.

The amplitude decay analysis could lead to a 1D propagation assumption in partially saturated medium ($G_x = 1$). Nevertheless, this assumption would not be consistent with Barrière [2011] and Barrière et al. [2012]. Moreover, in both seismic and seismoelectric measurements, we notice a specific behaviour of the shortest offsets. These very short offsets may show interferences between first and later arrival as clearly shown in time signals of figure 5.1. These interferences might disturb the linear regression, especially when the later arrivals disturb the waveform of the first arrival (for example at $S_w = 0.5$). At this point,

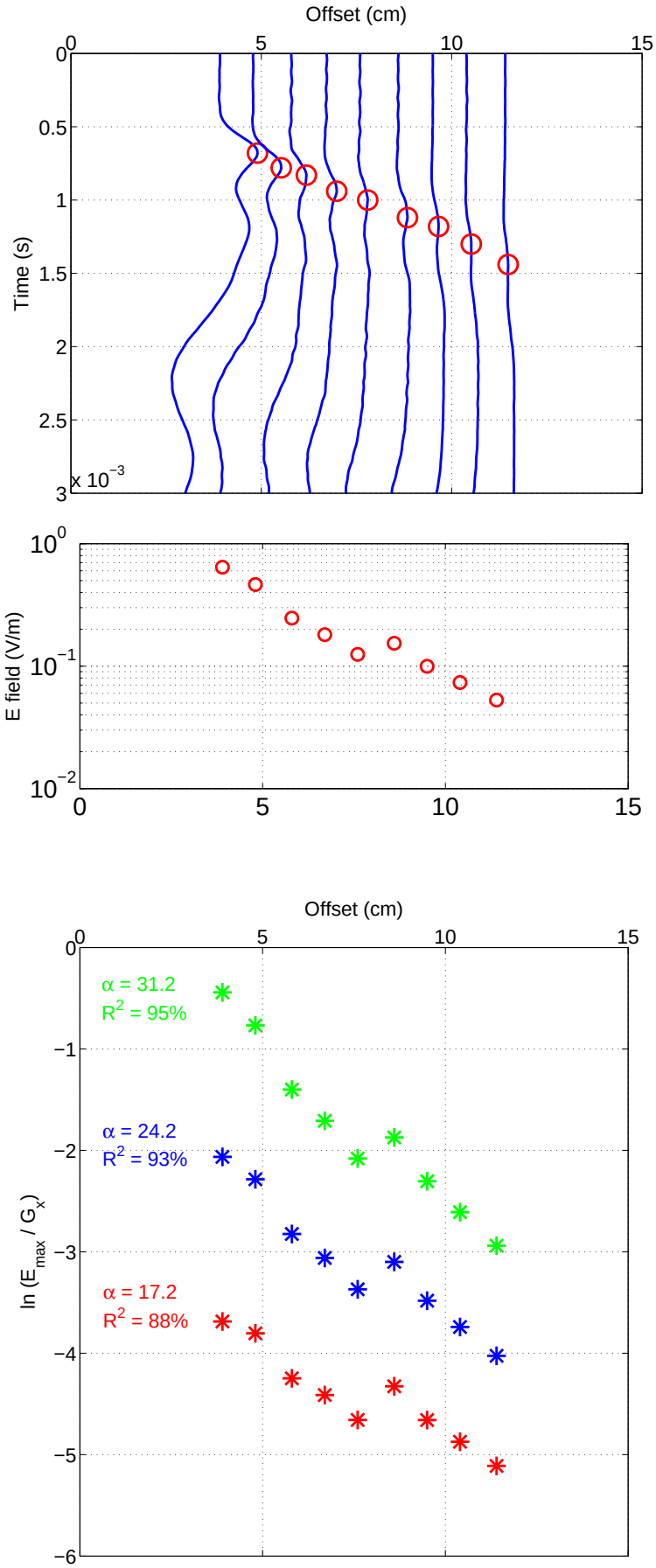

Figure 5.2: Test of the quality of linear regression regarding the evolution of $ln(E_{max}/G_x)$ as a function of offset x for different geometries of propagation. Red markers are associated to a 3D-, blue markers to a 2D- and green markers to 1D-propagation geometry. Data from experiment '20140305' acquired with the pneumatic source at a saturation degree exceeding 90%. Original electric data and picked E field are visible in the upper figure section.

we can not exclude neither 1D nor 3D propagation, and we will keep both assumptions as reasonable options.

Geometrical spreading in fluid-filled sand

Quite surprisingly, when reaching full saturation ($S_w = 1$) the highest R^2 displayed in figure 5.1 is still obtained for 1D propagation geometry, closely followed by residue for assumed 2D and 3D propagations. Yet this result stands in contradiction to computation of typical near-field length L_i (figure 5.3) defined as:

$$L_i = \lambda_i(f)/2\pi = V_i/2\pi f \tag{5.2}$$

Indeed, under full saturation conditions, wavelength λ would typically be multimetric, placing all offsets within near-field for all or some of our frequency band of interest.

Back to figure 5.3, the vertical axis stands for both offsets and near-field lengths. Offsets below the curve L_i would be located in the near field since they are shorter than the near-field length, at the corresponding frequency. We computed L_i for two typical velocities encountered in our experiment: first a minimum (blue curve) curve obtained for $V_1 = 200m/s$ typical of sub-saturated state, second a maximum (red curve) characteristic full saturation having velocity $V_2 = 1600m/s$.

From this figure, it is clear that for frequencies below 1 kHz all offsets are in the near field when the medium is fully saturated (red curve). For offsets larger than 10 cm near-field effect should wear off starting from $f = 2$ kHz. On the contrary, it would be reasonable to assume that under partially saturated conditions (blue curve), all experimental offsets should be out of near-field for frequencies higher than 500 Hz. Nevertheless, we notice that all frequencies lower than 300 Hz may be in the near field, whatever the velocity (*i.e.* the saturation).

Final assumptions for geometrical spreading

From this theoretical demonstration, we chose to consider offsets larger than 10 cm for determination of the seismic P-wave attributes. This would allow to process our data on the same offset range for any saturation, while considering a 3D geometrical spreading, to ensure comparable treatment of all data sets. Maximum offset was settled at 25 cm, being the maximum offset available at full saturation, drainage and secondary imbibition. The limited number of electric quality data available at large offsets prevents us from dealing likewise with seismoelectric, for which any available data is taken into consideration.

Fixing the range of investigated offset also permits to mitigate the impact of a wrongly defined geometrical spreading on the calculation and interpretation of the attenuation coefficient α. Indeed in section 4.3.1, we concluded that the error on the attenuation for mistaken propagation geometry would be a constant bias depending on the range of considered offset. Estimation of attenuation bias given on real data basis in table 5.1 supports our theoretical analysis. As expected from table 4.1, for offset ranges of approximately $10 - 25$ cm, α_{1D} differs from α_{3D} by approximately 6.5 ± 0.5 (when we expected 6 on synthetics) and from α_{2D}

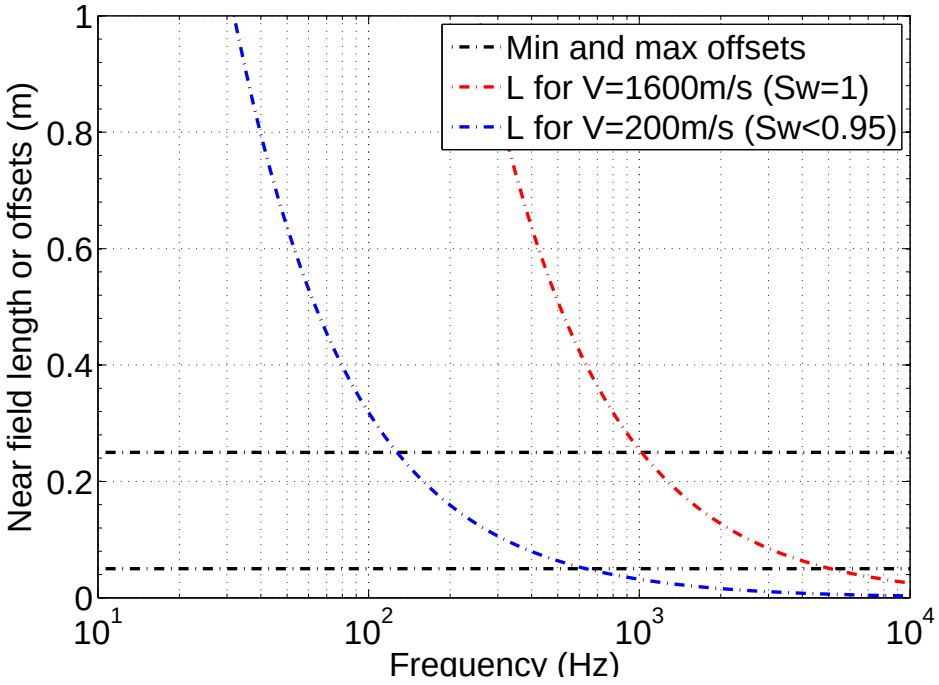

Figure 5.3: Near field length L for extreme velocities 140m/s and 1600m/s measured in our experiments. Measurements in fluid filled medium are expected to be in the near field.

Reference	S_w	α_{1D}	α_{2D}	α_{3D}	α_{NF}	Offsets	Frequencies
D-20140304	0	13.9	10.7	7.6±	1.3±	$10-25\ cm$	$1.25-0.4\ kHz$
20140408	0.5 ± 0.03	6.5	3.6	0.6±	−5.2±	$10-25\ cm$	$0.8-0.55\ kHz$
20140305	0.95 ± 0.033	15.8	12.1	8.4±	0.96±	$10-25\ cm$	$0.8-0.5\ kHz$
F-20140408	1 ± 0.033	13.7	10.5	7.4±	1±	$10-25\ cm$	$0.8-0.5\ kHz$

Table 5.1: Attenuation values depending on the choice of the geometrical spreading for data sets presented in figure 5.1. The error on attenuation values are given with a 80% confidence-interval. Further information regarding the span of offsets concerned by linear regression estimate as well as central frequencies of the first arrival at these extreme offsets are given. All data were acquired using a pneumatic source.

by 3.3 ± 0.4 (when we expected 3). This remains true for all presented experiment data acquired with the pneumatic source, and show the great importance of geometrical assumption for the relevance of attenuation measurements. Eventually, we will compute attenuations in partially saturated medium for both assumptions: 1D using all offsets, and 3D using offsets larger than 10 cm. In fluid filled medium, we will compare 3D and near field assumptions.

5.1.2 Seismic and seismoelectric spectral analysis

In previous chapter we defined how to characterize frequency-dependent attenuation $\alpha(f)$ and velocity dispersion $V_p(f)$ knowing geometrical spreading G_x. This processing involves several steps:

- A preprocessing including dipole reconstruction (mid-point), stacking and filtering procedures;

- First arrival selection using a Gabor window scaled on characteristic times of the first

arrival;

- Computation of linear regressions on amplitude spectra, for each frequency, and accounting for geometrical spreading G_x. This processing allows us to get the attenuation $\alpha(f)$;

- Computation of linear regressions on phase spectra, for each frequency. This processing allows us to get the phase velocity $V_p(f)$;

- Computation of the inverse quality factor $Q^{-1}(f)=\alpha(f)V_p(f)/\pi f$.

In the coming part, the analysis of three sets of data, representing dry sand, sub-saturated and fluid-filled sand, are to be shown. These data sets will respectively be referred to as $'D-20140304'$, $'20140305'$ and $'F-20140408'$. On these data sets, we will try to recognise main patterns of our dispersion and attenuation curves, in possible connection to existing attenuation models. The validity of attenuation and velocity results obtained by spectral analysis will also be checked by direct picking in the time domain.

Main frequency content

The spectral analysis first needs to define a frequency range where signal to noise ratio might be sufficient to ensure reasonable interpretation of the data. The figure 5.4 displays frequency spectra of the aforementioned three data sets for both seismic and seismoelectric signals. In this figure, frequencies lower than 500 Hz were not displayed since they might correspond to near field (see figure 5.3).

Seismic data presented here were recorded at offsets 4.8 cm, 10.4 cm and 17 cm; for electric data on the other hand, recorded in mid-point geometry with dipole length 18 mm, seismoelectric signals would only be observed within approximately 10 cm to the source. Consequently we present offset 4.8 cm and 10.4 cm when available. Besides the Fourier transform of the complete record in dashed lines, we present spectra as plain lines resulting from first arrival selection using a Gabor window. Following this section, all analysis will be lead on spectra resulting from signal selection.

A first striking feature is the absence of coseismic seismoelectric signal in dry sand where no electrokinetic phenomena can occur. Having no signal to pick, we only represent full-record spectra for dry-sand electric data. We note that all electric curves superpose, recording the same background noise. Interestingly, the dipoles pick higher noise level within dry-sand than once in partially or fully saturated condition.

On dry sand seismic, it appears that the signal is composed of two distinct frequency packages: a first in the 100 Hz order, a second in the kilohertz range. This subdivision can also be found in figure 5.4c where a gap in spectral amplitudes at 1 kHz separates the two frequency contributions. The selective attenuation of higher frequencies, however is more marked on dry-sand data: the frequency-shift of the M-formed spectra actually affects attenuation analysis up to 1500 Hz. If the effect remains observable on sub-saturated data it appears less dramatic and the influence is restricted to frequencies inferior to 1 kHz, so that spectral data may be used starting from the near-field limit frequency of 500 Hz under sub-saturated conditions. On the seismic, we also notice that spectra are broader

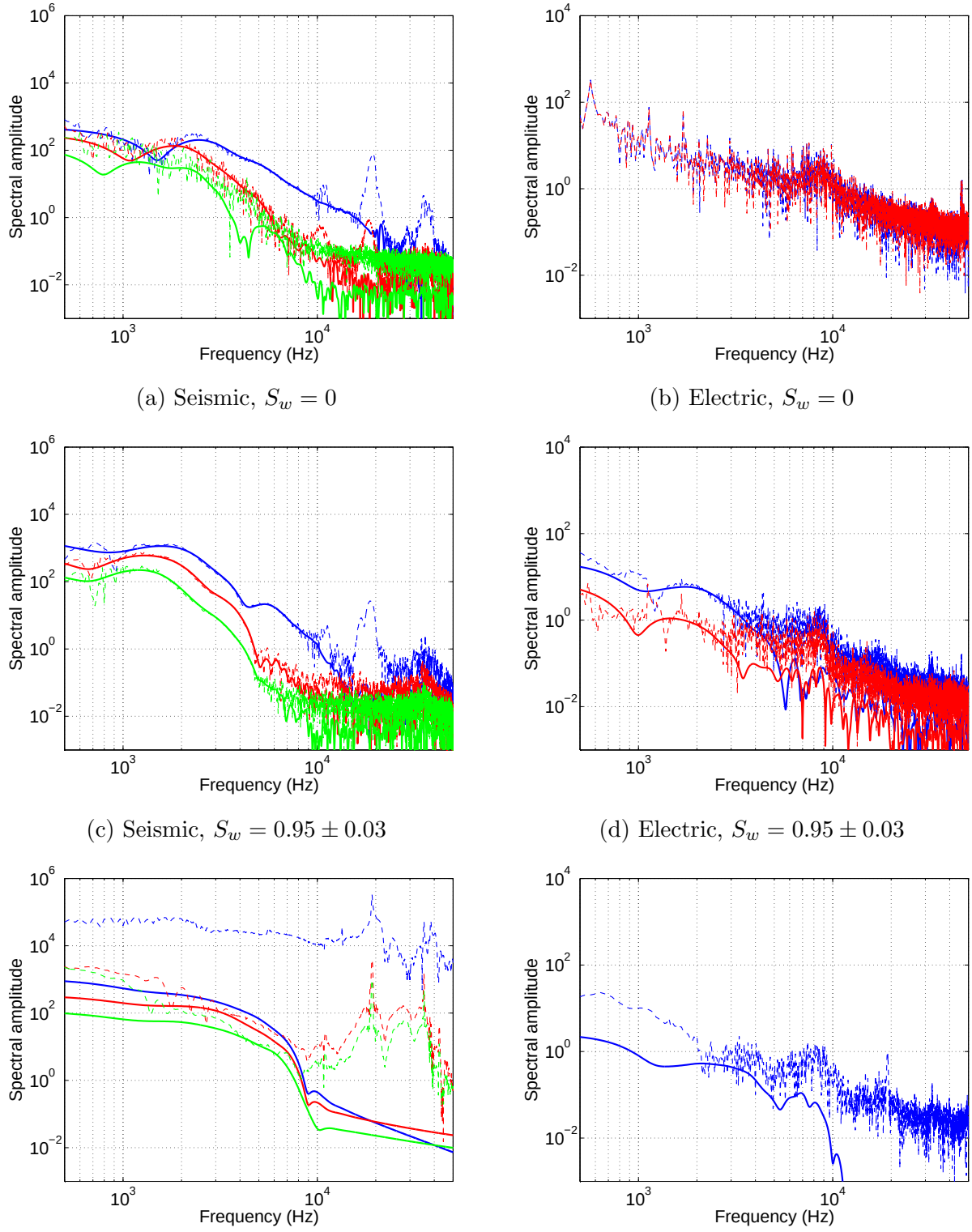

(a) Seismic, $S_w = 0$

(b) Electric, $S_w = 0$

(c) Seismic, $S_w = 0.95 \pm 0.03$

(d) Electric, $S_w = 0.95 \pm 0.03$

(e) Seismic, $S_w = 1 \pm 0.03$

(f) Electric, $S_w = 1 \pm 0.03$

Figure 5.4: Spectral data for seismic and electric receivers at 4.8 *cm* (blue) and 10.4 *cm* (red) and 17 *cm* (green - this last offset being only relevant for seismic), on dry, sub-saturated and fully saturated sand. Spectra in dashed lines were obtained on full records, whereas those appearing as thick lines are the result of first arrival selection; an additional low-pass Butterworth filter was applied on data at full saturation. We note a drop in the spectral amplitudes in the lower frequency band, particularly visible on seismic in dry sand.

band in fluid-filled medium, going from a limited range of $[1.5-3]\ kHz$ on dry sand, up to $[0.5-7]\ kHz$ when being fully saturated. Medium frequency range for sub-saturated data lays by $[0.5-5]Hz$ for seismic and $[1-3]kHz$ for seismoelectric signals. As described in section 4.1.1, we will always keep an eye on our time-picked results when working in the spectral domain, by using the nominal frequency f_{nom}, corresponding to the typical period of the first arrival, as a reference frequency for comparison of velocities and attenuations obtained by spectral analysis and time picking. For sub-saturated data f_{nom} would typically range between 500 Hz and 1.5 kHz.

Finally, the very large peak observed at 19 kHz, on figures 5.4a and 5.4c for seismic receiver 4.8 cm, corresponds to the resonance frequency of the source plate, as mentioned in section 3.2.1. It is interesting to notice that this resonance is not transmitted to further offsets within the medium until it is fully saturated. This phenomena may be the consequence of an improved coupling between the source and the medium combined to some strong changes in high frequency attenuation. This second effect will be discussed in following sections.

Dry sand

Applying the spectral analysis on data sets $'D-20140304'$, we get the results shown in figure 5.5; the study on geometrical spreading remaining inconclusive, we represent attenuation results corresponding to both 1D and 3D propagation geometries. Attenuation, inverse quality factor and velocity results obtained by direct picking in the time domain are represented by blue crosses. The discontinuous aspect of our dynamic curves when tending towards higher frequencies, traduces the retrieval of a captor coming too close to noise by passing below the water-level. Its contribution is suspected to be noisy and it is consequently subtracted from linear regression. As a consequence, the slope is less constrained: uncertainties grow at once and the curve may drift moderately.

Estimation of propagation velocity does not depend on the chosen geometrical spreading, they will be the same for 1D or 3D propagation assumptions. Velocities obtained here by spectral analysis and time picking are comparable, being respectively of $155 \pm 5\ m/s$ and $170 \pm 5\ m/s$ for a frequency of $1000 \pm 250\ Hz$. A Biot model for fast P-wave velocity is represented on the same figure: predicting a velocity of 175 m/s at comparable frequencies, the model appears in good agreement with the data, showing almost no velocity dispersion. As a generality, time-picked estimations appear mostly compatible with the results of spectral analysis. This good agreement supports our attempt to associate a nominal frequency to our time-domain data. It also echoes Bourbié et al. [1986] (pp.112) affirmation that, should the attenuation be reasonable, evolution of the peak amplitude may be taken as the attenuation at central frequency of the signal.

In section 5.1.1 we noticed from time signals of figure 5.1 that the for small offsets to the source later arrival may merge with the first one: at these offsets, the phase of first arrival may hence be disturbed by the later wave, leading to unexpected low velocities and large errors in spectral analysis. To prevent this from happening, we chose to consider only offsets with a minimum distance to the source superior to 10 cm. In sub-saturated and saturated

media, seismic first arrival should be better separated from later one.

In the dry sand, we expect very low velocities due to unconsolidated frame, with possible attenuation due to grain to grain friction. The simplest way to express these viscoelastic losses may be the Biot-Stoll model as formulated by Kimura [2007]. In this paper, the introduction of complex frame moduli enable to account for viscous losses at grain contact. Simple expressions allow the calculation of velocity dispersion as well as asymptote to the attenuation and quality factor at low and high frequency. Conversely, to the Biot model, only accounting for losses induced by fluid-flow, this model may be computed in the absence of water to estimate viscous losses due to sole grain friction on dry sand. In this case, by considering pores filled with air, it would provide us with low-frequency asymptotes to $\alpha(f)$ and $Q^{-1}(f)$ (here for our usual permeability of 20 D and a characteristic pore size diameter of $d_p = 60\ \mu m$). The obtained asymptotes follow the trend of the measured data, showing that in the LF domain P-wave attenuation α_p appears proportional to the square root of frequency $f^{1/2}$. Eventually, the Biot-Stoll model in dry sand is quite close to $\alpha(f)$ and $Q^{-1}(f)$ with the 3D assumption.

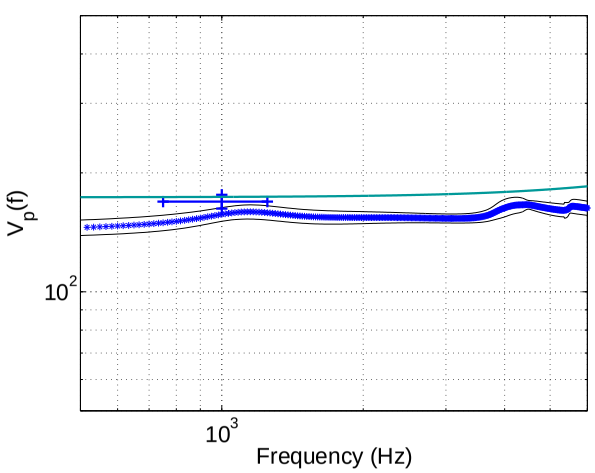

(a) $V_p(f)$

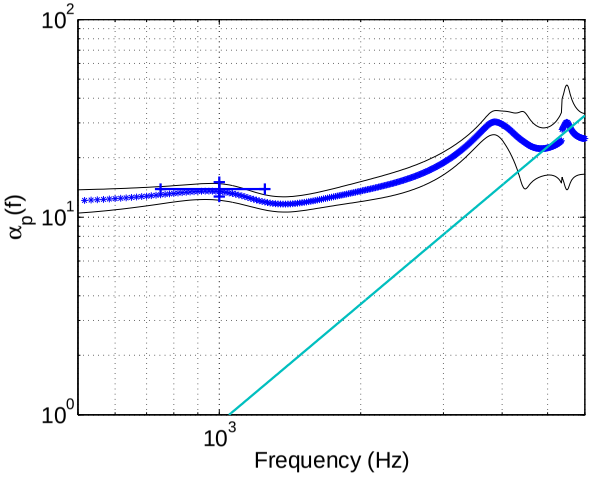

(b) $\alpha(f)$, 1D propagation

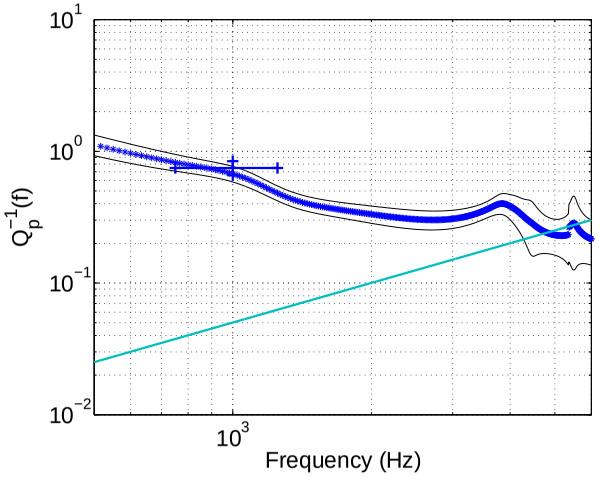

(c) $Q^{-1}(f)$, 1D propagation

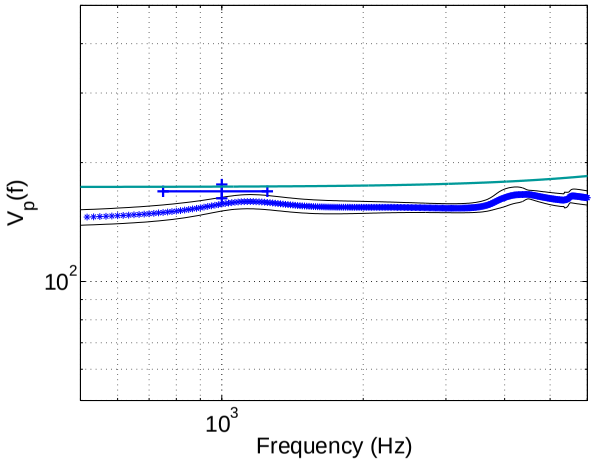

(d) $V_p(f)$, (same as (a))

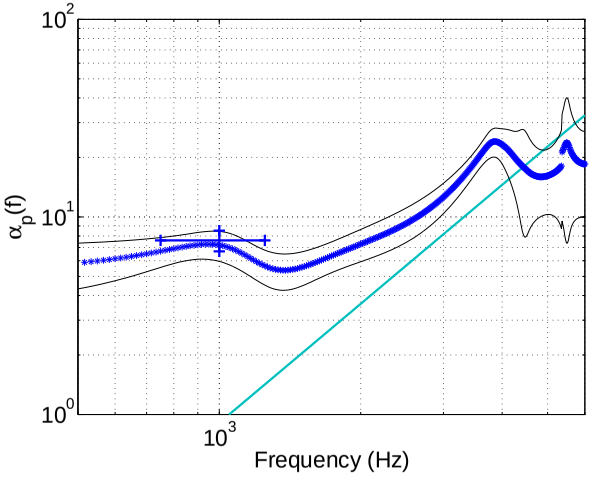

(e) $\alpha(f)$, 3D propagation

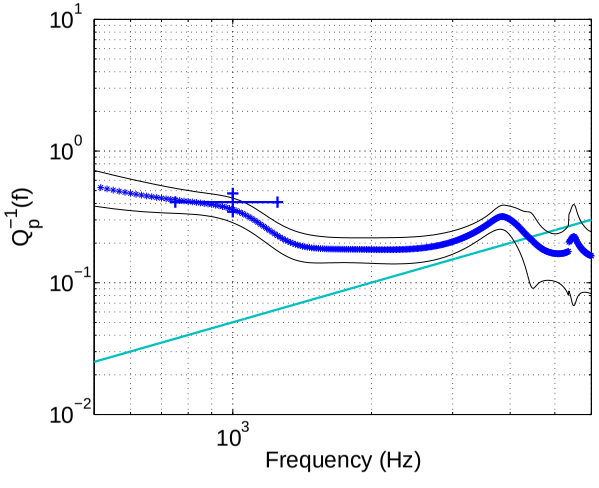

(f) $Q^{-1}(f)$, 3D propagation

Figure 5.5: Spectral analysis of seismic characteristics on dry unconsolidated sand for 1D (a,b,c) and 3D (e,f,g) propagation geometries. Linear regression for attenuation and phase velocity was conducted on captors between offsets 10 and 23 *cm*, confidence on the error bars is of 80%. Our local picked data are superimposed as blue crosses. On attenuation and inverse quality factor figures, blue lines are associated to the LF asymptote of Biot-Stoll model, whereas we used $\tilde{V}_p$ to represent velocity dispersion (see eq. (2.66)).

Partially saturated sand

We applied the same processing on data set $'20140305'$, for both seismic and seismoelectric measurements with 1D and 3D assumptions. Again, the time-picked estimations appear mostly compatible with the results of dynamic velocity and attenuation analysis in seismic measurements. For 3D propagation geometry, we may compare to our curves the results obtained by Barrière et al. [2012] on the same material under sub-saturated conditions ($S_w = 0.9 \pm 0.05$) for a frequency of $1700 \pm 100\ Hz$ (black crosses).

While, for seismic, the agreement between spectral analysis, model and time-picked data remains satisfactory, velocity and dispersion curves for seismoelectric measurements on figure 5.6 show a clear gap in velocities measured at low frequencies. The velocity measured in seismoelectric measurements reaches extremely low values around 70 m/s, when seismic measurements show a $140 - 180\ m/s$ velocity.

As a possible explanation, we suggest the already mentioned depression observed on electric record previously to the coseismic arrival. This event appears to enlarge with increasing offset, so that the delay between this drop and the first break actually picked increases with the offset. This observation raises the question whether the first break should be picked ahead or after -as we currently do- this event of small amplitude. Another explanation might be proposed concerning the extremely low velocities at lowest frequencies as resulting from a contribution of the Biot slow wave described in section 2.3.2. Indeed, we can not spare any electric records, hence while seismic is taken for offsets from $10 - 23\ cm$, we have to consider electric data much closer to the source, between $3 - 12\ cm$, for which fast P-wave arrivals may be tainted by S-wave or Biot slow wave components. Nevertheless, further signal processing would be necessary to confirm the residual contribution of such slow wave in seismoelectric data.

For attenuation and quality factor, we represented the prediction by standard Biot theory, along with the two LF and HF asymptotes to Biot-Stoll model. We see that Biot model does indeed converge towards the LF asymptotes as frequency decreases. Yet for our frequency domain of predilection $[1 - 3\ kHz]$, at a given f, LF asymptotes by Biot-Stoll (thick plain line) would predict energy losses two to five times higher than those announced by Biot (dashed curve). As was theoretically predicted in section 4.3.1, attenuation and inverse quality curves will be shifted downwards when changing a 1D for a 3D propagation geometry. In this last case, the measured attenuations come in close vicinity to Biot-Stoll asymptotes.

Yet, while seismic attenuation might near Biot-Stoll for a 3D propagation geometry, for a given frequency, attenuation measured in seismoelectric signals is about twice higher than that from seismic signals, no matter the considered propagation geometry. It is not possible, at this point, to ensure we do not have any bias in our dispersion and attenuation measurements. Nevertheless, this gap in apparent velocity and attenuation is very clear in figure 5.7 where we show the seismoelectric signals (red) for the characteristic dipole geometry, along with the corresponding seismic (blue). All curves were normalised relatively to the E-field or acceleration peak-value at common offset 4.8 cm. By doing so, normalised seismic and electric records may be compared while relative amplitude decrease is respected. In this matter, the electric peak amplitude appears to be attenuated much faster than its seismic

equivalent leading to stronger attenuations measured on E-field. If seismic and electric co-seismic first peak location seem in good agreement for nearest offsets (4.8 cm to 7.6 cm), first break velocities diverge by nearly $50 m.s^{-1}$.

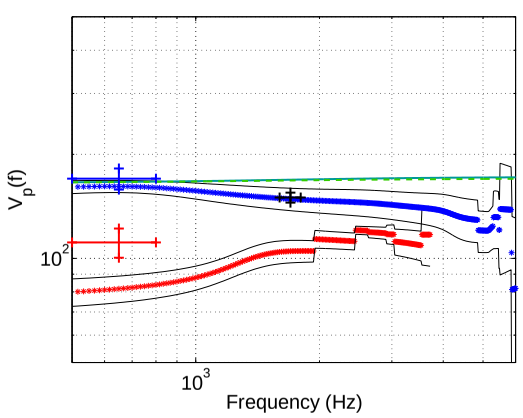

(a) $V_p(f)$

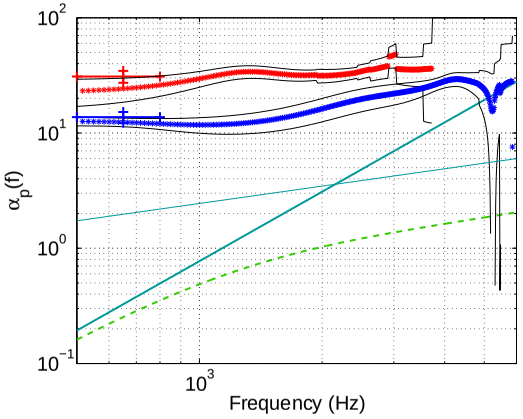

(b) $\alpha(f)$, 1D propagation

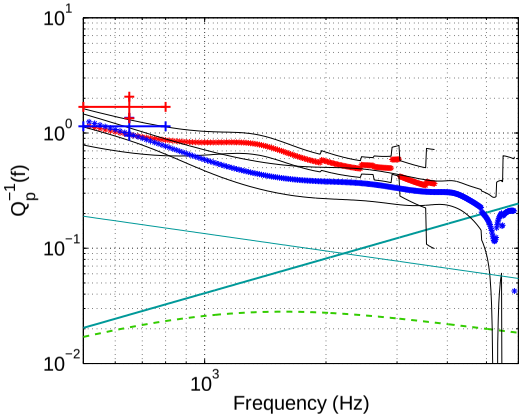

(c) $Q^{-1}(f)$, 1D propagation

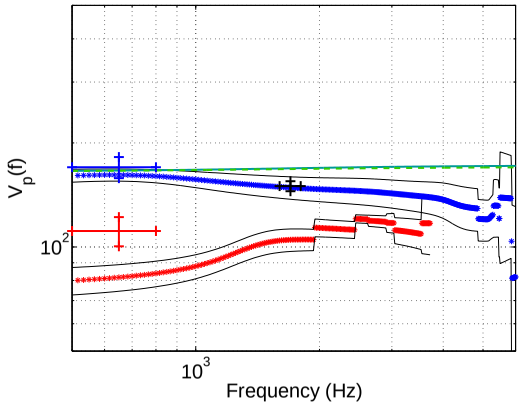

(d) $V_p(f)$, (same as (a))

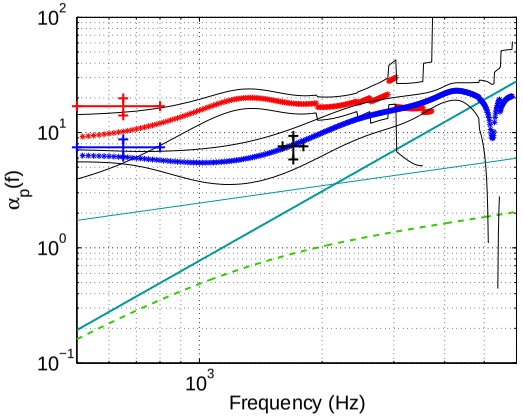

(e) $\alpha(f)$, 3D propagation

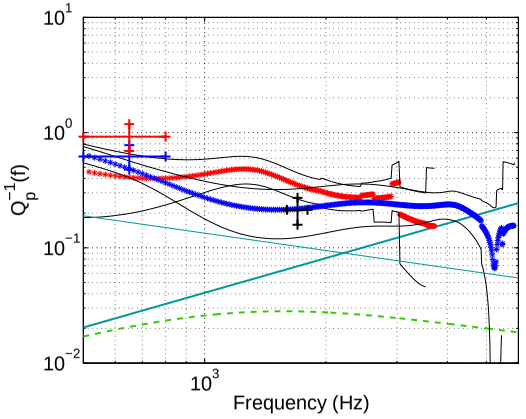

(f) $Q^{-1}(f)$, 3D propagation

Figure 5.6: Spectral analysis of seismic (blue) and electric (red) characteristics on sub-saturated sand ($S_w = 0.95 \pm 0.03$) for 1D (a,b,c) and 3D (e,f,g) propagation geometries. Linear regression for attenuation and phase velocity was conducted on seismic captors between offsets 10 and 23 cm and on electric mid-point dipole of length 18 mm between 3.9 and 11.4 cm (only captors with available electric signal), confidence on the error bars is of 80%. Our local picked data are superimposed in corresponding colors; results by Barrière et al. [2012] for 3D propagation geometry, acquired on the same sand under sub-saturated condition, is represented as a black cross. On attenuation and inverse quality factor figures, thick and light blue lines are respectively associated to LF and HF asymptotes of Biot-Stoll models, the green while dashed line shows prediction by regular Biot poroelasticity. Velocity dispersion curves by Biot and Biot-Stoll almost superpose. Models correspond to an effective fluid modulus calculated after the Wood model (K_R) with a $d_p = 60$ μm effective pore diameter.

Eventually, α and $Q^{-1}(f)$ measurements performed within the 1D assumption are systematically higher than predictions from all models and Barrière et al. [2012] measurements as well. Nevertheless, the results using 3D assumption are in good agreement with results from Barrière et al. [2012] and Biot-Stoll model, especially in the 1-2kHz range of seismic measurements. This hints at supporting the 3D propagation geometry assumption. Attenuation predicted by standard Biot model are significantly lower than the measurements since they do not account for losses due to grain to grain friction.

Water-filled sand

A similar processing was applied on data set $'F-20140408'$ obtained on a sand fully saturated by water electrolyte, focusing on 3D propagation and near-field assumption. Yet this time, despite the occurrence of a seismoelectric field, our analysis restricts to seismic. Indeed, a rather elevated fluid conductivity caused the seismoelectric signal to be only available at the first three dipoles, making the data poor material for attenuation calculation by linear regression. Results showed in figure 5.8, were obtained after using a Butterworth low-pass filter on the seismic data.

Proof for full saturation achievement was given by a first-arrival time-picked velocity of $V_p = 1635 \pm 57\ m/s$ (blue cross), here exactly correlated to Biot and Biot-Stoll models for phase velocity estimation, and consistent with the experimental dispersion curve. Both model and experimental curves agree in showing very little dependency of P-wave velocity to frequency. Large error bars on figure 5.8d, may be related to a time-resolution reaching its limit under such high propagation velocity. A further supporting element to full saturation achievement was the increase of nominal frequency f_{nom} associated to the first arrival, usually ranging between $[0.6-1]kHz$ and reaching here 1.8 kHz: it testifies from a global increase of the frequency content, associated to a general lowering of the attenuation level.

While we practically experienced this decrease in intrinsic attenuation by observing an overall increase of amplitude spectra in unfiltered full seismic records and most particularly a persistence of a high $19kHz$ component at furthest offsets (see figure 5.4e and figure 3.23), when considering 3D propagation the average attenuation at 1 kHz is estimated to be $\alpha_{3D} = 7.4 \pm 0.7$ at full saturation. This value is exactly comparable to that of $\alpha_{3D} = 7.4 \pm 1.2$ obtained for sub-saturated conditions supposed to be highly attenuative. Such contradiction between time and frequency-related observations at full saturation on the one hand, and the surprising evolution of α_{3D} when reaching full saturation on the other, should be enough to justify the exclusion of 3D geometrical spreading at full saturation.

With regard to the wavelength and its associated near-field characteristic length (figure 5.3), the most sensible assumption would be to consider all receivers to be near-field. By this process, the average levels of attenuation and inverse quality factor are mechanically decreased, coming nearer to the Biot-Stoll asymptotes, though not matching the form of the LF asymptotes in the least. A striking feature of the α and Q^{-1} curves, is the collapse they experienced starting from $[2-3\ kHz]$, eventually leading to non-physical negative values. This transition possibly corresponds to the frequency at which receivers at furthest offsets start to come out the near-field zone: geometrical correction of the geometrical spreading

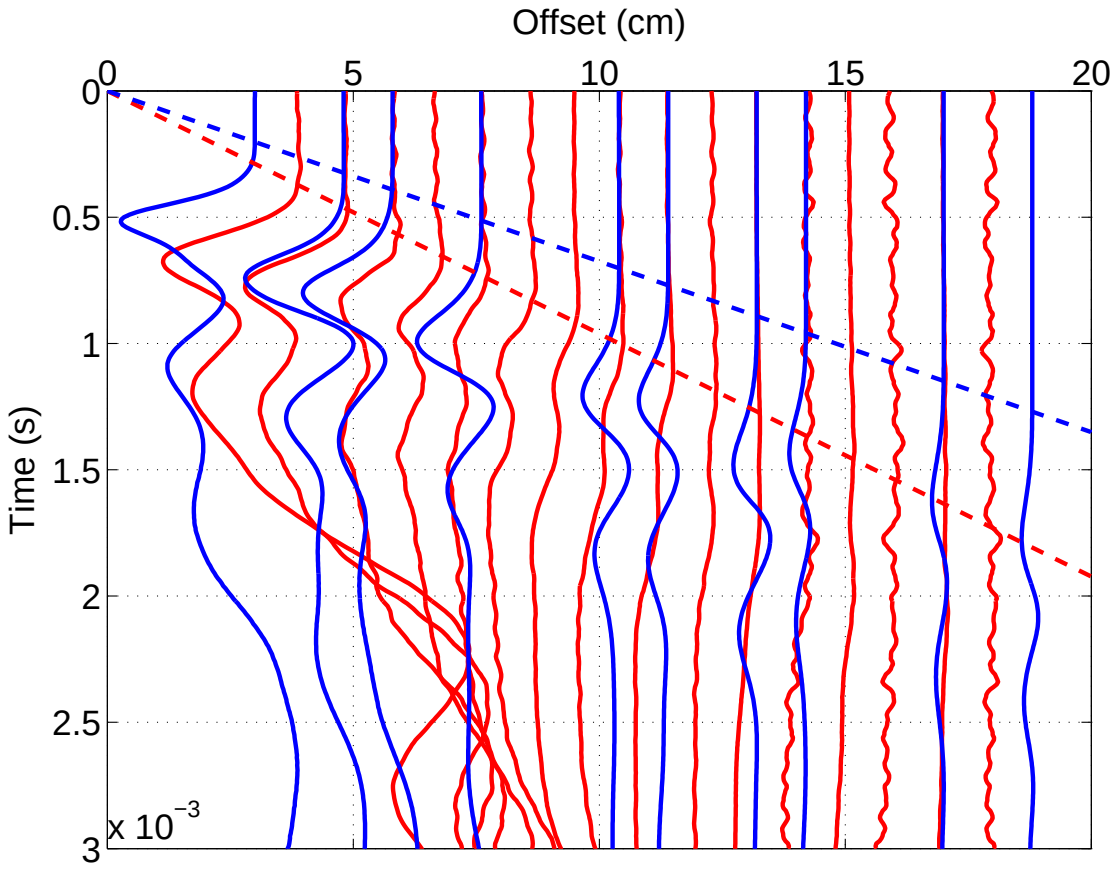

Figure 5.7: Superposition of seismic (blue) and reconstructed electric (red) for common mid-point geometry with 18 mm dipole-length on acquisition '20140305'; all amplitudes are normalised relatively to the respective first extremum observed at offset 4.8 cm. Records are arranged relatively to their offsets to the source. First arrival velocity of 105 $m.s^{-1}$ for electric and 150 $m.s^{-1}$ for seismic are respectively materialised in red and blue color lines.

effect being too elevated, spectral amplitudes would start to wrongfully increase with increasing offsets.

Hence, if near-field assumption appears to be justified, validity of our estimation on attenuation and inverse quality factor should be restricted to frequency inferior to 2 kHz. Interestingly, we see that near-field time-picked estimation associated to nominal frequency f_{nom} agree with spectral analysis up to the dimension of the error bars, supporting the reliability of our time-analysis process.

Conclusion

On basis of spectral data analysis for seismic recordings and their compatibility with a simplified Biot-Stoll asymptotic model [Kimura, 2007], we conclude that 3D propagation geometry is the most suited to account for geometrical attenuation in dry and sub-saturated sand, whereas our observations on fully-saturated sand tend to support near-field assumption. In this last case, proper attenuation characterisation is soon prevented ($f \approx 2\ kHz$) by the existence of a 'mixed mode', combining receivers at furthest offsets experiencing a 3D propagation while receiver closer to the source remain in near-field domain.

For comparable sub-saturated conditions ($S_w = 0.9 - 0.95$) and corresponding 3D propagation geometry, our data was consistent with the attenuation and inverse quality factor values measured by Barrière et al. [2012] at $f = 1700 \pm 100\ Hz$ on the very same material. For seismic, our time-picked data would generally be very consistent with spectral values at frequency f_{nom}; for electric the observed deviation may be linked to the consideration of the offsets closest to the source, for which first arrival might be tainted by S-wave or Biot slow-wave contributions.

Our data were systematically underestimated by model curves inferred from the standard Biot model, neglecting grain friction. Biot-Stoll asymptotes on the contrary would come close to our data, even showing a low-frequency evolution quite similar to that observed on our dry and sub-saturated data in the kilohertz range. Hence for future model comparison to seismic, we will systematically refer to Biot-Stoll asymptotic model by Kimura [2007].

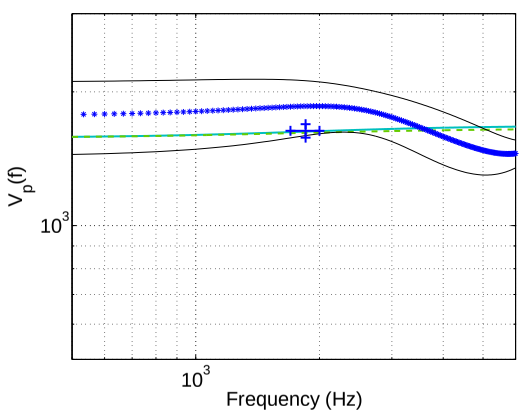

(a) $V_p(f)$

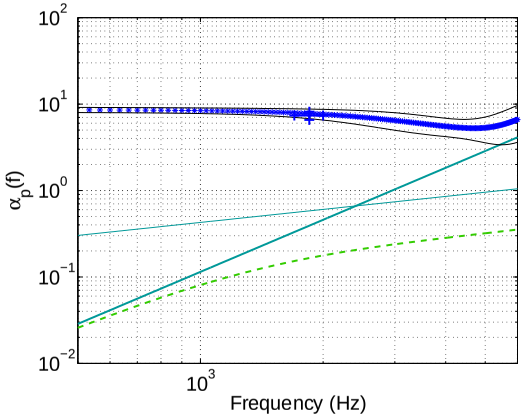

(b) $\alpha(f)$, 3D propagation

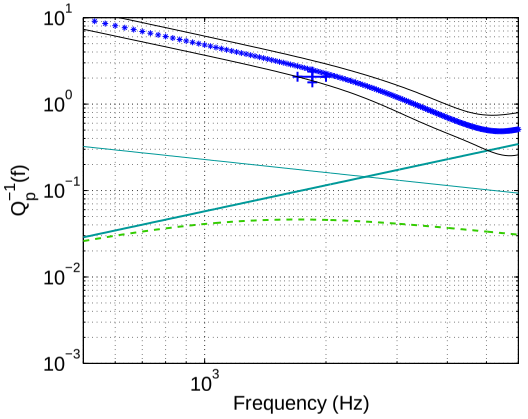

(c) $Q^{-1}(f)$, 3D propagation

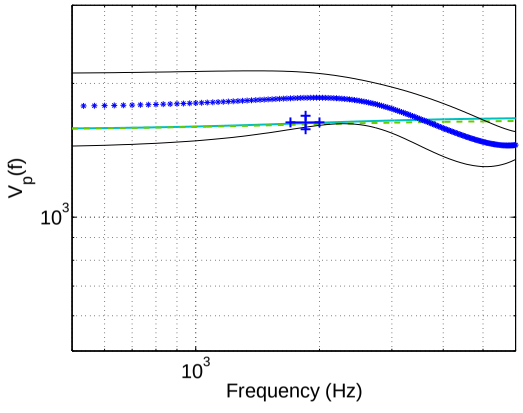

(d) $V_p(f)$, (same as (a))

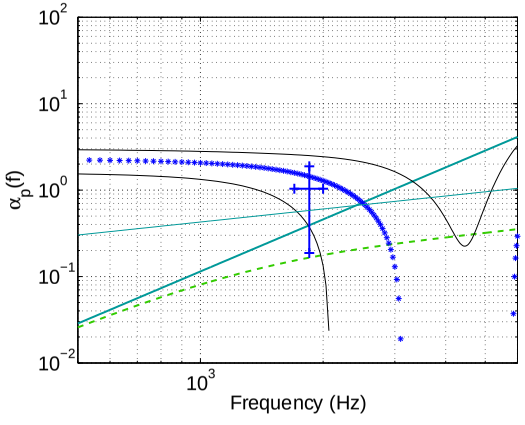

(e) $\alpha(f)$, near-field

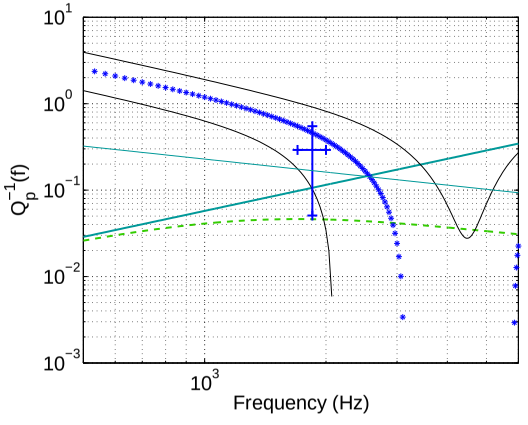

(f) $Q^{-1}(f)$, near-field

Figure 5.8: Spectral analysis of seismic characteristics on fully saturated sand ($S_w = 1$) for 3D (a,b,c) and near-field (e,f,g) propagation geometries. Linear regression for attenuation and phase velocity was conducted on captors between offsets between 10.4 and 22.6 cm, confidence on the error bars is of 80%. Our local picked data are superimposed in corresponding colors. On attenuation and inverse quality factor figures, thick and light blue are respectively associated to LF and HF asymptotes of Biot-Stoll models, the green while dashed line shows prediction by regular Biot poroelasticity. Velocity dispersion curves by Biot and Biot-Stoll almost superpose. Models correspond to an effective fluid modulus calculated after the Wood model (K_R).

5.1.3 Time-lapse monitoring with saturation variations

Our investigation on seismic and seismoelectric dependency to water saturation relies on three experiments rounds presented in figure 5.9. First we acquired data related to initial imbibition on dry sand (green data points), providing us with seismic properties of the medium under dry and sub-saturated condition following a rapid evolution of the system, in order to prevent differential capillary imbibition. As have been described in experimental protocols exposed in section 3.3, the medium was then put to a rest for one month, with occasional fluid re-equilibrations by water circulation. The achievement of full saturation launched the second experiments round, consisting in a monitored continuous drainage phase from $S_w = 1$ to $S_w \approx 0.3$ (blue data points). The medium was subsequently submitted to a rapid and poorly documented cycle of imbibition-drainage, not reported here, in a failed attempt to re-reach immediate full saturation before the medium has rested long. Eventually, for data completion, it was followed by a third experiments round documenting monitored re-imbibition with progressive addition of water from a saturation of $S_w \approx 0.25$ to $S_w \approx 0.9$ (red data points).

In this section we analyse saturation-dependency of the time-picked seismic attributes V_p and α for all three experimental phases. For attenuation calculation we considered a 3D geometrical spreading for data showing P-wave velocities inferior to 500 m/s, characteristic from dry and sub-saturated sand, while data having superior velocities were considered near-field. From those seismic attributes determined by linear regression, we eventually deduced the inverse quality factor Q^{-1} according to equation 4.28, for which frequency f would be calculated as the average of nominal frequencies picked at the first and the last receivers of the considered array.

On figure 5.9, we first noted the hysteresis associated to these curves: given the saturation, all observations depend from the medium history. Hence, while low-saturation velocities for the drainage and secondary imbibition tend to superpose, they do not converge towards dry sand velocity. Similarly, for higher saturation degrees such as $S_w > 50\%$, drainage velocities tend to be greater than those for imbibition at a given saturation. This type of behavior has repeatedly been reported by literature, testifying of higher velocities while draining than while imbibing. Some authors (Barrière et al. [2012], Walton [1987]) associate this phenomenon to the weakening of frame when injecting fluid during imbibition. Others (Knight and Nolen-Hoeksema [1990]; Cadoret et al. [1995]) attribute this discrepancy to a homogeneity loss of the effective fluid (air+water) while drying, in comparison to the homogeneity level experienced during imbibition (often under depressurization). According to them, while fluid and gas can coexist within a pore during imbibition phase, favouring homogeneity of the medium, drainage would rather see that a pore is either filled with or emptied from its water according to its aspect ratio.

In order to interpret our data we resorted to Biot-Stoll asymptotic curves. We considered that most reference frequencies, on which the Q^{-1} calculations were based, usually ranged between 1 kHz and 2 kHz, placing us at a frequency inferior or equivalent to f_{Biot} in

sand (see figure 2.16). We hence constructed saturation-dependent curves from the Biot-Stoll asymptotic model for frequencies of 1 kHz (dashed lines) and 2 kHz (plain lines). Velocities were directly calculated using Biot standard theory, as it appeared in previous figures 5.5, 5.6 and 5.8 that it was in all cases compatible with Geertsma and Smit [1961] formulation based on V_{LF} and V_{HF} (see eq. (2.66))

To account for the hysteresis, we adapted our model to the data by modifying some incompressibility moduli of the medium. In this case, each phase displaying a distinct velocity behaviour gave hints about specificities of its effective fluid and consolidation of its solid frame. Indeed, while the value of the base-line velocity at lowest water saturation degree appears connected to the incompressibility of the drained solid frame K_{fr}, departure-saturation from this base-line seems directed by the choice of an effective fluid modulus model K_f (see section 2.4.2).

For initial-imbibition data we found the effective fluid modulus provided by Wood model, $K_f = K_R$, to offer a fair estimate of our experimental velocities. For drainage and re-imbibition, we appealed to the empirical and adaptable model by Brie, calculated as a saturation power law of chosen exponent '$e = N$' noted as $K_f = K_{BN}$ (see eq. (2.75)). We concluded that reasonable approximations of drainage velocities were given by $K_f = K_{B8}$ while re-imbibition would be better describes by $K_f = K_{B40}$, meaning Brie models of respective exponents 8 and 40. As previously exposed in section 2.4.2, Brie empirical law has been widely used to account for inhomogeneous fluid conditions (as for patchy saturation by Carcione et al. [2006]). On the other side, exponent values superior to about 100 tend to produce velocity models in which the final velocity increase is even more delayed than in the Wood model suited to ideally homogeneous fluid. Consequently the exponent evolution from 8 for drainage to 40 for re-imbibition could traduce an homogeneity increase of the effective fluid. Under this light, our observations would be in agreement with conclusions of Knight and Nolen-Hoeksema [1990] and Cadoret et al. [1995]. As for bulk modulus K_{fr}, the initial value of 25.5 MPa deduced by Barrière et al. [2012], from Walton [1987] development on grain-contact theory, was well adapted to account for initial imbibition where low-saturation velocity plateau was estimated at 170 ± 5 m/s, based on measured velocities at extreme saturation degrees $S_w = 0$ and $S_w = 0.9 - 0.95$. For drainage and re-imbibition data, this well-monitored velocity has increased to $230 \pm 10 m/s$. To reproduce such plateau velocity value, bulk modulus K_{fr} had to be doubled to 50 MPa, no shocking value for sand yet a considerable increase relatively to the initially relevant K_{fr}. A possible explanation would be the consolidation of the frame as residual water produces surface tension (as in a sand castle).

Having defined our experiment-dependent moduli K_{fr} and K_f, we computed limit curves at 1 kHz and $2kHz$ after Biot-Stoll LF asymptotes. For a given experiment round, all model curves (lower and higher bound on attenuation and inverse quality factor) take minimum values for the same saturation S^* specific to the experiment, forming two lobes. Drop in the attenuation curves at S^* corresponds approximately to the sudden increase of P-wave velocities. With an analogous notation to effective fluid modulus, we note that $S^*_{B8} \approx 0.55 < S^*_{B40} \approx 0.9 < S^*_R \approx 0.98$ (corresponding respectively to drainage, re-imbibition

and initial imbibition) conveying the feeling that S^* increases echoes the assumed increase of effective fluid homogeneity. While the green model curves fail to approach data from initial imbibition, drainage data are particularly well constrained by the blue model curves, clearly initiating the same unexpected drop in attenuation. Re-imbibition data are closely flanked by the limit model-curves from $S_w = 0.2$ to $S_w = 0.8$, yet our records stop precisely before the drop predicted by model attenuation takes place, experimental data even showing a slight increase towards the end.

In the whole, while attenuation and inverse quality factor data for $S_w > 0.90$ are poorly predicted by the model curve tending to underestimation, their predictions at lower saturation degree ($S_w < 0.8$) appear rather consistent. The model curves work especially fine for drainage data. As it appears from figure 5.8, attenuation α_p on our sand on $[1 - 2\ kHz]$ should typically range by $[1 - 3]$, while inverse quality factor Q_p^{-1} commonly of 0.2 ± 0.1 at partial saturation could possibly increase by a factor 2 or 3 at full saturation.

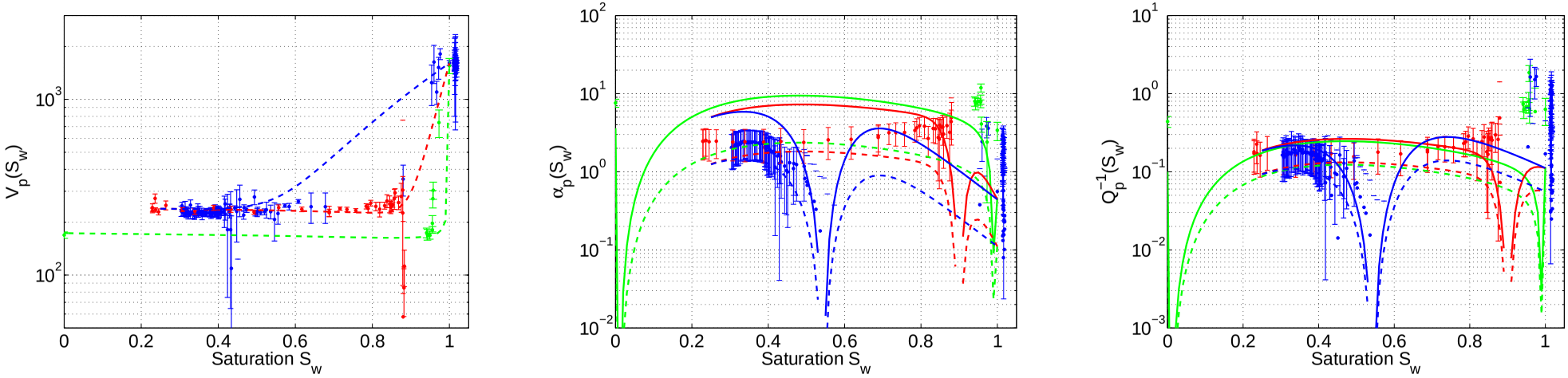

(a) $V_p(S_w)$ (b) $\alpha(S_w)$ (c) $Q^{-1}(S_w)$

Figure 5.9: Overview of time-picked characteristics from the first seismic arrival with regard to water saturation S_w, during initial imbibition (green), subsequent drainage (blue) and following re-imbibition (red). Attenuation and inverse quality factor data were compared to estimations of Biot-Stoll asymptotes α_{LF} and Q_{LF}^{-1} traced for 1 kHz (as dashed curves) and 2 kHz (as plain curves). Calculation of the model curves involves different approaches for effective fluid modulus: fluid mixture for green data -associated to initial imbibition- relies on a $K_f = K_R$, while blue drainage and red re-imbibition model curves are based on Brie models giving $K_f = K_{B8}$ for drainage and $K_f = K_{B40}$ for re-imbibition. For those two cases, we take a residual saturation $S_{irr} = 0.25$ and a pore diameter $d_p = 60\mu m$,while the bulk frame modulus is augmented to $K_{fr} = 50\ MPa$ to agree with the position of the low-saturation velocity plateau. Analysed data where considered between offsets of 10 to 23 cm, propagation geometry is considered to be 3D for data which velocity is inferior to $500m/s$, near field otherwise. Error bars are calculated from linear regression on a 80 % confidence interval.

5.1.4 Conclusions on attenuation and dispersion analysis of seismic and seismoelectric signals

In this section, we discussed the phase velocities, attenuation and inverse quality factors of fast P waves with time and spectral analysis under various saturations. First, we showed that geometrical spreading (*i.e.* the amplitude decay due to the wave spreading in volume) may be different in partially saturated medium ($S_w \leq 95\ \%$) and in fully saturated medium. Indeed, P-wave velocity in partially saturated sand is very low and short wavelengths are involved. In this case, we have shown the amplitude decay would fit with a 1D correction. Nevertheless, excluding the 5 first accelerometers, we showed a 3D correction could fit as well and decided to keep both options. In fully saturated medium, velocities become very high, and very long wavelength may be involved, leading to a geometrical spreading in the near field assumption.

Using these assumptions, we showed that time pickings give similar result to spectral analysis at the nominal frequency, except for seismoelectric velocities calculated at closest offsets, and potentially involving tainted P-waves. The Biot-Stoll model, modified by Kimura [2007], approaches fairly well the rather high attenuation measured in sub-saturated medium (about 7 at 1.5 kHz). This model allowing to account for grain to grain frictions, supposed to be dominant in attenuation by Barrière et al. [2012], seems to remain applicable for predicting friction contribution to attenuation within a dry medium.

We eventually monitored velocities and attenuations during drainage and imbibition phases. We found the Biot-Stoll model, combined to a Brie definition of the effective fluid modulus $Kf = K_{B8}$, to present the best fit to velocity variations due to drainage. Similarly, a good approach of re-imbibition data was given taking $K_f = K_{B40}$, while $K_f = K_R$ would be better suited to account for initial imbibition. These models, determined on velocity data would stand in good agreement to attenuation data, the drainage experiment being particularly well-fitted. An interesting feature of the saturation-dependent attenuation and inverse quality factor is the sudden and transitory drop of the model curves to negligible attenuation level. For at least one of our monitoring, that of the drainage phase, this drop was partly observed in the experimental data. Next section will offer the opportunity to come back to that phenomenon.

5.2 Transfer function analysis: towards the validation of the Pride's theory

In previous section, we have studied the temporal and spectral characteristics of the seismic and coseismic seismoelectric field on a number of experiments regarding the saturating state of the medium, treated either under their dynamic (constant S_w, varying f) or static (varying S_w, constant f) form. We have noticed in particular that the seismic and seismoelectric fields do not behave so closely in magnitude and in frequency as a coseismic field would call. The frequency-dependent velocity and inverse quality factor could indeed differ noticeably between the seismic and the seismoelectric fields.

In this new part, we focus on the seismoelectric transfer function, that is to say how the mechanical energy associated to the seismic waves transfer into seismoelectric energy. As previously seen in section 2.5.4, the amplitude of the coseismic electric response to a related compressional seismic excitation depends on a dozen parameters of the medium. A sensitivity analysis conducted against the various elastic, hydraulic and electric properties of the frame and saturating fluid showed that one of the most important effect on the amplitude was produced by a change in fluid conductivity.

Fluid conductivity also happens to be the most adjustable parameter within a sandbox experiment: as a fluid property, its change demands no great operation but to patiently equilibrate the medium towards the wanted value by continuous water circulation (*i.e.* the solid phase and captors can stay in place). Consequently, this dependency of the coseismic effect on fluid conductivity has been the first to be investigated in the laboratory. In a first part, it will allows us to test the validity of our experimental approach and setting for quantitative estimation of the coseismic seismoelectric transfer function.

In a second part, we will study the amplitude of the transfer function as a function of a second parameter saturation S_w, taking benefit of the imbibition and drainage experiments. We will bring together the observations made on seismic properties under varying saturation condition, while investigating an interesting sign change affecting the coseismic seismoelectric arrival during drainage.

Eventually, we will discuss the possibility to observe and characterize the frequency-dependent behaviour of our coseismic seismoelectric transfer function on the frequency band $[0.5 - 3\ kHz]$ typical for our seismoelectric experiment, before considering of to ease the measurements while expanding the frequency band of investigation.

5.2.1 Effect of fluid's conductivity: a simple analysis of time signals

Previous literature on the subject

As soon as the 70's, Parkhomenko and Gaskarov [1971] noted in their conclusions that "as the degree of mineralization of the solution saturating the rock increases, the magnitude of the E-effect is reduced approximately exponentially" for experiments conducted on partially saturated sand having NaCl concentration ranging from 0.3 to 150 $g.l^{-1}$ (equalling

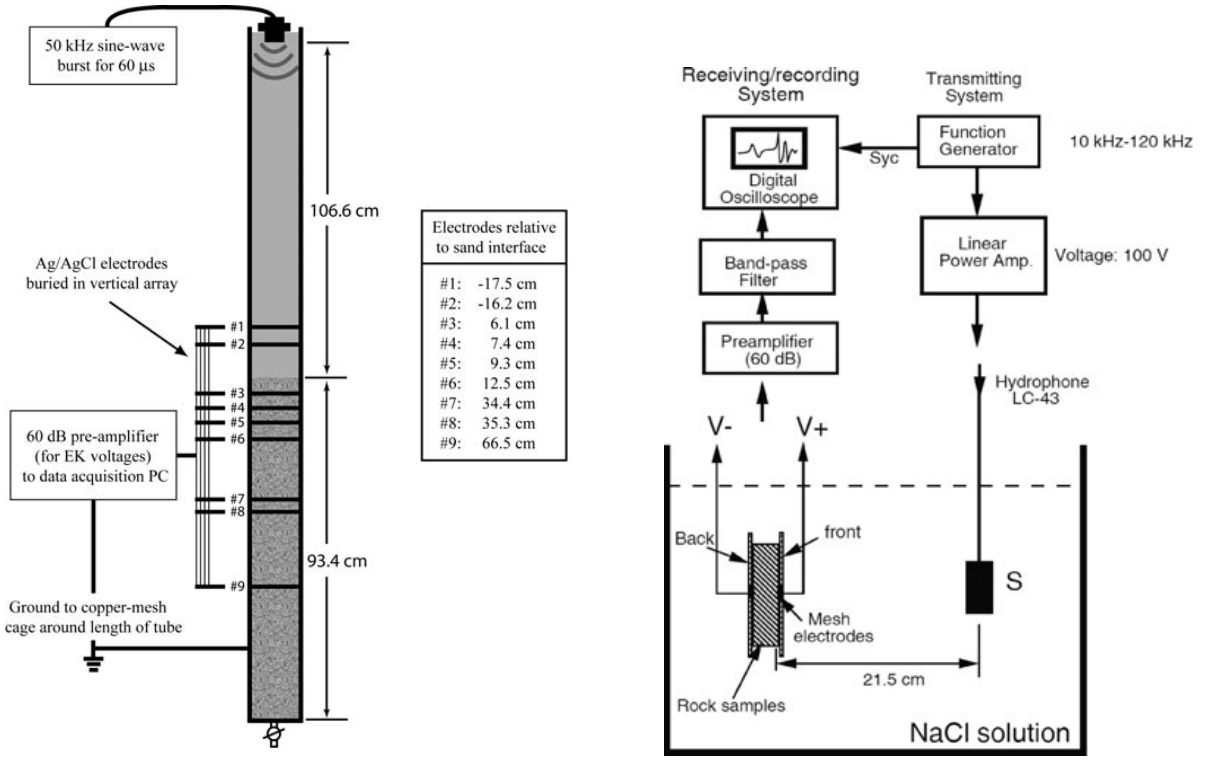

(a) Block and Harris [2006] (b) Zhu and Toksöz [2013]

Figure 5.10: (a) Seismoelectric apparatus by Block and Harris [2006] based on a cylindrical tube geometry with Ag/AgCl electrodes buried in a vertical array on each side of the water-sediment interface. A copper mesh Faraday cage was used to isolate the apparatus from electrical interference and to provide an universal ground (also to all dipoles). As the hydrophone is emitting a sine wave burst at 50 kHz for 60μs, electrodes are recording a potential difference relatively to the ground.(b) Schematic diagram of the Zhu and Toksöz [2013] measurement system at an high-frequency range ($10-120\ kHz$) within a water container: a potential difference is measured at the edges of the immersed sample of Berea sandstone as the hydrophone is activated as a source. In both experiments, fluid conductivity would be changed.

conductivities of 47 $mS.m^{-1}$ to 19 $S.m^{-1}$). This effect was particularly brought to light in the low frequency approximation of the coseismic transfer function given by Garambois and Dietrich [2001], which proved the dependency of the coseismic transfer function to be inversely proportional to fluid conductivity (see eq. (2.95)).

Within the last decade, further similar studies have been conducted either on sand and glass beads [Block and Harris, 2006] or on Berea sandstone [Zhu and Toksöz, 2013] for frequencies reaching some tens of kilohertz. Setting of these experiments, being respectively of the sand-column and the water-tank sort, are presented in figure 5.10. Figure 5.11 by Block and Harris [2006] offers a glimpse of the coseismic seismoelectric dependency obtained on sand and glass beads for fluid conductivities included between 0.01 to 0.04 S/m, and a seismic excitation frequency of 50 kHz. With this experiment, Block and Harris [2006] demonstrated that the normalized seismoelectric measured voltage decreases as expected as a function of the pore-fluid conductivity.

At the end of this part dedicated to the impact of conductivity on the coseismic seismoelectric transfer functions, we will use the results obtained by Block and Harris [2006] and Zhu and Toksöz [2013] in an attempt to compare them to present results inferred from our sandbox experiment (see table 5.2).

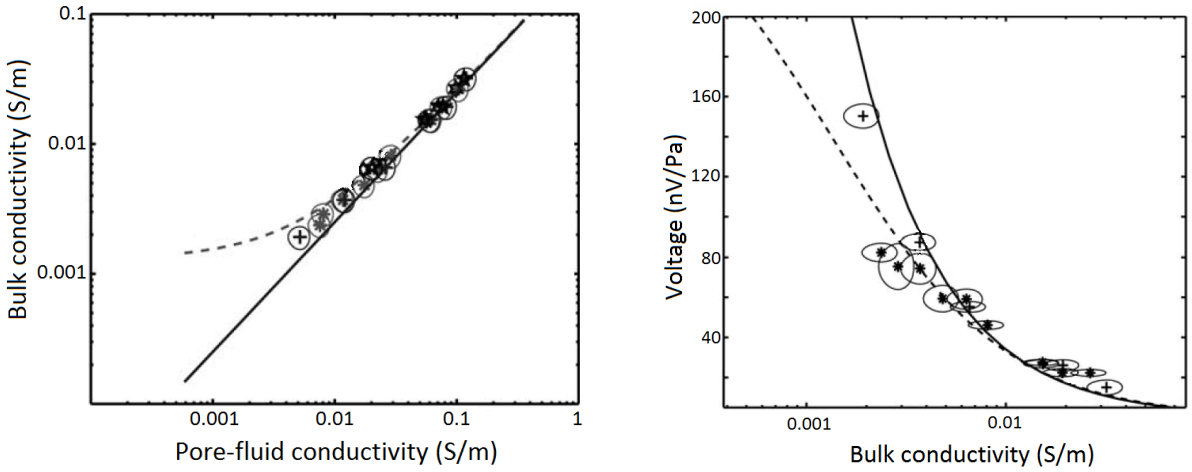

(a) (b)

Figure 5.11: (a)Bulk versus pore fluid conductivity for medium grain sand ('*') and loose glass microspheres ('+'). The $\sigma_{bulk} - \sigma_f$ relation that affects seismoelectric response follows an almost linear trend for both sample types. (b) Peak of the fast wave potentials versus the bulk conductivity. All potentials were measured at an offset from 35.3 cm of the water-sand interface that is located at 106.6 cm from the source, for a 50 kHz seismic excitation. For figures (a) and (b) data are compared to predictions for sand (dashed curve), on the basis of a fitted surface conductance and to glass (solid curve) using Pride [1994] theory. Error ellipses represent two standard deviations from the mean. Figures taken from Block and Harris [2006].

Experimental observation

Getting back to our experiment, our investigation of the transfer function dependency on fluid conductivity was conducted following initial imbibition. The medium was first equilibrated with demineralized water for a couple of hours (giving the measurement at lowest $\sigma_f = 1.7\ mS/m$) before fluid conductivity was controlled by progressive addition of NaCl salts to eventually cover fluid conductivities ranging from 2.5 mS/m to 10 mS/m. A more thorough description of initial filling and fluid equilibrating phases can be found within section 3.3.1, while a precise recap of the full experimental round is to be found in appendices 7.1.1.

As an introduction to our study regarding the coseismic seismoelectric dependency on conductivity, we present in figure 5.12 four acquisitions following initial imbibition of the medium by some days. Beside stacking, the sole treatment applied to these data would be on electric for reconstruction of the 18 mm mid-point dipoles. In each quadrant seismic records are compared to their synchronous electric records. Curves of corresponding colors in the seismic and the seismoelectric are from identical offsets. Seismic and electric curve are normalised relatively to one another; scale remains the same for the four presented cases. From the less to the most saline experiment, water saturation increased by only about 2 %, staying within the 95 ± 2 % range. Consequently, evolution of P-wave velocity remained limited, staying within $165 \pm 20\ m/s$. As mentioned in section 5.1.2, some discrepancies remain between the seismoelectric and seismic velocities, the latter being always slightly higher than the first. Yet the most interesting observation in figure 5.12 is that while seismic remains mostly invariant in amplitudes throughout the experiment, electric amplitudes decrease drastically, almost by one order of magnitude, as fluid conductivity increases from 1.7 mS/m to 7.7 mS/m.

For a better visualisation of this 'melting' of the coseismic seismoelectric signal with increasing fluid conductivity, figure 5.13 proposes to isolate the electric field recorded at offset 4.8 cm and superimposes the results for conductivities of 1.7 mS/m (blue), 2.5 mS/m (green), 5.6 mS/m (red) and 7.7 mS/m (black). Experimental measurements clearly showed a rough tendency to decrease as a function of $1/\sigma_f$ as expected from section 2.5.3. We compared this observed amplitude decrease, to that of an electric synthetic computed after Pride [1994] poroelastodynamic model, using the approached defined in section 2.6.2 for generating synthetic responses of various porous media to partial saturation. The synthetic curves were then scaled for the synthetic first extremum of the blue curve to equal its experimental equivalent: when computed ones against the others, real and computed data regrouped along the unity line. We note that our experimental records are sorted as expected; moreover, results at 5.6 mS/m and 7.7 mS/m seem in good agreement with synthetic projections.

The final step of our conductivity analysis consists in direct comparison from measured $E/\ddot{u}$ ratio to a computation of a conductivity dependent dynamic transfer function after Pride's formulation (eq. (2.94)). For a given conductivity, the estimation of the local $E/\ddot{u}$ values proceeds from linear regressions over seismic and electric captors at corresponding offsets, as exposed in figure 5.14. As a rule, electric fields are calculated on the 18 mm mid-point dipole. Again this local estimation of the coseismic transfer function has to be put in relation with computed dynamic transfer function. The frequency signature f_{nom} of the first arrival being grossly encompassed in the $[0.5 - 2\ kHz]$ range, we respectively represented this bordering frequencies as a dashed and a plain line. There are two sets of computed dynamic curves: the red set has been computed for partial water saturation of 95 %, for which effective fluid modulus followed a Wood model ($K_f = K_R$); black curves were computed for full water saturation.

Red curves are to be put in relation with the five red data points of measured $S_w = 95 \pm 2$ % and moderate P-wave velocities of 150 m/s to 350 m/s. Though the size of error bars mitigates the results, the agreement between experimental points and theoretical curves is good and the decreasing trend is well marked. A further point, marked in purple, meets similar characteristics, but proceeds from a previous filling involving larger mid-point dipole of 24 mm, inducing a bias in measurements as discussed in section 4.5.2, possibly explaining its falling out of the trend.

The three other black points were obtained for P-wave velocities ranging from 750 m/s to 1750 m/s corroborating the nearing to full saturation, ideally pictures as black lines. While the black curves are above the red ones, black points appear to stand lower than the red curves and corresponding red data points at similar conductivities.This disturbing fact may be due to a false evaluation of the in-situ conductivity of the pore fluid by our well and top water-layer conductivity measurements. Indeed, though conductivity has been re-equilibrated before every acquisition series (without which it inclined to increase gradually), for this particular set of points, the medium had already been saturated for 15 to 30 days. We can not rule out the possibility for smaller pores to remain inaccessible to fluid flow and hence avoid equilibration, eventually causing an underestimation of the actual conductivity

of the medium by relying on information provided by the top water-layer. Another outcome of this data is to point out our lack of resolution for discriminating between saturated and sub-saturated value of the coseismic transfer function: indeed in the last 5 % of saturation, while seismic velocities show tremendous changes and increases by one order of magnitude, the transfer function is expected to variate by a maximum of 50 % which is about our level of resolution.

As a conclusion, if the error associated to our data remains quite large offering poor resolution, our results are within the range of Pride theoretical predictions and support the quantitative reliability of our coseismic measurement method. Admittedly, being under partial saturation conditions, our model values depend on our definition of the effective fluid and more specifically upon its modulus K_f, here taken as K_R. As we use it as an adapting parameter it is worth noting that, with reference to figure 2.28 calculated for various effective K_f model relatively to a saturation of $S_w = 0.95$ matching that of our experimental points, model curves may be biased by 20%, but the general decreasing with saturation would be equivalent.

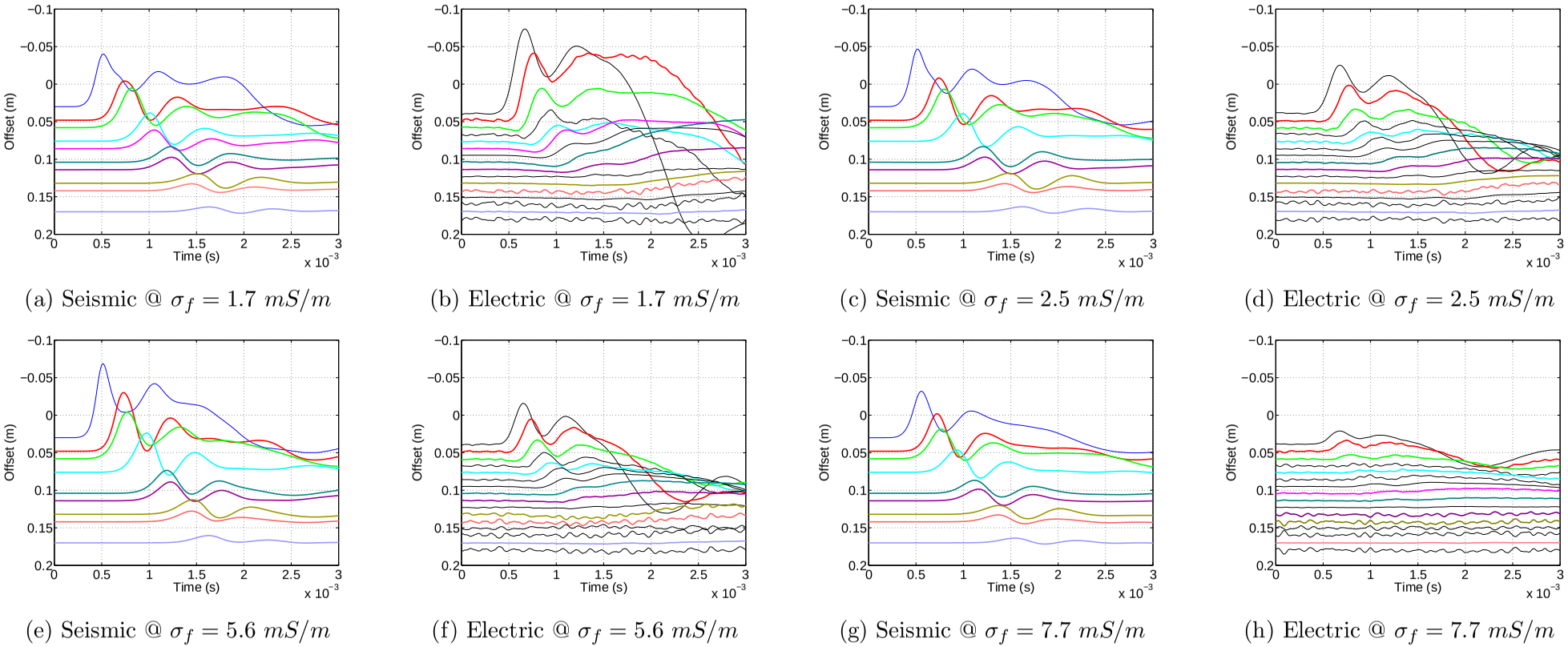

(a) Seismic @ $\sigma_f = 1.7\ mS/m$ (b) Electric @ $\sigma_f = 1.7\ mS/m$ (c) Seismic @ $\sigma_f = 2.5\ mS/m$ (d) Electric @ $\sigma_f = 2.5\ mS/m$

(e) Seismic @ $\sigma_f = 5.6\ mS/m$ (f) Electric @ $\sigma_f = 5.6\ mS/m$ (g) Seismic @ $\sigma_f = 7.7\ mS/m$ (h) Electric @ $\sigma_f = 7.7\ mS/m$

Figure 5.12: Representation of seismic and seismoelectric data for varying conductivities under quasi-constant water saturation (evolving from 94% to 96% on four days measurement). Electric was measured with a mid-point dipole configuration of 18 mm, both electric and seismic records were averaged on about 50 shots. Relative amplitudes are preserved as to give 50 $m.s^{-2}$ per vertical division for seismic and 0.5 $V.m^{-1}$ per division for electric. For the sake of data readability, electric curve were flipped in polarity. Corresponding colors in thick lines traduce corresponding offsets in seismic and SE. We observe that while seismic amplitudes remain unchanged at first order, electric amplitudes appear to decrease with increasing conductivity.

Comparison with published studies

We considered resituating our data relatively to those obtained in afore-mentioned studies, which main features are summarized in table 5.2. Along to main transport characteristics of the experimental medium, the explored conductivity range and values of measured coseismic seismoelectric quantities under various forms are to be found.
While we lack information on Parkhomenko and Gaskarov [1971] experimental medium and setup to risk any computation, experiments by Block and Harris [2006] and Zhu and Toksöz [2013] rely on a voltage-to-applied-pressure ratio they refer to as seismoelectric voltage coupling coefficient. This quantity may be expressed as L_{EK}/σ_b, were L_EK is as defined by eq. (2.87), and the effective conductivity of the medium σ_b is expressed as in eq. (2.6). Note that this seismoelectric voltage coupling coefficient, apart from depending on fluid conductivity σ_f, would also show dependency on saturation S_w.

For the purpose of their measurements, both studies recorded the fluid pressure impulse at the source using an hydrophone (see figure 5.10). Our approach differs from theirs, by recording frame acceleration $\ddot{u}$ and electric field E for a direct access to Pride's transfer function, when they rely on p_f and Δ_V for determination of quantity L_{EK}/σ_b. If a voltage measured on a sample of known dimensions might be convertible into an electric field [Zhu and Toksöz, 2013], we are in no position to presently estimate $\ddot{u}$ from p_f ; on the other hand estimation of L_{EK}/σ_b on basis of our experimental data remains out of reach. The three studies share no common ground for direct measurement comparison. Consequently, our present analysis will be restricted to comparisons of computed $|E/\ddot{u}|$ and L_{EK}/σ_b based on the model by Pride. This model initially using our parameters for unconsolidated sand as defined in table **??** will be adjusted to Block and Harris [2006] only by using the available experimental values given at the top of table 5.2 and to Zhu and Toksöz [2013] by using values from this table and complete the missing parameter with those of table 7.6. Results from this operation are to be found at the bottom of this same table.

Considering comparisons of experimental to computed values of seismoelectric coupling voltage L_{EK}/σ_b, we note that measurements by Block and Harris [2006] are largely overestimated by the model predictions by about one order of magnitude, while measurements on Berea sandstone are overestimated by a factor 4. In this last case, the reasonable discrepancy between actual and modeled value may be attributed to a poor knowledge of the actual material, not fully described by the article, but for which we took average parameters taken from Winkler [1985], or deduced from Hart and Wang [1995]. On the contrary, for the well-described medium sand the larger disparity might be due to the measuring technique relatively to a dematerialized grounded reference, skipping actual dipole reconstruction within the media.

In turn, if we consider transfer function values $|E/\ddot{u}|$ for our present work, we see that measured and predicted ratios are very consistent, offering an almost complete overlapping of experimental and modeled values. The correspondence of measurements and computations appears to be particularly good for our higher range of frequencies: hence for our reported measurement at either 7.2 mS/m or 9 mS/m, the error would lay by some 10%. While that degree of agreement partly results from our extended knowledge of the parameters de-

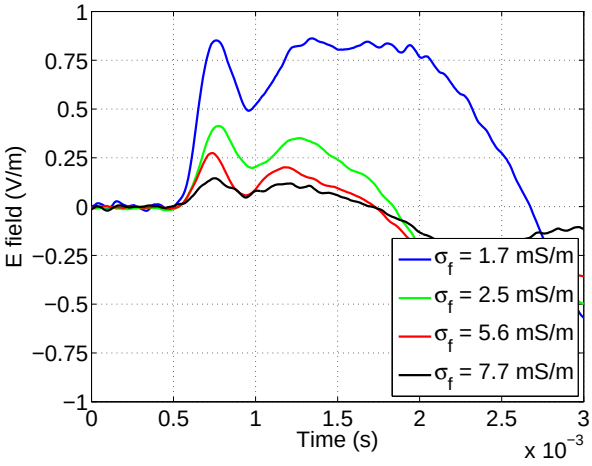

(a) Real data at offset 4.8 cm

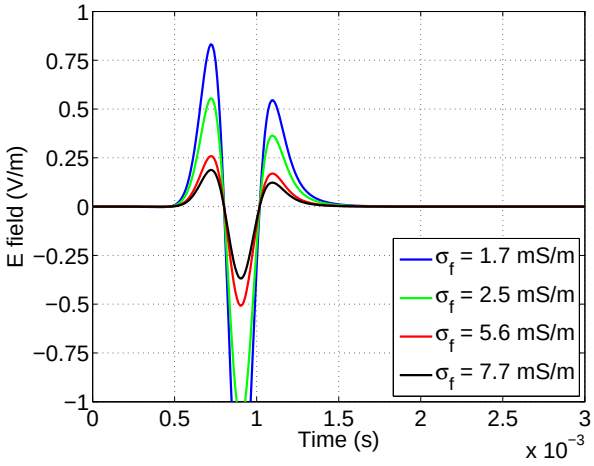

(b) Synthetic data

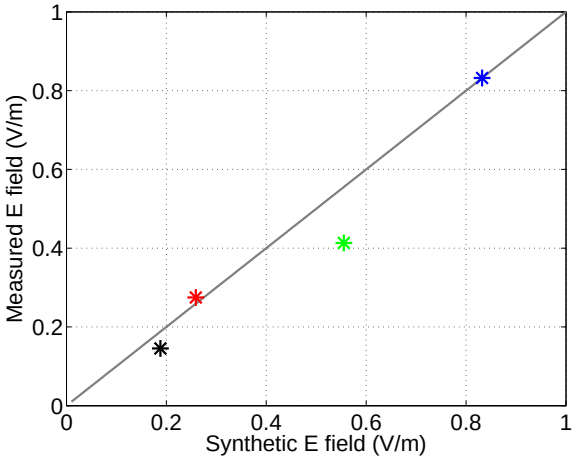

(c) Model to data comparison

Figure 5.13: (a) Potential difference recorded at offset 4.8 cm on a 18 mm mid-point dipole for four different fluid conductivities : 1.7 mS/m (blue curve), 2.5 mS/m (green curve),5.6 mS/m (red curve) and 7.7 mS/m (black curve). Electric fields have been normalised by seismic excitation observed at conductivity 7.7 mS/m. (b) Synthetic data obtained for those conductivities using the Pride model once the synthetic first arrival at 1.7 mS/m has been calibrated to the corresponding experimental arrival. (c) Comparison of measured E field values to that predicted from a synthetic computed using Pride theory at $f = 1kHz$, having $K_f = K_R$ and the initial $K_{fr} = 25.5\ MPa$. The grey line marks the ideal identity curve

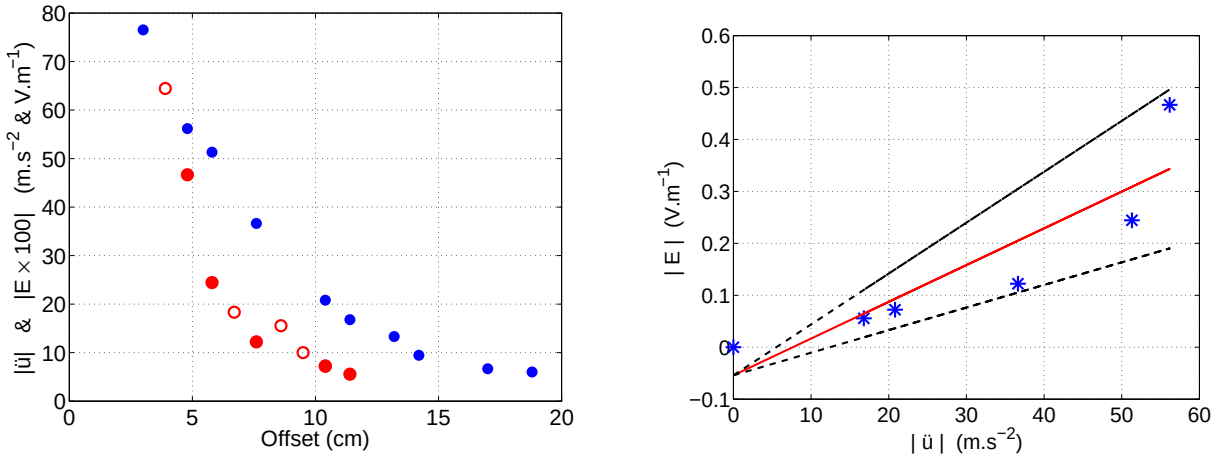

(a) (b)

Figure 5.14: (a) Absolute value of electric (red) and seismic (blue) first maxima extracted from record ′20140305′, electric fields are multiplied by 100 for representation sake. Markers of the electric are filled when having a corresponding seismic receiver at same offset. (b) Associated estimation of the local value $|E/\ddot{u}|$ ratio by linear regression on picked first maxima: $|E/\ddot{u}|$ is given by a slope of 7.1 ± 2.7 $mV.s^2.m^{-2}$, error bars are calculated with a 80% confidence.

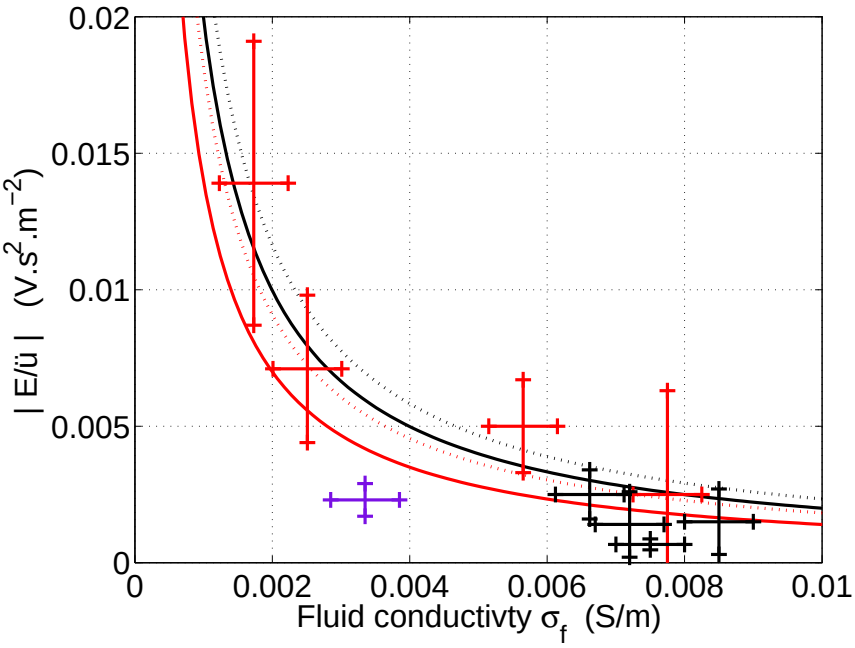

Figure 5.15: Estimation of local values of $E/\ddot{u}$ ratio by linear regression on first seismic and electric extrema at corresponding offsets. Error bars on conductivity are estimated by 0.5 mS/m while those on $E/\ddot{u}$ are given by linear regression with a 80 % confidence interval. Red data were obtained for moderate P-wave velocity not exceeding 350 m/s correlated to a 95 $\pm$ 2% saturation degree (experiment ′20140304′ to ′20140311′). Black data were obtained for higher P-wave velocity ranging from 750 m/s to 1750 m/s correlated to saturation degrees exceeding 97 % (experiment ′20140317′, ′20140402′ and 'F-20140408'). Associated model curves were computed by the Pride model at limit frequencies of 500 Hz (dashed line) or 2 kHz (plain line) with parameters of the Landes sand, at partial saturation $S_w = 0.95$ when red, or at full saturation when black. For this model the modulus of the effective fluid followed a Wood model ($K_f = K_R$) and residual water saturation zero; we took $K_{fr} = 25.5$ MPa. For all data electric field was recorded on 18 mm mid-point dipole. Purple data correspond to starting experiment '20131118' on a previous filling having a distinct dipole length of 24 mm.

scribing our Landes sand, knowledge that we lack relatively to the other presented data, its robustness with regard to conductivity and saturation variations supports the reliability of our measurements.

Study			Block and Harris [2006]	Zhu and Toksöz [2013]	Present work	
	Material		Medium sand	Berea sandstone	Landes sand	
	Porosity		38 %	23 %*	42 %	
	Permeability	m^2	8.10^{-12}	45.10^{-14}*	20.10^{-12}	
	Frame bulk modulus	MPa	44	12000	25.5	50
	Fluid modulus		$2.2GPa$	$2.2GPa$	$K_f = K_R$	$K_f = K_{B8}$
	Irreducible saturation S_{irr}		0	0	0	0.25
	Saturation S_w		1 [a]	1	0.95	0.3 – 1
	Biot frequency	kHz	4.5	158	1.7	0.4 – 2
	Frequency range	kHz	50	[15 – 120]	[1 – 3]	[1 – 3]
	Salinity	$g.L^{-1}$	0.043 – 0.75	0.076 – 2	0.01 – 0.055	0.044
	Conductivity	$S.m^{-1}$	0.007 – 0.12	0.012 – 0.32	0.0017 – 0.009	0.0072
DATA	SE coupling voltage	$nV.Pa^{-1}$	90 – 20	150 – 10 [d]	—	—
DATA	$\lvert E/\ddot{u}\rvert$	$mV.s^2.m^{-2}$	—	—	14 – 1.5 [b]	0.5 – 2.5 [c]
MODEL	SE coupling voltage	$nV.Pa^{-1}$	900 – 50	600 – 60 [d]	$1.3\ 10^4$ – $2.3\ 10^3$	$1.9\ 10^3$ – $2.6\ 10^3$
MODEL	$\lvert E/\ddot{u}\rvert$	$mV.s^2.m^{-2}$	1.1 – 0.065	0.3 – 0.03	9.5 – 1.6	0.55 – 2.6

Table 5.2: Summary of the studies regarding the dependency of the coseismic electric response on conductivity. In the reported experiments the electrolyte was obtained using NaCl of molar mass 58.44 g. The published values regarding experimental conductivities and associated seismoelectric measurements (SE voltage coupling coefficients or transfer function estimation) are reported. Values are indicated in their direction of evolution with increasing fluid conductivity. Models were computed after Pride and Haartsen [1996]. For modelisation on the medium and Landes sand, we worked on basis of parameter values gathered in table 3.3, only adjusting our existing model to 'medium sand' by modifying parameters indicated in the upper part of the present table accordingly. For Berea sandstone, parameters were taken from table 7.6 located in the appendices, when not given by the authors (parameters with an '*'). When not known, irreducible saturation are taken as $S_{irr} = 0$.
[a] Velocity observed on the Block and Harris [2006] sand experiment of approximately 1500 m/s supporting the full saturation assumption. [b] grossly estimated from figure 5.15. [c] grossly estimated from figure 5.18. [d] estimated at 50 kHz for the model and from figure 1.4 extracted from Zhu and Toksöz [2013].

As a final conclusion, we reckon that our data are in good agreement with our model predictions. As such, our processing tends to validate our approach for coseismic seismoelectric measurement and lay the basis for further investigations on less-addressed domains, as is the coseismic seismoelectric dependency on saturation.

5.2.2 The role of water content on seismoelectric transfer functions: a full saturation range analysis

Having validated our coseismic measuring method, both on a methodological point of view in section 4.5 and on its relevance for quantitative estimation thanks to preceding study of coseismic seismoelectric dependency to conductivity, we launched our study on coseismic seismoelectric dependency on water saturation S_w in an air-water fluid mixture. As we already mentioned in section 3.3.2, full saturation, attested by high P-wave velocity, was obtained after the sandbox was put to rest for about one month following first imbibition and a round of fluid equilibration phase. Before performing the drainage, we managed a last fluid equilibration to a fluid conductivity of $\sigma_f = 7.2\ mS/m$. Limitation of the drop in conductivity by fluid equilibration has to be put on account of a long stagnation of the electrolyte provoking a large increase of the salinity.

Seismoelectric measurements were conducted together with saturation monitoring during a drainage and an imbibition phase separated by a rapid and non-monitored imbibition-drainage cycle in a failed attempt to restore full saturation for reproducing the complete drainage experiment. The moisture sensors used in this experiment are granted a maximal precision of $\pm$ 3% (see section 3.2.2); yet given the high measurement density in saturation, we will not express the errors on saturation estimations within coming figures in order to preserve their readability.

Experimental observation of phase inversion between seismic and electric coseismic signal

When considering the evolution of the empirical $E/\ddot{u}$ ratio with water saturation on figure 5.16, we observed a change in behaviour characterized by a sign inversion due to the coseismic electric field during the drainage phase. In our experimental data, if the seismic waveform evolves much with saturation, the first arrival remains negative as expected for an initial compression. On the contrary, the electric appears to reverse its sign during the drainage course. Despite large errors due to a poor signal to noise ratio and a possible DC shift of the electric, we could determine that sign change happens for saturation of approximately $0.6\ \pm 0.1$. The presented electric data (in red) were recorded at offsets 3.9 cm and 5.8 cm, in the mid-point dipole configuration. They are shown in relation to corresponding seismic records (in blue). In the absence of related seismic receiver at offset 3.9 cm, we present seismic data at offsets 4.9 cm and 5.8 cm, while seismic amplitudes of the first maximum at 3.9 cm have been extrapolated from further amplitudes and attenuation coefficient in order to enable punctual calculation of the $E/\ddot{u}$ ratio. At further offsets the limited number of stacks (from 5 to 25), imposed by the time-lapse nature of the experiment, did not provide

us with observable coseismic seismoelectric signals

In figure 5.17 we show some selected electric records for chosen saturation degrees with more detail and relatively to the normalized seismic. This figure offers a better appreciation of the noise effect on electric records, as for instance on the reference level of the curve ideally set to zero. Thus, at offset 3.9 cm, the electric record usually starts above zero, in the interval $[0 \quad 0.01]V/m$; hence the measured electric field will tend to be overestimated. On the contrary for offset 5.8 cm, the measured electric field tends to be underestimated for the baseline appears to be located in the $[-0.01 \quad 0]$ V/m interval. We tried to take these biases into account while representing the $E/\ddot{u}$ ratio based on first max picking in figure 5.18, explaining the asymmetric error bars.

In this same figure, a thick black line represents the dynamic transfer functions computed at 1.5 kHz using a Reuss and a Brie's ($e = 8$) models for effective fluid modulus, this last model having previously served for seismic drainage velocity in section 5.1.3. To account for the effect of partial saturation on the electrokinetic coupling, we considered the correction by Jackson [2010], already considered by Bordes et al. [2015] on the same material. We note here that the model does not suit the multitude of high S_w data: it tends to underestimate the rather dispersed data cloud comprised between saturation of 0.95 to 1. Conversely, the agreement in the low saturation zone (below 0.5) seems more consistent: the errors are still great but the experimental points are pretty close to the model up to a saturation S_w of 45 % and model remains within error-bar range up to 0.55. Between 0.55 and 0.95 water saturation, our lack of data prevent from drawing any conclusion. Localisation of our electric receivers within the near-field domain at full saturation may justify our disability to find a model homogeneously connecting to all data point throughout the saturation range. Indeed during the drainage phase, in compliance with what can be seen in figure 5.9a, V_p velocities for saturation superior to 0.95 are greater than 1200 m/s. For our typical frequencies, measurements at 3.9 cm and 5.8 cm will surely be near-field as we have seen in section 5.1.1, figure 5.3. The first arrival may combine direct-wave to other wave-types, possibly altering the transfer function amplitudes. Meanwhile, for low saturation data (S_w below 50 %), V_p has reduced to an average of 230 m/s causing the characteristic near-field length to shrink by the same amount as velocity so that even the smallest offsets may come out of the near-field domain.

Finally, we notice that the electric records obtained during the drainage phase are of rather poor precision, while the monitoring is incomplete between saturation degree S_w comprised between 0.6 and 0.9 . Yet the continuity of the positive ratios calculated at low water saturation degrees combined to the cloud of negative ratios observed at maximal water saturation degree sustain our motivation to investigate this sign change in the following.

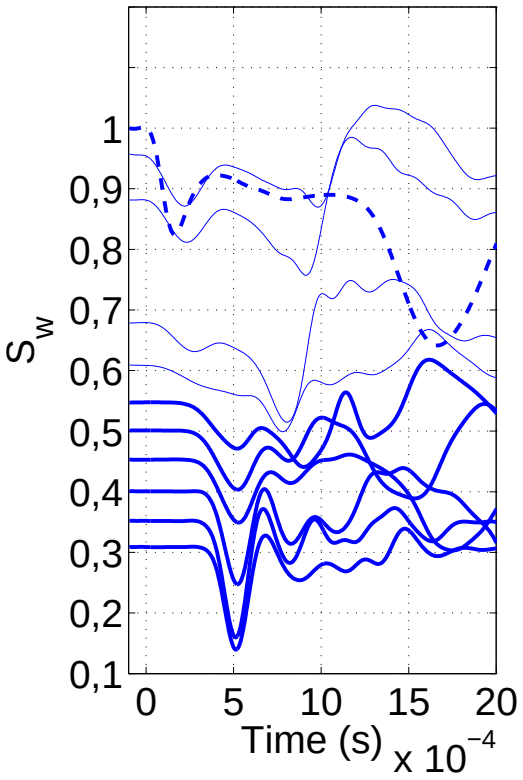

(a) Seismic @ 48 mm

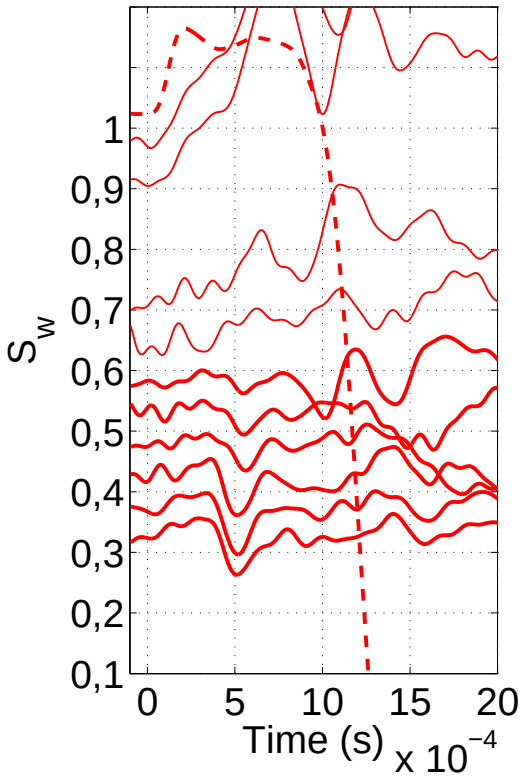

(b) Electric @ 39 mm

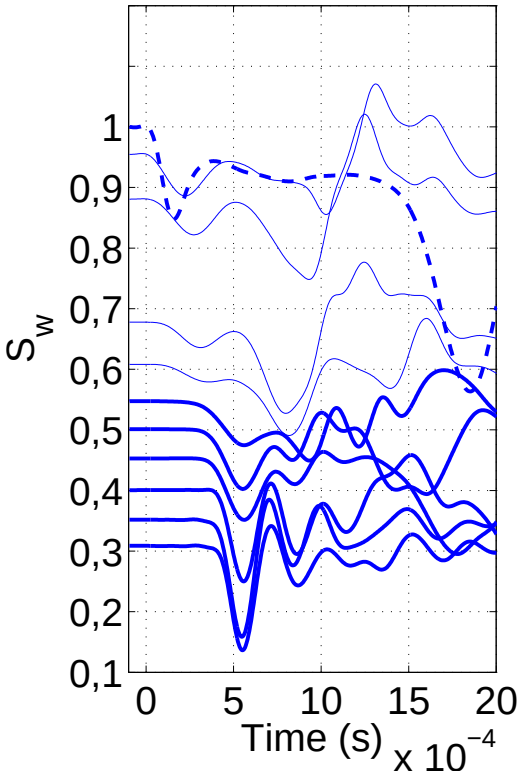

(c) Seismic @ 58 mm

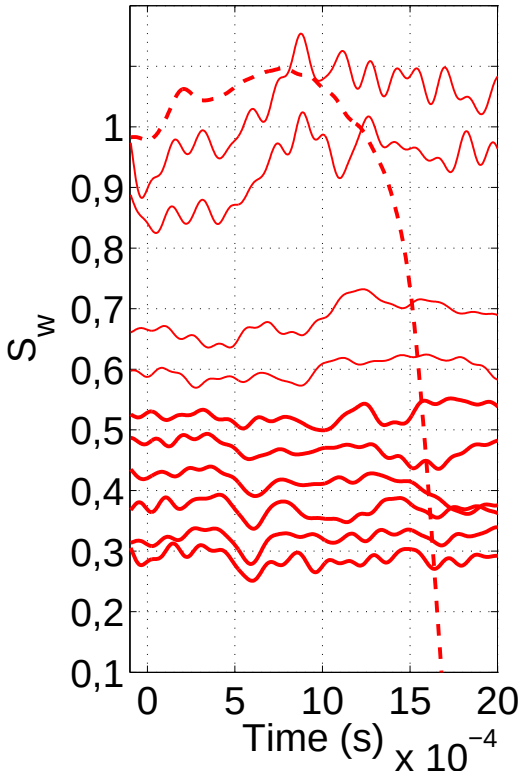

(d) Electric @ 58 mm

Figure 5.16: Evolution of waveforms and amplitudes with changes in water saturation (marked by the origin ordinate of each curve) for a set of experimental data acquired during drainage. Seismic in red was taken for the first and second receivers at respective offsets 4.8 cm and 5.8 cm; electric was taken for the mid-point dipole of length 18 mm placed at offset 3.9 cm (since records at 4.8 cm were much to noisy) and 5.8 cm. Data represented by a dashed line were resulting 100 stacks while bold lines stand for a stack 25 and fine lines for a stack 5. Real amplitudes of seismic curves corresponds to 10 $m.s^{-2}$ per vertical division, while the electric amplitudes read 25 mV/m per vertical division.

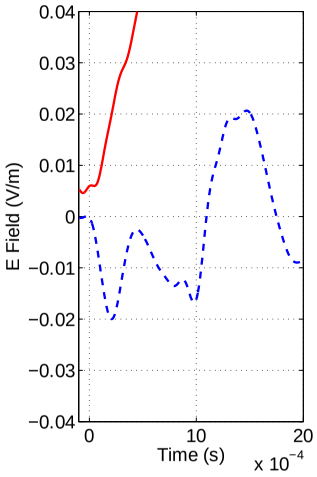

(a) $S_w = 100\%$ @ 3.9 cm

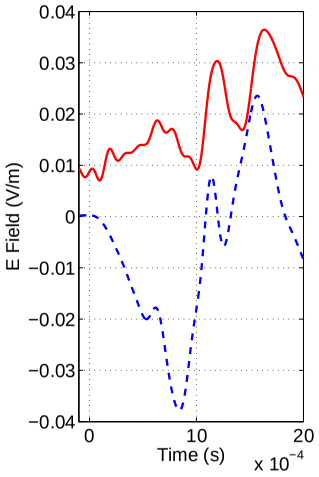

(b) $S_w = 60\%$ @ 3.9 cm

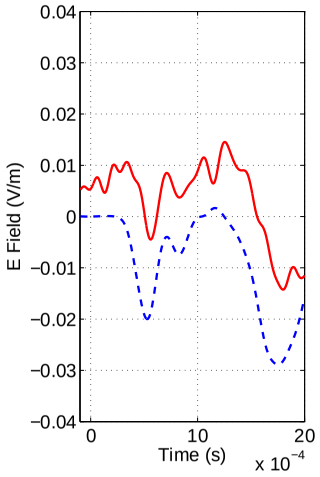

(c) $S_w = 45\%$ @ 3.9 cm

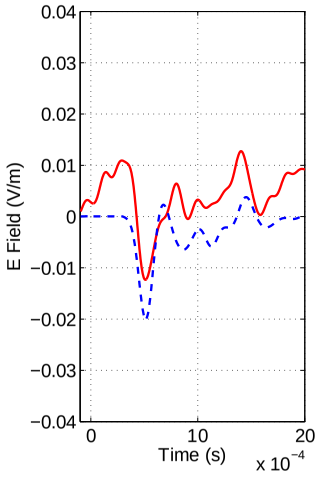

(d) $S_w = 30\%$ @ 3.9 cm

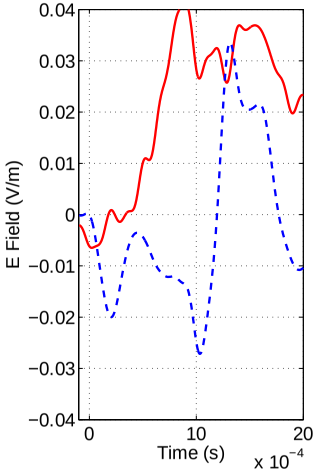

(e) $S_w = 100\%$ @ 5.8 cm

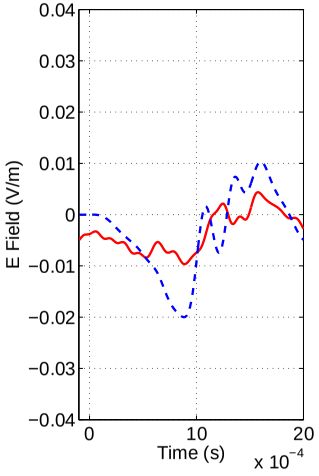

(f) $S_w = 60\%$ @ 5.8 cm

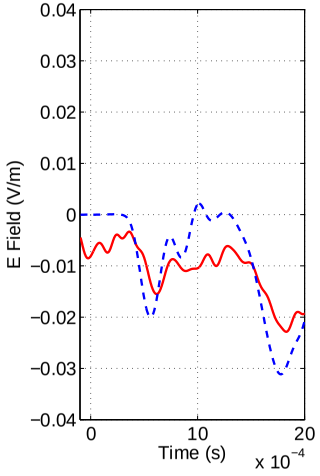

(g) $S_w = 45\%$ @ 5.8 cm

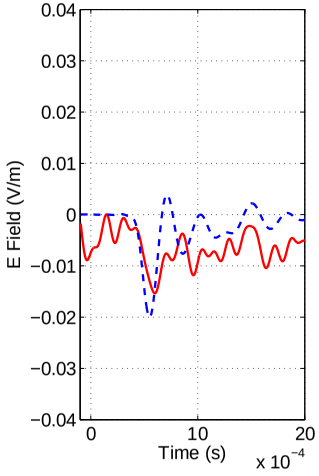

(h) $S_w = 30\%$ @ 5.8 cm

Figure 5.17: Recordings of the coseismic seismoelectric field (red curves) at chosen saturation degrees S_w during drainage, relatively to the corresponding normalized seismic (blue dashed curves) for 25 stacks. Figures (a) to (d) show a record at offset 3.9 cm, while figures (e) to (h) correspond to offset 5.8 cm. We note that on electric records at 3.9 cm reference level appeared shifted by a positive constant, while the same reference line appears shifted by a negative constant for offset 5.8 cm.

Global overview on saturation dependent coseismic measurement

We now consider all data associated to a saturation information, presently shown in figure 5.19 as $sgn(E/\ddot{u}) \times |E/\ddot{u}|$ versus water saturation S_w. This graph encompasses data acquired at various conductivities during initial imbibition (green), as well as data acquired at supposedly constant conductivity of $\sigma_{ref} = 7.2\ mS/m$ during the previously-treated drainage phase (blue) and a following imbibition phase (red). In order to be studied relatively to their saturation dependency, initial imbibition data, variable in conductivity σ_f, were grossly converted into their expected values at 7.2 mS/m by multiplying the $|E/\ddot{u}|$ ratio by a factor σ_f/σ_{ref}.

We attempted to fit the data by model predictions based on Pride [1994], the fit being more qualitative than quantitative with regard to errors on electric data (not represented here, but analogous to figure 5.18). To describe the three data sets, we resorted to the models previously used for seismic velocity characterization, main adjusting parameter being then the definition of the adapted effective fluid modulus in link to its homogeneity degree (see section 5.1.3). These models, matching colors with the corresponding data, were respectively considering $K_f = K_{B8}$ for the drainage (blue), $K_f = K_{B40}$ for re-imbibition (red) and $K_f = K_R$ for initial imbibition (dashed green line). This last model being incompatible with the negative sign of $E/\ddot{u}$ observed for $0.94 < S_w < 0.99$, we added one more model for primo-imbibition defined as $K_f = K_{B100}$ (green plain line), eventually computing two estimations of initial imbibition.

In section 2.4.2, we interpreted Brie exponent e as an homogeneity gauge of the effective fluid, increasing with its uniformity. Under this light, we may summarize how distribution of Brie exponent indicates:

- a high homogeneity level during initial imbibition, though not as complete as required by the Wood model: indeed local ratio measurements of $|E/\ddot{u}|$ at $S_w = 0.95$ provided us with only negative data (green), while a model using $K_f = K_R$ expects those ratio to be positive up to a saturation of $S_w = 0.998$. Model based on $K_f = K_{B100}$ are expected to flip phase by a lower saturation of approximately 0.95 in better agreement with our data.

- an increase in fluid heterogeneity while draining, a consideration repeatedly reported in literature (Knight and Nolen-Hoeksema [1990], Cadoret et al. [1995]) and already described in previous section 5.1.3. A fluid modulus $K_f = K_{B8}$ would cause the sign of $E/\ddot{u}$ to change at approximately $S_w = 0.54$, ratios being negative above this limit and positive below.

- an increased homogeneity level during re-imbibition, though not as complete as during primary imbibition. It explains the exponent of 40, being greater than the drainage value of 8 but much smaller than the initial imbibition value of 100. This might be due to the trapping of air bubbles within small pores. In this case a phase reversal is expected for saturation degree approaching 0.9. Though we seem to identify the initiation of the phase shift when looking at experimental points (red) over 0.8 saturation, we were never to reach the saturation break point, despite how long we waited and how often we put the fluid to circulate.

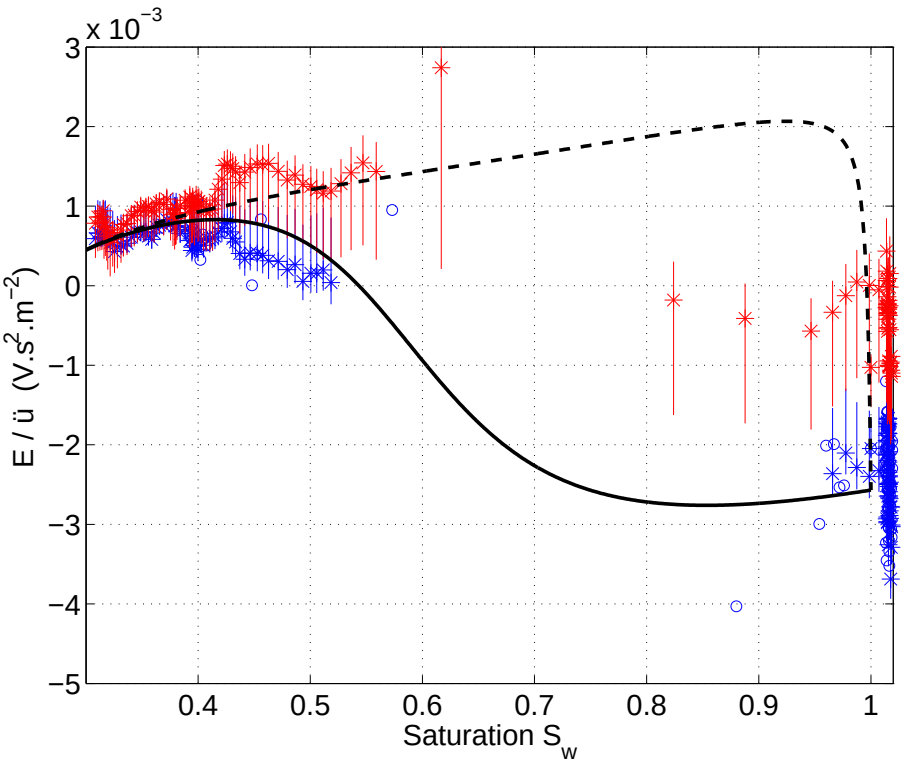

Figure 5.18: Collection of experimental values of local $E/\ddot{u}$ ratio estimated on first maximum picking at offset 3.9 *cm* (blue data) and 5.8 *cm* (red data), for mid-point dipole of length 18 *mm* and corresponding seismic. Seismic amplitudes at 3.9 *cm* were extrapolated from attenuation and real seismic maxima. Stacked value on 5 acquisition (25 stacks) are represented by asterisks, while single acquisition (5 stacks) show as circles. The quantity $sgn(E/\ddot{u}) \times |E/\ddot{u}|$, where the $E/\ddot{u}$ ratio has been calculated by Pride at 1.5 kHz for two types of effective fluid modulus: $K_f = K_R$ represented as a dashed line and $K_f = K_{B8}$ as a thick black line. Other variable parameters were set as having: a fluid conductivity of 7.2 mS/m (initial-imbibition data corrected to that value), a bulk modulus $K_{fr} = 50\ MPa$ and a residual water saturation of 0.25. Asymmetric error bars try to account for the baseline shift documented in figure 5.17.

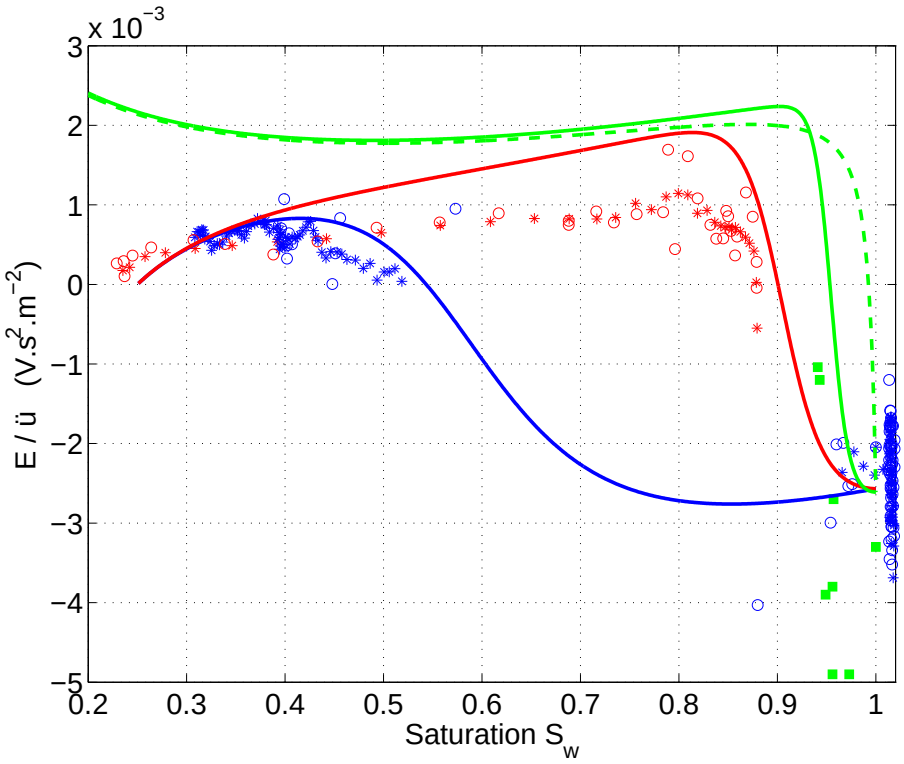

Figure 5.19: Collection of experimental values of local $E/\ddot{u}$ ratio estimated during drainage on first maximum picking for initial imbibition (green), consecutive drainage (blue) and final imbibition (red). We considered data acquired at mid-point dipoles of length 18 mm located at offset 3.9 cm combined to extrapolated corresponding seismic. Stacked value on 5 acquisition (25 stacks) are represented by asterisks, while single acquisition (5 stacks) show as circles. Primo-imbibition data (green) were normalised relatively to a fluid conductivity of 7.2 mS/m, common to drainage and re-imbibition measurements, by using eq. (2.96). Primo-imbibition data count between 35 and 70 stacks. The associated model prediction at 1.5 kHz after Pride are shown as quantity $sgn(E/\ddot{u}) \times |E/\ddot{u}|$. Plain curves are related to Brie empirical law for effective fluid modulus, with respective exponent $e = 100$ (green), $e = 8$ (blue) and $e = 40$ (red). The green dashed line stands for calculations made on first imbibition using Reuss model. We note that both green lines show very similar behavior for $S_w < 0.7$. For initial imbibition, residual water saturation is 0, while it is taken to lay by 0.25 for both drainage and re-imbibition cycles.

Finally, the sign change was experienced only once during the drainage phase, while initial imbibition resulting in $S_w > 0.95$ offered strictly negative ratios and secondary imbibition jamming at $S_w = 0.88$ gave only positive. In this last case, a notable drop of the ratio for water saturation of $[0.8 - 0.88]$ may indicate the approach of the sign change. Yet, despite long waiting and tedious refilling we got no evolution of the experimental system. As we had suggested on purely theoretical basis from eq. (2.114), β_P shifting phase implies that relative phase of U and W should reverse, as if changing the flowing mode. Our jamming at saturation $S_w \approx 0.9$, being possibly the threshold to the sign change associated to re-imbibition, might support the idea of a regime change requiring additional energy to take place.

Conclusions

Our present results on the saturation-dependent coseismic seismoelectric field, appears to support the existence of a 'no-flow' saturation point controlled to a great extent by the properties of the effective fluid while being frequency-independent. This critical saturation

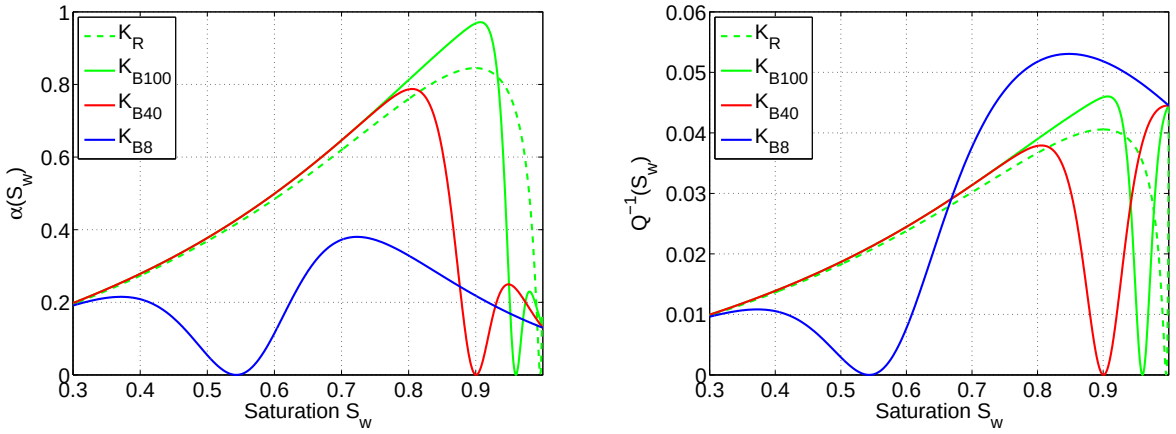

(a) (b)

Figure 5.20: Dependency of intrinsic attenuation (a) and inverse quality factor (b) on S_w and on the effective fluid model. For a given model of effective fluid modulus, α, Q^{-1} and $|E/\ddot{u}|$ go to the zero for the same saturation degree. Curves were calculated for a frequency of 1.5 kHz.

S^* would mark the sign reversal of the coseismic seismoelectric field. Yet, its cause being mechanical, this phenomenon would affect further quantities than the sole coseismic seismoelectric field.

Indeed, as β_P equals zero, meaning no fluid movement W according to eq. (2.114), there will be no Biot losses by macroscopic fluid movement, causing intrinsic attenuation α and inverse quality factor calculated after Biot to be zero. As Pride's model relies on the Biot theory for energetic losses characterisation, we checked our assumption numerically on a series of computation, involving the many models of effective fluid modulus, encountered in our characterisation of the hysteresis on saturation. As can be seen in figure **??**, attenuation and inverse quality factor associated to the fast P-wave do indeed go to zero for a critical saturation degree S^* identical to that marking the sign reversal in associated electric. Moreover, this calculated drop shows some similarity to decreasing attenuations actually observed during drainage observed on a saturation range of 0.4 to 0.6, as reported in figure 5.9b.

In the paper by Bordes et al. [2015] there is no account of such observation. Yet, through all drainage and imbibition cycles the medium remained partially saturated as attested by seismic and seismoelectric velocities ranging by 150 ± 20 m/s. With respect to velocity, drainage and imbibition data taken from the paper would both be rather comparable to our re-imbibition data-set (see red markers in figure 5.9a). Likewise, the sign of their transfer function $E/\ddot{u}$, being positive, matches that of our $E/\ddot{u}$ values at imbibition. For our data sets, we noted that the phase shift in the electric tended to coincide with the departure of seismic velocities from the low saturation baseline. In the experiment by Bordes et al. [2015], as full saturation was never reached, such major changes in seismic velocities were not to be expected. This might possibly explain why $|E/\ddot{u}|$ related to imbibition and drainage might appear comparable and quasi-constant in a first approximation under partial saturation (as visible in figure 1.5), while they might be so different when starting the drainage from full saturation.

5.2.3 Calculation of a dynamic transfer function

Initial motivation for this experimental work was the dynamic characterisation of the coseismic seismoelectric transfer function. Experimental material and source, of wide spectrum $[0.5 - 10kHz]$, were explicitly chosen as to enable propagation observation within a frequency band encompassing Biot transition frequency f_{Biot}, being of approximately 2 kHz in sub-saturated sand.

Our first try was to solicit the medium using a continuous sinus wave of fixed frequency to facilitate signal processing. Unfortunately, the dedicated piezoelectric source produced extremely coherent EM noise, while the information delivered by accelerometers became inconsequent (continuous excitation possibly triggering a resonance mode). We consequently moved to a pneumatic pulse source, free of EM noise. Yet, excitation modes were far less modulable than initially planed: our frequency band of SE investigation, limited by the electric, shrunk to $[0.5 - 3\ kHz]$ as can be observed in figure 5.4.

Having developed a tool for spectral calculation of the coseismic transfer function, we show in figure 5.21 the results extracted from data sets $'20140304'$ at conductivity 1.7 mS/m (blue), $'20140305'$ at 2.5 mS/m (green), $'20140306'$ at 5.6 mS/m (red) and $'20140307'$ at 7. 7 mS/m (black).

The dynamic transfer functions were obtained on experimental data processed by a Gaussian window for first arrival selection (see section 4.1.2). For each data set we selected the relevant channels on two criteria:

- first, the electric first arrival should be observable (which was usually possible for maximal offsets about $9 - 12\ cm$).

- second, there should be a seismic receiver at the dipole corresponding offset.

Under such conditions, experiments $'20140305'$ and $'20140306'$ provided five pairs of receivers, while $'20140304'$ offered four pairs and $'20140307'$ only two. For the selected channel, frequency spectra were smoothed using a sliding window of width 200 Hz centered on the considered frequency. We then calculated the spectral $|E/\ddot{u}|$ ratio at a given frequency by linear regression over available pairs of seismic and electric spectral amplitudes, similarly to what can be seen in figure 5.14 (yet this operation was repeated for each frequency). In order to better constraints our linear regression (or even to enable it in case of experiments $'20140307'$), we added the point at the origin $(E, \ddot{u}) = (0, 0)$. We chose a 50 % confidence interval for error calculation on linear regressions.

As a first impression, experimental curves are well-sorted and the order of magnitude is mainly respected with regard to the thick dashed model curves. The agreement between experimental and theoretical values is particularly striking for residual signal below 500 Hz. Yet, even with restricted requirements regarding the error confidence, error bars represented here as thin dashed lines are not selective enough, errors being usually greater than 200 %. Hence, there is no possibility to discriminate a specific domain associated to a definite conductivity and frequency band.

As a conclusion, on our narrow exploitable frequency band, our resolution is too gross to report the fine dynamic variations of the coseismic transfer function by about 50 % of the

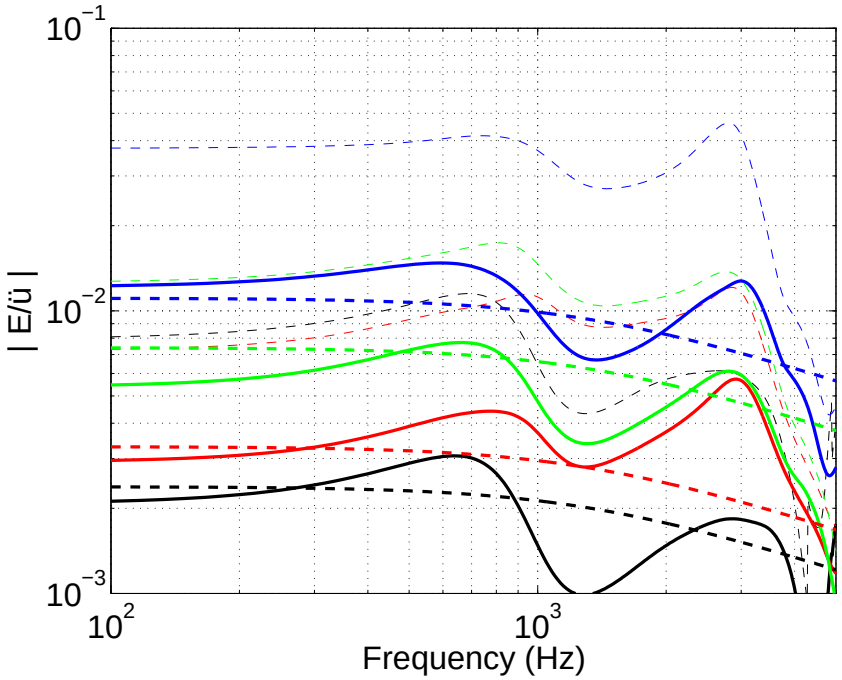

Figure 5.21: Dynamic transfer functions obtained by linear regression on experimental spectral data-sets (plain lines),associated to computed models (bold dashed lines) for varying conductivities. Seismic and electric spectra have previously been separately smoothed by a sliding window of width 200 Hz centered on the considered frequency. Experiments '20140304' and '20140305' stand respectively in blue and green while experiments '20140306' and '20140307' stand respectively in red and black. Confidence interval for linear regression was settled to 50 %, the associated error bars are the thin dashed lines of corresponding colors. Frequency pacing is of 16.67 Hz.

LF reference line, as predicted by the Pride model. The main problem of our investigation lies in the poor frequency selectivity of our source combined to the important attenuation of high-frequency components by our unconsolidated medium when being submitted to a wide spectrum source. The expansion of our exploration frequency-band would require using a continuous monochromatic source that imposes a selected frequency. Under such circumstances variations may become large enough for us to discriminate between values of the transfer function at 1 kHz, 10 kHz and 100 kHz.

5.3 Conclusion

As our preliminary analysis regarding the determination of the geometrical spreading by observing amplitude decrease on our experimental seismic data remained inconclusive, we decided to consider various possibilities of propagation geometry at a time. 1D and 3D propagation geometries, being the most commonly observed in the laboratory, we considered both to analyze experiments conducted in dry and sub-saturated sand. Under full-saturation, wavelength arguments led us to consider near-field configuration besides 3D propagation. This being settled, we comparatively processed seismic and electric recordings; with regard to first arrival selection and subsequent spectral treatment we could calculate velocity dispersion curves and dynamic attenuation from the data.

As expected seismic attenuation model obtained for strict Biot poroelasticity, estimating

losses on macroscopic fluid displacement at wavelength scale, considerably underestimated attenuation measurements on saturated and sub-saturated sand. By taking grain-to-grain friction into consideration, the Biot-Stoll asymptotic model would come close to actual attenuation curves calculated for a 3D propagation geometry, while our spectral data proved consistent with previous seismic acquired by Barrière [2011] on the same material. However the agreement between seismic and seismoelectric appeared partial, possibly due to difference in considered offsets: indeed, while seismic receivers were taken into account starting from a 10 cm offset to the source, due to the scarcity of seismoelectric data, nearest offsets had to be considered, for which the first arrival might be poorly separated. For full-saturation, only near-field geometry would account for the expected global decrease in attenuation.

In continuation, a first systematic analysis was conducted on seismic recordings monitored against saturation. The first massive imbibition, maintained for over a month till seismic velocities attested of full saturation, gave way to a continuous drainage and a step-like imbibition. Each phase showed a distinct signature in both attenuation and velocity, mainly controlled by the effective fluid (air-water) modulus $K_f(S_w)$ in possible link to its homogeneity level. Hence, the evolution of seismic velocities and attenuations with saturation degree S_w would provide us with the last refinement regarding relevant parameters to our poroelastic model. Estimation of the results by computations derived from Biot-Stoll asymptotes stood in fairly good agreement to the data. In particular, they seemed to support an apparent drop in attenuation observed during drainage

We eventually focused on the coseismic seismoelectric transfer function $E/\ddot{u}$ and its dependency on fluid conductivity, saturation degree and frequency. Our conclusions regarding the coseismic seismoelectric dependency on fluid conductivity corroborate former publications on the subject and support our quantitative measuring approach.

Supported by this result, we proceeded to the saturation-dependent part of the coseismic seismoelectric investigation. Similarly to the seismic, the electric data gathering a primo-imbibition - a drainage and a re-imbibition phase, displayed some hysteresis. The drainage data more specifically showed a phase shift of $E/\ddot{u}$ associated to a sign change of the first electric arrival for a saturation degree S_w of approximately 0.6 ± 0.1. These observations are in qualitative agreement with theoretical projections based on the extension of Pride's theory to partial saturation. Indeed, as expected by theory, on low-saturation time-records the seismic and electric first arrival are in phase; they flip out of phase for higher-to-full saturation. Practically, the sign change and its characteristic saturation for sign reversal may be theoretically accounted by using $K_f = K_{B8}$ while for evolution of $E/\ddot{u}$ with re-imbibition a $K_f = K_{B40}$: hence the same effective fluid modulus models quantitatively accounting for seismic succeed in qualitatively explaining local estimations of the coseismic seismoelectric transfer function.

We finally attempted to give a dynamic characterization of the coseismic seismoelectric transfer function on the $[1 - 4\ kHz]$ frequency-range for a selection of fluid conductivities. Yet, if the curves were sorted as expected and the measured and modeled amplitudes of the transfer functions grossly agreed, we were unable to document satisfyingly the expected

variations related to the crossing of Biot transition frequency.

Hence, if our resolution enabled conclusive observations on coseismic seismoelectric dependency to conductivity and allowed for a qualitative investigation on its evolution with the variation of water saturation, the much tinier dynamic changes are out of our resolution scope. These restrictions could be overrun by widening our exploration frequency band. This could be attempted by imposing high-frequency propagation within a low-pass unconsolidated material using a continuous monochromatic source and adapted seismic receivers.

Chapitre 6

Conclusions and outlooks

We started this study with purpose of completing existing works by Barrière et al. [2012] and Bordes et al. [2015], conducted on the same material with similar impact sources. Aim was to realise simultaneous acquisitions of seismic and coseismic seismoelectric on the full saturation range, while widening the original frequency domain of investigation with an eye for the dynamic characterisation of the transfer function $E/\ddot{u}$. As a correlated requirement, we had to complete quantitative measurements of seismic and electric signals in order to gain suitable data for comparison with Pride [1994] and Pride and Haartsen [1996] theoretical models. With this intent a conductivity-dependent experiment was developed, conductivity being chosen as the variable for its adjustability, its applicability and its important impact on electric measurements. In this context, we report what has been achieved and what remains for clarification or improvement.

6.1 Main results

Validation of temporal and spectral signal processing on synthetic signals

In order to study the coseismic seismoelectric phenomenon usually accompanying compressional P-waves, our experimental set-up was designed to facilitate the recording of direct waves and prevent the apparition of secondary sources. Yet, by using an impulsive source of wide-frequency spectrum, the direct P-wave arrival would be closely followed by further wave packets. The recovering of direct-wave information would consequently became of primary concern. With that purpose in mind we assembled and tested signal processing tools on a simple propagating synthetic, assembled from two Gaussian curves of known characteristics

We resolved to characterise the specific attributes of the first arrival - *i.e.* velocity and attenuation - following both time-series and spectral approaches. In the first case, an estimation of the first-arrival characteristic frequency f_{nom} was required for comparison with dynamic model predictions. In the second, the relevant signal had to be extracted from the record before taking the processing into the frequency domain. This last operation was enabled through the application of a Gaussian window scaling with the signal of interest by knowing the position of the signal first extremum t_{max} and estimating its first-break arrival time t_{1st}. Same information were also used for f_{nom} determination.

Tests on the synthetic data set permitted to retrieve the spectral signature of the first Gaussian arrival. Having the proper tool for first-arrival recovering, we developed our approach for dynamic investigation of common seismic attributes. We focused on velocity dispersion and attenuation determination that eventually enables to characterise the quality factor. At each step, the processing was applied on synthetic data, both before and after first arrival selection, and compared to the ideally isolated first arrival. Good agreement of selected signal attributes with the latter, supported our spectral processing as well as it sustained our first arrival selection process. When being applied to real seismic data, time-pickings gave indeed similar result to spectral analysis at the nominal frequency. For seismoelectric data the agreement was not so complete, yet by considering all available electric receiver with no offset restriction, we may have considered poorly separated P-waves, eventually tainting the spectral data with frequency information from later arrivals.

Development of quantitative electric measurements

In our ambition for quantitative measuring, special attention was given to spacial resolution of our electric measurements and to the dipole positioning relatively to its corresponding accelerometer. We started by assembling an electrode array from 30 rods spaced by 0.9 cm thus providing high receiver density. We then resolved to record each potential difference relatively to the last electrode of the array taken as a common reference, a procedure that would eventually facilitate dipole-reconstruction of any given length.

With this adjustable dipole-geometry we tried to determine the optimal dipole configuration for coseismic electric field observation by checking the acquired electric against characteristic features of the mother seismic wave (as central frequency or characteristic arrival times). This analysis pointed a better agreement of smaller dipoles with the seismic waveform. We concomitantly addressed stability issues of the coseismic seismoelectric field. For a given accelerometer position x_0 we either reconstructed a series of dipole all centered on offset x_0 (common mid-point geometry) or formed a series of dipole all sharing the electrode closest to the source placed at offset x_0 (first-electrode geometry): no real conclusion was given regarding the advantage of one configuration upon the other, as in both cases electric field tends to stabilise towards a fixed value E_0 when growing infinitely small. Based on empirical fit observations and signal-to-noise ratio arguments, we eventually favored the shortest mid-point dipole geometry.

We tested our selected dipole geometry on acquisitions obtained for varying fluid conductivity. The local estimations of the transfer function $|E/\ddot{u}|$ were monitored with σ_f within the range $[1 - 10\,mS/m]$. The good agreement between experimental point and simulation, regarding both evolution trend and absolute values, supports the legitimacy of our acquisition geometry to quantitative seismoelectric measurements.

Observation of a saturation-induced hysteresis on seismic data

A systematic analysis of time-picked seismic attributes was conducted on seismic recordings, monitored against saturation. The complete experiment regrouped three distinct cycles:

to a primo-imbibition, that was maintained in equilibration during a month until reaching full saturation, succeeded a continuous drainage eventually followed by a re-imbibition. Each cycle appeared to show a distinct signature in both attenuation and velocity, forming an hysteresis. In particular, for similar saturation degrees we observed the superiority of drainage velocity relatively to those associated to imbibition, an effect similarly experienced by Barrière et al. [2012] for a comparable experiment on the same material.

On basis of velocity data we observed that the model could be fitted to our results by defining the effective fluid (air-water) incompressibility $K_f(S_w)$ according to a Brie model of adjustable exponent e. By varying this exponent, the curve $K_{Be}(S_w)$ would describe the whole domain between upper Voigt- ($e = 1$) and lower Reuss-bound ($e > 100$), the first being characteristic of inhomogeneous system when the latter is traditionally associated to fully-homogeneous mixtures. While the drainage-related exponent would range as the lowest, the highest exponent value was associated with primo-imbibition on dry sand, likely to provide the best homogeneity degree (imbibition process not affected by preferential path or residual trapped water). This conclusion rather supports the possible connection of Brie's exponent to the effective-fluid homogeneity-level, expected to be greater during imbibition than drainage as reported by Knight and Nolen-Hoeksema [1990] and Cadoret et al. [1995].

Regarding attenuation calculations, we concluded that strict Biot poroelasticity, estimating losses on macroscopic fluid displacement at wavelength scale, considerably underestimated our data. By taking grain-to-grain friction into consideration, the Biot-Stoll asymptotic model developed by Kimura [2007] would come close to actual attenuation curves calculated for a 3D propagation geometry. The combination of Biot-Stoll asymptotic model to Brie's K_f formulation at partial saturation would stand in good agreement to our estimation of saturation-dependent attenuation. In particular, the apparent drop partly observed in experimental attenuation data during drainage appears to correlate with a sudden and transitory drop of the model curves at a characteristic saturation $S^* \simeq 0.6 \pm 0.1$, that will have further implications on seismoelectric.

Observation of a sign change in transfer function $E/\ddot{u}$ consistent with model projections

Similarly to the seismic, the electric data acquired during saturation variation showed hysteresis between the drainage and the imbibition phases. A particular feature of this hysteresis was a phase shift of $E/\ddot{u}$ associated to a sign change of the first electric arrival. This phenomenon was observed for a saturation degree S_w of approximately 0.6 $\pm$0.1 echoing characteristic saturation S^* that marks a drop in seismic attenuation. Generally speaking, when previously defined effective fluid modulus models, initially used for quantification of the saturation-dependent seismic attributes, were implemented in the calculation of the transfer function, the results did qualitatively account for variations of the coseismic seismoelectric transfer function with saturation.

This sign change is indeed in qualitative agreement with theoretical projections based on the extension of Pride's theory to partial saturation conditions: as predicted, seismic and electric first arrival are in phase within the lower saturation-range and eventually turn out of

phase for higher-to-full saturation. A theoretical investigation of this phenomenon ascribe its origin to parameter β_P, a dimensionless mechanical quantity known as the fluid-to-matrix displacement ratio that involves Biot's coefficient C and H. A more empirical approach, seems to put it in relation with the relative position of K_f and K_{fr}. For any effective fluid incompressibility model applied to sand, the sign change would occur within close range to saturation S_w verifying $K_f(S_w) = K_{fr}$, an ability usually restrained to 'soft' unconsolidated material.

Having qualitatively recovered by theoretical predictions the experimentally observed sign inversion, we tried to connect this observation to common elastic parameters of the medium. We found the sign change of $E/\ddot{u}$, actually born by the coseismic electric first arrival, to be concomitant with that of mechanical parameter β_P: hence all three quantities go to zero for a given saturation noted S^*, independent on frequency. Now, in its original definition, β_P is presented as the ratio $\mathbf{w}/\mathbf{u}$ of relative fluid to solid displacement. Under this light, nullifying β_P before changing sign appears of heavy consequences for both seismic and electric. Indeed, at saturation S^*, theory predicts the immobility of the fluid phase relatively to the frame. Under such 'no-flow' conditions there will be no Biot losses by macroscopic fluid movements, so that attenuation α_p and inverse quality factor Q_p^{-1} predicted by Biot will drop to zero at any frequencies for that precise saturation S^*, meaning that the medium should behave as a perfectly elastic solid. Naturally, flow interruption would prevent any electrokinetic effect, explaining why the coseismic electric field will be zero at that point.

6.2 Perspectives

Investigation on microscale implications of the $E/\ddot{u}$ sign change

Apart from that singular point, changing the sign of β_P under a constant seismic excitation implies that relative fluid displacement should change direction. Hence the whole system behaves as if changing regime; as changing regime might have some energetic implications, this last aspect could possibly play a role in the difficulty to reach full saturation by unassisted saturation processes.

Such concepts as 'immobile fluid' or 'relative fluid displacement changing direction' are hard to assimilate so even more to picture. Hence, the better understanding of larger implications of that sign inversion, or possible application to improved soil characterisation, would require a finer comprehension of that phenomenon. Ideally, we should investigate what happens at the pore scale, possibly by numerical simulation.

Contribution of numerical simulation to outstanding issues

We have studied the coseismic seismoelectric effect and its dependency to saturation or conductivity variation under an experimental light completed by an analytical approach. Though we found both aspects to be in fair agreement, some grey areas remain. Hence, we could not account for discrepancies between seismic and seismoelectric attenuation, the latter being usually twice as high as the first. While we suspect some implication of near-

field effects, we have little means of investigation. More generally, the scarcity of exploitable coseismic seismoelectric information compelled us to consider the electric field at any available location with no restrictions on shortest offset. As a consequence, part of our coseismic records might have been affected by poorly separated first arrival, while high-saturation observations during the drainage experiment clearly belonged to the near-field domain.

In all these matters, a direct numerical simulation scaled to our laboratory experiment might have brought some light. Indeed, by accounting for the near-field effect it may have helped us in identifying the affected receivers and in determining whether same near-field characteristics apply to seismic and electric. By quantifying and possibly correcting the effect of near-field it could improve data comparison to Pride's theory formulated in far-field. It would also prove useful in separating the contribution of mingled arrival where necessary. In addition, a suitable modeling of the source could possibly elucidate the irresolution of our geometrical spreading analysis with regard to first maxima amplitude ratio. Finally, as we just saw, numerical modeling could prove helpful in the fine comprehension of the coseismic electric field sign inversion with varying saturation. In practice, such numerical tool could be shaped by adapting to laboratory scale the full waveform code developed by Garambois and Dietrich [2002] and extended to partial saturation by Warden et al. [2013].

Experiment adaptation to continuous monochromatic seismic excitation

Thanks to repeated stack, we managed to extend our frequency range of seismoelectric investigation to approximately $[0.5 - 4\ kHz]$ using an impulsive pneumatic source. Yet limited resolution on the transfer function $E/\ddot{u}$ remained incompatible with the observation of fine dynamic variations occurring within such restricted frequency-range. Note that, by remaining so close to f_{Biot} estimated at 2 kHz on saturated sand, the dynamic decrease of $E/\ddot{u}$ with frequency would be limited to about 50% (fluid conductivities in the mS/m range).

Late results provided by Zhu and Toksöz [2013], regarding similar investigation on Berea sandstone $f_{Biot} \approx 100 - 160\ kHz$ for a pulse experiment, remain encouraging as to the dynamic behaviour observability of the coseismic transfer function. Indeed, their analysis of $L_{EK}(\omega)/\sigma_b$ within the $[15 - 150\ kHz]$ frequency-range managed to observe a total voltage diminution by approximately 40% for increasing frequency at $\sigma_f = 12\ mS/m$; the decrease neared 70% for a ten-times higher conductivity. This decrease,comparable to our resolution limit, was observed at frequencies inferior or equal to f_{Biot} within the low frequency domain of Berea sandstone ; for a similar frequency range on unconsolidated sand we would investigate the HF dynamic domain of the transfer function where large variations are expected. Hence, provided we could force comparable frequencies to propagate within our unconsolidated media as to cover the $[1 - 100\ kHz]$ range, we might succeed in singling out values of the transfer function at 1 kHz, 10 kHz and 100 kHz with comparable resolution.

This might be achieved by using a continuous sinusoid as a seismic excitation. Indeed, by imposing repeatedly and exclusively one single frequency possibly greater than 3 kHz, we may get better chances of observing that specific frequency, that would otherwise be diffused by the highly attenuating sand. However, such continuous excitation usually requires

a piezoelectric source, which tendency to EM-noise radiation is ill-suited to seismoelectric measurement. Insulating the source by a Faraday cage without altering its energy would hence be of primary interest. Moreover, as we experienced in our own attempt of continuous seismic excitation, such experiment demands seismic receiver designed for such purpose. Indeed most receivers adapted to seismic pulse detection seem to be driven to a resonance mode under continuous monochromatic excitation. In conclusion, forcing the extension of the frequency investigation domain to challenging frequencies (meaning not naturally observable), requires thoroughly adapted devices.

Extension of our present study to field observation and possible application

It would be interesting to verify wether the sign inversion of the coseismic seismoelectric transfer function $E/\ddot{u}$ might be observed at field scale. For finding it out, one could conduct a long-time monitoring on a similar principle to the study by Strahser et al. [2011], yet preferably in a Vertical-SeismoElectric-Profiling (VSEP) configuration. In their study Strahser et al. [2011] repeated seismoelectric acquisitions on horizontal profiles during several month, while monitoring the soil resistivity, and concluded to the increase of $E/\ddot{u}$ with increasing saturation. In the case of the VSEP configuration, we may measure the coseismic seismoelectric through all the vadose zone, possibly tracking subtle changes of saturation with depth. In favour of an 'oscillating' water-table, a monitoring of the imbibition and drainage phases could be run at a given point, with emphasis on the identification of a possible hysteresis. Yet, as we may deduce from our observations and those of Bordes et al. [2015], sign change of $E/\ddot{u}$ seems associated to large velocity variations only observable while draining a previously fully-saturated medium. Hence saturation at the testing site should be known for extreme cyclic variations possibly seasonal.

Finally, regarding the quantitative measuring of the coseismic seismoelectric field, simple propagating synthetics seemed to indicate a loss of $30 - 50$ % of the electric field amplitude by using a dipole length of 0.25 λ, where λ is the wavelength (figure 4.27). Though simplistic, this approach does warn against the use of long dipoles. It also offers some perspective for coseismic seismoelectric amplitude correction, where longer dipole-lengths are required to mitigate the random noise level [Strahser, 2006].

Chapitre 7

Appendices

Sommaire

7.1 Summary of the mentioned experiments and associated acquisition parameters

For each experiment, the reference name is given after the date of the measurement under the format $YYYYMMDD$. Hence by considering the reference name, we get an idea of the duration of a full experimental round, from several weeks for the primo-imbibition phase to one day for the drainage monitoring. When different rows of measurement happened within a single day, the experiment may be noted as $X - YYYYMMDD$, where letter X may be D for dry sand, F for full saturation, or PZ in case we are considering data acquired with the piezoelectric source. In this report, we considered only data acquired with the pneumatic

source described in section 3.2.1.

When looking at the considered channels in following table, you will note that the number of available seismic receivers tends to shrink with lasting experiments. Indeed, a major concern regarding the use of the Brüel & Kjær accelerometers was their lack of watertightness, as cable and captor are screwed together while the seal fail to assure the impermeability of the system. This problem had already been experienced during previous experimental campaigns and resolved with an addition of shrinkable heat sleeves and wax, yet these experiments went for a couple of days at the most. In anticipation of a prolonged immersion of the transducers within the saturated medium, a decision was made to weatherproof them with epoxy resin, causing among others the cable to be irremediably bond to the transducers connector while rigidifying that connection. Few captors were lost in the process, some others switched off after some days of measurement, probably due to eventual water leakage into the captor. As an example, in the case of primo-imbibition, we lost 4 accelerometers out of 20 after an immersion lasting over a month; all four captors were already lost within the first week of measurement.

7.1.1 Conductivity experiments

These conductivity-dependent experiments were led during primo-imbibition until full saturation was achieved. This first experimental round lasted about a month. Pneumatic source

Nb. of channels: either 31, parted as 13 seismic channels ($1 \rightarrow 13$) and 18 electric channels ($14 \rightarrow 31$) or 50, parted as 21 seismic channels ($1 \rightarrow 21$) and 29 electric channels ($22 \rightarrow 50$)

Sampling frequency: 100 kHz

Nb of samples: 50000 on initial records, 6000 after reconstruction

Attenuation geometry: 3D as long as $V_{P,1st} < 500m/s$, near-field otherwise (noted NF)

Data with $V_{P,1st} > 500m/s$, treated with a low-pass Butterworth filter

Considered dipoles: mid-point dipoles of length 18 mm

Confidence for calculations of errors on linear regression : 80%

Effective fluid incompressibility calculated after a Wood model with $K_f = K_R$. Frame modulus being taken as $K_{fr} = 2.55\ 10^7 Pa$

	Dry sand	**Conductivity 1**	**Conductivity 2**	**Conductivity 3**	**Conductivity 4**
Reference	$D - 20140304$	20140304	20140305	20140306	20140307
Stack number	15	25	25	25	25
Channel total number	50	50	50	50	50
Configuration	3D	3D	3D	3D	3D
Available file	1	1	1	1	1
Saturation S_w (%)	0	94.1	94.3	94.9	95.6
Conductivity σ_f (mS/m)	0	1.73	2.51	5.65	7.75
pH	—	7 $\pm$ 0.7	6.8 $\pm$ 0.4	7.6 $\pm$ 0.2	7.2 $\pm$ 0.1
Seismic channels	6 $\rightarrow$ 14 / 19	6 $\rightarrow$ 14 / 19	5 $\rightarrow$ 13 / 18	5 $\rightarrow$ 13 / 18	5 $\rightarrow$ 13 / 18
Seismic offsets (cm)	10.4 $-$ 22.6	10.4 $-$ 22.6	10.4 $-$ 22.6	10.4 $-$ 22.6	10.4 $-$ 22.6
Source max. acceleration ($m.s^{-2}$)	-1747	-5055	-5129	-6078	-4346
1^{st} max. @ 4.8cm ($m.s^{-2}$)	-15.52	-52.24	-56.17	-78.11	-49.83
$V_{P,1^{st}}$ ($m.s^{-1}$)	169 $\pm$ 7	174 $\pm$ 11	170 $\pm$ 12	169 $\pm$ 9	181 $\pm$ 8
$V_{P,max}$ ($m.s^{-1}$)	155 $\pm$ 4	151 $\pm$ 12	152 $\pm$ 12	151 $\pm$ 9	158 $\pm$ 9
Attenuation α_S	7.6 $\pm$ 0.9	8 $\pm$ 1.1	7.5 $\pm$ 1.3	7.9 $\pm$ 0.8	7.8 $\pm$ 0.5
Q_S^{-1}	0.44 $\pm$ 0.07	0.74 $\pm$ 0.15	0.63 $\pm$ 0.15	0.68 $\pm$ 0.11	0.69 $\pm$ 0.08
f_{S0}	1041	676	714	694	735
f_{Sn}	833	532	568	568	581
Stack number	15	48	50	50	50
Configuration	complete	near	near	near	near
Electric channels	—	1 $\rightarrow$ 7 / 16	1 $\rightarrow$ 9 / 16	1 $\rightarrow$ 9 / 16	1 $\rightarrow$ 7 / 16
Electric offsets (cm)	—	3.9 $-$ 9.5	3.9 $-$ 11.4	3.9 $-$ 11.4	3.9 $-$ 9.5
1^{st} max. E @ 4.8cm (V/m)	—	0.89	0.464	0.429	0.145
slope $\lvert E/\ddot{u}\rvert$ ($mV.s^2.m^{-2}$)	—	-13.9 $\pm$ 5.2	-7.1 $\pm$ 2.7	-5 $\pm$ 1.7	-2.5 $\pm$ 3.8
$V_{E,1^{st}}$ ($m.s^{-1}$)	—	118 $\pm$ 8	107 $\pm$ 8	121 $\pm$ 11	116 $\pm$ 27
$V_{E,max}$ ($m.s^{-1}$)	—	105 $\pm$ 2	101 $\pm$ 5	109 $\pm$ 8	173 $\pm$ 30
Attenuation α_E	—	19.6 $\pm$ 5.3	17.2 $\pm$ 3.3	14.5 $\pm$ 3.5	14.6 $\pm$ 13.2
Q_E^{-1}	—	0.81 $\pm$ 0.28	0.64 $\pm$ 0.17	0.49 $\pm$ 0.16	0.50 $\pm$ 0.57
f_{E0}	—	1000	961	1190	1042
f_{En}	—	806	862	1087	1137

Table 7.1: Information relatively to coseismic seismoelectric measurements on dry sand and at variable conductivity after initial rapid imbibition.

	Conductivity 5	**Conductivity 6**	**Conductivity 7**	**Conductivity 8**	**Conductivity 9**
Reference	20140308	20140311	20140313	20140317	20140402
Stack number	15	25	8	75	36
Channel total number	31	50	31	31	31
Configuration	3D	3D	3D	NF	NF
Available file	1	1	1	1	1
Saturation S_w (%)	95.6	95.7	95.8	97.3	100
Conductivity σ_f (mS/m)	—	6.62	—	8.5	7.5
pH	—	7.25 $\pm$ 0.2	—	7.15 $\pm$ 0.05	—
Seismic channels	3 $\rightarrow$ 6 / 10	4 $\rightarrow$ 10 / 17	4 $\rightarrow$ 9 / 9	4 $\rightarrow$ 9 / 9	4 $\rightarrow$ 8 / 8
Seismic offsets (cm)	10.4 $-$ 22.6	10.4 $-$ 19.8	10.4 $-$ 18.8	10.4 $-$ 18.8	4.8 $-$ 17
Source max. acceleration ($m.s^{-2}$)	-6525	-4813	-5865	-5859	-6296
1^{st} max. @ 4.8cm ($m.s^{-2}$)	-68.21	-42.36	-16.27	-35.82	-65.86
$V_{P,1^{st}}$ ($m.s^{-1}$)	197 $\pm$ 21	272 $\pm$ 31	304 $\pm$ 34	738 $\pm$ 132	1555 $\pm$ 154
$V_{P,max}$ ($m.s^{-1}$)	169 $\pm$ 31	164 $\pm$ 22	240 $\pm$ 25	302 $\pm$ 66	1263 $\pm$ 176
Attenuation α_S	8.1 $\pm$ 1.5	11.9 $\pm$ 1.4	4.1 $\pm$ 0.9	2.4 $\pm$ 2	3.4 $\pm$ 0.9
Q_S^{-1}	0.8 $\pm$ 0.24	1.86 $\pm$ 0.43	0.64 $\pm$ 0.22	0.59 $\pm$ 0.59	0.63 $\pm$ 0.24
f_{S0}	714	714	893	1316	2777
f_{Sn}	555	397	555	625	2500
Stack number	15	75	8	75	36
Configuration	B	near	near	near	near
Electric channels	1 $\rightarrow$ 4 / 16	1 $\rightarrow$ 9 /16	—	1 $\rightarrow$ 5 / 16	1 $\rightarrow$ 4 / 16
Electric offsets (cm)	3.9 $-$ 6.7	3.9 $-$ 11.4	—	3.9 $-$ 7.8	3.9 $-$ 6.7
1^{st} max. E @ 4.8cm (V/m)	0.201	0.131	—	0.065	0.019
slope $\lvert E/\ddot{u}\rvert$ ($mV.s^2.m^{-2}$)	-4.9 $\pm$ 0.02	-2.5 $\pm$ 0.9	—	-1.5 $\pm$ 1.2	-0.67 $\pm$ 0.2
$V_{E,1^{st}}$ ($m.s^{-1}$)	105 $\pm$ 87	219 $\pm$ 34	—	138 $\pm$ 142	501 $\pm$ 313
$V_{E,max}$ ($m.s^{-1}$)	115 $\pm$ 1	253 $\pm$ 48	—	424 $\pm$ 301	-296 $\pm$ 718
Attenuation α_E	15 $\pm$ 38	2.7 $\pm$ 11.8	—	13.7 $\pm$ 5.9	26.5 $\pm$ 39.1
Q_E^{-1}	0.48 $\pm$ 1.6	0.15 $\pm$ 0.72	—	0.38 $\pm$ 0.55	0.69 $\pm$ 1.53
f_{E0}	1041	926	—	1389	1526
f_{En}	3000	1042	—	1786	4167

Table 7.2: Continuity of the coseismic seismoelectric measurements relatively to conductivity variations while fluid keeps being circulated to favour the achievement of full saturation. Value with an asterisk where obtained with a Butterworth low-pass filter.

7.1.2 Full saturation, Drainage and Imbibition experiments

Pneumatic source

Nb. of channels: 31, parted in 13 seismic channels ($1 \rightarrow 13$) and 18 electric channels ($14 \rightarrow 31$)

Sampling frequency: 200 kHz

Nb of samples: 50000 on initial records, 6000 after reconstruction

Attenuation geometry: 3D as long as $V_{P,1st} < 500m/s$, near-field otherwise (noted NF)

Data with $V_{P,1st} > 500m/s$, treated with a low-pass Butterworth filter

Considered dipoles: mid-point dipoles of length 18 mm

Confidence for calculations of errors on linear regression : 80%

Effective fluid incompressibility calculated after a Wood model with $K_f = K_R$. Frame modulus being taken as $K_{fr} = 5.10^7 Pa$

	Full saturation	**Drainage**		**Imbibition**	
Reference	$F-20140408$	20140408		20140414	
Stack number	100	5		5	
Channel total number	31	31		31	
Configuration	NF	NF | 3D		3D	
Available file	1	147		41	
Saturation S_w (%)	100	100 $\rightarrow$ 30		23 $\rightarrow$ 87	
Conductivity σ_f (mS/m)	7.2	7.2		5.5	
pH	—	—		—	
Seismic channels	4 $\rightarrow$ 11 / 12	4 $\rightarrow$ 10 / 12	4 $\rightarrow$ 11 / 12	4 $\rightarrow$ 11 / 12	4 $\rightarrow$ 11 / 12
Seismic offsets (cm)	10.4 $-$ 22.6	10.4 $-$ 21.6	10.4 $-$ 22.6	10.4 $-$ 22.6	10.4 $-$ 22.6
Source max. acceleration ($m.s^{-2}$)	-4419	-3940	-5080		
1^{st} max. @ 4.8cm ($m.s^{-2}$)	-17.58	-12.09	-17.04		
$V_{P,1^{st}}$ ($m.s^{-1}$)	1635 $\pm$ 57	1517 $\pm$ 52	221 $\pm$ 11		
$V_{P,max}$ ($m.s^{-1}$)	1599 $\pm$ 201	1610 $\pm$ 161	195 $\pm$ 6		
Attenuation α_S	1.04 $\pm$ 0.85	0.86 $\pm$ 0.96	2 $\pm$ 0.97		
Q_S^{-1}	0.29 $\pm$ 0.25	0.24 $\pm$ 0.27	0.135 $\pm$ 0.07		
f_{S0}	1852	1724	1250		
f_{Sn}	1852	1785	877		
Electric channels	1 $\rightarrow$ 3 / 16	1, 3 / 16	1, 3 / 16	1, 3 / 16	1, 3 / 16
Electric offsets (cm)	3.9 $-$ 5.8	3.9 $-$ 5.8	3.9 $-$ 5.8	3.9 $-$ 5.8	3.9 $-$ 5.8
1^{st} max. E @ 4.8cm (mV/m)	0.0296	0.0385	-0.0145		
slope $\lvert E/\ddot{u}\rvert$ ($mV.s^2.m^{-2}$)	-1.4 $\pm$ 1.2	—	—	—	—
$V_{E,1^{st}}$ ($m.s^{-1}$)	-700 $\pm$ 1334	—	—	—	—
$V_{E,max}$ ($m.s^{-1}$)	2800 $\pm$ 5335	—	—	—	—
Attenuation α_E	9 $\pm$ 30.3	—	—	—	—
Q_E^{-1}	-1.38 $\pm$ 2	—	—	—	—
f_{E0}	1562	—	—	—	—
f_{En}	1351	—	—	—	—

Table 7.3: Information relatively to coseismic seismoelectric measurements at full saturation and during the following drainage and imbibition phases. Due to the lack of data for linear regression, values with asterisk were calculated as averages.

7.1.3 Preparatory experiments on pneumatic source

Pneumatic source

Nb. of channels: 31, parted in 13 seismic channels ($1 \rightarrow 13$) and 18 electric channels ($14 \rightarrow 31$)

Sampling frequency: 100 kHz

Nb of samples: 50000 on initial records, 6000 after reconstruction

Attenuation geometry: 1 D

Considered dipoles: mid-point dipoles of length 24 mm

Confidence for calculations of errors on linear regression : 80%

Problem with the source from 18/11/2013 to 03/12/2013

	Dry sand	**Conductivity a**	**Conductivity b**	**Conductivity c**	**Conductivity d**	**Conductivity e**
Reference	20131115	20131118	20131203	20131205	20131206	20131210
Stack number	17	49	10	36	38	8
Channel total number	51	31	31	31	31	31
Configuration	3D	3D	3D	3D	3D	3D
Available file	1	1	1	1	1	1
Saturation S_w (%)	0	—	—	—	—	100
Conductivity σ_f (mS/m)	0	3.35	7.7	8.35	6.9	—
pH	—	—	—	—	—	—
Seismic channels	3 $\rightarrow$ 14 / 20	1 $\rightarrow$ 10 / 12	1 $\rightarrow$ 7 / 9	1 $\rightarrow$ 7 / 9	1 $\rightarrow$ 8 / 9	1 $\rightarrow$ 4 / 7
Seismic offsets (cm)	6.6 $-$ 27	3 $-$ 19.8	3 $-$ 16.2	3 $-$ 16.2	3 $-$ 17.4	3 $-$ 9
Source max. acceleration ($m.s^{-2}$)	-3176	-2731	-1505	-1426	-674	-6688
1^{st} max. @ 5.4cm ($m.s^{-2}$)	-21.84	-41.1	-3.04	-5.63	-4	-20.79
$V_{P,1^{st}}$ ($m.s^{-1}$)	168 $\pm$ 5	280 $\pm$ 29	169 $\pm$ 31	1101 $\pm$ 285	1450 $\pm$ 290	1790 $\pm$ 4
$V_{P,max}$ ($m.s^{-1}$)	161 $\pm$ 6	160 $\pm$ 10	120 $\pm$ 14	606 $\pm$ 83	998 $\pm$ 286	1790 $\pm$ 4
Attenuation α_S	11.4 $\pm$ 0.9	19.3 $\pm$ 1.3	26.3 $\pm$ 4	23.2 $\pm$ 2.2	21.4 $\pm$ 1.8	14.7 $\pm$ 4.7
1D Q^{-1} @ 2 kHz						
f_{S0}	806	1190	893	1041	1190	
f_{Sn}	714	373	379	714	926	
Electric channels	—	1 $\rightarrow$ 7 /16	—	—	—	—
Electric offsets (cm)	—	4.2 $-$ 10.2	—	—	—	—
1^{st} max. E @ 5.4cm (V)	—	0.092	—	—	—	—
slope $\lvert E/\ddot{u}\rvert$ ($mV.s^2.m^{-2}$)	—	-2.3 $\pm$ 0.6	—	—	—	—
$V_{E,1^{st}}$ ($m.s^{-1}$)	—	256 $\pm$ 22	—	—	—	—
$V_{E,max}$ ($m.s^{-1}$)	—	103 $\pm$ 18	—	—	—	—
Attenuation α_E	—	2.6 $\pm$ 5.3	—	—	—	—
Q_E^{-1}	—	0.22 $\pm$ 0.46	—	—	—	—
f_{E0}	—	1087	—	—	—	—
f_{En}	—	862	—	—	—	—

Table 7.4: First measurement with the pneumatic source with an attempt on conductivity monitoring. attention pour l'instant ds ce tableau seule la sismoelec est calculee 3D

Calibration Chart for DeltaTron® Accelerometer Type 4513-001

Brüel & Kjær

Serial No.: 56369

Reference Sensitivity [1] at 159.2 Hz (ω = 1000 s^{-1}), 20 ms^{-2} RMS, 4 mA supply current and 23.1 °C: 10.62 mV/ms^{-2} (104.1 mV/g)

Frequency Range: Amplitude (±10%): 1 Hz to 10 kHz

Mounted Resonance Frequency: 32 kHz

Transverse Sensitivity [2]**:**
Maximum (at 30 Hz, 100 ms^{-2}): < 5% re Reference Sensitivity

Calculated Values for TEDS [3]**:**

Resonance frequency:	31.4 kHz
Quality factor @ f_{res}:	272
Amplitude slope:	-2.2 % / decade
High-pass cut-off frequency:	0.15 Hz
Low-pass cut-off frequency:	40 kHz

Measuring Range: ± 490 ms^{-2} peak (± 50 g peak)

Polarity of the signal is positive for an acceleration into the accelerometers mounting surface. For triaxial accelerometers and accelerometers with multiple mounting surfaces, the polarity of the signal is positive for an acceleration in the direction of the arrow on the drawing.

Electrical:

Low-frequency Roll-off:		20 dB/decade
Bias Voltage:	at 25°C:	+ 11 V to + 13 V
	Full Temperature Range:	+ 8 V to + 16 V
Power Supply Requirements:	Constant Current:	+ 2 to + 10 mA
	Unloaded Supply Voltage:	+ 24 V to + 30 V
Output Impedance:		120 Ω
Start-up Time:		< 1 s
Inherent Noise (RMS): Broadband (1 Hz to 10 kHz):		20 µV corresponding to 0.002 ms^{-2} (200 µg)
Isolation:		Case Isolated
Recommended cables:		see Product Data Sheet

Environmental:

Temperature Range:	– 51 to + 100°C (– 60 to + 212°F)
Temperature Coefficient of Sensitivity:	+ 0.24%/°C
Temp. Transient Sensitivity (3 Hz Low. Lim. Frq. (–3 dB, 6 dB/oct)):	0.023 ms^{-2}/°C
Base-strain Sensitivity (at 250 µε in base plane):	0.03 ms^{-2}/µε
Max. Non-destructive Shock:	49 kms^{-2} peak (5000 g peak)

Mechanical:

Case Material:	Titanium
Sensing Element:	Ceramic
Construction:	PlanarShear®
Sealing:	Hermetic
Weight:	8.6 gram (0.30 oz.)
Electrical Connector:	10–32 UNF–2A
Mounting Surface Flatness:	25 µm
Mounting:	10–32 UNF–2A (Internal Thread) Depth 3.8 mm
Mounting Torque:	Max. 2.3 Nm (20 lbf.in) Typ. 1.7 Nm (15 lbf.in)

[1] This calibration is obtained on a modified Brüel & Kjær Calibration System Type 9610, System No.: 150157.3 and is traceable to the National Institute of Standards and Technology, USA and Physikalisch-Technische Bundesanstalt, Germany.
The expanded uncertainty is 1.0% determined in accordance with EAL-R2. A coverage factor $k = 2$ is used. This corresponds to a coverage probability of 95% for a normal distribution.

[2] The uncertainty is 0.3% of Reference Sensitivity.

[3] Transducer Electronic Data Sheet according to IEEE P1451.4. Built-in ID-information not included.

[4] Deviation from Reference Sensitivity.

Mounting Technique:
Examine the mounting surface for cleanliness and smoothness. If necessary, machine surfaces as per drawing of recommended mounting surface. Fasten the accelerometer using the 10 – 32 UNF – 2 A stud. Take care not to exceed the max. recommended mounting torque and that the stud does not bottom in the mounting holes. A thin film of oil or grease on the mounting surface improves the mounting stiffness. For other types of mounting see Brüel & Kjær "Piezoelectric Accelerometers and Vibration Preamplifiers" handbook.

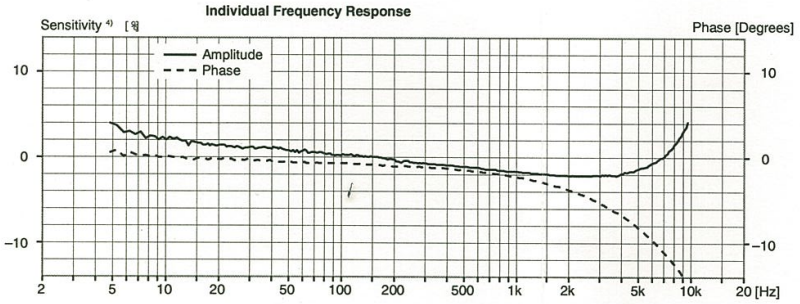

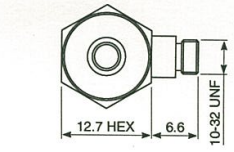

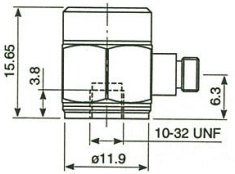

All dimensions in millimetres

Date 21 jun 2008, 09:30 Operator SN

Specifications obtained in accordance with ANSI S2.11-1969 and parts of ISO 5347.

All values are typical at 25°C (77°F) unless measurement uncertainty is specified.

BC 0388–12

Serial No.: 56369

Calibration Chart for DeltaTron® Accelerometer Type 4513-002

Brüel & Kjær

Serial No.: 57109

Reference Sensitivity [1] at 159.2 Hz (ω = 1000 s^{-1}), 20 ms^{-2} RMS, 4 mA supply current and 22.5 °C: 50.94 mV/ms^{-2} (499.6 mV/g)

Frequency Range:	Amplitude (±10%):	1 Hz to 10 kHz
Mounted Resonance Frequency:		32 kHz
Transverse Sensitivity [2]: Maximum (at 30 Hz, 100 ms^{-2}):		< 5% re Reference Sensitivity
Calculated Values for TEDS [3]:	Resonance frequency:	31.1 kHz
	Quality factor @ f_{res}:	93.4
	Amplitude slope:	-1.6 % / decade
	High-pass cut-off frequency:	0.23 Hz
	Low-pass cut-off frequency:	66 kHz
Measuring Range:		± 98 ms^{-2} peak (± 10 g peak)

Polarity of the signal is positive for an acceleration into the accelerometers mounting surface. For triaxial accelerometers and accelerometers with multiple mounting surfaces, the polarity of the signal is positive for an acceleration in the direction of the arrow on the drawing.

Electrical:

Low-frequency Roll-off:		20 dB/decade
Bias Voltage:	at 25°C:	+ 11 V to + 13 V
	Full Temperature Range:	+ 8 V to + 16 V
Power Supply Requirements:	Constant Current:	+ 2 to + 10 mA
	Unloaded Supply Voltage:	+ 24 V to + 30 V
Output Impedance:		< 120 Ω
Start-up Time:		< 1 s
Inherent Noise, X-, Y- and Z-axes (RMS): Broadband (1 Hz to 10 kHz):		50 µV corresponding to 0.001 ms^{-2} (100 µg)
Isolation:		Case Isolated
Recommended cables:		see Product Data Sheet

Environmental:

Temperature Range:	– 51 to + 100°C (– 60 to + 212°F)
Temperature Coefficient of Sensitivity:	+ 0.24%/°C
Temp. Transient Sensitivity (3 Hz Low. Lim. Frq. (–3 dB, 6 dB/oct)):	0.023 ms^{-2}/°C
Base-strain Sensitivity (at 250 µε in base plane):	0.03 ms^{-2}/µε
Max. Non-destructive Shock:	49 kms^{-2} peak (5000 g peak)

Mechanical:

Case Material:	Titanium
Sensing Element:	Ceramic
Construction:	PlanarShear®
Sealing:	Hermetic
Weight:	8.6 gram (0.30 oz.)
Electrical Connector:	10–32 UNF–2A
Mounting Surface Flatness:	25 µm
Mounting:	10–32 UNF–2A (Internal Thread) Depth 3.8 mm
Mounting Torque:	Max. 2.3 Nm (20 lbf.in) Typ. 1.7 Nm (15 lbf.in)

[1] This calibration is obtained on a modified Brüel & Kjær Calibration System Type 9610, System No.: 150157.3 and is traceable to the National Institute of Standards and Technology, USA and Physikalisch-Technische Bundesanstalt, Germany.
The expanded uncertainty is 1.0% determined in accordance with EAL-R2. A coverage factor $k = 2$ is used. This corresponds to a coverage probability of 95% for a normal distribution.

[2] The uncertainty is 0.3% of Reference Sensitivity.

[3] Transducer Electronic Data Sheet according to IEEE P1451.4. Built-in ID-information not included.

[4] Deviation from Reference Sensitivity.

Mounting Technique:
Examine the mounting surface for cleanliness and smoothness. If necessary, machine surfaces as per drawing of recommended mounting surface. Fasten the accelerometer using the 10 – 32 UNF – 2 A stud. Take care not to exceed the max. recommended mounting torque and that the stud does not bottom in the mounting holes. A thin film of oil or grease on the mounting surface improves the mounting stiffness. For other types of mounting see Brüel & Kjær "Piezoelectric Accelerometers and Vibration Preamplifiers" handbook.

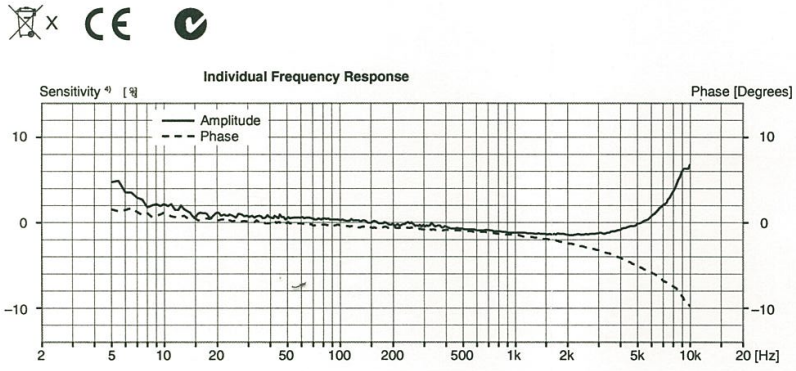

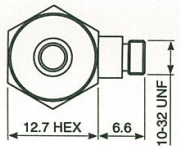

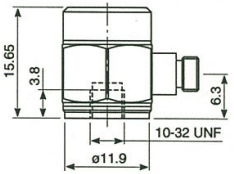

All dimensions in millimetres

Date 24 sep 2009, 15:02 Operator AH

Specifications obtained in accordance with ANSI S2.11-1969 and parts of ISO 5347.

All values are typical at 25°C (77°F) unless measurement uncertainty is specified.

BC 0389–12

Serial No.: 57109

7.3 Complementary information

7.3.1 Further parameters for computation of Pride's model

Complete formulation of Pride's theory at partial saturation for air water mixture requires to know 21 parameters describing the porous medium. Among them we count:

- 4 parameters describing the solid phase: density ρ_S (also called grain density), intrinsic bulk modulus K_S, intrinsic shear modulus G_S, zeta potential ζ.
- 9 parameters describing the fluid phase: salinity C_f, water and air density ρ_w and ρ_g, water and air dynamic viscosity η_w and η_g, water and air incompressibility K_w and K_g, water and air relative permittivity κ_w and κ_g.
- 9 parameters describing the porous medium in its integrity: porosity ${}_phi$, intrinsic permeability k_0, tortuosity α_∞, water saturation degree S_w, residual saturation degree S_{irr}, temperature T, drained bulk modulus K_{fr}, frame shear modulus G_{fr}, 2^{nd} Archie parameter n.

For the calculation of the model, some constants have to be defined:
- vacuum permittivity $\epsilon_0 = 8.854188\ 10^{-12}\ A^2 s^4 kg^{-1} m^{-3}$
- pore geometry factor $m = 6$
- Boltzmann's constant $k_B = 1.38066\ 10^{-23}\ J.K^{-1}$
- elementary charge $e = 1.60218\ 10^{-19}\ C$
- valence $z = 1$
- 1000 $\times$ Avogadro Number $\mathcal{N} = 6.02205\ 10^{26}$
- ionic mobility for cation and anion $b = b_- = b_+ = 3\ 10^{11}\ m.s^{-1}.N^{-1}$
- $pH = 7$

Calculated parameters of the media

Debye length :

$$\tilde{d} = \sqrt{\frac{\epsilon_0 \kappa_f k_B T}{e^2 z^2 C_f\, \mathcal{N}}} \tag{7.1}$$

Pore geometry factor :

$$\Lambda = \sqrt{\frac{k_0\ m\ \alpha_\infty}{\phi}} \tag{7.2}$$

Skin depth :

$$\delta(\omega) = \sqrt{\frac{\eta_w}{\rho_w \omega}} \tag{7.3}$$

Dimensionless parameter P :

$$P = \frac{16 k_B T \, \tilde{d}^2 \, C_f \, \mathcal{N}}{\epsilon_0 \kappa_f \zeta^2} \left[\cosh\left(\frac{ez\zeta}{2k_B T} \right) - 1 \right] \tag{7.4}$$

Electro-migration conductance :

$$C_{em} = 4\tilde{d} e^2 z^2 \, C_f \, \mathcal{N} b \left[\cosh\left(\frac{ez\zeta}{2k_B T} \right) - 1 \right] \tag{7.5}$$

Electro-osmotic conductance :

$$C_{os}(\omega) = \frac{(\epsilon_0 \kappa_f)^2 \, \zeta^2}{2\tilde{d} \, \eta_f} P \left[1 - \frac{2i^{3/2}}{P} \frac{\tilde{d}}{\delta(\omega)} \right]^{-1} \tag{7.6}$$

Poisson-Boltzmann equation : allows to calculate the electric potential within the diffuse layer of the EDL.

$$\nabla^2 \psi = -\sum_{l=1}^{L} \frac{e \, z_l \, C_{f_l} \, \mathcal{N}}{\epsilon_0 \kappa_f} exp\left(\frac{e \, z_l}{k_B T_K} \psi \right) \tag{7.7}$$

$$\psi(\chi) = \zeta \, exp\left(-\frac{}{\tilde{d}} \right) \tag{7.8}$$

Knowing the required media parameter, the aforementioned constant and the calculated parameter of the media, one may proceed to the computation of Pride's formulation by filling the gaps with poroelastic equations from section 2.3.2 and seismoelectric relations from section 2.5.2. For adaptation to partial saturation, effective fluid parameters $\eta_f(S_w)$, $\rho_f(S_w)$ and $K_f(S_w)$ have to be retrieved from section 2.4.2 while saturation-dependent electric parameters $C_{EK}(S_w)$ and $\sigma_b(S_w)$ must be taken from section **??**.

7.3.2 Permeability and pore size models for spherical grains

Many models have been developed to estimate permeabilities of spherical grains'pile-up by considering their effective grain diameter d or the associated pore diameter d_P. We choose to present two of them: first the Kozeny-Carman model [Carman and Machefer, 1961] massively used, second the Glover-Walker model [Glover and Walker, 2009] newly proposed. Kozeny-Carman's permeability model is based on flux calculation resulting from Poiseuille flow through pipes. It depends on hydraulics and eventually requires tortuosity α, porosity ϕ and the already-mentioned effective pore diameter d_P linked to d by means of hydraulic

Figure 7.1: Explanatory scheme to Kozeny-Carman model based on the flow in a capillary of length L and radius R.

diameter r_h.
Beside the effective grain diameter d, the Glover-Walker model relies on the electric definition of the formation factor F, according to Archie's law, to quantify permeabilities on the basis of the electrokinetic theory. We shall demonstrate that both formulations are formally very similar.

Kozeny-Carman model (1927)

We consider the Navier-Stokes equation and solve it for a tube of radius R in which velocities have a parabolic evolution $\vec{w}(r)$ as expected for a Poiseuille flow.

$$\vec{\nabla}.(\rho\vec{w}) + \frac{\partial\rho}{\partial t} = 0 \tag{7.9}$$

$$\vec{w}(r) = -\frac{R^2}{4\eta_f}(1-\frac{r^2}{R^2})\frac{\Delta P}{L} \tag{7.10}$$

$$Q = -\frac{R^2}{4\eta_f}\frac{\Delta P}{L}\int_0^R 2\pi r(1-\frac{r^2}{R^2})dr = -\frac{\pi R^4}{8\eta_f}\frac{\Delta P}{L} \tag{7.11}$$

$$\tag{7.12}$$

It subsequently gives the local velocity of the fluid phase $\vec{w}$ within the capillaries. When crossing a planar section of the porous medium, the ratio of the capillaries section to the whole surface should amount to porosity ϕ and the averaged fluid velocity should be given by $\vec{W}$.

$$\vec{w} = \frac{Q}{\pi R^2} = -\frac{R^2}{8\eta_f}\frac{\Delta P}{L} \tag{7.13}$$

$$\vec{W} = \phi\vec{w} = -\frac{\phi R^2}{8\eta_f}\frac{\Delta P}{L} \tag{7.14}$$

$$\tag{7.15}$$

When comparing the upper expression of flow Q to the usual Darcy's law for a flow q in a sample of length $\Delta x = L$ and section S under a pressure difference of ΔP

$$q = -\frac{kS}{\eta_f}\frac{\Delta P}{L} \tag{7.16}$$

$$\tag{7.17}$$

the Kozeny-Carman formula for permeability, first developed for tubular pores of radius noted R, can be identified to :

$$k = \frac{\phi R^2}{8} = \frac{\phi r_h^2}{2} \tag{7.18}$$

where the hydraulic radius r_h would be :

$$r_h = \frac{V_p}{S_p} = \frac{\pi R^2 L}{2\pi R L} = \frac{R}{2} \tag{7.19}$$

This relation would be valid for parallel tubular pores normal to the sample edges, so that the pore length equals the sample dimensions. Under this assumption we recover Darcy's low. But permeability can also be expressed as a function of the averaged fluid velocity $\vec{W}$. We note $A_\perp = \pi R^2$ the section of the pore:

$$k_0 = -\eta_f |\vec{W}| \frac{\Delta x}{\Delta P} = \eta_f (\frac{\vec{w} A_\perp}{A}) \frac{\Delta x}{\Delta P} \tag{7.20}$$

$$k_0 = -\eta_f (\frac{R^2}{8\eta_f} \frac{\Delta P}{L}) (\frac{A_\perp}{A_{eff}} \times \frac{A_{eff}}{A}) (\frac{\Delta x}{L} \times \frac{L}{\Delta P}) \tag{7.21}$$

$$k_0 = -\frac{r_h^2}{2} \frac{A_\perp}{A_{eff}} \frac{\phi}{\alpha_\infty} \tag{7.22}$$

with $\frac{A_{eff}}{A} = \phi$, for by taking a 2D-slice of the medium, the ratio of the pore surface to the total surface should be equal to porosity ϕ. Moreover, we have $\frac{A_{eff}}{A_\perp} = \frac{L}{\Delta x} = \alpha_\infty$ the tortuosity, for the angle $\hat{i}$ is equivalent to the angle formed by the intersection of L and Δx, according to the properties of a right triangle, as can be seen in figure 7.1. Having given those precisions, we can hence write that:

$$k_0 = \frac{\phi R^2}{8\alpha_\infty^2} \tag{7.23}$$

$$k_0 = \frac{\phi r_h^2}{2\alpha_\infty^2} \tag{7.24}$$

Moreover the porous volume V_p can easily be associated to the volume of the solid phase V_S, inducing a reformulation of permeability:

$$V_p = \frac{\phi}{1-\phi} V_S \tag{7.25}$$

$$k_0 = \frac{1}{2\alpha_\infty^2} \frac{\phi^3}{(1-\phi)^2} (\frac{V_S}{S_p})^2 \tag{7.26}$$

When considering unimodal distribution of spherical grains there is a direct link between V_S and S_P considering the diameter of the grains d_g. As a result the permeability can eventually be expressed as a function of the porosity ϕ, the tortuosity α_∞ and the grain diameter d_g [Barrière, 2011] :

$$\frac{V_S}{S_P} = \frac{\pi d_g^3}{6} \frac{1}{\pi d_g^2} = \frac{d_g}{6} \tag{7.27}$$

$$k_0 = \frac{1}{36 K_0 \alpha_\infty^2} \frac{\phi^3}{(1-\phi)^2} d_g^2 \tag{7.28}$$

K_0 being a form factor equalling 2 for random packing of spherical grains [Mota et al., 2001].

Glover-Walker model (2009)

In an effort to connect the effective grain diameter d_g to the effective pore-size diameter d_p, Glover and Walker [2009] proposed the Θ transform defined in agreement with electrokinetic properties as :

$$d_g = \Theta d_p \tag{7.29}$$

Where Θ can be expressed as a function of the cementation factor $m = 1.45$, the packing constant $a = 8/3$ and porosity ϕ or formation factor $F = \phi^{-m}$:

$$\Theta = \sqrt{\frac{am^2}{8\phi^{2m}}} = \sqrt{\frac{am^2F^2}{8}} \tag{7.30}$$

The intrinsic permeability of the porous medium in DC-mode may then be estimated by the Glover-Walker model using the above mentioned mean pore diameter d_p.

$$k = \frac{d_p^2}{32F} = \frac{d_p^2\phi^m}{32} \tag{7.31}$$

By taking $F = \alpha_\infty^2/\phi$ and by replacing the pore diameter d_p by its hydraulic radius $r_h = d_p/4$, we then get back to eq. (7.24), on which the Kozeny-Carman model is based.

7.3.3 Uncertainties estimation on linear regression by least-square method

Rouaud [2012] provides a robust least-square method, for uncertainties estimation on linear regression. We expose here its general principle.

For an ensemble of N points $M_i(x_i, y_i)$, as represented on figure 7.2, one can draw a straight line of equation $\widehat{y}_i = ax_i + b$. If we consider summing squared distances d_i of real data point to the ideal curve, we get:

$$\sum_i d_i^2 = \sum_i (y_i - \widehat{y}_i)^2 \tag{7.32}$$

The best linear fit will minimise this quantity, so that its partial derivative relatively to slope a and origin ordinate b should be:

$$\sum_i (y_i - ax_i - b)x_i = 0 \tag{7.33}$$

$$\sum_i (y_i - ax_i - b) = 0 \tag{7.34}$$

As a result we obtain the characteristics of the best fitting curve:

$$a = \frac{\bar{xy} - \bar{x}\bar{y}}{\bar{x^2} - \bar{x}^2} \tag{7.35}$$

$$b = \bar{y} - a\bar{x} \tag{7.36}$$

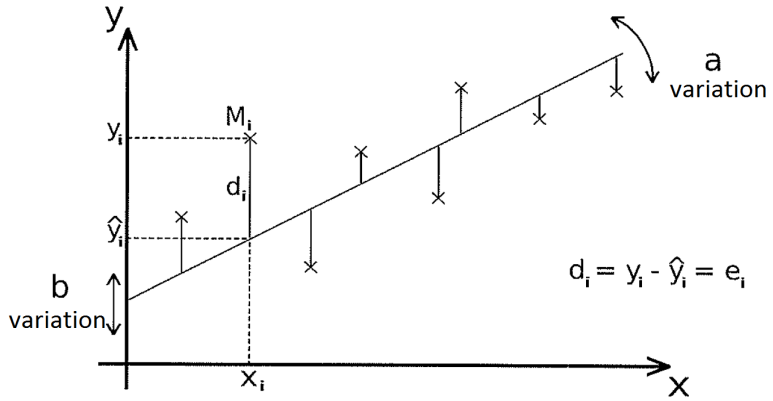

Figure 7.2: Error estimation on a data set fitted by linear regression (from Rouaud [2012]).

and having define the residue e_i as $y_i = \widehat{y_i} + e_i$, we have a link to the associated standard deviation s_r, s_a and s_b repectively characterising the residue e_i, the slope a and the origin b:

$$s_r = sqrt\frac{\sum e_i^2}{N-2} \tag{7.37}$$

$$s_a = \frac{s_r}{\sqrt{\sum (x_i - \bar{x})^2}} \tag{7.38}$$

$$s_a = s_r sqrt\frac{\sum x_i^2}{N\sum (x_i - \bar{x})^2} \tag{7.39}$$

Finally, we choose the confidence interval for our error bars and select the associated Student coefficient t_{N-2} for $N-2$ degrees of freedom (see table 7.5 for Student coefficient values). The error Δa on the slope a and δb on origin b is consequently written as:

$$\Delta a = t_{N-2} s_a \tag{7.40}$$

$$\Delta b = t_{N-2} s_b \tag{7.41}$$

This method can be extended to take error bars into account. Note that in our study, confidence interval for data analysis were usually taken by 80 %; for estimation on seismoelectric transfer function, we went down to a 50 % interval of confidence.

Table 7.5 is reproduced from Rouaud [2012] for a data set of N points.

7.3.4 Compared action of Gabor- and Stockwell-transforms

For a better understanding of the effect of the Gaussian width on time-frequency resolution, we decided to introduce an auxiliary synthetic support specifically designed for this purpose. We constructed a sweep-like signal assembled from successive sinusoids of increasing frequencies, starting at 500 Hz up to 5000 Hz in a 500 Hz frequency-step (see figure 7.3). For each frequency, the sinusoid lasts 3 periods ; throughout the signal the peak-to-peak amplitude remains constant. Note that this signal is no real sweep in the common sense, for the frequency does not increase continuously ; but it is this step-like aspect that is of particular help to picture the time-frequency resolution dependency on the width of the

Student's coefficients t		Confidence (%)								
		50	**80**	**90**	**95**	**98**	**99**	**99.5**	**99.8**	**99.9**
Freedom degrees (N-2)	**1**	1.00	3.08	6.31	12.7	31.8	63.7	127	318	637
	2	0.82	1.89	2.92	4.30	6.96	9.92	14.1	22.3	31.6
	3	0.76	1.64	2.35	3.18	4.54	5.84	7.45	10.2	12.9
	4	0.74	1.53	2.13	2.78	3.75	4.60	5.60	7.17	8.61
	5	0.73	1.48	2.02	2.57	3.36	4.03	4.77	5.89	6.87
	6	0.72	1.44	1.94	2.45	3.14	3.71	4.32	5.21	5.96
	7	0.71	1.41	1.89	2.36	3.00	3.50	4.03	4.79	5.41
	8	0.71	1.40	1.86	2.31	2.90	3.36	3.83	4.50	5.04
	9	0.70	1.38	1.83	2.26	2.82	3.25	3.69	4.30	4.78
	10	0.70	1.37	1.81	2.23	2.76	3.17	3.58	4.14	4.59
	11	0.70	1.36	1.80	2.20	2.72	3.11	3.50	4.02	4.44
	12	0.69	1.36	1.78	2.18	2.68	3.05	3.43	3.93	4.32
	13	0.69	1.35	1.77	2.16	2.65	3.01	3.37	3.85	4.22
	14	0.69	1.35	1.76	2.14	2.62	2.98	3.33	3.79	4.14
	15	0.69	1.34	1.75	2.13	2.60	2.95	3.29	3.73	4.07
	16	0.69	1.34	1.75	2.12	2.58	2.92	3.25	3.69	4.01
	17	0.69	1.33	1.74	2.11	2.57	2.90	3.22	3.65	3.97
	18	0.69	1.33	1.73	2.10	2.55	2.88	3.20	3.61	3.92
	19	0.69	1.33	1.73	2.09	2.54	2.86	3.17	3.58	3.88
	20	0.69	1.33	1.72	2.09	2.53	2.85	3.15	3.55	3.85
	∞	0.67	1.28	1.64	1.96	2.33	2.58	2.81	3.09	3.29

Table 7.5: Student's coefficient for error calculation on slope and origin ordinate determined thanks to linear regression by ordinary least square method.

windowing function.

We summarise observations on signal selection and related time-frequency resolution in figure 7.4. At the top of it, time-series and Fourier spectrum associated to this signal are shown along with the symbolic representations of their respective time-frequency resolution-diagrams. We see that for fully resolute time-location of amplitudes, there is no related frequency information; conversely with the Fourier transform, raw spectral amplitudes bear no time information. In the mid- and lower part of this same figure , we present ways of selecting a signal by translation of a window function(left) in order to generate spectrograms (middle) and associated to them a schematic representation of the time-frequency resolution as elementary bricks (right). In the central part of this figure picture we tested of a set of Gabor transforms on our sweep-like signal. These Gabor-transforms were computed for given σ window-width of 30, 100 and 200 samples corresponding respectively to time-periods of 0.3, 1 and 2 ms. These Gaussian functions are represented as envelopes while windowing the signal at different time location on the left side. We observe on the associated spectrograms how the Gabor-transform is bound to enhance frequencies related to the characteristic width of the Gaussian window. As an example, the 200 samples window of 2 ms duration appears particularly adapted for 500 Hz detection but fails at locating any frequency component beyond 1 kHz. As for the 30 samples window of duration 0.3 ms, best-fitted for the detection of frequencies close to 3 kHz, is correctly depicting the frequency increase of the signal up to 5 kHz. However, low frequencies show poor frequency-resolution and jerky time-localization: for the first sinus pack at 500 Hz time frequency amplitude is divided into six elongated lobes corresponding to each lobe of the 3-periods signal, with their maxima pointing at $0Hz$ (a similar observation as on our synthetic made of Gaussian curves). The intermediate window length provides the best time-frequency resolution[1], but we lose the evidence for equal amplitudes at each frequency, a characteristic that was better accounted for using the narrower window.

On the contrary, the Stockwell-transform allows for amplitude conservation, as observable in the lower part of figure 7.4 and reported by Ventosa et al. [2008]: for sine-waves having various frequencies but a same amplitude in the time domain, the S-transform will impart them equal amplitude in the (τ, f) domain independently of the frequency.

Hence, with our sweep-like synthetic we verified the limitations mentioned in section 4.1.3. When using a fixed window-width STFT we determine once and for all a fixed analysis pattern indifferently applied to all frequency components. We can choose to favour the analysis of the lower frequency-band by using wider windows adapted to longer events ; if applied to higher-frequency events they will all mix up within a single window and smear on the time-frequency diagram. Conversely, to enhance the analysis of the upper frequency-band, one should adopt a narrower window ; when applied to unadapted longer events, it may chop it into bits as the 500 Hz component in the $\sigma = 0.3\ ms$ Gaussian window. Thus, in

[1]It should be noted that the actual pixel in the spectrogram, which area is determined by the time and frequency sampling pace Δt and Δf, does not stand for the bounded resolution $2\sigma_f \times 2\sigma_t$. As a matter of fact, the pixel area will most probably be smaller, which seems in contradiction with the uncertainty principle. However, this pixel of coordinate (t, f) stands for a value averaged over the domain $[t - \sigma_t \quad t + \sigma_t \mid f - \sigma_f \quad f + \sigma_f]$ in connection with the Heisenberg limit on resolution.

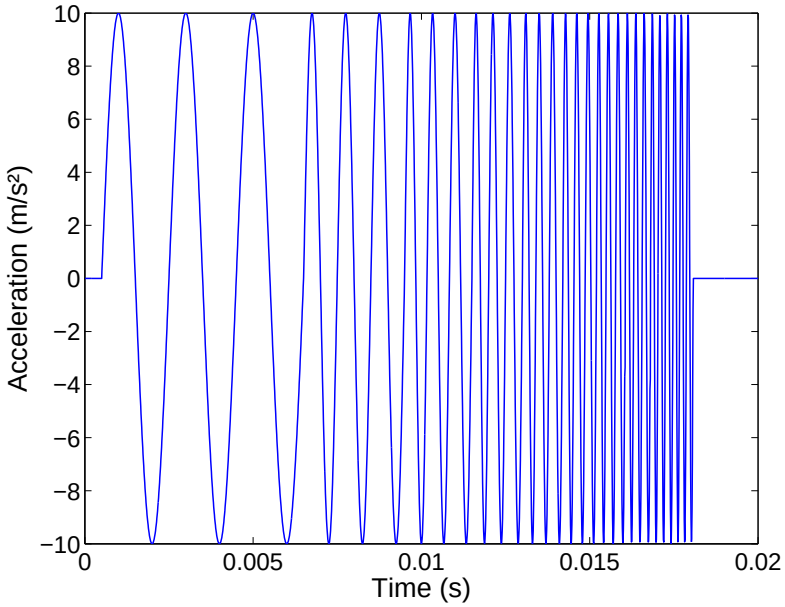

Figure 7.3: Sweep synthetic signal constituted of a succession of sine-wave with increasing frequencies (starting at 500 Hz up to 5000 Hz in a 500 Hz frequency-step). For each frequency, the sinusoid lasts 3 periods.

every case a fixed window will not be able to process equally the whole frequency spectrum, for the number of signal oscillations extracted by the selecting window will depend on the frequency.

Observation of figure 7.4 confirms the superiority of the S-transform over the Gabor transform. First, it validates the S-transform ability to amplitude conservation throughout the frequency spectrum, unlike its Gabor counterpart. Second, the successive parts of the sweep-like signal appear better resolute than with any of the Gabor transform examples, with the subsidiary advantage that no previous knowledge of the signal is required. Yet in our case, this comes with a tremendous increase in computation time. Despite this fact, it gains our preference for time-frequency analysis. We will consequently resort to the S-transform whenever a time-frequency analysis is needed, should it be for a full comparison of seismic and seismoelectric records or as an help in identifying receivers showing unmingled first arrivals.

7.3.5 Parameter for various geomaterials

Pore diameter d_p were calculated using the θ-relation in Glover and Walker [2009]. Other results from Murphy et al. [1984] in consolidated rocks indicate that e of cracks have to be between 10^{-3} and 10^{-5} to play a part: we took $e = 5.10^{-}4$ for the Berea sandstone.

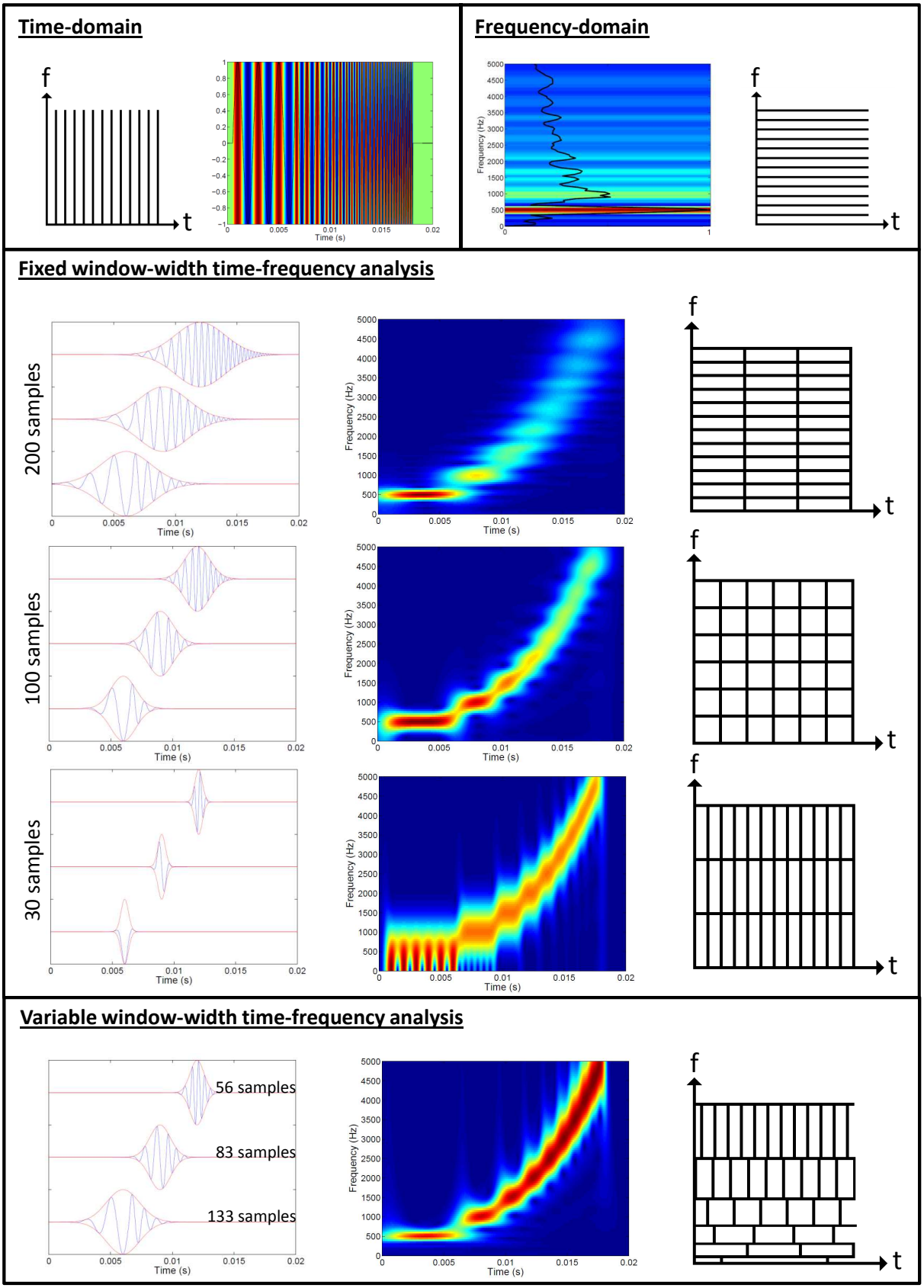

Figure 7.4: Representation of the sweep synthetic signal in the time domain, in the frequency domain and for a variety of time-frequency representation. The Gabor-transform was chosen to stand for the fixed window-width analysis whereas the hereafter introduced S-transform represents the variable window-width analysis. For each transform we give a symbolic representation of the time-frequency resolution. Moreover, for all time-frequency transforms we show the window selection of the signal in the time-domain. Inspired by Lau and Weng [1995] and Gaillot [2000]

	Mount Gambier Limestone	Berea Sanstone	Landes Sand
ϕ	0.25	0.2*	0.42
$k\ (m^2)$	5.10^{-12}	10^{-13}*	2.10^{-11}
α_∞	1.8	2*	1.65
$\rho_s\ (kg.m^{-3})$	2650	2650	2650
$K_S\ (Pa)$	—	37.10^9	36.10^9
$K_U\ (Pa)$	—	12.10^9	54.10^6
$K_{fr}\ (Pa)$	26.10^9	12.10^9	$2.55.10^7$
$G_{fr}\ (Pa)$	15.10^9	8.10^9	$1.53.10^7$
$d_g\ (m)$	150.10^{-6}	$175e-6$*	250.10^{-6}
m	2	1.8	1.45
$d_p\ (\mu m)$	10	10	60
e	5.10^{-4}	5.10^{-4}	10^{-2}
$\zeta\ (V)$	—	-0.04	-0.035

Table 7.6: Values for Berea sanstone taken from Winkler [1985]*, or deduced from Hart and Wang [1995]. Values for sand where taken from our lab experiment data. m is the cementation factor, e is the aspect ratio factor (for sand taken from the assumption of Palmer and Traviolia [1980] that it had to be more than 0.01, other clues from Murphy et al. [1984] that they have to be between 10^{-3} and 10^{-5}), d_p calculated from d_g thanks to Glover and Walker [2009] where d_g were either given or assumed, Mount Gambier limestone data from Toms-Stewart et al. [2009]

7.4 Glossary

Symbol	Signification	Unit	Definition
$\mathbf{B}$	magnetic induction	T	-
B_S	Skempton's coefficient	-	eq. (2.23)
C_f	salinity	$mol.L^{-1}$	
C_{EK}	static electrokinetic coupling coeff.	$V.Pa^{-1}$	eq. (2.41)
$\tilde{d}$	Debye length	m	eq. (7.1)
d_g	mean grain diameter	m	
$\bar{d}$	effective grain diameter	m	
d_p	effective pore diameter	m	
$\mathbf{D}$	dielectric displacement	$C.m^{-2}$	
$\mathbf{E}$	electric field	$V.m^{-1}$	
F	formation factor	-	eq. (2.6), (2.7), (2.8)
f	frequency	Hz	-
f_{Biot}	Biot critical frequency	Hz	eq. (2.50)
f_{nom}	central frequency of 1^{st} arrival	Hz	eq. (4.1)
$\mathbf{g}$	Earth's gravity vector	9.81 $m.s^{-2}$	-
G_{fr}	frame shear modulus	Pa	eq. (2.24)
G_S	intrinsic shear modulus of the solid	Pa	-
$\mathbf{H}$	magnetic field	$A.m^{-1}$	-
$\mathbf{J}$	current density	$A.m^{-2}$	eq. (2.84)
k	dynamic permeability	m^2	eq. (2.53)
k_0	intrinsic permeability	m^2	
k_{KC}	permeability after Kozeny-Carman	m^2	eq. (2.14)
k_{GW}	permeability after Glover-Walker	m^2	eq. (2.17)
K_G	Gassmann incompressibility	Pa	eq. (2.27)
K_S	intrinsic bulk modulus of the solid	Pa	-
K_f	fluid bulk modulus	Pa	
K_{fr}	drained bulk modulus	Pa	
L_{EK}	dynamic seismoelectric coupling coeff.	$m^2.s^{-1}.V-1$	eq. (2.86)
L_0	static seismoelectric coupling coeff.	$m^2.s^{-1}.V-1$	
l_{dip}	dipole length	m	-
m	cementation factor	-	
M	cementation factor	-	
n	second Archie parameter	-	
P_c	confining pressure	Pa	eq. (2.48)
p_f	fluid pressure	Pa	eq. (2.49)
Q_p	quality factor of fast P-wave	Pa	eq. (2.58)
r_h	hydraulic radius	m	
s_P	slowness of fast P-wave	$s.m^{-1}$	eq. (2.55),(2.91)
S_e	effective saturation degree	-	
S_{irr}	residual saturation degree	-	-
S_w	water saturation degree	-	-
T_C	fluid temperature	$°C$	-
T_K	fluid temperature	K	-
$\mathbf{u}$	absolute frame velocity	$m.s^{-1}$	-
$\mathbf{U}$	average frame velocity	$m.s^{-1}$	-
$\ddot{\mathbf{u}}$	seismic acceleration	$m.s^{-2}$	-
V_P	pore volume	m^3	-
V_p	velocity of fast P-wave	$m.s^{-1}$	eq. (2.57)
V_{se}	velocity of seismoelectric wave	$m.s^{-1}$	
$\mathbf{w}$	absolute fluid velocity	$m.s^{-1}$	-
$\mathbf{W}$	average fluid velocity	$m.s^{-1}$	-

Table 7.7: Notation for employed parameters (for Latin symbols).

Symbol	Signification	Unit	Definition
α_p	intrinsic attenuation of P-wave	-	eq. (2.56)
α_∞	tortuosity	-	eq. (2.4),(2.5),(2.8)
β_P	fluid/matrix displacement ratio	-	eq. (2.92)
ϵ_0	vacuum permittivity	8.85 10^{-12} $A^2 s^4 kg^{-1} m^{-3}$	-
η_f	dynamic viscosity	$Pa.s$	eq. (2.34)
κ_f	relative fluid permittivity	-	eq. (2.35)
λ	wavelength	m	eq. (4.29)
Λ	pore geometry factor	m	eq. (7.2)
μ_0	permeability of free space	$H.m^{-1}$	-
ω	angular frequency	$rad.s^{-1}$	$2\pi\ f$
ω_c	Biot characteristic pulsation	$rad.s^{-1}$	$2\pi\ f_{Biot}$
ϕ	porosity	-	
ρ	bulk density	$kg.m^{-3}$	
$\tilde{\rho}$	effective density	$kg.m^{-3}$	eq. (2.51)
ρ_f	fluid density	$kg.m^{-3}$	
ρ_S	solid phase density	$kg.m^{-3}$	
ρ_t	complex density	$kg.m^{-3}$	eq. (2.89)
σ	dynamic conductivity	$S.m{-}1$	
σ_b	bulk conductivity	$S.m{-}1$	eq. (2.6)
σ_f	fluid conductivity	$S.m{-}1$	eq. (2.33)
τ_B	stress tensor	Pa	
τ^D	deviatoric stress tensor	Pa	eq. (2.47)
ζ	zeta potential	V	eq. 2.36,2.37,2.38

Table 7.8: Notation for employed parameters (for Greek symbols).

Bibliography

Ageeva, O., B. Svetov, G. Sherman, and S. Shipulin (1999). E-effect in rocks (data from laboratory experiments). *Russian Geology and Geophysics c/c of Geologiia i Geofizika 40*(8), 1232–1237.

Aki, K. and P. Richards (2002). *Quantitative seismology*, Volume 1.

Allègre, V. (2010). *Couplages électrocinétiques en milieux poreux non-saturés*. Ph. D. thesis, Université de Strasbourg.

Allègre, V., L. Jouniaux, F. Lehmann, and P. Sailhac (2010). Streaming potential dependence on water-content in fontainebleau sand. *Geophysical Journal International 182*(3), 1248–1266.

Allègre, V., L. Jouniaux, F. Lehmann, and P. Sailhac (2011). Reply to comment by a. revil and n. linde on Śstreaming potential dependence on water-content in fontainebleau sandŠ. *Geophysical Journal International*.

Allègre, V., F. Lehmann, P. Ackerer, L. Jouniaux, and P. Sailhac (2012). A 1-d modelling of streaming potential dependence on water content during drainage experiment in sand. *Geophysical Journal International 189*(1), 285–295.

Archie, G. (1942). The electrical resistivity log as an aid in determining some reservoir characteristics. *Trans. Am. Inst. Mech. Eng. 146*, 54–62.

Barrière, J. (2011). *Atténuation et dispersion des ondes P en milieu partiellement saturé : approche expérimentale*. Ph. D. thesis, Université de Pau et des Pays de l'Adour, France.

Barrière, J., C. Bordes, D. Brito, P. Sénéchal, and H. Perroud (2012). Laboratory monitoring of p waves in partially saturated sand. *Geophysical Journal International 191*(3), 1152–1170.

Beamish, D. (1999). Characteristics of near-surface electrokinetic coupling. *Geophysical Journal International 137*(1), 231–242.

Beamish, D. and R. Peart (1998). Electrokinetic geophysics - a review. *Terra Nova 10*(1), 48–55.

Berryman, J. (1981). Elastic wave propagation in fluid-saturated porous media. *Journal of the Acoustical Society of America 69*, 416.

Biot, M. (1956a). Theory of propagation of elastic waves in a fluid-saturated porous solid. i. low-frequency range. *Journal of Acoustical Society of America 28*(2), 168–178.

Biot, M. (1956b). Theory of propagation of elastic waves in a fluid-saturated porous solid. ii. higher frequency range. *Journal of Acoustical Society of America 28*(2), 179–191.

Biot, M. (1962a). Generalized theory of acoustic propagation in porous dissipative media. *Journal of Acoustical Society of America 34*(9), 1254–1264.

Biot, M. (1962b). Mechanics of deformation and acoustic propagation in porous media. *Journal of Applied Physics 33*(4), 1482–1498.

Blau, L. and L. Statham (1936, September 15). Method and apparatus for seismic.

Block, G. and J. Harris (2006). Conductivity dependence of seismoelectric wave phenomena in fluid-saturated sediments. *Journal of Geophysical Research 111*, B01304.

Bordes, C. (2005). *Etude expérimentale des phénomènes transitoires sismo-électromagnétiques: Mise en oeuvre au Laboratoire Souterrain de Rustrel, Pays d'Apt*. Ph. D. thesis, Université de Grenoble 1.

Bordes, C., L. Jouniaux, M. Dietrich, J. Pozzi, and S. Garambois (2006). First laboratory measurements of seismo-magnetic conversions in fluid-filled fontainebleau sand. *Geophysical Research Letters 33*, L01302.

Bordes, C., L. Jouniaux, S. Garambois, M. Dietrich, J. Pozzi, and S. Gaffet (2008). Evidence of the theoretically predicted seismo-magnetic conversion. *Geophysical Journal International 174*(2), 489–504.

Bordes, C., P. Sénéchal, J. Barrière, D. Brito, E. Normandin, and D. Jougnot (2015). Impact of water saturation on seismoelectric transfer functions: a laboratory study of coseismic phenomenon. *Geophysical Journal International 200*(3), 1317–1335.

Born, W. (1941). The attenuation constant of earth materials. *Geophysics 6*(2), 132–148.

Bourbié, T., O. Coussy, and B. Zinszner (1986). *Acoustique des milieux poreux*. Editions Technip.

Bouriat, P. (1997). *Etude par électro-osmose des propriétés électriques de surface du polyamide immergé en solution aqueuse*. Ph. D. thesis, Université de Pau et des Pays de l'Adour, France.

Bouriat, P., P. Saulnier, P. Brochette, A. Graciaa, and J. Lachaise (1999). A convenient apparatus to determine the zeta potential of grains by electro-osmosis. *Journal of colloid and interface science 209*(2), 445–448.

Brennan, B. and F. Stacey (1977). Frequency dependence of elasticity of rockŮtest of seismic velocity dispersion. *Nature 268*, 220–222.

Brie, A., F. Pampuri, A. Marsala, and O. Meazza (1995). Shear sonic interpretation in gas-bearing sands. In *SPE Annual Technical Conference*, Volume 30595, pp. 701–710.

Broding, R., S. Buchanan, and D. Hearn (1963). Field experiments on the electroseismic effect. *Geoscience Electronics, IEEE Transactions on 1*(1), 23–31.

Brown, R. (1980). Connection between formation factor for electrical resistivity and fluid-solid coupling factor in biot's equations for acoustic waves in fluid-filled porous media. *Geophysics 45*(8), 1269–1275.

Butler, K., S. Fleming, and R. Russell (1999). Field test for linearity of seismoelectric conversions. *Canadian Journal of Exploration Geophysics 35*, 20–23.

Butler, K. and R. Russell (1993). Short note subtraction of powerline harmonics from geophysical records. *Geophysics 58*(6).

Butler, K. and R. Russell (2003). Cancellation of multiple harmonic noise series in geophysical records. *Geophysics 68*(3), 1083.

Butler, K., R. Russell, A. Kepic, and M. Maxwell (1996). Measurement of the seismoelectric response from a shallow boundary. *Geophysics 61*(6), 1769–1778.

Cadoret, T., D. Marion, and B. Zinszner (1995). Influence of frequency and fluid distribution on elastic wave velocities in partially saturated limestones. *Journal of Geophysical Research: Solid Earth (1978–2012) 100*(B6), 9789–9803.

Carcione, J., S. Picotti, D. Gei, and G. Rossi (2006). Physics and seismic modeling for monitoring co2 storage. *Pure and Applied Geophysics 163*(1), 175–207.

Carman, P. and J. Machefer (1961). *L'écoulement des gaz à travers les milieux poreux*. Institut national des sciences et techniques nucléaires.

Chapman, D. (1913). Li. a contribution to the theory of electrocapillarity. *The London, Edinburgh, and Dublin Philosophical Magazine and Journal of Science 25*(148), 475–481.

Chen, B. and Y. Mu (2005). Experimental studies of seismoelectric effects in fluid-saturated porous media. *Journal of Geophysics and Engineering 2*, 222.

Chotiros, N. and M. Isakson (2004). A broadband model of sandy ocean sediments: Biot–stoll with contact squirt flow and shear drag. *The Journal of the Acoustical Society of America 116*(4), 2011–2022.

Darcy, H. (1857). *Recherches expérimentales relatives au mouvement de l'eau dans les tuyaux*. Mallet-Bachelier.

De Ridder, S., E. Slob, and K. Wapenaar (2009). Interferometric seismoelectric green's function representations. *Geophysical Journal International 178*(3), 1289–1304.

Dean, D. and C. Dupuis (2011). The vibroelectric method - a new tool for near-surface characterization and improved seismic data quality. In *73rd EAGE Conference*.

Deckman, H., E. Herbolzheimer, and A. Kushnick (2005). Determination of electrokinetic coupling coefficients. SEG.

Diallo, M. and E. Appel (2000). Acoustic wave propagation in saturated porous media: reformulation of the biot/squirt flow theory. *Journal of Applied Geophysics 44*(4), 313–325.

Doussan, C. and S. Ruy (2009). Prediction of unsaturated soil hydraulic conductivity with electrical conductivity. *Water resources research 45*(10).

Dupuis, J. and K. Butler (2006). Vertical seismoelectric profiling in a borehole penetrating glaciofluvial sediments. *Geophysical Research Letters 33*(16), L16301.

Dupuis, J., K. Butler, and A. Kepic (2007). Seismoelectric imaging of the vadose zone of a sand aquifer. *Geophysics 72*(6), A81.

Dupuis, J., K. Butler, A. Kepic, and B. Harris (2009). Anatomy of a seismoelectric conversion: Measurements and conceptual modeling in boreholes penetrating a sandy aquifer. *Journal of Geophysical Research 114*(B10), B10306.

Dutta, N. and H. Odé (1979). Attenuation and dispersion of compressional waves in fluid-filled porous rocks with partial gas saturation (white model)-part i: Biot theory. *Geophysics 44*(11), 1777–1788.

Dutta, N. and A. Seriff (1979). On white's model of attenuation in rocks with partial gas saturation. *Geophysics 44*(11), 1806–1812.

Dvorkin, J. and A. Nur (1993). Dynamic poroelasticity: A unified model with the squirt and the biot mechanisms. *Geophysics 58*(4), 524–533.

El Mouhtadi, A. (2011). *Caractérisation ultrasonore de plaques viscoélastiques homogènes et composites*. Ph. D. thesis, Université du Havre.

Frenkel, J. (1944). Orientation and rupture of linear macromolecules in dilute solutions under the influence of viscous flow. *Acta Physicochimica URSS 19*(1), 51–76.

Gabor, D. (1946). Theory of communication. part 1: The analysis of information. *Journal of the Institution of Electrical Engineers-Part III: Radio and Communication Engineering 93*(26), 429–441.

Gaillot, P. (2000). *Ondelettes continues en Sciences de la Terre-méthodes et applications*. Ph. D. thesis, Université Paul Sabatier-Toulouse III.

Gao, Y. and H. Hu (2010). Seismoelectromagnetic waves radiated by a double couple source in a saturated porous medium. *Geophysical Journal International 181*(2), 873–896.

Garambois, S. and M. Dietrich (2001). Seismoelectric wave conversions in porous media: Field measurements and transfer function analysis. *Geophysics 66*(5), 1417.

Garambois, S. and M. Dietrich (2002). Full waveform numerical simulations of seismoelectromagnetic wave conversions in fluid-saturated stratified porous media. *Journal of Geophysical Research 107*(B7), 2148–2165.

Gardner, G., M. Wyllie, and D. Droschak (1964). Effects of pressure and fluid saturation on the attenuation of elastic waves in sands. *Journal of Petroleum Technology 16*(02), 189–198.

Gassmann, F. (1951). Elasticity of porous media. *Vierteljahrsschrder Naturforschenden Gesselschaft 96*, 1–23.

Geertsma, J. and D. Smit (1961). Some aspects of elastic wave propagation in fluid-saturated porous solids. *Geophysics 26*(2), 169–181.

Glover, P. and N. Déry (2010). Streaming potential coupling coefficient of quartz glass bead packs: Dependence on grain diameter, pore size, and pore throat radius. *Geophysics 75*(6), F225–F241.

Glover, P. and M. Jackson (2010). Borehole electrokinetics. *The Leading Edge 29*(6), 724–728.

Glover, P. and E. Walker (2009). Grain-size to effective pore-size transformation derived from electrokinetic theory. *Geophysics 74*, E17.

Gordon, R. and L. Davis (1968). Velocity and attenuation of seismic waves in imperfectly elastic rock. *Journal of Geophysical Research 73*(12), 3917–3935.

Gouy, M. (1910). Sur la constitution de la charge electrique a la surface d'un electrolyte. *Journal Phys. Theor. Appl. 9*(1), 457–468.

Grobbe, N. and E. Slob (2013). Validation of an electroseismic and seismoelectric modeling code, for layered earth models, by the explicit homogeneous space solutions. *SEG Technical Program Expanded Abstracts 2013*.

Grossmann, A. and J. Morlet (1984). Decomposition of hardy functions into square integrable wavelets of constant shape. *SIAM journal on mathematical analysis 15*(4), 723–736.

Guan, W., H. Hu, and Z. Wang (2013). Permeability inversion from low-frequency seismoelectric logs in fluid-saturated porous formations. *Geophysical Prospecting 61*(1), 120–133.

Guichet, X., L. Jouniaux, and J. Pozzi (2003). Streaming potential of a sand column in partial saturation conditions. *Journal of Geophysical Research 108*(2141), 10–1029.

Gurevich, B., D. Makarynska, O. de Paula, and M. Pervukhina (2010). A simple model for squirt-flow dispersion and attenuation in fluid-saturated granular rocks. *Geophysics 75*(6), N109–N120.

Haartsen, M. (1995). Coupled electromagnetic and acoustic wavefield modeling in poro-elastic media and its applications in geophysical exploration.

Haartsen, M. and S. Pride (1997). Electroseismic waves from point sources in layered media. *Journal of Geophysical Research 102*(B11), 24745–24.

Haines, S. (2004). *Seismoelectric imaging of shallow targets*. Ph. D. thesis, Stanford University, Stanford, California, USA.

Haines, S. and S. Pride (2006). Seismoelectric numerical modeling on a grid. *Geophysics 71*(6), N57.

Haines, S., S. Pride, S. Klemperer, and B. Biondi (2007). Seismoelectric imaging of shallow targets. *Geophysics 72*(2), G9.

Hama, N., T. Ouahbi, S. Taibi, A. Pantet, J. Fleureau, and H. Souli (2014). Numerical analysis of internal stability of granular materials using discrete element method. *Geomechanics from Micro to Macro* (1).

Hamilton, E. (1974). Prediction of deep-sea sediment properties: state-of-the-art. In *Deep-Sea Sediments*, pp. 1–43. Springer.

Harris, F. (1978). On the use of windows for harmonic analysis with the discrete fourier transform. *Proceedings of the IEEE 66*(1), 51–83.

Hart, D. and H. Wang (1995). Laboratory measurements of a complete set of poroelastic moduli for berea sandstone and indiana limestone. *Journal of Geophysical Research: Solid Earth (1978–2012) 100*(B9), 17741–17751.

Heisenberg, W. (1927). Über den anschaulichen inhalt der quantentheoretischen kinematik und mechanik. *Zeitschrift für Physik 43*(3-4), 172–198.

Helmholtz, H. v. (1879). Studien über electrische grenzschichten. *Annalen der Physik 243*(7), 337–382.

Hertz, H. (1882). Über die berührung fester elastischer körper. *Journal für die reine und angewandte Mathematik 92*(156-171).

Hu, H., W. Guan, and J. Harris (2007). Theoretical simulation of electroacoustic borehole logging in a fluid-saturated porous formation. *The Journal of the Acoustical Society of America 122*(1), 135–145.

Ishido, T. and H. Mizutani (1981). Experimental and theoretical basis of electrokinetic phenomena in rock-water systems and its applications to geophysics. *Journal of Geophysical Research 86*(B3), 1763–1775.

Ivanov, A. (1939). Effect of electrization of earth layers by elastic waves passing through them. *Comptes Rendus (Doklady) de l'Academie des Sciences de L'URRS 24*, 42–45.

Ivanov, A. (1940). The seismoelectric effect of the second kind. In *Proc Academy of Sciences USSR series of geography and geophysics*, Volume 4, pp. 699–726.

Jackson, M. (2008). Characterization of multiphase electrokinetic coupling using a bundle of capillary tubes model. *Journal of Geophysical Research: Solid Earth 113*(B4).

Jackson, M. (2010). Multiphase electrokinetic coupling: Insights into the impact of fluid and charge distribution at the pore scale from a bundle of capillary tubes model. *Journal of Geophysical Research: Solid Earth 115*(B7).

Johnson, D. (2001). Theory of frequency dependent acoustics in patchy-saturated porous media. *Journal of the Acoustical Society of America 110*(2), 682–694.

Johnson, D. and T. Plona (1982). Acoustic slow waves and the consolidation transition. *The Journal of the Acoustical Society of America 72*(2), 556–565.

Johnston, D., M. Toksöz, and A. Timur (1979). Attenuation of seismic waves in dry and saturated rocks: Ii. mechanisms. *Geophysics 44*(4), 691–711.

Jones, T. (1986). Pore fluids and frequency-dependent wave propagation in rocks. *Geophysics 51*(10), 1939–1953.

Jones, T. and A. Nur (1983). Velocity and attenuation in sandstone at elevated temperatures and pressures. *Geophysical Research Letters 10*(2), 140–143.

Jougnot, D., N. Linde, A. Revil, and C. Doussan (2012). Derivation of soil-specific streaming potential electrical parameters from hydrodynamic characteristics of partially saturated soils. *Vadose Zone Journal 11*(1), 0–0.

Jouniaux, L., A. Maineult, V. Naudet, M. Pessel, and P. Sailhac (2009). Review of self-potential methods in hydrogeophysics. *Comptes Rendus Geoscience 341*(10), 928–936.

Jouniaux, L. and J. Pozzi (1995). Permeability dependence of streaming potential in rocks for various fluid conductivities. *Geophysical Research Letters 22*(4), 485–488.

Kim, D. and H. Park (2002). Determination of dispersive phase velocities for sasw method using harmonic wavelet transform. *Soil dynamics and earthquake engineering 22*(8), 675–684.

Kimura, M. (2007). Study on the biot-stoll model for porous marine sediments. *Acoustical science and technology 28*(4), 230–243.

Kjartansson, E. (1979). Constant q-wave propagation and attenuation. *Journal of Geophysical Research: Solid Earth (1978–2012) 84*(B9), 4737–4748.

Klimentos, T. and C. McCann (1990). Relationships among compressional wave attenuation, porosity, clay content, and permeability in sandstones. *Geophysics 55*(8), 998–1014.

Knight, R. and R. Nolen-Hoeksema (1990). A laboratory study of the dependence of elastic wave velocities on pore scale fluid distribution. *Geophysical Research Letters 17*(10), 1529–1532.

Knopoff, L. (1964). Q. *Reviews of Geophysics and Space Physics 2*, 625–660.

Knopoff, L. and G. MacDonald (1960). Models for acoustic loss in solids. *Journal of Geophysical Research 65*(7), 2191–2197.

Kröger, B. (2007). Modellierung und sensitivitatsanalysen für seismoelektrik mit finiten elementen. Master's thesis, Technische Universität Berlin.

Kröger, B., U. Yaramanci, and A. Kemna (2014). Numerical analysis of seismoelectric wave propagation in spatially confined geological units. *Geophysical Prospecting 62*(1), 133–147.

Kulessa, B., T. Murray, and D. Rippin (2006). Active seismoelectric exploration of glaciers. *Geophysical Research Letters 33*(7), L07503.

Lau, K. and H. Weng (1995). Climate signal detection using wavelet transform: How to make a time series sing. *Bulletin of the American Meteorological Society 76*(12), 2391–2402.

Linde, N., D. Jougnot, A. Revil, S. Matthäi, T. Arora, D. Renard, and C. Doussan (2007). Streaming current generation in two-phase flow conditions. *Geophysical Research Letters 34*(3).

Liu, H.-P., D. Anderson, and H. Kanamori (1976). Velocity dispersion due to anelasticity; implications for seismology and mantle composition. *Geophysical Journal International 47*(1), 41–58.

Lockner, D., J. Walsh, and J. Byerlee (1977). Changes in seismic velocity and attenuation during deformation of granite. *Journal of Geophysical Research 82*(33), 5374–5378.

Lomnitz, C. (1957). Linear dissipation in solids. *Journal of Applied Physics 28*(2), 201–205.

Long, L. and W. Rivers (1975). Field measurement of the electroseismic response. *Geophysics 40*, 233.

Lorne, B., F. Perrier, and J.-P. Avouac (1999). Streaming potential measurements: 1. properties of the electrical double layer from crushed rock samples. *Journal of Geophysical Research: Solid Earth 104*(B8), 17857–17877.

Maalej, Y. (2007). *Comportement mécanique d'un milieu granulaire injecté par un coulis de ciment: étude expérimentale et modélisation micromécanique*. Ph. D. thesis, Ecole Nationale des Ponts et Chaussées.

Martner, S. and N. Sparks (1959). The electroseismic effect. *Geophysics 24*(2), 297–308.

Mavko, G. (1979). Frictional attenuation: An inherent amplitude dependence. *Journal of Geophysical Research: Solid Earth (1978–2012) 84*(B9), 4769–4775.

Mavko, G., T. Mukerji, and J. Dvorkin (2003). *The rock physics handbook: Tools for seismic analysis of porous media*. Cambridge University Press.

Mavko, G. and A. Nur (1975). Melt squirt in the asthenosphere. *Journal of Geophysical Research 80*(11), 1444–1448.

Mavko, G. and A. Nur (1979). Wave attenuation in partially saturated rocks. *Geophysics 44*(2), 161–178.

Mikhailov, O. (1998). *Borehole electroseismic phenomena: Field measurements and theory*. Ph. D. thesis, Massachusetts Institute of Technology, Dept. of Earth, Atmospheric, and Planetary Sciences.

Mikhailov, O., M. Haartsen, and M. Toksöz (1997). Electroseismic investigation of the shallow subsurface: Field measurements and numerical modeling. *Geophysics 62*, 97.

Mikhailov, O., J. Queen, and M. Toksöz (2000). Using borehole electroseismic measurements to detect and characterize fractured (permeable) zones. *Geophysics 65*(4), 1098.

Mindlin, R. (1949). Compliance of elastic bodies in contact. *Journal of Applied Mechanics, vol. Trans. ASME, Series E* (16), 259–268.

Mindlin, R. and H. Deresiewicz (1953). Elastic spheres in contact under varying oblique forces. *Journal of Applied Mechanics 20*, 327–344.

Morlet, J., G. Arens, E. Fourgeau, and D. Glard (1982). Wave propagation and sampling theory-part i: Complex signal and scattering in multilayered media. *Geophysics 47*(2), 203–221.

Mota, M., J. Teixeira, W. Bowen, and A. Yelshin (2001). Binary spherical particle mixed beds: porosity and permeability relationship measurement.

Müller, T., B. Gurevich, and M. Lebedev (2010). Seismic wave attenuation and dispersion resulting from wave-induced flow in porous rocksŮa review. *Geophysics 75*(5), 75A147–75A164.

Murphy, W. (1982). Effects of partial water saturation on attenuation in massilon sandstone and vycor porous glass. *The Journal of the Acoustical Society of America 71*(6), 1458–1468.

Murphy, W., K. Winkler, and R. Kleinberg (1984). Frame modulus reduction in sedimentary rocks: The effect of adsorption on grain contacts. *Geophysical Research Letters 11*(9), 805–808.

Nazarova Cherriere, M. (2014). *Wettability study through x-ray micro-ct pore space imaging in eor applied to lsb recovery process*. Ph. D. thesis, Université de Pau et des Pays de l'Adour, France.

Neev, J. and F. Yeatts (1989). Electrokinetic effects in fluid-saturated poroelastic media. *Physical Review B 40*(13), 9135.

Neishtadt, N., L. Eppelbaum, and A. Levitski (2006). Application of piezoelectric and seismoelectrokinetic phenomena in exploration geophysics: Review of russian and israeli experiences. *Geophysics 71*(2), B41.

O'Connell, R. and B. Budiansky (1977). Viscoelastic properties of fluid-saturated cracked solids. *Journal of Geophysical Research 82*(36), 5719–5735.

Palmer, I. and M. Traviolia (1980). Attenuation by squirt flow in undersaturated gas sands. *Geophysics 45*(12), 1780–1792.

Pandit, B. and J. Savage (1973). An experimental test of lomnitz's theory of internal friction in rocks. *Journal of Geophysical Research 78*(26), 6097–6099.

Parkhomenko, E. (1971). *Electrification phenomena in rocks*. Pleunum Press.

Parkhomenko, E. and I. Gaskarov (1971). Borehole and laboratory studies of the seismoelectric effect of the second kind in rocks. *Izv. Akad. Sci. USSR, Physics Solid Earth 9*, 663–666.

Parkhomenko, I., C. Tsze-San, and C. Chien-San (1964). A study of the influence of moisture on the magnitude of the seismoelectric effect in sedimentary rocks by a laboratory method. *Bull.(Izv.) Acad. Sci., USSR, Geophys. Ser 2*, 115–118.

Perrier, F. and P. Morat (2000). Characterization of electrical daily variations induced by capillary flow in the non-saturated zone. *Pure and Applied Geophysics 157*(5), 785–810.

Peselnick, L. and I. Zietz (1959). Internal friction of fine-grained limestones at ultrasonic frequencies. *Geophysics 24*(2), 285–296.

Phillips, S., H. Ozbek, and R. Otto (1978). Basic energy properties of electrolytic solutions database. In *6th Int. CODATA Conference*.

Ploix, M. (2006). *Étude de l'atténuation des ondes ultrasonores. Application au contrôle non destructif des soudures en acier inoxydable austénitique*. Ph. D. thesis, Thèse de Doctorat. Lyon: Thèse de doctorat: Institut National des Sciences Appliquées de Lyon, 144 p.

Pride, S. (1994). Governing equations for the coupled electromagnetics and acoustics of porous media. *Physical Review B 50*(21), 15678–15696.

Pride, S. (2005). Relationships between seismic and hydrological properties. In *Hydrogeophysics*, pp. 253–290. Springer.

Pride, S., J. Berryman, and J. Harris (2004). Seismic attenuation due to wave-induced flow. *Journal of Geophysical Research: Solid Earth (1978–2012) 109*(B1), B01201.

Pride, S. and S. Garambois (2002). The role of biot slow waves in electroseismic wave phenomena. *Journal of the Acoustical Society of America 111*, 697.

Pride, S. and S. Garambois (2005). Electroseismic wave theory of frenkel and more recent developments. *Journal of Engineering Mechanics 131*, 898.

Pride, S. and M. Haartsen (1996). Electroseismic wave properties. *Journal of the Acoustical Society of America 100*, 1301.

Pride, S. and F. Morgan (1991). Electrokinetic dissipation induced by seismic waves. *Geophysics 56*(7), 914–925.

Quincke, G. (1861). Ueber die fortführung materieller theilchen durch strömende elektricität. *Annalen der Physik 189*(8), 513–598.

Reine, C., M. van der Baan, and R. Clark (2009). The robustness of seismic attenuation measurements using fixed-and variable-window time-frequency transforms. *Geophysics 74*(2), WA123–WA135.

Reppert, P. and F. Morgan (2002). Frequency-dependent electroosmosis. *Journal of Colloid and Interface Science 254*(2), 372–383.

Reppert, P., F. Morgan, D. Lesmes, and L. Jouniaux (2001). Frequency-dependent streaming potentials. *Journal of Colloid and Interface Science 234*(1), 194–203.

Reuss, F. (1809). Sur un nouvel effet de l'électricité galvanique. *Mem. Soc. Imp. Natur. Moscou 2*, 327–337.

Revil, A., G. Barnier, M. Karaoulis, P. Sava, A. Jardani, and B. Kulessa (2013). Seismoelectric coupling in unsaturated porous media: theory, petrophysics, and saturation front localization using an electroacoustic approach. *Geophysical Journal International 196*(2), 867–884.

Revil, A. and A. Cerepi (2004). Streaming potentials in two-phase flow conditions. *Geophysical research letters 31*(11).

Revil, A. and A. Jardani (2010). Seismoelectric response of heavy oil reservoirs: theory and numerical modelling. *Geophysical Journal International 180*(2), 781–797.

Revil, A., N. Linde, A. Cerepi, D. Jougnot, S. Matthäi, and S. Finsterle (2007). Electrokinetic coupling in unsaturated porous media. *Journal of Colloid and Interface Science 313*(1), 315–327.

Revil, A., P. Pezard, and P. Glover (1999). Streaming potential in porous media: 1. theory of the zeta potential. *Journal of Geophysical Research 104*(B9), 20021–20031.

Revil, A., H. Schwaeger, L. Cathles, and P. Manhardt (1999). Streaming potential in porous media: 2. theory and application to geothermal systems. *Journal of Geophysical Research: Solid Earth (1978–2012) 104*(B9), 20033–20048.

Rouaud, M. (2012). *Probabilités, Statistiques Et Approches Multicritéres*. BoD-Books on Demand France.

Russell, R., K. Butler, A. Kepic, and M. Maxwell (1997). Seismoelectric exploration. *The Leading Edge 16*, 1611.

Sahu, S., G. Panda, and N. George (2009). An improved s-transform for time-frequency analysis. In *Advance Computing Conference, 2009. IACC 2009. IEEE International*, pp. 315–319. IEEE.

Savage, J. (1969). Comments on paper by rb gordon and la davis,Śvelocity and attenuation of seismic waves in imperfectly elastic rockŠ. *Journal of Geophysical Research 74*(2), 726–728.

Schakel, M. and D. Smeulders (2010). Seismoelectric reflection and transmission at a fluid/porous-medium interface. *Journal of the Acoustical Society of America 127*, 13.

Schakel, M., D. Smeulders, E. Slob, and H. Heller (2011a). Laboratory measurements and theoretical modeling of seismoelectric interface response and coseismic wave fields. *Journal of Applied Physics 109*, 074903.

Schakel, M., D. Smeulders, E. Slob, and H. Heller (2011b). Seismoelectric fluid/porous-medium interface response model and measurements. *Transport in Porous Media*, 1–12.

Schakel, M., D. Smeulders, E. Slob, and H. Heller (2011c). Seismoelectric interface response: Experimental results and forward model. *Geophysics 76*(4), N29.

Schoemaker, F., N. Grobbe, M. Schakel, S. De Ridder, E. Slob, and D. Smeulders (2012). Experimental validation of the electrokinetic theory and development of seismoelectric interferometry by cross-correlation. *International Journal of Geophysics 2012*.

Sen, P. and P. Goode (1992). Influence of temperature on electrical conductivityon shaly sands. *Geophysics 57*(1), 89.

Simon, C., S. Ventosa, M. Schimmel, A. Heldring, J. Dañobeitia, J. Gallart, and A. Mànuel (2007). The s-transform and its inverses: Side effects of discretizing and filtering. *Signal Processing, IEEE Transactions on 55*(10), 4928–4937.

Singarimbun, A., H. Mahardika, and U. Srigutomo, W.and Fauzi (2009). A preliminary result of seismoelectric responses study on shallow fluid-saturated layer: Numerical modeling using transfer function approach. *Indonesian Journal of Physics 19*(3), 61–68.

Slob, E. and K. Wapenaar (2007). Electromagnetic green's functions retrieval by cross-correlation and cross-convolution in media with losses. *Geophysical Research Letters 34*(5).

Smeulders, D., N. Grobbe, H. Heller, and M. Schakel (2014). Seismoelectric conversion for the detection of porous medium interfaces between wetting and nonwetting fluids. *Vadose Zone Journal 13*(5).

Spencer, J. (1981). Stress relaxations at low frequencies in fluid-saturated rocks: Attenuation and modulus dispersion. *Journal of Geophysical Research: Solid Earth (1978–2012) 86*(B3), 1803–1812.

Stern, O. (1924). Zur theorie der elektrolytischen doppelschicht. *Zeitschrift für Elektrochemie und angewandte physikalische Chemie 30*(21-22), 508–516.

Stockwell, R., L. Mansinha, and R. Lowe (1996). Localization of the complex spectrum: the s transform. *Signal Processing, IEEE Transactions on 44*(4), 998–1001.

Stoll, R. (1974). Acoustic waves in saturated sediments. In *Physics of sound in marine sediments*, pp. 19–39. Springer.

Stoll, R. (1977). Acoustic waves in ocean sediments. *Geophysics 42*(4), 715–725.

Stoll, R. (1985). Marine sediment acoustics. *The Journal of the Acoustical Society of America 77*(5), 1789–1799.

Stoll, R. (1989). Stress-induced anisotropy in sediment acoustics. *The Journal of the Acoustical Society of America 85*(2), 702–708.

Strahser, M. (2006). *Near surface seismoelectrics in comparative field studies*. Ph. D. thesis, Christian-Albrecht-Universität zu Kiel, Germany.

Strahser, M., L. Jouniaux, P. Sailhac, P. Matthey, and M. Zillmer (2011). Dependence of seismoelectric amplitudes on water content. *Geophysical Journal International*.

Strahser, M., W. Rabbel, and F. Schildknecht (2007). Polarisation and slowness of seismoelectric signals: a case study. *Near Surface Geophysics 5*(2), 97–114.

Suman, R. and R. Knight (1997). Effects of pore structure and wettability on the electrical resistivity of partially saturated rocks-a network study. *Geophysics 62*(4), 1151–1162.

Teja, A. and P. Rice (1981). Generalized corresponding states method for the viscosities of liquid mixtures. *Industrial & Engineering Chemistry Fundamentals 20*(1), 77–81.

Terzaghi, K. (1943). *Theoretical soil mechanics*, Volume 18. Wiley New York.

Thompson, A. and G. Gist (1993). Geophysical applications of electrokinetic conversion. *The leading edge 12*, 1169.

Thompson, A., S. Hornbostel, J. Burns, T. Murray, R. Raschke, J. Wride, P. McCammon, J. Sumner, G. Haake, M. Bixby, et al. (2007). Field tests of electroseismic hydrocarbon detection. *Geophysics 72*(1), N1.

Thompson, R. (1936). The seismic electric effect. *Geophysics 1*(3), 327.

Toksöz, M., C. Cheng, and A. Timur (1976). Velocities of seismic waves in porous rocks. *Geophysics 41*(4), 621–645.

Toksöz, M., D. Johnston, and A. Timur (1979). Attenuation of seismic waves in dry and saturated rocks: I. laboratory measurements. *Geophysics 44*(4), 681–690.

Toms-Stewart, J., T. Müller, B. Gurevich, and L. Paterson (2009). Statistical characterization of gas-patch distributions in partially saturated rocks. *Geophysics 74*(2), WA51–WA64.

Ventosa, S., C. Simon, M. Schimmel, J. Dañobeitia, and A. Mànuel (2008). The s-transform from a wavelet point of view. *Signal Processing, IEEE Transactions on 56*(7), 2771–2780.

Walsh, J. (1966). Seismic wave attenuation in rock due to friction. *Journal of Geophysical Research 71*(10), 2591–2599.

Walton, K. (1987). The effective elastic moduli of a random packing of spheres. *Journal of the Mechanics and Physics of Solids 35*(2), 213–226.

Wang, H. (2000). *Theory of linear poroelasticity*. Princeton University Press.

Wapenaar, K. and J. Fokkema (2006). GreenŠs function representations for seismic interferometry. *Geophysics 71*(4), SI33–SI46.

Wapenaar, K., E. Slob, and R. Snieder (2006). Unified greenŠs function retrieval by cross correlation. *Physical Review Letters 97*(23), 234301.

Wapenaar, K., E. Slob, and R. Snieder (2008). Seismic and electromagnetic controlled-source interferometry in dissipative media. *Geophysical Prospecting 56*(3), 419–434.

Ward, R. and M. Toksöz (1971). Causes of regional variation of magnitudes. *Bulletin of the Seismological Society of America 61*(3), 649–670.

Ward, S. and G. Hohmann (1987). Electromagnetic theory for geophysical applications, *in* nabighian m.n., electromagnetic methods in applied geophysics. *Society of Exploration Geophysicists 1*, 131–311.

Warden, S. (2012). *Conversions sismo-électromagnétiques en milieux poreux*. Ph. D. thesis, Université de Strasbourg.

Warden, S., S. Garambois, L. Jouniaux, D. Brito, P. Sailhac, and C. Bordes (2013). Seismoelectric wave propagation numerical modelling in partially saturated materials. *Geophysical Journal International 194*(3), 1498–1513.

Warden, S., S. Garambois, P. Sailhac, L. Jouniaux, and M. Bano (2012). Curvelet-based seismoelectric data processing. *Geophysical Journal International 190*(3), 1533–1550.

Waxman, M. and L. Smits (1968). Electrical conductivities in oil-bearing shaly sands. *Society of Petroleum Engineers Journal*, 107–122.

White, B. (2005). Asymptotic theory of electroseismic prospecting. *SIAM Journal on Applied Mathematics*, 1443–1462.

White, J. (1966). Static friction as a source of seismic attenuation. *Geophysics 31*(2), 333–339.

White, J. (1975). Computed seismic speeds and attenuation in rocks with partial gas saturation. *Geophysics 40*(2), 224–232.

Winkler, K. (1985). Dispersion analysis of velocity and attenuation in berea sandstone. *Journal of Geophysical Research: Solid Earth (1978–2012) 90*(B8), 6793–6800.

Winkler, K. and A. Nur (1979). Pore fluids and seismic attenuation in rocks. *Geophysical Research Letters 6*(1), 1–4.

Winkler, K. and A. Nur (1982). Seismic attenuation: Effects of pore fluids and frictional-sliding. *Geophysics 47*(1), 1–15.

Winkler, K., A. Nur, and M. Gladwin (1979). Friction and seismic attenuation in rocks. *Nature 277*, 528–531.

Wood, A. (1955). *WA textbook of sound*. New York: The Maclillan Corporation.

Wyllie, M., G. Gardner, and A. Gregory (1962). Studies of elastic wave attenuation in porous media. *Geophysics 27*(5), 569–589.

Zhu, Z., S. Chi, X. Zhan, and M. Toksöz (2008). Theoretical and experimental studies of seismoelectric conversions in boreholes. *Communications in Computational Physics 3*(1), 109–120.

Zhu, Z., M. Haartsen, and M. Toksöz (1999). Experimental studies of electrokinetic conversions in fluid-saturated borehole models. *Geophysics 64*(5), 1349.

Zhu, Z., M. Haartsen, and M. Toksöz (2000). Experimental studies of seismoelectric conversions in fluid-saturated porous media. *Journal of Geophysical Research 105*(B12), 28055–28.

Zhu, Z. and M. Toksöz (2003). Crosshole seismoelectric measurements in borehole models with fractures. *Geophysics 68*(5), 1519.

Zhu, Z. and M. Toksoz (2003). Effects of saturant conductivity on seismoelectric conversion. Technical report, Massachusetts Institute of Technology. Earth Resources Laboratory.

Zhu, Z. and M. Toksöz (2005). Seismoelectric and seismomagnetic measurements in fractured borehole models. *Geophysics 70*, F45.

Zhu, Z. and M. Toksöz (2013). Experimental measurements of the streaming potential and seismoelectric conversion in berea sandstone. *Geophysical Prospecting 61*(3), 688–700.

Zyserman, F., P. Gauzellino, and J. Santos (2010). Finite element modeling of shte and psvtm electroseismics. *Journal of Applied Geophysics 72*(2), 79–91.

Zyserman, F., L. Jouniaux, S. Warden, and S. Garambois (2015). Borehole seismoelectric logging using a shear-wave source: Possible application to co_2 disposal *International Journal of Greenhouse Gas Control 33*, 89–102.